Time-dependent wave packet dynamics of adiabatic and nonadiabatic reactive scattering

A Thesis
submitted for the Degree of

Doctor of Philosophy

by

Jayakrushna Sahoo

हैदराबाद विश्वविद्यालय
University of Hyderabad

प्रतिष्ठित संस्थान
INSTITUTION OF EMINENCE
राष्ट्रीय अपेक्षाएँ, वैश्विक मानक
National Needs, Global Standards

School of Chemistry
University of Hyderabad
Hyderabad - 500 046, INDIA

December 2022

Dedicated

to
my Family

STATEMENT

I hereby declare that the matter embodied in the thesis entitled **"Time-dependent wave packet dynamics of adiabatic and nonadiabatic reactive scattering"** is the result of investigations carried out by me in the School of Chemistry, University of Hyderabad, India under the supervision of Prof. Susanta Mahapatra.

In keeping with the general practice of reporting scientific investigations, acknowledgements have been made wherever the work described is based on the finding of other investigators.

29/12/2022

Date

Hyderabad 500046

Jayakrushna Sahoo

Signature of the candidate

Certificate

School of Chemistry
University of Hyderabad
Hyderabad-500 046
India

हैदराबाद विश्वविद्यालय
University of Hyderabad

प्रतिष्ठित संस्थान
INSTITUTION OF EMINENCE
राष्ट्रीय अपेक्षाएँ, वैश्विक मानक
National Needs, Global Standards

This is to certify that the work contained in this thesis, titled "**Time-dependent wave packet dynamics of adiabatic and nonadiabatic reactive scattering**"by **Jayakrushna Sahoo (Reg.No. 16CHPH12)**, has been carried out under my supervision and is not submitted elsewhere for a degree.

This thesis is free from plagiarism and has not been submitted previously in part or in full to this or any other University or Institution for award of any degree or diploma.

Parts of this thesis have been published in the following publications:

1. Sugata Goswami, **Jayakrushna Sahoo**, Suranjan K. Paul, T. Rajagopala Rao and S. Mahapatra*, J. Phys. Chem. A **124**, 9343 (2020).
2. **Jayakrushna Sahoo**, Ajay Mohan Singh Rawat and S Mahapatra*, J. Phys. Chem. A **125**, 3387 (2021).
3. **Jayakrushna Sahoo**, Ajay Mohan Singh Rawat and S Mahapatra*, Phys. Chem. Chem. Phys. **23**, 27327 (2021).

and presented in following conferences :

1. 16^{th} Theoretical Chemistry Symposium (TCS-2019), 13-16 February, 2019, at BITS Pilani, Pilani campus, Rajasthan, India (International).
2. The DAE Symposium in Current Trends in Theoretical Chemistry (CTTC-2020), 23-25 September, 2021, (Virtual) by Chemistry Division, Bhabha Atomic Research Centre, Mumbai, India (National).
3. 17^{th} Theoretical Chemistry Symposium (TCS-2021), 11-14 December, 2021, (Virtual) by Department of Chemistry, IISER Kolkata, India (International).

Further, the student has passed the following courses towards fulfilment of coursework requirement for Ph.D.

Course code	Name	Credits	Pass/Fail
1. CY-801	Research Proposal	3	Pass
2. CY-805	Instrumental Methods-A	3	Pass
3. CY-806	Instrumental Methods-B	3	Pass
4. CY-404	Symmetry and Mathematics	3	Pass
5. CY-457	Physical Chemistry Lab	3	Pass
6. CY-503	Chemical Dynamics	3	Pass
7. CY-577	Computational Chemistry	3	Pass

29/12/2022

Date

Hyderabad 500046

S Mahapatra

(Prof. Susanta Mahapatra)

Supervisor

Susanta Mahapatra
Professor
School of Chemistry
University of Hyderabad
Hyderabad-500 046 A.P. India

28/12/2022

Dean

School of Chemistry

University of Hyderabad

Dean
SCHOOL OF CHEMISTRY
University of Hyderabad
Hyderabad-500 046

" Of course! I was an ordinary person who studied hard. There is no miracle people! It just happens they got interest in these things and then learned all the stuff. They are just people. There is no talent or special miracle ability to understand Quantum Mechanics or miracle ability to imagine electromagnetic fields that comes without practice and reading and learning and study. So if you say you take an ordinary person who is willing to devote a great deal of time and study and work and thinking and mathematics then he's become a scientist! "

- *Richard P. Feynman*

Acknowledgements

It is my great pleasure to express my deepest gratitude to my Ph.D. supervisor Prof. S. Mahapatra for his inspiration throughout my Ph.D. This endeavour would not have been possible without his constant encouragement, guidance and support. I will always be indebted to him for giving me the opportunity to learn how to approach a research problem and how to take it forward. I am also thankful to him for giving me the appropriate freedom to envisage and work on my research problems. I have always admired his high scientific standard and his art of thoughtful scientific writing of the papers. I am really grateful that I got the opportunity to learn all this from him and still continuing doing it. I am grateful to him for introducing me to the century old and forever fascinating the H + H_2 reactive system which helped me to deepen my understanding of reactive scattering dynamics.

I extend my thanks to my doctoral committee members, Prof. M. Durga Prasad and Dr. D. Barik for their valuable suggestions and encouragements. I am grateful to Prof. M. Durga Prasad for many valuable discussions and clarifying my countless doubts on quantum mechanics and quantum chemistry. I am thankful to him for allowing me to attend his lectures on chemical binding. I also thank Prof. K. D. Sen for allowing me to be a teaching assistant of him.

I thank the present and former deans, all faculty members, all non-teaching staff and all other colleagues of School of Chemistry, and also thank all the non-teaching staff of the admin block of the University who helped me in various occasions .

I would like to extend my sincere thanks to all my present and former Labmates with whom I had an opportunity to work. Thanks to all of them for providing me a friendly and cheerful environment in the lab. I think words would not be enough for me to thank Dr. Sugata Goswami whose influence has shaped up my approach towards my research problems. I think I am very fortunate to get senior colleague like him who has helped me in every aspect of my research career, and still I receive many assistance from him when I reach out to him. I always admire his level of dignity and code of ethics towards scientific research and hope that I will keep on learning from him. I am very much thankful to him for teaching me Linux terminal, FORTRAN progaming and of course the basics of reaction dynamics. I always admire and also sometimes envy his way of teaching and explaining things in a simple manner. I thank Dr. Rudraditya Sarkar for treating me like a friend when I joined the group and showing me around the beautiful campus of our University. I also thank him for introducing me to the

campus life, various functions and of course night cup cricket and football tournaments. I also thank him for many valuable discussions on nonadiabatic dynamics, symmetry and group theory. I thank Dr. Krishna Reddy Nandipati for many helpful suggestions and countless discussions on the fundamentals of quantum mechanics and wave packet dynamics. I thank Mr. Arun Kumar Kanakati for his immense help and being a great colleague throughout my PhD career. I thank him for all his support and kindness during my entire Ph.D. I thank Mrs. Daradi Baishya for being a delightful colleague, labmate, friend and helping me in various occasions. I thank Mr. Ajay Rawat for assisting me in many of my research problems. I also thank my other former and present labmates, Dr. Arpita Ghosh, Dr. Karunamoy Rajak, Dr. Satyendra Gupta, Nitai, Jhansi, Alamgir, Rani, Yarram Ajay and Dr. B. Majusha for maintaining a great and stimulating atmosphere in the lab. I also thank Soubhik, Shachi, Bishwamohan and Jagori for being colleagues of mine at different times.

I thank all of my Ph.D. batchmate for their help, support and care in various times. Particularly, I thank Prachi and Mamina (my tea partners) for their enormous help and favour, and making me a tea person. I am thankful to both of them for their help, support and care and helping in my difficult times during my Ph.D. I also thank my other bachmates, Soutrick, Anupam Da, Gorachand, Subham Dutta, Subham Debnath, Suman Mondal, Alim, Pritam, Saradamoni, Jada Ravi, Ravinder, Nilanjan, Irfan, Narshimhulu, Soumya, Jyotsna, Laxman and Akram for their help and support.

A special thanks to Tanmaya Bhai, Sameeta Di, Sipra Di and Rajendra Bhai for being like my elder brother and sister and helping me in various occasions in my Ph.D. life. I am very lucky to come to know a person like Tanmaya Bhai who has been a brother, senior colleague, friend, and what not. I also thank to my Chemistry Odia Family, Pradeepta, Santanu, Tejmani, Satya, Umashis, Saritha, Priya, Biswa, Baikuntha, Chiru, Sailendra, Saroj Panda, Gopendra, Jagannath, Abhipsa, Smrutilipi, Soumya Srimayee, Deepu, Itishree, Jyoti Prakash, Subhashree for their love and care during my stay at Hyderabad. Thanks to all of them for many loving and unforgettable memories. I also thank Tapan Bhai, Prasanta Bhai, Pratap Bhai, Dibakar Bhai, Raaj Bhai, Kunal Bhai, Dhiren Bhai, Dillip Bhai, Kali Bhai, Nitya Bhai, Ranjit Bhai, Abhaya Bhai, Goura Bhai, Rashmi Di, Rekha Di, Atasi Nani, Hemadri Bhai, Ashis Bhai, Chakra Bhai, Dhub Bhai, Manas Bhai, Abhisek, Prakash, Goutam, Ajaya Satyabrata, Swayam Sikha, Partha, Alibha for their love and support. I thank all of my Odia Cultural Committee (OCC; now OCA) members, particularly, Sidharth Sir, Pramod Sir, Pragnya Madam. I beg pardon

if I miss to acknowledge someone. I thank all of them who assisted me in various ways at different times.

I would like to acknowledge UGC for doctoral fellowship and DST-SERB for funding. I also acknowledge the Center for Modelling Simulation and Design (CMSD), University of Hyderabad, and Translational Research Facility (UPEII of UGC), School of Chemistry, University of Hyderabad for computational facility.

Finally, I thank my brother Mr. Jitendra Sahoo, my sister Mrs. Nirupama Sahoo, and my family members for their huge support and encouragement to do Ph.D. I would never forget the contribution and sacrifices they have made for me for choosing a research career and doing Ph.D. I am also grateful to all my teachers since my childhood for their encouragement to do science.

Jayakrushna Sahoo

Abbreviations

ADT	adiabatic to diabatic transformation
aug-cc-pVQZ	augmented correlation-consistent polarized Valence Quadrapule-ζ
BO	Born-Oppenheimer
BH	Born-Haung
BSSE	Basis set superposition error
CASSCF	complete active space self consistent field
CC	Coriolis coupling
CDM	Chaotic dynamical model
CI	Configuration interaction
CID	Collision induced dissociation
CS	centrifugal sudden
DCS	Differential cross section
DMBE	Double many body expansion
DMBE-SEC	Double many body expansion-scaled external correlation
DPEM	Diabatic potential energy matrix
DVR	discrete variable representation
E_{col}	collision energy
FBR	Finite basis representation
FFT	Fast Fourier transform
FVCAS	Full velance complete active space
GP	Geometric phase
ICS	Integral cross section
IREP	irreducible representation
IVR	Intramolecular vibrational redistribution
JT	Jahn-Teller
LOCNESS	Line-of-centers nearly elastic specular scattering model
MEP	Minimum energy path
MRCI	Multi-reference configuration interaction
MR-CISD	Multi-reference configuration interaction singles and doubles
PES	Potential energy surface
PHOTOLOC	Photoinitiated reaction analyzed by the law of cosines
PCB	Product coordinate based
QBS	Quantum bottleneck state
QCT	Quasi-classical trajectory
QM	Quantum mechanical

QM-CC	Quantum mechanical including Coriolis coupling
QM-CS	Quantum mechanical with centrifugal sudden
QM-GDF	Quantum mechanical generalized deflection function
QSSBSS	Quantum-state-specific backward scattering spectroscopy
RCB	Reactant coordinate based
R-CSA	Reactive-centrifugal sudden approximation
REMPI	Resonance-enhanced multiphoton ionization
R-IOSA	Reactive infinite-order sudden approximation
RPA	Random phase approximation
RPD	Reactant-product decoupling
RRKM	Rice-Ramsperger-Kassel-Marcus
RWP	Real wave packet
SARP	Stark-induced adiabatic Raman passage
SF	Space-fixed
SQM	Stastical quantum mechanical
SVP	Sudden vector projection
TDSE	Time-dependent Schrödinger equation
TDQM	Time-dependent quantum mechanical
TDWP	Time-dependent wave packet
TIQM	Time-independent quantum mechanical
TSWP	Transition-state wave packet
WP	Wave packet

Contents

Chapter 1

Introduction

Understanding the chemical transformation of substances and predicting its outcomes lies in the heart of chemistry. As is well known, a chemical change takes place when the reacting species, or say the reagents change their chemical identity by breaking the old chemical bonds to produce the products forming new bonds. These chemical transformations take place in between the atoms or molecules of the reagents. Hence, a molecular level understanding of these processes is necessary in order to explain the underlying mechanism. This field of study falls under a broad umbrella of molecular reaction dynamics [1]. The central theme of molecular reaction dynamics is to gain an in-depth understanding of the chemical processes at the microscopic level. Basically, it concerns with the answers to the fundamental questions, "*how exactly does a chemical reaction occur? how to predict and control its outcomes?*". Studies of reaction dynamics in many senses is different from the bulk kinetics study of the chemical reactions. Most importantly, in bulk kinetics studies the reaction rate is measured under the thermal equilibrium condition. In such cases the measured rate constant involves many averages over all the accessible states of reagent and product. As a limitation such studies are not capable to provide the detailed required information about the reaction at a molecular level which is lost due to averaging. In contrast, the study of molecular reaction dynamics offers a microscopic level understanding of the reactions without averaging any information, and seek to explicate what actually happens to the atoms or molecules during the reaction events. In addition, the informations obtained from reaction dynamical studies can provide any particulars of the reaction in regard to the bulk kinetics with appropriately averaging whenever required. Hence, studying reaction dynamics is also crucial in interpreting the chemical kinetics of a reaction at a macroscopic level.

Most of the chemical phenomena occuring in the universe involves a series of or a chain of basic single reaction steps. These individual steps are known as *elementary chemical reactions*. For example, the reaction between hydrogen (H_2) and oxygen (O_2) to form water (H_2O),

$$H_2 + O_2 \rightarrow 2H_2O$$

generally involves the following elementary reaction steps.

$$H_2 + O_2 \rightarrow H^\bullet + HO_2^\bullet$$
$$H^\bullet + O_2 \rightarrow O^\bullet + OH^\bullet$$
$$O^\bullet + H_2 \rightarrow OH^\bullet + H^\bullet$$
$$OH^\bullet + H_2 \rightarrow H_2O + H^\bullet$$

The elementary reactions are generally part of big chemical reaction networks which spans from simple molecules to complex molecular systems. They play a central role in elucidating the mechanism of the whole reaction network. Hence understanding of the elementary reactions is important in order to provide any information about the chains of reactions they are involved in. Among various types of elementary reactions the bimolecular reactions are most common. Research on the bimolecular reactions were started in the preliminary days from studying the simple atom-diatom collisions in gas phase, and still it is one of the most important area of research, both in experimental and theoretical chemical dynamics [2]. Studying such reactions has immmense importance in the chemistry of primordial universe, interstellar media and planetary atmosphere, as well as in exploring the chemistry of various combustion processes [3]. Many of such bimolecular reactions, particularly those involving alkali and alkaline earth metals have been studied at the cold (temperature below 1 K) and ultracold (temperature below 1 mK) condition because of their potential applications in quantum information science [4].

The bimolecular elementary reactions can be thought of as collisional events between the reacting species, scattering products into various possible directions. Every single collision corresponding to the elementary reaction are uniquely characterized by the velocity distributions, angular distributions, and rotational and vibrational quantum state distributions of the newly formed products. These properties demonstrate the nature of force acting among the constituent species during the reaction. Furthermore, the outcome of a reactive chemical collision also depends on the chemical identity and structure of the reacting species, and also on the relative orientation, velocity, and their electronic, vibrational and rotational states. For example, consider a typical S_N2 raction,

$$F^- + CH_3Cl \rightarrow CH_3F + Cl^-.$$

For this reaction, the product formation will be more facile if the methyl chloride is oriented in such a way that it faces the approaching F^- ion from the CH_3 side rather than the Cl side. In such situation, the Cl^- ion is expected to scatter into the forward direction with reference to the initial approach direction of F^- ion. Moreover, the products are expected to scatter with high relative velocity as a consequence of breaking of C-Cl bond, and the reaction cross section can be enhanced by exciting the C-Cl stretching mode. The intricate dependency of the outcome of a bimolecular collisional encounter on a broad range of aspects has made their study highly exciting and also very challenging too.

On the experimental side, many sophisticated techniques have been developed in the last few decades to accurately examine the reaction dynamics of bimolecular collisions. Most importantly, the emergence of crossed molecular beam apparatus in combination with suitable detection strategy has made the investigation of gas phase reactions possible to a single collision event level by isolating the molecules/atoms of interest spatially and also temporally. With the use of state-of-the-art pump-probe femtosecond spectroscopic techniques the fast time scale measurements can be perfomed not only in the gas phase, but also in the liquid and other condensed phases [5, 6]. Furthermore, with the inception of futuristic detection techniques, like the laser induced fluorescence, resonance-enhanced multiphoton ionization (REMPI), time-of-flight mass spectrometry, Rydberg atom tagging time-of-flight spectroscopy, and velocity map imaging, the angular distribution of quantum state-resolved products can be measured with highest possible resolution and unprecedented accuracy [7]. In case of certain reagents that are difficult to generate in molecular beams, PHOTOLOC (Photoinitiated reaction analyzed by the law of cosines) [8] technique can work as an alternative to generate the required reagent with appropriate velocity by photodissociating some precursor molecules [9–12]. The Quantum-state-specific backward scattering spectroscopy (QSSBSS) technique [13] can be used to measure the collision energy dependent angular distribution of quantum state-resolved products which is mainly helpful in characterizing the reactive resonances in bimolecular reactions. Moreover, with the use of Stark-induced adiabatic Raman passage (SARP) technique [14], the reagent molecules can now be prepared efficiently in their highly rovibrational excited quantum states with a large population density. With the help of this technique the stereo-dynamical coherent control of inelastic cold collision between He and D_2/HD have recently been perfomed by the Zare group [15–17], which showed many interesting phenomena such as the role of shape

resonance, the double-slit like molecular quantum interferometry etc. Reactive scattering experiment with rovibrationally excited reagent using the SARP technique is yet to be explored.

Besides their importance in elucidating the scattering mechanisms, the experimental study of molecular collisions, particularly at cold and ultracold temperature conditions, also aims at for the effective probe of the interaction potential among the colliding atoms. In this regard the complementarity between experimental measurements and theoretically calculated results plays an extremely important role. The connection between theory and experiment is especially strong and has been compelling in the field of molecular reaction dynamics [18].

The entity that serves as a bridge between theory and experiment is the *potential energy surface* (PES), a fundamentally crucial concept in reaction dynamics. The PES describes the potential energy with respect to a particular electronic state of the system under study as a function of nuclear coordinates of each atom involved. The potential energy arises from the electrostatic interactions among the electrons and nuclei of the system in a given electronic state. The determination of PES is generally done by invoking the celebrated Born-Oppenheimer (BO) approximation [19]. The BO approximation eases the theoretical procedure by disentangling the electronic and nuclear motion from each other and then treating them separately. This is justified since the nuclei are $\approx$1836 times heavier than the electrons and hence remain almost stationary when the electrons complete a cycle of their motion. Therefore, to a good approximation it is reasonable to treat the electronic and nuclear motion separately, such that the nuclei can be thought as to move under the average potential established by electrons, while the electrons move instantaneously in a field of fixed nuclei. In principle, the PES is generated by solving the electronic Schrödinger equation by *ab initio* electronic structure methods for different chosen fixed nuclear configurations, and then by fitting globally the *ab initio* generated potential energy points to suitable analytic function or following interpolation techniques. In recent years the field of quantum chemistry has seen an enormous advancement in the development of more accurate *ab initio* electronic structure theory which has made the precise calculation of highly accurate *ab initio* electronic energies feasible. On the other hand, the advancement of fitting techniques, particularly the emergence of machine-learning based artificial neural network and gaussian process regression techniques [20] has perfected the ability to map out the global PESs with high accuracy and efficiency, not only for atom-diatom systems but also for bimolecular reactive systems involving many nuclear degrees of freedom.

The PES acts as a force field and provides the potential energy for nuclear motion. The gradient of the PES at a given point corresponding to a particular nulear configuration determines the force acting on the atoms on that point, defining their subsequent motion. Different region of the PES corresponds to different molecular structure of the system under investigation. The region corresponding to the reagents and products occur at the asymptotic part of PES. The most important points on a PES are the stationary points which correspond to the structures where the system remain stationary without any external force *i.e.,* the first partial derivative of the potential energy with respect to at least one nuclear degrees of freedom is equal to zero. These points occur in the interaction region of the PES, and include the molecular structure representing the equilibrium minima and the transition states. The stationary points uniquely define the topography or landscape of the underlying PES of a system. The chemical reaction can be imagined as the movement of the nuclei over a potential energy landscape from reagent asymptote to the product asymptote through the interaction region. Hence, once the PES of the system under study is available, the dynamics of the reaction can be studied by solving the equations for nuclear motion on the PES.

The BO approximation relies on the assumption that the electronic wave function behaves *adiabatically* with respect to the nuclear wave function, hence it is also known as the BO adiabatic approximation. Here the term *adiabatic* is in the context of the adiabatic theorem of quantum mechanics which in simpler terms means that if a quantum mechanical system is subjected gradually to a changing external condition, it adjusts/adapts itself to remain in the same functional form (wave function) during the process. In that sense the PES which is calculated by solving the electronic Schrödinger equation is referred to as adiabatic PES, and the electronic and nuclear wave functions are said to be in the adiabatic representation. The validity of the BO approximation remains intact as long as different electronic state PESs of the system are energetically far apart from each other at all possible nuclear configurations. This may seem as an oversimplification because in many cases, even starting from triatomic systems, there is an increasing number of evidence that the adiabatic electronic states can come energetically closer and eventually cross or intersect with each other at certain nuclear configurations, forming avoided crossings and conical intersections [21]. In such situations the electronic states are said to be coupled to each other through the nuclear degrees of freedom, and this coupling is very strong in cases of electronic degeneracies. This leads to break-down of the BO approximation and the situation is no longer adiabatic as the electronic transition now can happen in between the electronic states through the coupling with change in nuclear configurations. This is known as *electronic*

nonadiabatic phenomenon and the coupling between the electronic states are known as *nonadiabatic couplings*. Sometimes the nonadiabatic coupling terms can be ignored under strict BO approximation so as to confine the nuclear motion to a single adiabatic PES, mostly to the ground electronic state PES. This is generally valid in most cases of the bimolecular collisions under thermal conditions, if not all. In such cases a single state adiabatic dynamics is carried out to obtain the reaction observables. However, recent studies have shown that the bimolecular collisions can also be strongly influenced by electronic nonadiabatic transitions [22, 23],even at cold and ultracold temperature conditions [24–27]. In such cases a single state adiabatic dynamics is not sufficient, and the reaction dynamical calculation must be perfomed in a coupled manifold involving more than one electronic states with the inclusion of the nonadiabatic couplings among them. This is generally done numerically efficiently in a *diabatic representation* [28, 29] where the complicacy due to singular nature of the nonadiabatic coupling is circumvented by a suitable unitary transformation [21].

The reliability of the dynamical outcomes depends upon the accuracy of the underlying PES. However, only the accuracy of the PES is not sufficient if the underlying physical principle for describing the dynamics of the quantum mechanical objects, *i.e.,* the atoms and molecules, is not accurate enough to reproduce the experimental measurements within the experimental uncertainties. In principle, the nuclear dynamics can be studied by following various methods with different underlying theory such as quantum mechanical, classical or quasi-classical and statistical methods. The main aim of the theoretical calculation is to compute a few reaction observables whose thorough examination reveals the details of the reaction dynamics. The most common observables for the bimolecular reactions are reaction probability, opacity function, integral and differential cross section, rate constant etc. A more detailed reaction mechanism, *e.g.,* the energy disposal and angular distribution of products, can be elucidated by resolving the reaction observables into the quantum states of product diatom. In such cases it is called as state-to-state dynamical study. The fundamental quantity from which various reaction observables are computed quantum mechanically is known as the scattering matrix or the *S-matrix* [30]. It is a unitary matrix and borrows the similar concept as in particle scattering in theoretical physics [30]. In simpler terms it is defined as a matrix whose individual elements represent the transition probability of an initial quantum state to a final quantum state of a physical system encountering a scattering process. Various quantum mechanical and semi-classical methods can be used to obtain the S-matrix elements of the reactive scattering events in bimolecular collisions.

In quantum mechanical methodologies, the time-dependent quantum mechanical (TDQM) and time-independent quantum mechanical (TIQM) methods are generally followed to study the reactive dynamics, which respectively solve the time-dependent and time-independent Schrödinger equations. In the TIQM approach, the coupled-channel Schrödinger equation is solved as an boundary value problem which involves the diagonalization of the Hamiltonian matrix. Thus this method scales steeply with the size of the problem as $\propto N^3$. For reactive scattering of triatomic systems, it is convenient to use hyperspherical coordinates, which are independent of the arrangement channels. However, it is not very straightforward to use hyperspherical coordinates for larger systems. Due to its potential of handling very low collision energies, the TIQM method is best suited for cold and ultracold collisions. Moreover, the extraction of S-matrix is done for only a single collision energy for each TIQM calculation.

Alternatively, in TDQM approach the time-dependent Schrödinger equation (TDSE) is solved as an initial value problem by wave packet (WP) propagation techniques. That is why this technique is also known as the time-dependent wave packet (TDWP) method. In this thesis, the two acronyms TDQM and TDWP are used synonymously. The TDWP method scales much better than the TIQM methods with respect to the problem size ($\propto N \log N$). Therefore, most of the atom-diatom quantum reactive scattering calculations, and particularly those beyond the triatomic systems, have employed such TDWP methods. Using TDWP method is advantageous in a way that the dynamics of the process can be visualized pictorially by recording the WP snapshots intermittently. For atom-diatom systems, Jacobi coordinates pertinent to either reagent or product channel are most convenient to use in the TDWP methods. However, for state-to-state calculations where the extraction of S-matrix is required, a time-consuming tedious procedure of transformation between the two coordinate systems is inevitable. There are various approaches exist in the literature which uses the TDWP methodology for the calculation of S-matrix elements namely the reactant coordinate based (RCB) [31–33], the product coordinate based (PCB) [34–36] , reactant product decoupling (RPD) [37, 38], and the transition state wave packet (TSWP) [39–41] methods. Moreover, the scattering observables can be computed by calculating the outgoing flux at a dividing surface. In such type of approaches, however, the reaction observables can not be resolved into product internal quantum states. Another major advantage of using the TDWP approach is that the scattering information can be computed for a range of energy, corresponding to the energy range of the initial WP, for a single calculation. Inspite of many advantages of the TDWP method, its major drawback is its inability to operate at very low collision energies. This is because of the long de Broglie wave

length of the WP at low collision energy which consequently needs a longer absorption range, and also a longer grid range, to efficiently damp out the reflected part of the WP at the edge of the grid. Moreover, it needs a longer propagation time for the WP. This particular problem had made the TDWP approach computationally unfeasible for the study of low energy bimolecular collisions. However, with a recent crucial development in the TDWP formalism, particularly in the absorption of the WP at the long range region, it can now be used in the study of bimolecular reactive scattering at cold and ultracold conditions even all the way down to the Wigner threshold regime [42].

There is another quantum mechanical method for studying the dynamics of bimolecular reactions particularly those involve intermediate complex during the reaction which are supported by the deep wells present on the underlying PES. This is known as the statistical quantum mechanical (SQM) method [43–50]. The fundamental supposition underlying the SQM method is that because of the long-lived nature of the intermediate complexes a complete randomization of the available energy into its all degrees of freedom is assumed. This leads to a statistical behaviour of the energy disposal in products. This statistical behaviour is also reflected in the isotropic angular distribution of the products which comes as a consequence of the random nature of the phases of the reactive S-matrix elements. This is due to the fact that the collision complex for such reactions can survive more than a few of its rotational periods. In the formalism of SQM method, the reaction observables are generally computed by calculating the capture probabilities of various reagent and product quantum states into the potential well. The capture probabilities can be efficiently obtained by using TIQM or TDWP methods [48, 49]. The SQM method is generally suitable for the complex-forming bimolecular reactions and can be perfomed with low computational cost particularly when the scalar observables like the integral cross section (ICS) and rate constant are desirable.

The detailed mechanism and the characteristic feature of a bimolecular reaction can be examined from the knowledge of the various reaction observables. The reaction probability gives the probability of the reactive event to occur and is generally expressed as a function of energy. A sharp fluctuation or any type of undulation in the energy dependence of the reaction probability is generally considered as the signature of the reactive resonances in the reaction. When the reaction probabilities are expressed as a function of the impact parameter or the total angular momentum (J) at a particular value of collision energy, it is known as the opacity function. The knowledge of opacity function is crucial in determining the maximum number of partial waves required to obtain the converged reaction cross section. The ICS is defined as the effective area of

target where the reacting species approach to each other and form the products. The differential cross section (DCS) is also called the angular distribution of the products as it provides the information as to which most probable angular direction the product is scattered with reference to the direction of the attacking reagent atom. The DCS has directional property and hence is crucial in examining the scattering mechanism of the reaction. The integration of the DCS over the scattering angle provides the ICS. The rate constant as is well known provides the information about the rate of the reaction and is expressed as a function of the temperature. In addition, the product internal state-resolved state-to-state reaction probabilities, ICSs and DCSs can be examined as a function of product vibrational and rotational levels to elucidate the energy disposal and scattering mechanism of products.

An extensive number of studies on a vast number of bimolecular reactions have been done in the last few decades [2, 3, 51, 52]. Generally the dynamics of the reactions is perceived and then categorized in terms of the type of mechanism they follow. Moreover, the mechanism of the reaction is intimately connected to mainly the topography of the underlying PES of the reactive system. Nevertheless, other various factors also affect the dynamics and mechanism of the reaction. This connection was first pioneered by John C. Polanyi in the seventies, who studied an extensive number of atom-diatom bimolecular reactions and led to establish the well known Polanyi's rule [53, 54]. This rule gives a qualitative idea about the energy disposal and energy requirement for various reactions based on the location of the transition-state barrier, whether it is early or late, on the PES. Reactions with a barrier on the reaction path normally undergo direct mechanism. These reactions are generally very fast and involves a simultaneous bond breaking and forming at the transition-state geometry. The DCS of such reactions strongly depends on the scattering angle and are very specific toward a particular scattering direction, either backward or forward. However, reactions without barrier generally involve complex formation during the reaction and are said to undergo indirect mechanism. These reactions generally take more time to complete as compared to the direct reactions because the collision complex spends a significant amount of time inside the potential wells. The DCS of such reactions is generally symmetric with respect to forward and backward region along the scattering angle. In addition to the topography of the underlying PES, there are other major factors which can affect the mechanism of the reaction such as the exoergicity or endoergicity of the reaction, the mass combination of the reactive system and some additional factors such as the energy supplied to the reagents in the form of vibration, rotation or translation.

1.1 Objective of the thesis

The main objective of the current investigation is to understand and interpret the detailed dynamical mechanism of various atom-diatom bimolecular reactions with varying complexity in the topography of the underlying PES. In particular, to study the product energy disposal and the scattering mechanism by carrying out accurate quantum dynamics. The reactions studied in this thesis are H (D) + $LiH^+ \rightarrow H_2$ (HD) + Li^+ on the electronic ground state, the benchmark H + $H_2 \rightarrow H_2$ + H reaction and the S + OH $\rightarrow$ SO + H reaction on the ground electronic state PES of HSO reactive system. These reactions are relevant to study of interstellar medium in astrochemistry. In addition the hydrogen exchange reaction has its fundamental importance in understanding of the chemical reaction dynamics. Although a number of studies have been performed on these reactions a comprehensive an accurate dynamical study relating to the mechanism is lacking particularly for the first three reactions. Hence, the aim of the present work is to provide an understanding of the mechanism of these reactions as well as to obtain the accurate reaction observables like rate constant which can be used in the astrophysical modelling of the corresponding reaction networks for the prediction of accurate abundances of the interstellar ions and molecules. From the mechanistic point of view, another goal is to emphasize on importance of the effect of extra energy given initially in terms of vibrational and rotational excitation of reagent diatom and the collision energy on dynamical outcomes and the consequent effect of the topography of the underlying PES on the reaction observables. The notion to distinguish the statistical or non-statistical nature of a reaction histrorically lies on the forward-backward symmetry of the product angular distribution. Another objective of the present work is to quantity the interference terms due to the coherence among the partial waves which can be used to distinguish the non-statistical nature of a reactions. Moreover, the magnitude of the interference terms corresponding to different reactions can be related to the topography of the PES of reactive system. The reactive dynamics of all the above mentioned reactions are carried out by means of a product coordinate based TDWP method [34, 36]. The first three reactions are studied in the adiabatic framework where single state adiabatic state-to-state dynamics is carried out to obtain the necessary reaction observables. For the hydrogen-exchange reaction, the dynamics is carried out in a nonadiabatic framework in order to illuminate on the effect of nonadiabatic coupling on the state-to-state reactive scattering dynamics.

1.2 Overview of the thesis

In chapter 2, the details of the theoretical and computational methodologies for studying the nuclear dynamics of the above mentioned reactions is presented. It begins with a short introduction of the real wave packet (RWP) based TDWP method [34] to study the nuclear dynamics of the three reactions. The method employed to study the single state adiabatic state-to-state dynamics is described in detailed. The same methodology is then extended to the nonadiabatic framework involving two strongly coupled electronic states. The methodology and the relevant equations for the nonadiabatic state-to-state quantum reactive scattering study are introduced. The relevant equations for the calculation of various reaction observables are presented and discussed. The importance of quantitying the interference terms among the partial waves and its relation to the non-statistical nature of a chemical reaction is analyzed by introducing the relevant equations. Finally, a short outline of the flux based TDWP method is given.

In chapter 3, a detailed state-to-state quantum dynamical study of the astrochemically relevant $H + LiH^+ \rightarrow H_2 + Li^+$ and $D + LiH^+ \rightarrow HD + Li^+$ reactions is reported. Fully converged quantum mechanical calculations accurately involving the coriolis coupling terms are performed by a TDWP method at state-to-state level on the *ab initio* electronic ground state PES of the LiH_2^+ ionic system. Initial state-selected total reaction probabilities, ICSs, DCSs and thermal rate constants are calculated and compared with the available results in the literature. Product state-resolved cross sections and product vibrational and rotational quantum level distributions are also presented to understand the state-to-state dynamics. The average fractions of available energy entering into product vibration, rotation and translation are calculated from the quantum mechanical cross sections to examine the energy disposal mechanism of the two reactions. The scattering mechanism of the two reactions is also elucidated by calculating the product state-resolved DCSs and the coherent partial wave contribution to the DCS as a function of the scattering angle. The interference terms existing due to the coherence between the partial waves are quantified and the nature of the interference, whether constructive or destructive, is deduced by plotting along the scattering angle. The effect of ro-vibrational excitation of the reagent LiH^+ on various reaction observales is examined for the former reaction.

In chapter 4, the state-to-state quantum dynamical study of the benchmark $H + H_2 \rightarrow H_2 + H$ reaction both in the adiabatic and nonadiabatic framework is presented. The adiabatic dynamical calculations are performed on the lower adiabatic BKMP2

PES by following the TDWP methodology. For the nonadiabatic calculations a two-state coupled diabatic theoretical model is used to include all the nonadiabatic coupling present in the $1E'$ electronic manifold of the H_3 system. The nonadiabatic couplings are considered here up to the quadratic approximation. The chapter is primarily divided into three parts. The first part contains the findings on the effect of nonadiabatic coupling in the state-to-state dynamics of the reaction with vibrationally hot reagent H_2 (v=3,4, j=0). In the second part, the effect of reagent vibrational excitation from v=0 to v=4 on the scattering mechanism of the eaction is discussed from a mechanistic point of view. The third part contains the findings on the effect of rotational excitation of the reagent diatom in its ground vibrational (v=0) manifold on the state-to-state as well as overall dynamics of the reaction.

In chapter 5, the dynamics of the S + OH $\rightarrow$ SO + H reaction at the the state-to-state level is presented. The dynamical calculations are perfomed on the electronic ground state ($\tilde{X}^2A''$) PES and by following the TDWP method. Initial state-delected total as well as state-to-state reaction probabilities, ICSs, DCSs and product vibrational and rotational level distributions are obtained to elucidate the mechanistic details of the reaction. Coriolis coupling terms of the nuclear Hamiltonian are included accurately. The effect of reagent rovibrational excitations on the dynamics is examined in terms of reaction probabilities, and the ICSs and DCSs are calculated for the reagent OH (v=0, j=0). The dynamical observables are related to the topographical details of the underlying PES.

Finally, in chapter 6 a short summary of all the work repoted in the thesis is presented along with the concluding remarks and a brief outlook.

Chapter 2

Theoretical and computational details

The theoretical formalism employed to study the state-to-state dynamics of different atom-diatom bimolecular reactions are presented in this chapter. A real wave packet (RWP) based TDWP method [34, 36] is used to obtain the state-to-state information both in the adiabatic and nonadiabatic dynamics situations. In this method, the Schrödinger equation for nuclear motion is solved numerically on a grid created in the Jacobi coordinate system corresponding to the product arrangement channel. An initial WP corresponding to the reagent channel is constructed in a grid representation and then is transformed to the Jacobi coordinates of the product arrangement channel. Then only the real part of the WP is propagated in time by a Chebyshev polynomial based iterative equation which is derived from the RWP formalism [34]. Finally the WP is analyzed at the product channel to obtain the required reaction observables. The purpose of using product Jacobi coordinate is to efficiently compute the S-matrix elements. The Coriolis coupling terms present in the nuclear Hamiltonian is treated explicitly by this method. This TDWP method in conjuction with the two-state coupled diabatic theoretical model of Mahapatra *et al.* [55] is used for the nonadiabatic dynamical calculations. In the nonadiabatic picture the WP is however propagated in a diabatic representation but is analyzed in the adiabatic representation.

2.1 Methodology for adiabatic dynamics

Within the BO approximation the TDSE for the nuclear motion on a single adiabatic PES is given as,

$$i\hbar\frac{\partial\Psi}{\partial t} = \hat{H}_N\Psi \tag{2.1}$$

where $\hat{H}_N$ (=$\hat{T}_N+\hat{V}$) is the nuclear Hamiltonian, which include the kinetic energy operator for the nuclei, $\hat{T}_N$ and the PES $\hat{V}$, and $|\Psi(t)\rangle$ is the wave function for nuclear motion. The coordinate dependency of the wave function is omitted here for brevity and will be expressed later. In case of a explicitly time-independent Hamiltonian, the solution of the TDSE can be written as

$$|\Psi(t)\rangle = \exp\left[\frac{-i\hat{H}_N t}{\hbar}\right]|\Psi(t=0)\rangle. \tag{2.2}$$

From the above equation of the solution of the TDSE, the working iterative equations in the formalism of RWP method can be derived. In the formalism of the RWP method, the system is allowed to satisfy a modified Schrödinger equation where a function of the Hamiltonian replaces the Hamiltonian operator itself [34].

$$i\hbar\frac{\partial\Psi'}{\partial\tau} = f(\hat{H}_N)\Psi'. \tag{2.3}$$

Here, $|\Psi'(\tau)\rangle$ is the modified wave function, which has similar information as $|\Psi(t)\rangle$, and τ is the modified time [34]. After separating the real and imaginary part of the equation from each other, the two different equations of motion are given as,

$$q(\tau+\Delta\tau) = -q(\tau-\Delta\tau) + 2\cos\left(\frac{f(\hat{H}_N)\Delta\tau}{\hbar}\right)q(\tau), \tag{2.4}$$

$$q(\Delta\tau) = \cos\left(\frac{f(\hat{H}_N)\Delta\tau}{\hbar}\right)q(0) + \sin\left(\frac{f(\hat{H}_N)\Delta\tau}{\hbar}\right)p(0), \tag{2.5}$$

where, $|p(\tau)\rangle$ and $|q(\tau)\rangle$ represent the imaginary and real part of the wave function $|\Psi(\tau)\rangle$, and $f(\hat{H}_N)$ is a function of the Hamiltonian which satisfies the modified Schrödinger equation. Here $\Delta\tau$ represents the discrete time step for the modified time. For the time propagation of the WP, the Chebyshev polynomial based three term iterative equation is obtained by a $\cos^{-1}$ functional mapping, $f(\hat{H}_N) = -\frac{\hbar}{\Delta\tau}\cos^{-1}(\hat{H}_{N,s})$, of the Hamiltonian [34], where, $\hat{H}_{N,s} = a_s\hat{H}_N + b_s$, is the scaled and shifted Hamiltonian whose spectrum lies in the interval $-1 \leq \hat{H}_{N,s} \leq 1$. Such type of scaling and shifting is necessary to ensure a one-to-one mapping of the Hamiltonian. Here a_s and b_s are the scaling parameters and are defined as,

$$\begin{aligned} a_s &= \frac{2}{E_{max} - E_{min}} \\ b_s &= -1 - a_s E_{min}, \end{aligned}$$

where E_{max} and E_{min} are the upper and lower bound of the Hamiltonian spectrum. Now replacing the $f(\hat{H}_N)$ in equations 2.4 and 2.5 with its functional mapping, the three term iterative equation including the absorption boundary condition reads as [34, 56]

$$q(n+1) = \hat{A}\Big[-\hat{A}\ q(n-1) + 2\ \hat{H}_{N,s}\ q(n)\Big] \tag{2.6}$$

where n is the order of the Chebyshev polynomials, similar to the order/angle formulation of Chen and Guo [57], and is related to the time as $\tau = n\Delta\tau$ [58, 59]. $\hat{A}$ is a damping function applied at each iteration step to absorb the reflected omponents of WP near the finite sized grid edges and given by the following functional form.

$$\hat{A}(x) = \exp\Big[-c_{abs}e^{\frac{-2(x_{max}-x_{abs})}{x-x_{abs}}}\Big], \tag{2.7}$$

where x_{abs} is the grid point at which the absorption function is activated and c_{abs} is the strength of the absorption. Since the equation 2.6 can not be used to obtain the WP at the first iteration step, the iteration is started by using the following equation [34],

$$q(1) = \hat{H}_{N,s}\ q(0) - \sqrt{1-\hat{H}^2_{N,s}}\ p(0). \tag{2.8}$$

The action of the operator $\sqrt{1-\hat{H}^2_{N,s}}$ on $p(0)$ is achieved by expanding it in the Chebyshev polynomials as [59],

$$\sqrt{1-\hat{H}^2_{N,s}} = \sum_k c_k T_k(\hat{H}_{N,s}). \tag{2.9}$$

The equations 2.6 and 2.8 serve as the principal iterative equations for the WP propagation in the RWP formalism. According to the two equations, sufficient information can be obtained by propagating only the real part of the WP. However, the imaginary part is required only once at the first iteration step.

For a A + BC → AB + C reactive scattering problem, the two equations are solved in the grid prepared in Jacobi coordinates corresponding to the product AB + C arrangement channel. We define the reagent and product Jacobi coordinates as (R, r, γ) and (R', r', γ'), respectively, where, R (R') is the distance of A (C) atom from the center-of-mass of BC (AB) diatom, r (r') is the internuclear distance of BC (AB) diatom and γ (γ') is the approach angle of A (C) to the center-of-mass of BC (AB). These Jacobi coordinates are schematically shown in Figure 2.1. An initial WP describing a particular initial condition and a range of energies is prepared at the reagent asymptote in the body-fixed

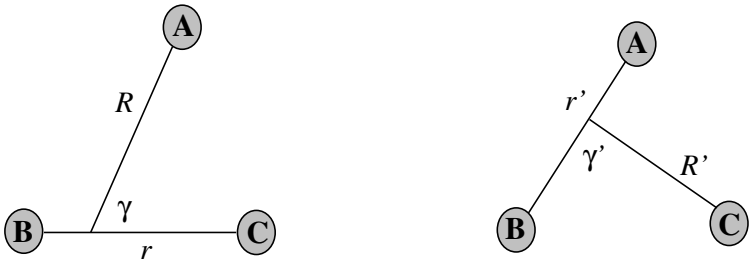

Figure 2.1: Schematic representation of the Jacobi coordinates corresponding to the reagent (A + BC) and product (C + AB) arrangement channels used in the TDWP method.

(BF) reagent Jacobi coordinate system. The real part of the WP is given as [36]

$$q^{j\Omega}(R, r, \gamma, 0) = F(R)\phi_{vj}^{BC}(r)\sqrt{w_\gamma}P_j^{\Omega}(\cos\gamma), \tag{2.10}$$

where

$$F(R) = \frac{\sin[\delta(R - R_0)]}{R - R_0}\cos[k_0(R - R_0)]e^{-\beta_s(R-R_0)^2} \tag{2.11}$$

is the translation component of the initial WP and represents the real part of a Gaussian WP centered at, R=R_0, multiplied with a Sinc function. The use of Sinc function is advantageous in the sense that it helps the WP to produce a constant amplitude in the distribution of desired range of momentum (or energy) [60]. The quantities δ and β_s are the width and smoothness parameter of the WP, and k_0 represents the magnitude of the wave vector corresponding to the negative momentum given to the WP equivalent to the mean translational energy, E_{trans}. The term, ϕ_{vj}^{BC} is the rovibrational eigenfunction of BC diatom in its v^{th} vibrational and j^{th} rotational level which is evaluated here by the sine-DVR approach of Colbert and Miller [61]. $P_j^{\Omega}(\cos\gamma)$ are the associated Legendre polynomials where Ω represents the projection of the total angular momentum, $\boldsymbol{J}$, onto the BF z-axis of the reagent Jacobi coordinate system. The imaginary part of the initial WP, $p^{j\Omega}(R, r, \gamma, 0)$ is given in the same way as $q^{j\Omega}(R, r, \gamma, 0)$ [cf., equation 2.10] but with $\cos[k_0(R - R_0)]$ is replaced with $-\sin[k_0(R - R_0)]$ in equation 2.10.

In order to propagate the WP in product Jacobi coordinates, both the real and imaginary part of the initial WP are transformed from the reagent to product Jacobi coordinate system before the start of the propagation. After the transformation, each $J\Omega'$ component (corresponds to the projection state (Ω') of $\boldsymbol{J}$ on the $\vec{R'}$ vector which is chosen as the BF z-axis of product Jacobi coordinate system) is given by the relation

[36]

$$q^{J\Omega'}(R', r', \gamma', 0) = N q^{j\Omega}(R, r, \gamma, 0) \frac{R'r'}{Rr} d^{J}_{\Omega\Omega'}(\vartheta). \tag{2.12}$$

In the above equation, N represents the normalization constant, $d^{J}_{\Omega\Omega'}(\vartheta)$ is the element of reduced Wigner rotation matrix [62, 63] and ϑ is the angle between $\vec{R'}$ and $\vec{R}$. After preparation of the initial WP, the equations 2.6 and 2.8 are used for its propagation.

The action of the nuclear Hamiltonian $\hat{H}_{N,s}$ on the real part of the WP is given by the following equations [36] (atomic units used here).

$$\begin{aligned}
\hat{H}_{N,s}\ q^{J\Omega'}(R', r', \gamma', n) &= \left[-\frac{1}{2\mu_{R'}}\frac{\partial^2}{\partial R'^2} - \frac{1}{2\mu_{r'}}\frac{\partial^2}{\partial r'^2}\right] q^{J\Omega'}(R', r', \gamma', n) \\
&- \left(\frac{1}{2\mu_{R'}R'^2} + \frac{1}{2\mu_{r'}r'^2}\right)\left[\frac{1}{\sin\gamma'}\frac{\partial}{\partial\gamma'}\sin\gamma'\frac{\partial}{\partial\gamma'} - \frac{\Omega'^2}{\sin^2\gamma'}\right] \\
&\quad \times q^{J\Omega'}(R', r', \gamma', n) \\
&+ \hat{V}(R', r', \gamma') q^{J\Omega'}(R', r', \gamma', n) \\
&+ \left(\frac{J(J+1) - 2\Omega'^2}{2\mu_{R'}R'^2}\right) q^{J\Omega'}(R', r', \gamma', n) \\
&- \frac{C^{+}_{J\Omega'}}{2\mu_{R'}R'^2}\left[\frac{\partial}{\partial\gamma'} - \Omega'\cot\gamma'\right] q^{J(\Omega'+1)}(R', r', \gamma', n) \\
&- \frac{C^{-}_{J\Omega'}}{2\mu_{R'}R'^2}\left[-\frac{\partial}{\partial\gamma'} - \Omega'\cot\gamma'\right] q^{J(\Omega'-1)}(R', r', \gamma', n)
\end{aligned} \tag{2.13}$$

In the above equation, $C^{\pm}_{J\Omega'} = \sqrt{J(J+1) - \Omega'(\Omega' \pm 1)}$, represent the Coriolis coupling terms. The quantities, $\mu_{R'} = m_C(m_A + m_B)/(m_A + m_B + m_C)$ and $\mu_{r'} = m_A m_B/(m_A + m_B)$ represent the three body and two body reduced masses corresponding to the product Jacobi arrangement channel. The Hamiltonian operator forms a tridiagonal matrix in Ω' for each J. The diagonal part of the matrix contains the radial kinetic energy operator in R' and r', the angular kinetic energy operator for $\hat{\boldsymbol{j}}'^2$ and $\hat{\boldsymbol{J}}^2$ and the potential energy operator, $\hat{V}(R', r', \gamma')$. The off-diagonal part contains the Coriolis coupling terms and is responsible for the coupling of the WP $q^{J\Omega'}$ with $q^{J\Omega'+1}$ and $q^{J\Omega'-1}$ components.

The action of the radial kinetic energy operator along R' and r' are evaluated by fast sine transformation (sine-FFT) technique [64]. The action of the angular part of the kinetic energy operator, which contains both the centrifugal and Coriolis coupling terms, is evaluated by a discrete variable representation (DVR)- finite basis representation (FBR) transformation. The DVR basis constructed along γ' are based on the Gauss-Legendre quadrature [65–67] rule where each node of the quadrature points are

considered as the grid points along the Jacobi angle γ'. The action of the potential energy operator is evaluated by simple multiplication in the grid representation. The evaluation of the Coriolis coupling terms becomes easier by parallelizing the calculation over different Ω'. In this case each combination of the J, $J\Omega'$ and parity p (0 and 1) quantum numbers is assigned to different processors so that the overall parity corresponds to $(-1)^{J+p}$. The communication is necessary only between the adjacent processors having same J and same parity quantum numbers. It is noteworthy to mentioned here that the calculations involving rotationally excited reagent are computationally more expensive than those for reagent (j=0). This is because both the parities are required to be considered for all values of $J(>0)$ [36, 68] in case of rotationally excited reagent. For every J, a total of J+1 and (2J+1) values of Ω' are required for the reagent (j=0) and ($j \neq 0$), respectively.

At every step of iteration, the propagated WP is analyzed at the product asymptote (at $R' = R'_d$) by projecting it onto the specific product rovibrational states, $\phi^{AB}_{v',j'}$, which yields the iteration number dependent coefficients as [59]

$$C^{J}_{v,j,\Omega\rightarrow v',j',\Omega'}(n) = \int \phi^{AB\ *}_{v',j'}(r',\gamma')q^{J\Omega'}(R' = R'_d, r', \gamma', n)dr' \sin\gamma' d\gamma'. \tag{2.14}$$

The product rovibrational wave functions $\phi^{AB}_{v',j'}$ are evaluated prior to the WP propagation by solving the diatomic Hamiltonian of AB diatom at product asymptote, $R' \rightarrow \infty$. This is numerically evaluated by the sine-DVR approach of Colbert and Miller [61].

These coefficients are then used to obtain the energy dependent amplitudes in the f-scale [34, 59], $A^{J}_{v,j,\Omega\rightarrow v',j',\Omega'}(f)$, by the discrete Fourier transform method.

$$A^{J}_{v,j,\Omega\rightarrow v',j',\Omega'}(f) = \frac{1}{2\pi}\sum_{n=0}^{N}\left(1 - \frac{\delta_{0,n}}{2}\right)C^{J}_{v,j,\Omega\rightarrow v',j',\Omega'}(n)e^{ifn} \tag{2.15}$$

Here the symbol f represents $f(E_s) = -\frac{\hbar}{\Delta\tau}\cos^{-1}(a_sE + b_s)$ which is the scaled and shifted energy eigenvalue of $f(\hat{H}_s)$. The energy dependent amplitudes are transformed to the space-fixed (SF) frame in order to account for the effect of long-range nature of the centrifugal potential and the Coriolis couplings. This BF to SF transformation is done by the following equation,

$$A^{J}_{v,j,l\rightarrow v',j',l'}(f) = \sum_{\Omega'\Omega}^{min(j',J)} T^{J}_{l\Omega}A^{J}_{v,j,\Omega\rightarrow v',j',\Omega'}(f)T^{J}_{l'\Omega'}. \tag{2.16}$$

In the above equation $T^J_{l\Omega}$ and $T^J_{l'\Omega'}$ represent the elements of the transformation matrices, **T** and **T′**, corresponding to the reagent and product arrangement, respectively. The matrices are the eigen vector matrix which diagonalizes the one-dimendional tridiagonal Coriolis coupling matrix at separate arrangement channels. The terms l and l' represent the orbital angular momentum quantum numbers for teh relative motion of reagents and products, respectively.

The energy dependent amplitudes in the SF frame are then used to calculate the S-matrix elements in $E-$scale. With necessary phase correction, the equation reads as,

$$S^J_{v,j,l\to v',j',l'}(E) = -\frac{a_s}{\Delta\tau\sqrt{1-E_s^2}}\sqrt{\frac{k'k}{\mu_{R'}\mu_R}}\frac{2A^J_{v,j,l\to v',j',l'}(f)}{\bar{g}(-k)}e^{-i(k'R'_d+\delta\eta_{v'j'l'}+\delta\eta_{vjl})}. \quad (2.17)$$

In the above equation, k and k' define the wave vector components associated with the reagent and product channels, respectively. The term $\mu_R = m_A(m_B+m_C)/(m_A+m_B+m_C)$ is the three body reduced mass corresponding to the reagent Jacobi arrangement channel. The quantity, $\bar{g}(-k)$, is the incoming component of the initial WP having negative wavevector, $-k$, and is determined at the reagent asymptote by the back propagation method [69]. Here E_s represents the scaled energy. The above S-matrix elements are then transformed back to the BF frame by using the transpose of the transformation matrices **T** and **T′** to obtain $S^J_{v,j,\Omega\to v',j',\Omega'}(E)$ in helicity representation.

$$S^J_{v,j,\Omega\to v',j',\Omega'}(E) = \sum_{l'l} T^J_{\Omega l} S^J_{v,j,l\to v',j',l'}(E) T^J_{\Omega' l'}. \quad (2.18)$$

These S-matrix elements in the helicity representation can be used to obtain various state-to-state observables.

2.2 Methodology for nonadiabatic state-to-state scattering dynamics

The methodology used to carry out the nonadiabatic state-to-state scattering dynamics in the thesis is presented in this section. The RWP based TDWP method discussed in the previous section is modified and extended to the nonadiabatic picture involving two strongly coupled electronic states. A two-state coupled diabatic theoretical model is used to include all the nonadiabatic couplings. In the present version of this formalism,

only two electronic states have been considered, but due to its simplicity it can be readily extended to the coupled states situations involving any number of electronic states provided the diabatic potentials and diabatic couplings are given in advance.

For a coupled states situation involving two electronic states, the time-independent nuclear Schrödinger equation in the adiabatic electronic representation is given as [55],

$$\left[\hat{T}_N(Q)\begin{pmatrix}1 & 0\\ 0 & 1\end{pmatrix}+\begin{pmatrix}V_-(Q) & 0\\ 0 & V_-(Q)\end{pmatrix}+\begin{pmatrix}\Lambda_{11}(Q) & \Lambda_{12}(Q)\\ \Lambda_{21}(Q) & \Lambda_{22}(Q)\end{pmatrix}\right]\begin{pmatrix}\Psi_-^{ad}(Q)\\ \Psi_+^{ad}(Q)\end{pmatrix}=E\begin{pmatrix}\Psi_-^{ad}(Q)\\ \Psi_+^{ad}(Q)\end{pmatrix}. \tag{2.19}$$

In the above equation, $\hat{T}_N(Q)$ refers to the nuclear kinetic energy operator and $\{Q\}$ collectively represents the set of nuclear coordinates. $V_-(Q)$ and $V_+(Q)$ refer to the lower and upper components of the adiabatic PESs, and $\Psi_-^{ad}(Q)$ and $\Psi_+^{ad}(Q)$ are the corresponding nuclear wave functions. The terms, Λ_{ij} (i, j=1,2), are known as the nonadiabatic coupling elements which couples the two electronic states in the adiabatic representation. These elements are given as [21],

$$\Lambda_{ij}=-\sum_m\frac{\hbar^2}{2M_m}\left(2F_{ij}\frac{\partial}{\partial Q_m}+G_{ij}\right), \tag{2.20}$$

where, M_m represents the mass of m^{th} nucleus and

$$F_{ij}^{(m)}(Q) = \left\langle\varphi_i^{el}(q_{el};Q)\left|\frac{\partial}{\partial Q_m}\right|\varphi_j^{el}(q_{el};Q)\right\rangle \tag{2.21}$$

$$G_{ij}^{(m)}(Q) = \left\langle\varphi_i^{el}(q_{el};Q)\left|\frac{\partial^2}{\partial Q_m^2}\right|\varphi_j^{el}(q_{el};Q)\right\rangle. \tag{2.22}$$

In the above, $|\varphi_i^{el}(q_{el};Q)\rangle$ represents the adiabatic electronic wave functions which depends on the set of electronic coordinates $\{q_{el}\}$ and also parametrically on the nuclear coordinates $\{Q\}$. The terms $F_{ij}^{(m)}(Q)$ and $G_{ij}^{(m)}(Q)$ are known as the derivative coupling and scalar coupling, respectively. When these two terms are non-zero, it is obvious from the equations 2.21 and 2.22 that the two electronic states i and j are coupled through nuclear motion.

Applying the Hellmann-Feynman theorem to the electronic Schrödinger equation ($H^{el}(q_{el};Q)\varphi_i^{el}(q_{el};Q)=V_i(Q)\varphi_i^{el}(q_{el};Q)$; $H^{el}(q_{el};Q)$ being the electronic Hamiltonian), it can be proved for the derivative coupling operator that [70],

$$F_{ij}^{(m)}(Q)=\frac{\left\langle\varphi_i^{el}(q_{el};Q)\left|\frac{\partial}{\partial Q_m}H^{el}(q_{el};Q)\right|\varphi_j^{el}(q_{el};Q)\right\rangle}{V_i(Q)-V_j(Q)}, \tag{2.23}$$

where, $V_i(Q)$ and $V_j(Q)$ are the adiabatic PESs and are same as the $V_-(Q)$ and $V_+(Q)$. When the two electronic states i and j are degenerate at some point in the nuclear coordinates then $V_i(Q) = V_j(Q)$, and $F_{ij}(Q)$ exhibit singularity at those nuclear configurations. Because of the diverging nature of the derivative of the electronic wave function, the adiabatic electronic states lack analytical continuity [71]. This makes the adiabatic representation unsuitable for numerically solving the Schrödinger equation in case of strongly coupled electronic state situations.

This difficulty of adiabatic representation is circumvented by resorting to a diabatic representation [28, 29]. These two representations are related by an adiabatic-to-diabatic unitary transformation (ADT). The diabatic representation is derived in such way that the problematic singular derivative couplings vanishes in the new representation, making it suitable for numerical evaluation. Actually, in the new representation the singular kinetic couplings are transformed to smooth potential couplings. Mathematically, this transformation can be written as,

$$\mathbf{\Psi^d} = \mathbf{S\Psi^{ad}}, \tag{2.24}$$

$$\mathbf{H^d} = \mathbf{SH^{ad}S^\dagger} = \hat{T}_N\mathbf{I}_n + \mathbf{U}, \tag{2.25}$$

where $\mathbf{H^d}$ is the diabatic Hamiltonian and $\mathbf{U}$ is called the diabatic potential energy matrix (DPEM). The transformation matrix $\mathbf{S}$ is called as the ADT matrix. In the above equation $\mathbf{I}_n$ is a $n \times n$ unit matrix, n being the number of electronic states involved.

For a coupled two-state situation as in the present case, the diabatic Hamiltonian is given as [55],

$$\mathbf{H^d} = \hat{T}_N(Q)\begin{pmatrix}1 & 0\\ 0 & 1\end{pmatrix} + \begin{pmatrix}U_{11}(Q) & U_{12}(Q)\\ U_{21}(Q) & U_{22}(Q)\end{pmatrix}, \tag{2.26}$$

and the time-independent nuclear Schrödinger equation in the diabatic electronic representation is given as,

$$\left[\hat{T}_N(Q)\begin{pmatrix}1 & 0\\ 0 & 1\end{pmatrix} + \begin{pmatrix}U_{11}(Q) & U_{12}(Q)\\ U_{21}(Q) & U_{22}(Q)\end{pmatrix}\right]\begin{pmatrix}\Psi_1^d(Q)\\ \Psi_2^d(Q)\end{pmatrix} = E\begin{pmatrix}\Psi_1^d(Q)\\ \Psi_2^d(Q)\end{pmatrix}, \tag{2.27}$$

from where the corresponding TDSE can be obtained. The DPEM elements can be

obtained by diabatizing the diagonal adiabatic potential energy matrix through the following similarity transformation,

$$\begin{aligned}\begin{pmatrix} U_{11} & U_{12} \\ U_{21} & U_{22} \end{pmatrix} &= \mathbf{S}\begin{pmatrix} V_- & 0 \\ 0 & V_+ \end{pmatrix}\mathbf{S}^\dagger \\ &= \frac{V_+ + V_-}{2}\mathbf{I}_2 + \frac{V_+ - V_-}{2}\begin{pmatrix} -\cos 2\alpha & \sin 2\alpha \\ \sin 2\alpha & \cos 2\alpha \end{pmatrix} \end{aligned} \tag{2.28}$$

with

$$\mathbf{S} = \begin{pmatrix} \cos\alpha(Q) & \sin\alpha(Q) \\ -\sin\alpha(Q) & \cos\alpha(Q) \end{pmatrix}. \tag{2.29}$$

In equation 2.28, the dependency of the nuclear coordinate $\{Q\}$ of different terms has been omitted for brevity. The term $\alpha(Q)$ is known as the ADT angle and depends upon the nuclear coordinates. It is system dependent and uniquely defines the DPEM elements. The determination of the ADT angle and hence the DPEM is the central part of constructing the diabatic representation where the nonadiabatic dynamics can be carried out conveniently.

The initial WP is prepared in the adiabatic representation at the asymptotic reagent channel. It can be located initially on either of the adiabatic PESs depending upon the choice of the reaction dynamics study. The WP is first prepared in the BF reagent Jacobi coordinate system (R, r and γ) and then transformed to the product Jacobi coordinate (R', r' and γ') system. The real part of the adiabatic WP located on the lower adiabatic PES V_- is expressed as a column matrix,

$$\mathbf{q}^{\mathbf{ad},J\Omega'}(R', r', \gamma', 0) = F(R)\phi_{vj}^{BC}(r)\sqrt{w}P_j^{\Omega}(\cos\gamma)\frac{R'r'}{Rr}d^J_{\Omega\Omega'}(\vartheta)\begin{pmatrix} 1 \\ 0 \end{pmatrix}, \tag{2.30}$$

where $F(R)$ is the same as given in equation 2.11. The definition of rest of the terms is the same as given in equation 2.10. The imaginary part of the adiabatic WP ($\mathbf{p}^{\mathbf{ad},J\Omega'}$) is similar to the real counter part $\mathbf{q}^{\mathbf{ad},J\Omega'}$ except the function $\cos[k_0(R - R_0)]$ in $F(R)$ is replaced by $-\sin[k_0(R - R_0)]$. The initial real and imaginary parts of the WP defined in the above equations are transformed to the diabatic representation by using the ADT matrix (equation 2.29) prior to the propagation. In the diabatic representation these functions can be written as

$$\mathbf{q}^{\mathbf{d},J\Omega'}(R', r', \gamma', 0) = \begin{pmatrix} q_1^{d,J\Omega'}(R', r', \gamma', 0) \\ q_2^{d,J\Omega'}(R', r', \gamma', 0) \end{pmatrix} = \mathbf{S}\,\mathbf{q}^{\mathbf{ad},J\Omega'}, \tag{2.31}$$

$$\mathbf{p}^{\mathbf{d},J\Omega'}(R',r',\gamma',0) = \begin{pmatrix} p_1^{d,J\Omega'}(R',r',\gamma',0) \\ p_2^{d,J\Omega'}(R',r',\gamma',0) \end{pmatrix} = \mathbf{S}\,\mathbf{p}^{\mathbf{ad},J\Omega'}. \tag{2.32}$$

Having prepared the initial diabatic WP and the diabatic Hamiltonian, the dynamics is then carried out in the coupled diabatic representation by the RWP methodology. In case of this coupled two-states situation, the main three-term iterative equation for the propagation of the WP in time is given as,

$$\begin{pmatrix} q_1^{d,J\Omega'}(n+1) \\ q_2^{d,J\Omega'}(n+1) \end{pmatrix} = \hat{A}\left[-\hat{A}\begin{pmatrix} q_1^{d,J\Omega'}(n-1) \\ q_2^{d,J\Omega'}(n-1) \end{pmatrix} + 2\,\mathbf{H}_s^{\mathbf{d}}\begin{pmatrix} q_1^{d,J\Omega'}(n) \\ q_2^{d,J\Omega'}(n) \end{pmatrix}\right], \tag{2.33}$$

where the coordinate dependence of the WP is omitted for brevity. In the above equation $\hat{A}$ is the absorption function which has same functional form as given in 2.7. Moreover, $\mathbf{H}_s^{\mathbf{d}} = a_s\mathbf{H}^{\mathbf{d}} + b_s\mathbf{1}$ is the scaled Hamiltonian matrix whose individual elements are scaled and shifted so as to keep the respective eigenvalues in the range of -1 to +1. The scaling parameters have been calculated in the same way as explained in the section 2.1. Moreover, the initial step of the iterative propagation is evaluated in similar way as given in equation 2.8 but with required modification.

The action of the 2×2 diabatic Hamiltonian matrix $\mathbf{H}^{\mathbf{d}}$ on the real ($\mathbf{q}^{\mathbf{d},J\Omega'}$) and imaginary ($\mathbf{p}^{\mathbf{d},J\Omega'}$) part of the diabatic WP column vectors is carried out by a straightforward matrix multiplication. This is be given as,

$$\mathbf{H}^{\mathbf{d}}\begin{pmatrix} q_1^{d,J\Omega'}(n) \\ q_2^{d,J\Omega'}(n) \end{pmatrix} = \begin{pmatrix} \hat{T}_N q_1^{d,J\Omega'}(n) & 0 \\ 0 & \hat{T}_N q_2^{d,J\Omega'}(n) \end{pmatrix} + \begin{pmatrix} U_{11}q_1^{d,J\Omega'}(n) & U_{12}q_2^{d,J\Omega'}(n) \\ U_{21}q_2^{d,J\Omega'}(n) & U_{22}q_1^{d,J\Omega'}(n) \end{pmatrix}. \tag{2.34}$$

The action of the nuclear kinetic energy and the diabatic potential on the diabatic WP is carried out in the same way as it is done in the adiabatic dynamics study, given in equation 2.13 and explained in section 2.1. It is important to note here that the computational time for the WP propagation in diabatic representation (involving both the electronic states) increases twice as compared to the adiabatic single surface propagation. This is because the number of operations of the Hamiltonian on the WPs become doubled in case of the former. Hence the calculations involving both the electronic states are more time consuming than the single surface adiabatic calculations.

At each step of iteration the diabatic WP is transformed to the adiabatic representation by using the ADT matrix as follows,

$$\mathbf{q}^{\mathbf{ad},J\Omega'}(R',r',\gamma',n) = \begin{pmatrix} q_{-}^{ad,J\Omega'}(R',r',\gamma',n) \\ q_{+}^{ad,J\Omega'}(R',r',\gamma',n) \end{pmatrix} = \mathbf{S}^{\dagger}\ \mathbf{q}^{\mathbf{d},J\Omega'}(R',r',\gamma',n). \tag{2.35}$$

After obtaining the adiabatic WP, any of its component can be analyzed depending upon which product channel is to be investigated. The analysis is done at the product asymptote (at $R' = R'_d$) by projecting the adiabatic components of the WP onto the specific product rovibrational states, $\phi^{AB}_{v',j'}$, which yields the iteration number dependent coefficients as,

$$C^{J}_{v,j,\Omega\rightarrow v',j',\Omega'}(n) = \int \phi^{AB}_{v',j'}{}^{*}(r',\gamma') q^{ad,J\Omega'}_{-/+}(R' = R'_d, r',\gamma',n) dr' \sin\gamma' d\gamma'. \tag{2.36}$$

These coefficients are then subsequently used to obtain the S-matrix elements. The procedure of obtaining the S-matrix elements from the iteration number dependent coefficients is the same as that is done in section 2.1. After obtaining the S-matrix elements, various reaction observables can be calculated.

2.3 Calculation of reaction observables

2.3.1 Reaction probability, integral and differential cross section, rate constant

For reactive scattering problem various reaction observables can be obtained from the S-matrix elements to characterize the reaction dynamics. First of all, the state-to-state reaction probabilities are obtained by taking the modulus square of the S-matrix elements as

$$P_{v,j,\Omega\rightarrow v',j',\Omega'}(E) = \left| S^{J}_{v,j,\Omega\rightarrow v',j',\Omega'}(E) \right|^2. \tag{2.37}$$

The initial state-selected total reaction probabilities can be calculated by summing the state-to-state reaction probabilities over all the final product quantum numbers. Similarly, the product vibrational and rotational level resolved reaction probabilities can be obtained by summing over appropriate final quantum numbers.

The state-to-state ICSs and DCSs can be directly calculated from the S-matrix elements by including all the partial wave contributions as,

$$\sigma^{\mathrm{ICS}}_{v,j\to v',j'}(E) = \frac{\pi}{k^2}\sum_{\Omega=0}^{j}\frac{g_\Omega}{2j+1}\sum_{J\geq\Omega}^{J_{max}}(2J+1)\sum_{\Omega'}\left|S^{J}_{v,j,\Omega\to v',j',\Omega'}(E)\right|^2 \tag{2.38}$$

$$\sigma^{\mathrm{DCS}}_{vj\to v'j'}(\theta) = \frac{1}{4k^2}\sum_{\Omega\Omega'}\frac{g_\Omega}{2j+1}\left|\sum_{J\geq\Omega}^{J_{\max}}(2J+1)S^{J}_{vj\Omega\to v'j'\Omega'}d^{J}_{\Omega\Omega'}(\pi-\theta)\right|^2. \tag{2.39}$$

In the above equation, $d^J_{\Omega\Omega'}(\pi-\theta)$ are the elements of reduced Wigner rotation matrix [62, 63] and $k = \sqrt{2\mu_R \mathrm{E_{col}}}/\hbar$. The term g_Ω equals to 1 and 2 for $\Omega = 0$ and $\Omega > 0$, respectively. In equation 2.39, the definition of the scattering angle, θ, as given by Zhang and Miller [72] ("$\pi-\theta$" convention) is used. In this case it is defined as the angle between the relative velocity vectors of the product diatom and the attacking atom. This assumes $\theta = 0°$ and $180°$ as forward and backward scattering, respectively.

The state-to-state rate constants are obtained from the corresponding ICSs as,

$$k_{v,j\to v',j'}(T) = \sqrt{\frac{8k_BT}{\pi\mu}}\frac{1}{(k_BT)^2}\int_0^\infty \sigma_{v,j\to v',j'}(E)e^{-E/k_BT}EdE, \tag{2.40}$$

where k_B is the Boltzmann constant.

The initial state-selected total ICS, DCS and rate constant can be obtained by summing up the corresponding state-to-state observables over the v' and j' quantum numbers.

The rotationally averaged thermal rate constant for v=0 is calculated as [73, 74],

$$k(T) = \sum_j \frac{k_{vj}(T)}{Q_{rot}}(2j+1)e^{-\frac{(Bj(j+1)hc)}{(k_BT)}}, \tag{2.41}$$

where B is the rotational constant of the reagent diatom, $k_{vj}(T)$ is the initial state-specific total rate constant, and Q_{rot} is the rotational partition function which is given as,

$$Q_{rot} = \sum_j (2j+1)e^{-\frac{(Bj(j+1)hc)}{(k_BT)}}. \tag{2.42}$$

2.3.2 Calculation of product energy disposal

The energy disposal in products can be examined by calculating the average fraction of the available energy entering into product vibration ($\langle f'_V \rangle$), rotation ($\langle f'_R \rangle$) and translation ($\langle f'_T \rangle$) from the state-to-state ICSs. The $\langle f' \rangle$ values are calculated at a particular value of collision energy by the following equations.

$$\langle f'_V \rangle = \frac{1}{E_{\rm av}\sigma^{\rm ICS}_{vj}} \sum_{v'} \sum_{j'} \sigma^{\rm ICS}_{v,j\to v',j'} \varepsilon_{v'j'=0} \tag{2.43}$$

$$\langle f'_R \rangle = \frac{1}{E_{\rm av}\sigma^{\rm ICS}_{vj}} \sum_{v'} \sum_{j'} \sigma^{\rm ICS}_{v,j\to v',j'} (\varepsilon_{v'j'} - \varepsilon_{v'j'=0}) \tag{2.44}$$

$$\langle f'_T \rangle = 1 - \Big(\langle f'_V \rangle + \langle f'_R \rangle \Big) \tag{2.45}$$

where

$$E_{\rm av} = E_{\rm col} + \varepsilon_{vj} - \Delta E \tag{2.46}$$

is the energy available to the products. In the above equations ε_{vj} and $\varepsilon_{v'j'}$ represent the rovibrational energy of the reagent and product diatoms, respectively. These energy values are taken with respect to the asymptotic reagent and product channels, respectively. The term, ΔE denotes the exo- or endoergicity of the reaction without the zero-point energy. The total ($\sigma^{\rm ICS}_{vj}$) and state-to-state ($\sigma^{\rm ICS}_{v,j\to v',j'}$) ICSs are considered at a particular collision energy of interest, $\rm E_{col}$.

2.3.3 Quantification of the interference between partial waves

It is well known that the DCS calculated by SQM methods [43–50] or by invoking the random phase approximation (RPA) [43, 44], turns out to be forward-backward symmetric. In the RPA, all coherence between different Js are neglected considering the phases of the reactive S-matrix elements to be random. This is generally justified for reactions involving deep well where the collision complex survives more than few rotational periods [44]. However, according to the study of Larrégaray and Bonnet [75], the quenching of interference between partial waves may not be significant particularly around the forward and backward scattering regions, which leads to an asymmetric forward-backward scattering in the state-to-state DCSs. This can happen even for complex-forming reactions. In their study [75], the deviation (due to the interference) from the SQM or RPA DCSs was estimated by means of the chaotic dynamical model

(CDM) [75] where different random numbers were assigned to the modulus and phase of the S-matrix elements [75].

In the following, however, we quantify the interference terms from the S-matrix elements calculated by the exact quantum scattering method. The deviation of these terms from the RPA DCS can shed light on the importance of the non-statistical nature of the reaction.

The DCS is generally defined as the modulus square of the scattering amplitude. For the state-to-state DCS, this can be written as

$$\sigma^{\mathrm{DCS}}_{vj\to v'j'}(\theta) = \sum_{\Omega\Omega'} \frac{g_\Omega}{2j+1} \left| f_{vj\Omega\to v'j'\Omega'}(\theta) \right|^2, \tag{2.47}$$

where

$$f_{vj\Omega\to v'j'\Omega'}(\theta) = \frac{1}{2ik} \sum_{J=0}^{J_{\max}} (2J+1) S^J_{vj\Omega\to v'j'\Omega'} d^J_{\Omega\Omega'}(\pi-\theta) \tag{2.48}$$

is the reactive scattering amplitude. From the equation 2.48 onwards the value of Ω quantum number is considered as 0 without loss of generality which makes the summation in equation 2.48 starts from 0. According to Jambrina *et al.* [76], the J-partial dependent state-to-state scattering amplitude can be expressed as,

$$f^J_{vj\Omega\to v'j'\Omega'}(\theta) = \frac{1}{2ik}(2J+1) S^J_{vj\Omega\to v'j'\Omega'} d^J_{\Omega\Omega'}(\pi-\theta), \tag{2.49}$$

so that equation 2.48 becomes

$$f_{vj\Omega\to v'j'\Omega'}(\theta) = \sum_{J=0}^{J_{\max}} f^J_{vj\Omega\to v'j'\Omega'}(\theta). \tag{2.50}$$

Upon substitution of equation 2.50 into equation 2.47, we get

$$\begin{aligned}
\sigma^{\mathrm{DCS}}_{vj\to v'j'}(\theta) &= \sum_{\Omega\Omega'}\frac{g_\Omega}{2j+1}\left|\sum_{J=0}^{J_{\max}} f^J_{vj\Omega\to v'j'\Omega'}(\theta)\right|^2 \\
&= \sum_{\Omega\Omega'}\frac{g_\Omega}{2j+1}\left|f^0_{\Omega\Omega'}+f^1_{\Omega\Omega'}+f^2_{\Omega\Omega'}+\cdots\right|^2 \\
&= \sum_{\Omega\Omega'}\frac{g_\Omega}{2j+1}\left[(f^0_{\Omega\Omega'}+f^1_{\Omega\Omega'}+f^2_{\Omega\Omega'}+\cdots)^*(f^0_{\Omega\Omega'}+f^1_{\Omega\Omega'}+f^2_{\Omega\Omega'}+\cdots)\right] \\
&= \sum_{\Omega\Omega'}\frac{g_\Omega}{2j+1}\sum_{J=0}^{J_{\max}}\left|f^J_{\Omega\Omega'}(\theta)\right|^2+\sum_{\Omega\Omega'}\frac{g_\Omega}{2j+1}\sum_{J=0}^{J_{\max}}\sum_{\substack{J_a=0\\J_a\neq J}}^{J_{\max}} f^{J*}{}_{\Omega\Omega'}(\theta)f^{J_a}_{\Omega\Omega'}(\theta) \\
&= \sum_{\Omega\Omega'}\frac{g_\Omega}{2j+1}\sum_{J=0}^{J_{\max}}\left|f^J_{\Omega\Omega'}(\theta)\right|^2+\sum_{\Omega\Omega'}\frac{g_\Omega}{2j+1}\sum_{J=0}^{J_{\max}-1}\sum_{J_a>J}^{J_{\max}} 2\mathrm{Re}\left\{f^{J*}{}_{\Omega\Omega'}(\theta)f^{J_a}_{\Omega\Omega'}(\theta)\right\} \\
&= \sigma^{\mathrm{RPA}}_{vj\to v'j'}(\theta)+\sigma^{\mathrm{INT}}_{vj\to v'j'}(\theta) \qquad (2.51)
\end{aligned}$$

In the above equations, the subscripts for v, j, v' and j' were omitted whenever required without altering the definition of the observables. The first term on the right hand side of equation 2.51,

$$\sigma^{\mathrm{RPA}}_{vj\to v'j'}(\theta)=\frac{1}{4k^2}\sum_{\Omega\Omega'}\frac{g_\Omega}{2j+1}\sum_{J=0}^{J_{\max}}(2J+1)^2 d^J_{\Omega\Omega'}(\pi-\theta)^2\left|S^J{}_{vj\Omega\to v'j'\Omega'}\right|^2, \qquad (2.52)$$

is the DCS due to the random phase approximation and is similar to the equation (30) of Ref. [44]. The second term,

$$\begin{aligned}
\sigma^{\mathrm{INT}}_{vj\to v'j'}(\theta) &= \frac{1}{4k^2}\sum_{\Omega\Omega'}\frac{g_\Omega}{2j+1}\sum_{J=0}^{J_{\max}-1}\sum_{J_a>J}^{J_{\max}}(2J+1)(2J_a+1)d^J_{\Omega\Omega'}(\pi-\theta) \\
&\quad\times d^{J_a}_{\Omega\Omega'}(\pi-\theta)2\mathrm{Re}\left\{S^{J*}{}_{vj\Omega\to v'j'\Omega'}S^{J_a}{}_{vj\Omega\to v'j'\Omega'}\right\}, \qquad (2.53)
\end{aligned}$$

is the interference term and is similar to the equation (31) of Ref. [44]. This interference originates due to the coherence among the partial waves which is neglected in the RPA. The corresponding initial state-selected quantities can be obtained by an incoherent summation over the v' and j' quantum numbers.

It is important to note some points regarding the nature of $\sigma^{\mathrm{RPA}}_{vj\to v'j'}(\theta)$ and $\sigma^{\mathrm{INT}}_{vj\to v'j'}(\theta)$.

- Since $\sigma^{\mathrm{RPA}}_{vj\to v'j'}$ involves modulus square of the complex number $S^J{}_{vj\Omega\to v'j'\Omega'}$, it is always positive. Moreover, it involves modulus square of the reduced rotation matrix elements, due to which it becomes symmetric with respect to $\theta=\pi/2$.

- Since $\sigma^{\mathrm{INT}}_{vj\to v'j'}$ involves multiplication of two different complex numbers *i.e.,* the scattering amplitude corresponding to two different Js, it can have both positive and negative values corresponding to constructive and destructive interference, respectively.

- Most importantly, $\sigma^{\mathrm{INT}}_{vj\to v'j'}$ can be plotted as a function of θ to illustrate the nature of interference (constructive or destructive) and their effect on the DCS corresponding to a particular scattering angle.

- The interference terms or the cross terms can be highly oscillatory along θ, particularly at the state-to-state level and can leave their oscillatory signature in the state-resolved or even total DCSs.

The above points are true for the total (summed over final states) as well as the state-resolved quantities. It is important to note here that the magnitude of the interference terms can be compared with the DCS due to RPA in order to examine their contribution towards the total DCS. However, the only quantity that contributes to the ICS is $\sigma^{\mathrm{RPA}}_{vj\to v'j'}$, because once equation 2.51 is integrated over θ (with weight factor of $sin\theta$), the $\sigma^{\mathrm{INT}}_{vj\to v'j'}$ term vanishes due to orthogonality of the reduced rotation matrix elements. Hence, the importance of the interference terms can only be assessed when the reaction cross section is resolved over the scattering angle.

2.3.4 Partial wave contribution to the DCS

An important tool to contemplate the details of scattering phenomena is to examine the contributions of different partial waves to the DCS. These partial DCSs can be calculated by confining the summation over J in equation 2.39 to a specific range, $J \in [J_i, J_f]$ [76], which can be chosen arbitrarily or by examining the variation of the opacity function as a function of J [77]. However, the partial DCSs calculated in this way include the coherence between the Js only inside the $[J_i, J_f]$ range but not outside of it [76]. In order to account for the full coherence between the all Js, it is useful to calculate the partial DCSs by the following equation,

$$\sigma^{\mathrm{DCS}}(\theta;[J_i,J_f]) = \sum_{\Omega\Omega'}\frac{g_\Omega}{2j+1}\left[\left|\sum_{J=J_i}^{J_f} f^{J}_{\Omega\Omega'}(\theta)\right|^2 + \sum_{J=J_i}^{J_f}\sum_{\substack{J_a=0\\ J_a<J_i\\ J_a>J_f}}^{J_{\max}} f^{J*}_{\Omega\Omega'}(\theta) f^{J_a}_{\Omega\Omega'}(\theta)\right], \quad (2.54)$$

where the second term on the right hand side denotes the coherence terms outside the $[J_i, J_f]$ range. As the impact parameter is proportional to the total angular momentum J, this kind of analysis helps to find a direct correlation between the scattering angle and the impact parameter from which the scattering of products arises from different mechanistic paths.

In addition, the first summation over J (from J_i to J_f]) in equation 2.54 can be omitted to obtain the $J-$dependent partial DCSs which becomes a function of J. This is given as,

$$\sigma^{\mathrm{DCS}}_{vj\to v'j'}(\theta, J) = \sum_{\Omega\Omega'} \frac{g_\Omega}{2j+1}\left[\left|f^{J}_{\Omega\Omega'}(\theta)\right|^2 + \sum_{J_a>J}^{J_{\max}} 2\mathrm{Re}\left\{f^{J*}_{\Omega\Omega'}(\theta) f^{J_a}_{\Omega\Omega'}(\theta)\right\}\right]. \tag{2.55}$$

In the above two equations, the subscripts for v, j, v' and j' were omitted for simplicity without altering the definition of the observables. The equation 2.55 is quite similar to the quantum mechanical generalized deflection function (QM GDF) derived by Jambrina *et al.* [cf., Ref. [76]] except the term sin θ is not multiplied in the above equation. This is because for the products scattered at $\theta = 0°$ and 180° the QM GDF exactly becomes zero making the partial wave analysis difficult. The QM GDF is an important tool to describe the quantum mechanical correlation between the scattering angle, θ and the total angular momentum, J.

2.4 Flux operator based TDWP method

The methodology of the flux operator based TDWP approach is discussed in this section which is used to calculate the reaction probabilities of the S + OH → SO + H reaction in chapter 5 in order to compare with the probabilities obtained from the RWP based TDWP approach. The details of this methodology are already discussed in Refs. [78–80], hence only a brief description is provided here.

Unlike the RWP based TDWP method the complex WP in this case is propagated on a grid constructed in the BF reagent Jacobi coordinate system (R, r, γ). Therefore, the various parts of the Hamiltonian *i.e.,* the kinetic energy and potential energy operators are discretized by a grid representation in the reagent Jacobi coordinates. The expression for the initial WP is same as in equation 2.10 but with the difference that it is

complex and the $F(R)$ is given by a Gaussian WP having the minimum uncertainty as,

$$F(R) = (2\pi\delta^2)^{-1/4} \exp\left[-\frac{(R-R_0)^2}{4\delta^2} - ik_0(R-R_0)\right]. \tag{2.56}$$

Once the initial WP is prepared, it is propagated in time and space by using a kinetic-energy-referenced second order split order method. This is simply given as,

$$|\Psi(Q, t+\Delta t)\rangle = e^{i\hat{V}\Delta t/2\hbar}\, e^{i\hat{T}_N\Delta t/\hbar}\, e^{i\hat{V}\Delta t/2\hbar}\, |\Psi(Q,t)\rangle, \tag{2.57}$$

where $\{Q\}$ collectively denotes the reagent Jacobi coordinates (R, r, γ). The action of the radial kinetic energy operator is perfomed by a fast Fourier transform (FFT) technique [64], whereas, the action of its angular part is perfomed by a DVR-FBR transformation [65–67]. The action of potential energy is done by simple multiplication. At each time step, the reflections of the WP at the grid boundaries are eliminated by using a sine type damping function [81].

The initial state-specific total reaction probabilities are obtained from the average value of the flux operator, $\hat{F} = -\frac{i\hbar}{2\mu_R}[\frac{\partial}{\partial r}\delta(r-r_d) + \delta(r-r_d)\frac{\partial}{\partial r}]$, in the basis of energy-dependent scattering wave function calculated at a dividing surface (r=r_d) located at the product asymptote as

$$\begin{aligned} P_{v,j}(E) &= \left\langle \psi(R, r=r_d, \gamma, E) \middle| \hat{F} \middle| \psi(R, r=r_d, \gamma, E) \right\rangle \\ &= \frac{\hbar}{\mu_r} \mathrm{Im}\left[\left\langle \psi(R, r=r_d, \gamma, E) \middle| \frac{\partial \psi(R, r=r_d, \gamma, E)}{\partial r} \right\rangle \right], \end{aligned} \tag{2.58}$$

where, $\mu_r = m_B m_C/(m_B + m_C)$ is the reduced mass of the BC reagent diatom and $|\psi(R, r=r_d, \gamma, E)\rangle$ is the energy-resolved scattered wave function. The latter is obtained by doing a Fourier transform the time-dependent WP $|\Psi(R, r, \gamma, t)\rangle$ at the dividing surface $r = r_d$.

Chapter 3

State-to-state quantum dynamics of H (D) + $LiH^+ \rightarrow H_2$ (HD) + Li^+ reaction

3.1 Introduction

According to the standard Big Bang nucleosynthesis model the cooling of the universe after the Big Bang was accompanied by the formation of first bound atoms and ions of the universe *i.e.,* helium, hydrogen and a very small amount of lithium [82–84]. During this recombination era when the temperature was down to some appropriate value, formation of molecules and molecular ions began by the radiative association between various atoms and thier corresponding ions. The first molecular species formed in the early universe is the HeH^+ ion [84–86]. Afterwards the formation of various molecular species like H_2^+, H_2, He_2^+, HD, LiH and LiH^+ took place[82–84]. Dalgarno and Lepp [87] first postulated the formation of LiH^+ by the following ion-atom radiative association processes.

$$Li^+ + H \rightarrow LiH^+ + \nu,$$
$$Li + H^+ \rightarrow LiH^+ + \nu.$$

Moreover, they suggested that the cation LiH^+ might be more abundant than the neutral LiH species in the cosmic environment as the ionization of LiH is feasible at low redshifts due to its low ionization potential. However, soon after its formation the LiH^+ ion can undergo various collisional processes with the more abundant H and D atoms present in the early universe. Because of its primordial astrochemical relevance, the

chemistry of LiH_2^+ has received a great deal of attention in the past two decades [88–115].

For the LiH_2^+ ionic system, Bodo *et al.* [89] carried out a computational analysis of possible reactions occurring on the ground and first excited electronic states. According to their study, the H + LiH^+ collision leads to the following allowed reactions on the adiabatic singlet ground electronic state.

$$\begin{aligned}
&H + LiH^+ \rightarrow H_2 + Li^+ && \text{(depletion)}\\
&H + LiH^+ \rightarrow LiH^+ + H && \text{(hydrogen exchange)}\\
&H + LiH^+ \rightarrow H + LiH^+ && \text{(Non-reactive)}\\
&H + LiH^+ \rightarrow H + H + Li^+ && \text{(Collision induced dissociation, CID)}
\end{aligned}$$

Among these the first two collisional processes involve reactive encounter. The depletion reaction is highly exoergic ($\Delta E_0 \approx -4.36$ eV), as a result of of the large binding energy difference between the LiH^+ (≈ 0.112 eV) and H_2 (≈ 4.47 eV) molecules. The second reaction involves exchange of H atom and is thermoneutral. Both the depletion and hydrogen exchange reactions are barrierless in nature. The third process is non-reactive and involves elastic and inelastic energy transfer between H and LiH^+. The fourth one is the collision induced dissociation (CID) and can be assessible in the early universe condition because of the low binding energy of LiH^+. It was predicted that the two processes, depletion and CID, serve as the major destruction mechanism for the LiH^+ ion in the early universe [96, 116]. In fact it was found that the CID process can become dominant at intermediate collision energies and the depletion process is dominated only at the low collision energy range [96, 108]. However, the other two processes *viz.,* non-reactive and hydrogen exchange, are responsible for the survival of the ionic LiH^+. Various theoretical predictions have been made for the above four processes to estimate the rate of destruction and survival of the LiH^+ ion and its relative abundance in the post-recombination era.

3.1.1 Electronic ground state PES of LiH_2^+ reactive system

The LiH_2^+ ion has a relatively simple electronic configuration involving only four electrons. Because of its unique structural features several global adiabatic PESs have been

constructed for the electronic ground state in order to understand its spectral and reactive behaviour [88, 92, 94, 95, 111, 112, 117–119]. Among these the 3D PES developed by Martinazzo *et al.* [92] have been widely employed in a number of spectral (bound and quasi-bound states calculation) and scattering studies [96–98, 100–102, 105, 108, 110, 114]. The PES was first constructed by calculating more than 11000 *ab initio* points with a multi-reference valence bond approach [91] and later corrected with about 600 points calculated by MRCI method with CASSCF reference wave functions and large basis sets [92]. The PES of Martinazzo *et al.* lacks the BSSE correction, however, explicitly includes the long-range interactions. For the latter purpose the quadrupole-charge and polarisability-charge interactions between H_2 and Li^+ were calculated at the full-CI level [92]. Subsequent theoretical studies at the CASSCF/MRCISD [94] and full-CI [95, 120] levels showed that the PES is reasonably accurate. Recent calculation of PES includes that of He *et al.* [111] and Dong *et al.* [112]. He *et al.* [111] reported the PESs of both the ground and first excited electronic state of the LiH_2^+ system. They incorporated the correction for the BSSE in their calculations of *ab initio* points and studied the dynamics of the reaction on the first excited state only. Another PES has been reported by Dong *et al.* [112] for the ground state of the LiH_2^+ system. This new PES is based on 7228 *ab initio* points calculated at the MRCI level with CASSCF reference wave functions using aug-cc-pVQZ basis for H atom and the cc-pwCVQ basis for Li atom with BSSE correction. It is worthwhile to mention here that neither the PES of He *et al.* nor that of Dong *et al.* includes the long-range interactions which can have a significant impact on the dynamics of such ion-molecule reactions particularly at low collision energies.

The electronic ground state PES of LiH_2^+ is characterized by a T-shaped shallow potential well at the C_{2v} geometry. The energy of the potential minimum is −0.286 eV with respect to the H_2 + Li^+ asymptote. The global minimum structure of the LiH_2^+ corresponds to a weakly bound complex resulting from the polarization-charge interaction between H_2 and Li^+. At the equilibrium minimum R_{H_2} distance is 1.42 a_0 and R_{Li-H_2} distance (from Li^+ to the center of mass of H_2) is 3.62 a_0 with R_{H_2} and R_{Li-H_2} are perpendicular to each other. Two schematic representations of the PES is shown in Figures 3.1 and 3.2 in order to understand its topography. These two figures show the change in potential energy occurred when the H/Li^+ atom attacks the LiH^+/H_2 diatom form various angular approach. Figure 3.1 shows the 3D and contour plot for the H atom moving around the LiH^+ diatom fixed at a distance of 3.7 a_0 which corresponds to its value at the C_{2v} minimum structure. Whereas Figure 3.2 shows the contour plot for the Li^+ ion moving around the H_2 diatom fixed at its equilibrium bond distance of

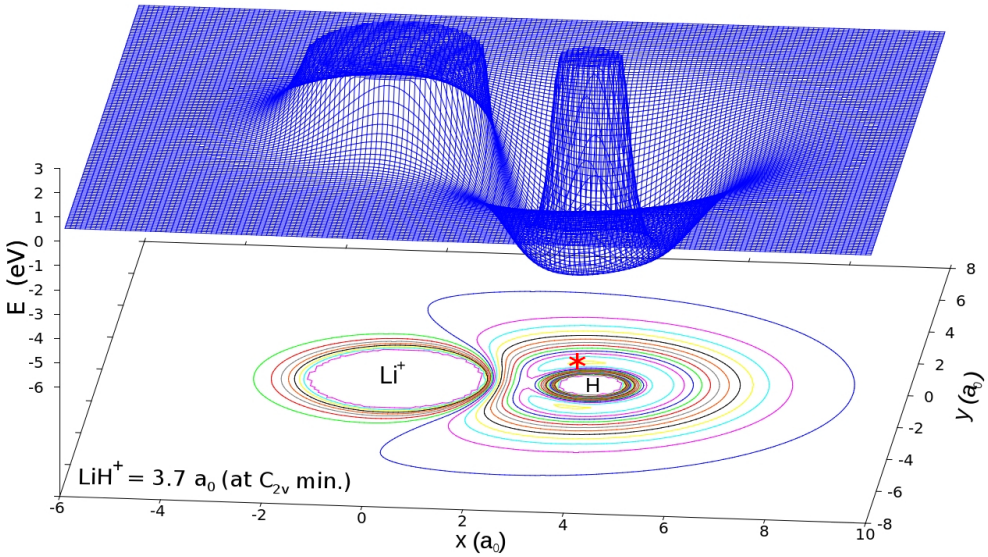

Figure 3.1: 3D perspective and contour plot of the PES of the LiH_2^+ constructed by Martinazzo *et al.* shown for the H atom moving around the LiH^+ diatom fixed at R_{LiH} = 3.7 a_0 corresponding to the C_{2v} minimum structure.

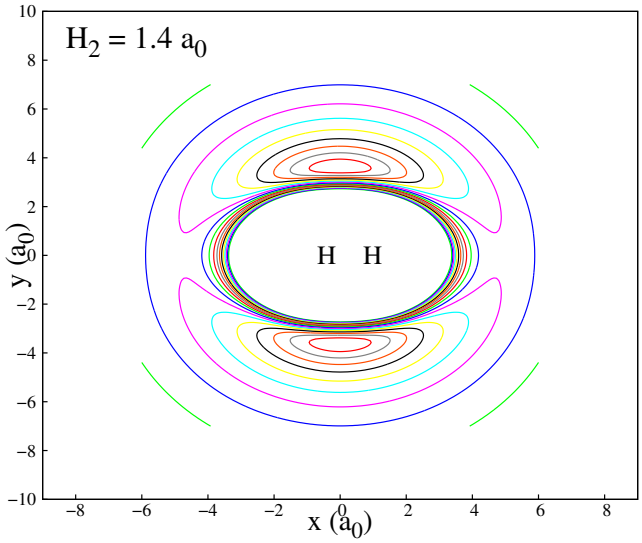

Figure 3.2: Contour plot of the PES of the LiH_2^+ shown for the Li^+ ion moving around the H_2 diatom fixed at its equilibrium bond length R_{H_2} = 1.4 a_0.

1.4 a_0. The zero of energy is set at the minimum value of the LiH^+ diatomic potential (its equilibrium minimum) when it is infinitely separated from the H atom. From the Figure 3.1 it can be seen that when H attacks LiH^+ it will favour to approach from the H-side as it encounters attractive interactions rather than the Li-side. The star ($*$) represents the C_{2v} minimum in the diagram. Similarly it can be seen from the Figure 3.2 that the shallow well appears when the Li^+ ion approaches the H_2 molecule in a direction perpendicular to the H−H bond forming a T-shaped structure at C_{2v} geometry.

The minimum energy paths (MEPs) for the depletion reaction are shown in Figure 3.3 for different angular approaches. These MEPs are constructed from the PES of Martinazzo *et al.* as a function of the distance $R_{LiH^+} - R_{HH}$ at various fixed ∠LiHH bond angles. It can be seen from the MEPs that the depletion reaction follows a pure downhill path from the reagent side to the product side with no barrier in the entrance channel. The MEP that goes through the T-shaped well occurrs at ∠LiHH ≈ 80° suggesting a favourable glancing collision condition for the depletion reaction.

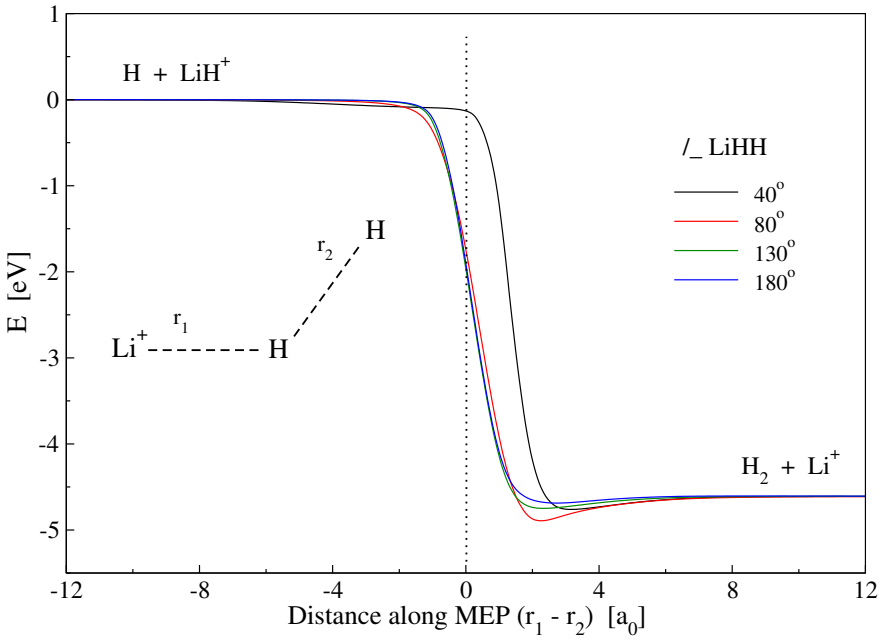

Figure 3.3: Minimum energy paths for the depletion reaction, $H + LiH^+ \rightarrow H_2 + Li^+$, at different approach angles (indicated in the panel) of the attacking H atom (∠LiHH bond angle).

3.1.2 Current state of research

Among the above four processes the depletion reaction is the most studied one. Using the 3D PES of Martinazzo *et al.* [92], Pino and co-workers [96] have calculated the

ICSs and rate constants for the depletion, hydrogen exchange and CID processes for different ro-vibrational states of the reagent LiH^+. They employed a QCT method and found an inhibiting effect of ro-vibrational excitation of reagent on the depletion process. However, this was found to be opposite in case of the hydrogen exchange and the CID processes. The CID process was in fact found to be dominant at higher collision energies. Bovino *et al.* [102] calculated the ICSs and rate constants for the survival and depletion processes of LiH^+ (v=0, j=0) by employing a TIQM method and the PES of Martinazzo *et al.* within the reactive infinite-order sudden approximation (R-IOSA) and centrifugal sudden (CS) approximation. They found that the survival of LiH^+ to be the most likely at low temperature, however, the depletion process still remains to be an important reactive process that is responsible for the destruction of LiH^+ in the recombination era.

Roy *et al.* [105] studied the dynamics of both depletion and hydrogen exchange reactions by a TDWP approach on the PES of Martinazzo *et al.* The ICSs and rate constants were calculated within the CS approximation at thermal condition. Sharp resonance oscillations were found in the reaction probabilities for both the processes at low collision energies. Overall they concluded that the depletion process to be more favoured over the hydrogen exchange process. In a later work [110] they extended their study of both the reactions to cold and ultracold conditions where state-to-state reaction probabilities, ICSs and rate constants were reported. They found that the product vibrational and rotational distributions remain similar at both cold and ultracold conditions. Dong *et al.* [112] studied the ICSs and DCSs of the depletion reaction calculated by both QCT and TDWP method on a new PES. They found a good agreement between their QCT and TDWP ICSs and a clear disagreement with the QCT ICS of Pino *et al.* at higher collision energies. At lower collision energy, the disagreement between their own QCT and TDWP ICSs was attributed to the possible quantum effects of the resonance states due to presence of a shallow well on the PES (cf., Figure 6 of Ref. 112).

The depletion reaction has also been subjected to many stereodynamical studies along with its isotopic variants. The DCS and different stereodynamical observables were calculated by the QCT method on the PES developed by Martinazzo *et al.* [92]. The total DCS calculated by Li *et al.* [97] suggested a dominant direct mechanism at low collision energies owing to more forward scattering than the backward one. At higher collision energies it showed more backward and sideways behaviour suggesting the possibility of insertion mechanism. In a later study, [101] they found that for

heavier isotopes of the attacking atom the insertion mechanism at higher collision energies tends to disappear and the reaction becomes more direct. However, the DCS calculated by Duan *et al.* [98] at collision energies below the binding energy of LiH^+ shows asymmetric forward-backward behaviour predicting that the depletion reaction is not a typical atom-diatom insertion reaction. Later Yang *et al.* [108] calculated the total DCS for the depletion reaction for different ro-vibrational states of reagent LiH^+ and reported that the insertion mechanism appears at low collision energies but with a dominant direct mechanism. Recent QCT calculation of Li and Lei [114] showed a fast abstraction mechanism for the depletion process at collision energies above 0.5 eV. Moreover, using the PES of Dong *et al.* [112], a state-to-state quantum dynamical study was carried out by Zhu *et al.* [113] for the depletion reaction. Product state resolved ICS and DCS have been calculated by a TDWP method for the ground ro-vibrational state of the reagent LiH^+. The reaction was shown to follow a dominant direct mechanism along with complex forming nature at low collision energies and a complete direct mechanism at high collision energies.

3.1.3 Motivation of the present work

Although the above studies either employed the same PES of Martinazzo *et al.* [92] or that of Dong *et al.* [112], the expected agreement between the QCT and quantum mechanical (QM) results for the highly exoergic and barrierless depletion reaction was not satisfactory [105, 112]. The disagreement could be attributed to the various approximations used in the numerical implementation of the theoretical methods or different PES used in the calculations. It is to be noted here that for the four processes mentioned above, the exact QM ICSs and DCSs are yet to be determined on the PES of Martinazzo *et al.* Therefore, one of the objective of the present work is to calculate the numerically exact QM ICS and DCS for the depletion reaction on the PES of Martinazzo *et al.* for a meaningful comparison with the previous QCT results.

Moreover, for the depletion reaction, the energy disposal to the various degrees of freedom of product is not considered so far. It is clear from Figure 3.3 that for the depletion reaction, the potential energy profile along the reaction path bears similar features as that of an "attractive" PES, as classified by Polanyi [53], but with two important differences that it is barrierless and has a shallow well along the reaction path. Since the PES has no barrier along the reaction path, it is very unlikely that the Polanyi's rule [53, 54] or the sudden vector projection (SVP) model [121–123] can be applied

to predict the product energy disposal. This is because these models or rules primarily rely on the information of the transition state located at the energetic barrier. Rather, an attempt is made here to find the correlation between the results of standard "attractive" PES with barrier (predicted by Polanyi's rule or SVP model) and the present results of an attractive PES without a barrier.

Another important point to note here is that due to the shallow nature of well present on the reactive PES, it is not clear so far that whether the mechanism of the depletion reaction would behave statistically or non-statistically. In fact the previous mechanistic details for the depletion reaction were predicted based upon the forward-backward symmetry of the total DCS.[] However, according to Larrégaray and Bonnet, [75] this notion of classification *i.e.,* determining the statistical or non-statistical nature from the forward-backward symmetry of the DCS, may not always hold true, especially at the state-to-state level in the quantum limit. [75] This is because at the quantum limit the interference between the partial waves may become significant around the extreme forward and backward regions even for the complex-forming reactions [75]. Therefore, another objective of the present work is to quantify the interference effects due to coherence of the partial waves which then can be used to distinguish the statistical or non-statistical nature of a reaction.

Since the LiH^+ ion is not amenable to direct experiment due to its low binding energy, an accurate quantum dynamical study of the depletion reaction is essential to understand the detailed reaction mechanism. In this chapter, a detailed quantum dynamical study of the depletion reaction and its isotopic variant

$$H + LiH^+ \rightarrow H_2 + Li^+ \quad \text{(R1)}$$
$$D + LiH^+ \rightarrow HD + Li^+ \quad \text{(R2)}$$

is reported.

3.2 Computational details

The theoretical method described in section 2.1 of chapter 2 is followed here to carry out the dynamical calculations for the two reactions, R1 and R2 on the *ab initio* PES of Martinazzo *et al.* [92]. Various numerical parameters characterizing the WP and the underlynig grid for the TDWP method need to be converged before the calculation of any reaction observable. First, the convergence of each parameter is checked with

respect to the energy resolved total reaction probability for J=0 where the WP is propagated for only 20000 chebyshev iteration steps. The value of the concerned parameter is varied until the total reaction probability is found to be unchanged. For the reagent H + LiH^+ (v=0, j=0) reaction the initial values of the parameters are guessed arbitrarily. However, for H + LiH^+ (v=1, j=0), H + LiH^+ (v=0, j=1) and D + LiH^+ (v=0, j=0) the converged parameters for H + LiH^+ (v=0, j=0) are used as initial values.

It is important to note here that in order to ensure the convergence of the final results, particularly in the low collision energy range, numerous test calculations are performed with respect to each parameter for different reagent quantum levels of the two reactions. The details of the converged parameters are given in Table 3.1 for R1 and in Table 3.2 for R2. The description of the parameters are given separately in Table 3.3. The results are converged up to a collision energy as low as 10^{-3} eV for which the

Table 3.1: Details of the numerical parameters used in the time-dependent wave packet calculations for the, H + LiH^+ (v=0−1, j=0−1) → H_2 (v', j') + Li^+, reaction. (*For J >0)

Parameter	LiH^+(v=0, j=0)	LiH^+(v=1, j=0)	LiH^+(v=0, j=1)
$N_{R'}/N_{r'}/N_{\gamma'}$	255/255/55	255/255/65	255/255/50
R'_{min}/R'_{max} (a_0)	0.3/28.0	0.3/30.0	0.3/28.0
r'_{min}/r'_{max} (a_0)	0.3/34.0	0.3/34.0	0.3/34.0
R'_d (a_0)	19.0	19.5	21.0
V_{cut} (E_h)	0.3	0.3	0.3
R'_{abs}/r'_{abs} (a_0)	24.0/24.0	24.0/24.5	23.0/26.0
C_{abs}/c_{abs}	0.24/0.3	0.3/0.3	0.4/0.4
R_0 (a_0)	18.0 (23.0*)	18.0	18.5 (21.5*)
E_{trans} (eV)	0.12	0.12	0.14
δ	7.0	7.5	8.0
β_s	0.7	0.7	0.7
$nvab$	15	15	15
$njab$	32	32	32
$nstep$	60000	60000	60000
Time (fs)	2265.5	2275.4	2261.4
J range	J=0-86	J=0-88	J=0-70

WP is propagated for longer times. A fine energy grid is prepared with equal spacing of ≈0.001 eV in order to account for any possible resonances. The parameters listed in Table 3.1 and 3.2 are also used for $J > 0$ calculations except for the location of the center of the initial WP, R_0. Since the centrifugal potentials for $J > 0$ decrease slowly at large R and also due to the long-range interaction, R_0 must be considered far out in the reagent asymptote than that for J=0. Moreover, the total number of Chebyshev iterations ($nstep$) decreases for $J > 0$ calculations because of the increase of the energy

Table 3.2: Same as in Table 3.1 but for the, D + LiH^+ (v=0, j=0) → HD (v', j') + Li^+, reaction. (*For J >0)

Parameter	LiH^+(v=0, j=0)
$N_{R'}/N_{r'}/N_{\gamma'}$	255/255/55
R'_{min}/R'_{max} (a_0)	0.3/28.0
r'_{min}/r'_{max} (a_0)	0.3/34.0
R'_d (a_0)	19.0
V_{cut} (E_h)	0.3
R'_{abs}/r'_{abs} (a_0)	24.0/24.0
C_{abs}/c_{abs}	0.24/0.3
R_0 (a_0)	18.0 (23.0*)
E_{trans} (eV)	0.26
δ	7.5
β_s	0.7
$nvab$	18
$njab$	37
$nstep$	60000
Time (fs)	2297.48
J range	J=0-97

Table 3.3: The description of the numerical parameters used in the time-dependent wave packet calculations.

Parameter	Description
$N_{R'}/N_{r'}/N_{\gamma'}$	Number of grid points along three product Jacobi coordinates (R', r', γ')
R'_{min}/R'_{max}	Extension of the grid along R_c
r'_{min}/r'_{max}	Extension of the grid along r_c
R'_d	Location of the dividing surface in the product channel
V_{cut}	Cut-off potential
R'_{abs}/r'_{abs} (a_0)	Starting point of absorption along R_c and r_c
C_{abs}/c_{abs}	Strength of absorption along R_c and r_c
R_0 (a_0)	Center of the initial WP in reagent Jacobi coordinate
E_{trans} (eV)	Initial translational energy
δ	Width of the initial WP
β_s	Smoothness of the initial WP
$nvab$	Number of vibrational levels of the product diatom
$njab$	Number of rotational levels of the product diatom
$nstep$	Number of iteration steps
Time	Total propagation time

threshold with an increase in J. This makes the reaction probabilities to converge for less number of iterations. For H + LiH^+ (v=0, j=0) the converged values of the *nstep* are found to be 60000 and 25000 for J=0-75 and J=76-86, respectively, corresponding to a total propagation time of 2265.5 fs and 931.3 fs. Similarly, for H + LiH^+ (v=1, j=0) the converged values of *nstep* are 60000, 30000 and 15000 for J=0-41, J=42-62 and J=63-88, respectively, corresponding to the total propagation time of 2275.4 fs, 1137.7 fs and 563.4 fs. For H + LiH^+(v=0, j=1) these are 60000, 40000, 30000, 21000 and 15000 for J=0-28, J=29-40, J=41-50, J=51-60 and J=61-70, respectively, corresponding to the total propagation time of 2261.4 fs, 1507.6 fs, 1130.7 fs, 791.5 fs and 565.3 fs. The number of partial waves considered to obtain converged cross ections up to E_{col} = 1.0 eV are given in the Tables for each initial state of LiH^+.

3.3 Results and Discussion

The initial state-selected total as well as state-to-state reaction probability, ICS, DCS and rate constants of both the reactions are presented and discussed in this section. The energy disposal mechanism of both the reactions is examined in terms of the product ro-vibrational level distribution and the average fraction of available energy enetering into product vibration, rotation and translation. The interference due to coherence among the partial waves are quantified which can be used as a tool to distinguish the non-statistical nature of a reaction. The effect of collision energy and reagent ro-vibrational excitation on various state-to-state dynamical observables of reaction R1 is investigated. A few computed reaction observables are also compared with the available literature results.

3.3.1 Reaction probability and opacity function

The initial state-selected total reaction probabilities of both reaction R1 and R2 for J=0 are shown in Figure 3.4 as a function of collision energy. For R1 the probabilities are shown for different initial states of the reagent LiH^+. It can be seen from the figure that for each of the initial ro-vibrational states of the reagent LiH^+, the reaction probability curves exhibit sharp resonance oscillations below collision energy of 0.2 eV. For energies above 0.2 eV, the resonance oscillations almost disappear and the reaction probability decreases monotonically as collision energy increases. The resonance oscillations are due to the formation of quasi-bound complexes during the course of the reaction which are supported by the shallow well present on the PES. This behaviour

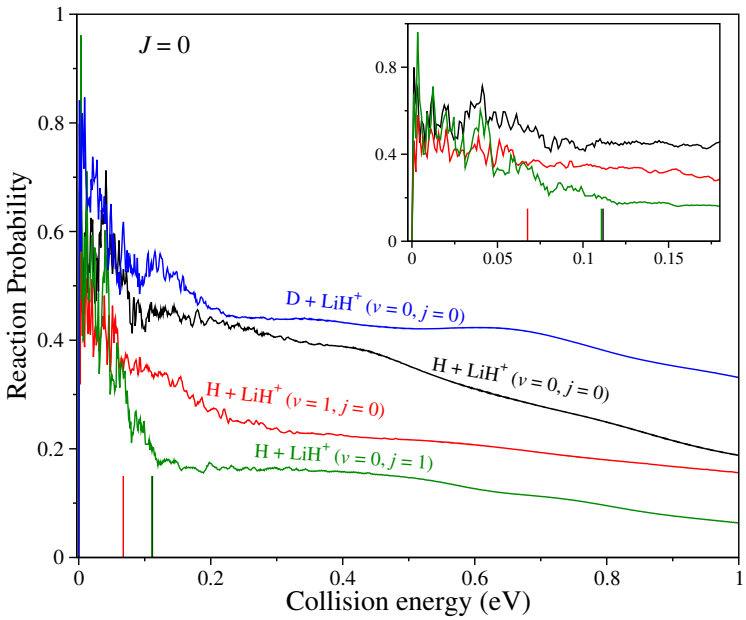

Figure 3.4: Initial state-selected total reaction probabilities of the H + LiH^+ (v=0-1, j=0-1) → H_2 + Li^+ and D + LiH^+ (v=0, j=0) → HD + Li^+ reactions for J=0 as a function of collision energy. The vertical lines represent the energy required to dissociate of Li^+–H bond from different ro-vibrational levels.

primarily suggests that for J=0, the reaction proceeds *via* a complex-mode mechanism at low collision energies and a direct mechanism at higher collision energies. The absence of threshold in the J=0 probability curves signifies the barrierless nature of both the reactions R1 and R2. In case of R1 the overall reaction probability decreases with internal excitation of the reagent. Vibrational excitation is more effective than the rotational excitation in reducing the probability within the binding energy range (marked as vertical lines, see the inset). However, as collision energy increases, the probability of LiH^+ (v=0, j=1) product yield suddenly decreases and continued to be remain so at higher collision energies. The reduction of reaction probability with internal excitation of reagent can perhaps be attributed to the opening up of the competing CID channel. This is because disposal of more internal energy in the weak Li–H bond facilitate the dissociation of LiH^+. Moreover, for the J=0 case, rotational excitation of LiH^+ leads to strong centrifugal distortion of the weak Li–H bond and can effectively promote the CID process. now comparing R1 and R2, it can be seen that the probability of formation of HD is higher than that of H_2 at almost entire range of collision energy considered here. This suggests that with substitution of heavier isotopes on the attacking atom, the reactivity of the depletion process increases.

In order to show the J dependence of both the reactions, the total reaction probabilities for different $J \geq 0$ and the opacity functions summed over all final states,

$(2J+1)P(J;\ E)$, are plotted in Figure 3.5 as a function of collision energy and J, respectively. It can be seen from the probability plots that small resonance oscillations

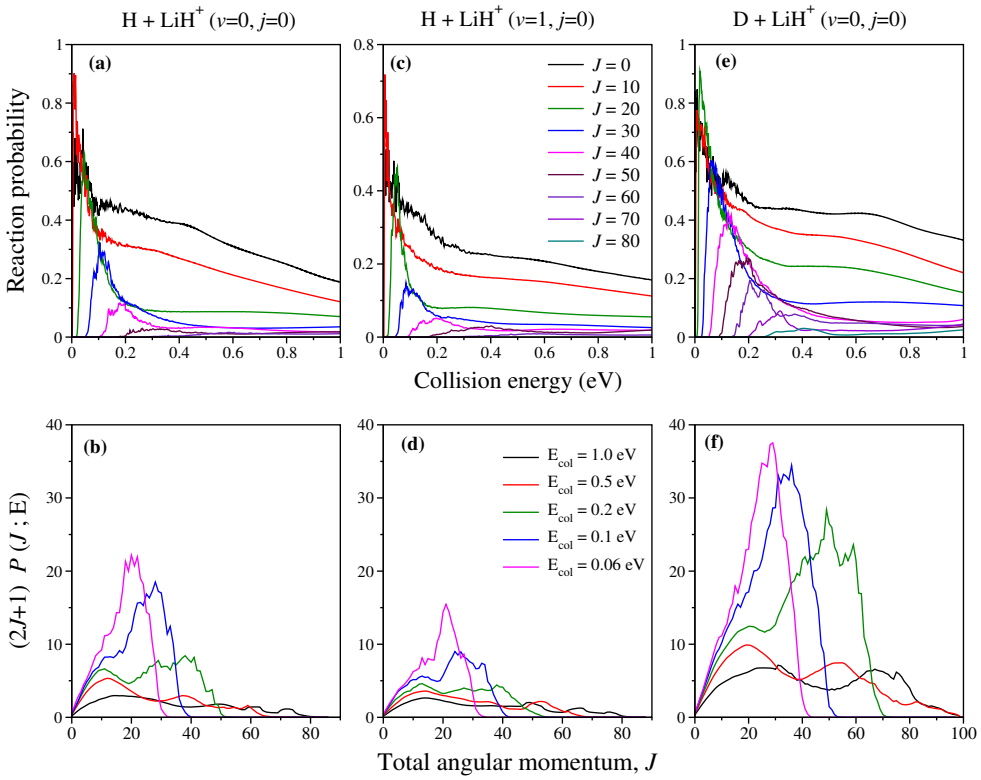

Figure 3.5: Initial state-selected energy-resolved total reaction probabilities and opacity functions of the H + LiH^+ (v=0-1, j=0-1) → H_2 ($\sum v'$, $\sum j'$, $\sum \Omega'$) + Li^+ and D + LiH^+ (v=0, j=0) → HD ($\sum v'$, $\sum j'$, $\sum \Omega'$) + Li^+ reactions. (a)-(b) for H + LiH^+ (v=0, j=0), (c)-(d) for H + LiH^+ (v=1, j=0) and (e)-(f) for D + LiH^+ (v=0, j=0).

remain in case of $J > 0$ below collision energy of 0.2 eV, and these oscillations get completely disappeared at higher collision energies. With increase in J, the threshold of both the reaction increases, although it is slower in case of R2. This is because increase in the centrifugal barrier height as J increases. The slow increase in reaction threshold of R2 as compared to R1 is a direct consequence of the higher reduced mass of the D + LiH^+ reactive system. The overall reactivity of R1 is very high in the low collision energy range and it decreases with reagent vibrational excitation for each J. However, with heavier isotopic substitution on the attacking atom the overall reactivity increases for each J quantum number. For higher J values the probability of both the reactions decreases [cf., Figure 3.5(a), (c) and (e)]. This is due to an increase of centrifugal potential for higher J values which makes the PES repulsive at high collision energies. With increasing collision energy there is very less contributions from higher J [cf., Figure 3.5(b), (d) and (f)], implying both the reactions are selective to specific

$J-E_{col}$ region irrespective of the initial state of LiH^+. Similar results are also found for H + LiH^+ (v=0, j=1) case of R1 but are not shown here for brevity.

It is well known that the total angular momentum, J, for the j=0 case, is proportional to the impact parameter, b of the collisional system. So the maximum value of b (b_{max}) can be estimated by the relation, $b_{max} = \sqrt{\frac{J_{max}(J_{max}+1)}{2\mu E_{col}}}\hbar$, where J_{max} is the maximum number of partial waves contributing to the reaction at the collision energy, E_{col}. This information can provide a qualitative estimate of the maximum range of interaction region in which the reaction occurs. The calculated values of b_{max} for H + LiH^+ (v=0, j=0) collision are found to be 12.05 a_0, 11.7 a_0, 11.33 a_0 and 10.25 a_0 at E_{col} = 0.05, 0.1, 0.2 and 0.3 eV, respectively, with J_{max} values 29, 40, 55 and 61 in that order. Since the overall feature of the opacity functions of R1 for LiH^+ (v=0, j=0), (v=1, j=0) and (v=0, j=1) resemble each other, similar values of b_{max} can be anticipated for LiH^+ (v=1, j=0) and (v=0, j=1). Moreover, the b_{max} values for D + LiH^+ (v=0, j=0) collision are found to be 8.94 a_0, 11.74 a_0, 15.84 a_0 and 19.07 a_0 at E_{col} = 0.05, 0.1, 0.2 and 0.3 eV, respectively, with corresponding J_{max} values of 41, 54, 73 and 88. Such large values of b_{max} at such low collision energies suggest that the reactions R1 and R2 are feasible at higher impact parameter collisions. This is due to the long-range interaction between the reacting species in the LiH_2^+ system. For such a large range of b, two different kinds of reaction mechanisms can operate. One at small and another at large impact parameter collisions. The scattering of products from these two kinds of collisions can be extracted from the DCSs of the reactions which is discussed later in the chapter.

3.3.2 Integral reaction cross section

The initial state-selected total ICSs of the reactions R1 and R2 are plotted in Figure 3.6 as a function of collision energy in the *log-log* scale. The present QM results of R1 which include the Coriolis coupling (QM-CC) are compared in panel (a) with various literature results obtained by QM-CC, QCT and QM-CS (QM method with CS approximation) methods using different PESs. The results which is obtained by using a PES other that of Martinazzo *et al.* are marked with a star ($*$). The effect of reagent ro-vibrational excitation and isotopic substitution is shown in panle (b). It can be seen from panels (a) and (b) of Figure 3.6 that the total ICS decreases with increasing collision energy which characteristically features a barrierless reaction. Reagent ro-vibrational excitation reduces the reactivity at all collision energies with a marked reduction in the low collision energy range. The ICS of reaction R2 is found to larger than that of R1 in the

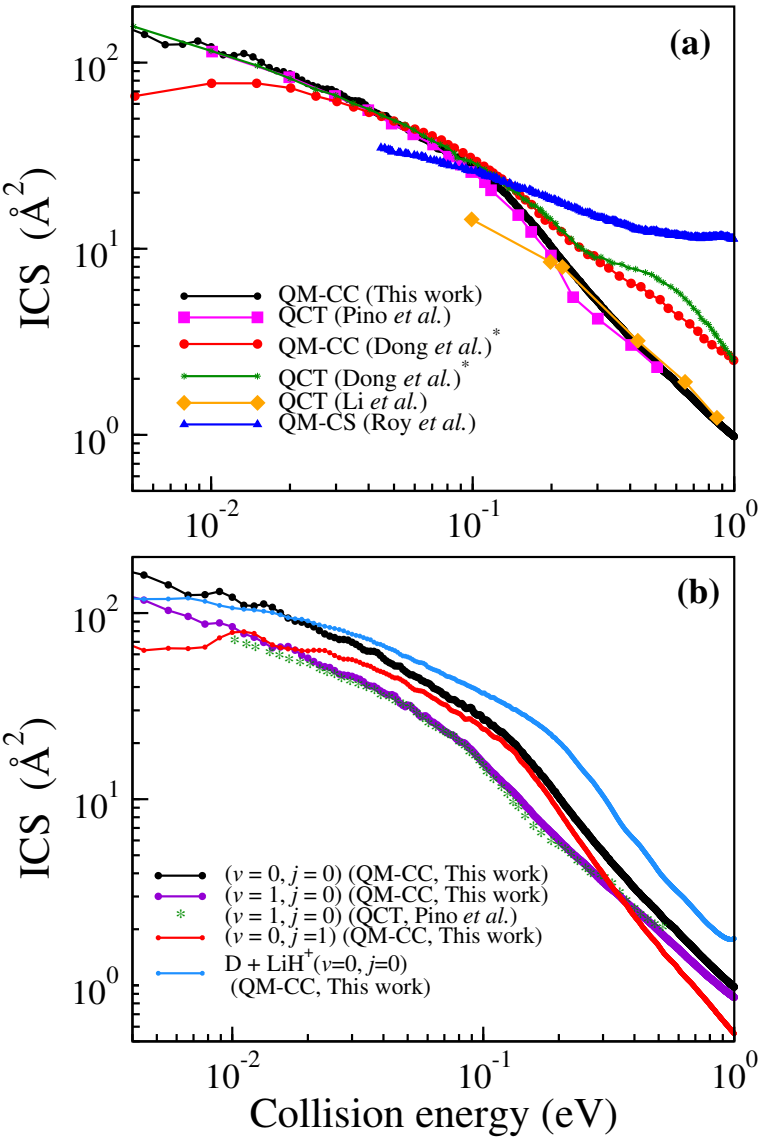

Figure 3.6: Initial state-selected total ICSs of the H + LiH^+ (v=0-1, j=0-1) → H_2 ($\sum v'$, $\sum j'$, $\sum \Omega'$) + Li^+ and D + LiH^+ (v=0, j=0) → HD ($\sum v'$, $\sum j'$, $\sum \Omega'$) + Li^+ reactions as a function of collision energy. The ICSs are plotted in logarithmic scale to clearly portray the low-energy behaviour. (a) The present QM-CC total ICS of H + LiH^+ (v=0, j=0) is compared with previous literature results. (b) Total ICSs of H + LiH^+ (v=0-1, j=0-1) and D + LiH^+ (v=0, j=0) showing the effect of reagent ro-vibrational excitation and isotopic substitution.

higher collision energy range. This means upon substitution with a heavier isotope of the attacking atom, the reactivity of the depletion process increases, more substantially at higher collision energies than the lower one. The ICSs hardly carry any signature of resonance oscillations. However, the reaction probabilities exhibited sharp oscillations at low collision energies as shown in Figure 3.4 and 3.5 above. The resonance oscillations in the reaction probability, regarded as the quantal features and attributed to the presence of a shallow well, are completely washed out in the ICS. This may be due to an averaging over different partial waves and the sum over product internal states.

It can be seen from Figure 3.6(a) that a marked difference is found when the present ICS values of R1 are compared with that of Roy *et al.* [105] This poor agreement appears to be due to the use of CS approximation in their calculations which excludes the Coriolis coupling terms. The agreement between the present QM-CC ICS of H + LiH^+ (v=0, j=0) and that of the QCT ICS of Pino *et al.* [96] obtained using the same PES is excellent in the entire collision energy range. In case of an exoergic and barrierless reaction such an agreement between the QM and QCT results is obvious and is obtained in the present case. This observation is further complemented with the very good agreement of the present QM-CC ICS of H + LiH^+ (v=1, j=0) with that of Pino *et al.* [96] calculated by a QCT method on the same PES [cf., Figure 3.6(b)]. The QCT ICS of Dong *et al.* [112], obtained by using a different PES, agree well with the present ICS values and also with the QCT ICS values of Pino *et al.* [96] at low collision energies but disagree at high collision energies. This good agreement between the QM and QCT results suggests that the quantum effects due to the presence of the shallow well do not show up in the total ICS even at low collision energies for this exoergic barrierless reaction because the quantal resonance features average out in the ICS. Since the total energy of the system is conserved, even at low collision energy, the products of the reaction may have large energy content owing to the high exoergicity of the reaction ($\approx$ 4.6 eV) and the fact that a well is present at the product channel. At such high energy content of products, the QM and QCT results are expected to agree with each other for an exoergic and barrierless reaction even if the collision energy is low.

The comparison between the present QM-CC ICS of reaction R1 and the QM-CC ICS of Dong *et al.* [112] shows a clear disagreement with each other and the pattern of the variation of the latter as a function of collision energy approaches to the QM-CS result of Roy *et al.* [105] [cf., Figure 3.6(a)]. The disagreement can be attributed to the differences in the PESs used for the study. At a very low collision energy the reagents move very slowly relative to each other. As a consequence, the dynamics is largely

governed by the interaction forces compared to other factors and the latter depends on the potential energy of the system. Therefore, the differences in the dynamical results at such low collision energies must be attributed to the difference between the PES used rather than the quantum effects. It has been observed that such quantum effects disappear in the ICSs even at cold and ultracold conditions [110]. We mention here that the PES of Martinazzo *et al.* explicitly considers the long range interactions between H_2 and Li^+ [92]. However, in case of the PES of Dong *et al.*, these long range interactions are not included [112]. This can have significant impact on the dynamics particularly at lower collision energies. Moreover, the depth of the C_{2v} minimum is found to be ≈0.286 eV with respect to the product (H_2 + Li^+) asymptote in case of the PES of Martinazzo *et al.*, [92] whereas, it is ≈0.23 eV with respect to the product asymptote in case of the PES of Dong *et al.* [112] These differences in the PESs explain the differences in the ICS values both at low and high collision energies. Moreover, for the H + LiH neutral reaction, which has the same mass combination as the present system, such differences have been reported below 0.06 eV of collision energy and were attributed to the differences in the PESs used [124]. The QCT ICS of Li and Lei [114] obtained using the PES of Martinazzo *et al.* [92] agree well with the present results at very high collision energies. It is important to note here that for the H + LiH^+ (v=0, j=0) reaction, all of the ICS plots (except that of Li and Lei [114]) shown in Figure 3.6(a) converge up to ≈ 0.11 eV of collision energy. The latter interestingly coincides with the D_0 value of LiH^+ in its ground ro-vibrational state.

3.3.3 Total differential cross section

The initial state-selected total DCSs of both the reactions R1 and R2 are shown in Figure 3.7 as a function of the center-of-mass scattering angle (θ) at a few collision energies. The effect of reagent ro-vibrational excitation and isotopic substitution on the attacking atom are also shown. The total DCS values for H + LiH^+ (v=0, j=0) reaction calculated on the PES of Martinazzo *et al.* [92] are compared with the QM-CC DCS results of Dong *et al.* [112] obtained on a different PES. The results are shown in the inset of each panel of Figure 3.7. It can be seen from the figure that for LiH^+ (v=0, j=0) of both R1 and R2, the DCS is dominated by forward scattering at low collision energies with little backward scattering, except at E_{col}=0.1 eV, where a significant backward peak at θ=180° is observed in case of R1. This indicates that both direct and complex-mode mechanisms contribute to the reaction dynamics at low collision energy for H (D) + LiH^+ (v=0, j=0). At higher collision energies, however, the backward scattering almost

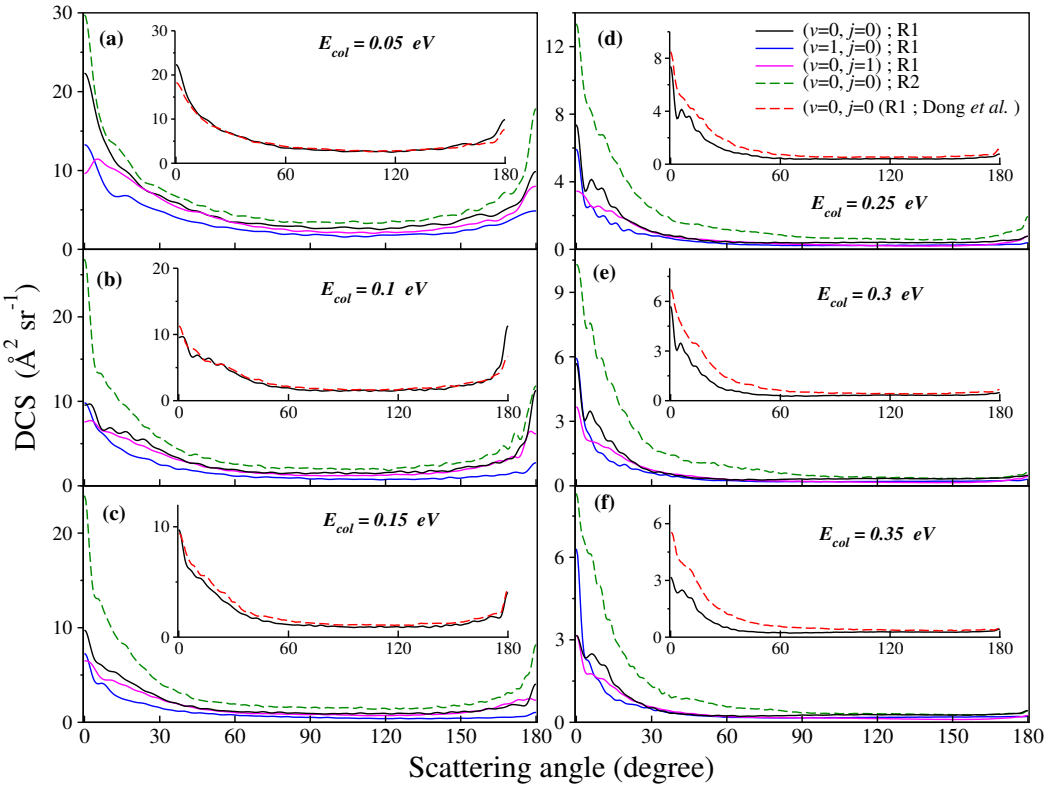

Figure 3.7: Initial state-selected total DCSs of the H + LiH^+ (v=0-1, j=0-1) → H_2 ($\sum v'$, $\sum j'$, $\sum \Omega'$) + Li^+ and D + LiH^+ (v=0, j=0) → HD ($\sum v'$, $\sum j'$, $\sum \Omega'$) + Li^+ reactions as a function of center-of-mass scattering angle (θ) at various fixed collision energies. The present QM-CC results for H + LiH^+ (v=0, j=0) calculated on the PES of Martinazzo *et al.* [92] (black solid lines) are also compared with QM-CC results of Dong *et al.* [112] (red dashed lines) obtained on a different PES and shown in the inset of each panel.

disappears leading to only forward scattering in the total DCS. This indicates both the reactions in general are dominated by a direct mechanism at higher collision energy. It is noted here that the total DCSs are also calculated for collision energy greater than 0.35 eV (but up to E_{col}=1.0 eV). These DCSs exhibit similar complete forward scattering and are not shown here for brevity.

Vibrational excitation of the reagent decreases the magnitude of the total DCS of reaction R1 in the collision energy range below 0.3 eV. However, as collision energy increases, a forward peak in the DCS emerges and becomes more intense than that of H + LiH^+ (v=0, j=0) [cf., Figure 3.7(f)]. Since the reduction occurs at almost all scattering angles and is probably more in the backward region than the forward, it can be said that the vibrational excitation of LiH^+ partially inhibits the indirect mechanism of R1. Moreover, the backward scattering seen in case of H + LiH^+ (v=0, j=0) disappears with vibrational excitation of the reagent. Therefore, the total DCS for H + LiH^+ (v=1,

j=0) becomes completely forward dominated as compared to H + LiH^+ (v=0, j=0). This indicates that the reagent vibrational excitation facilitates the breaking of Li-H bond making the abstraction of the hydrogen atom easier and the reaction becomes more direct as compared to H + LiH^+ (v=0, j=0). It is to be noted here that with the vibrational excitation of reagent LiH^+, the reactivity of reaction R1 decreases. This is because of the mirroring effect that the internal excitation of reagent LiH^+ enhances the reactivity of the two competing processes *i.e.,* the hydrogen exchange reaction and the CID [96]. The DCS for H + LiH^+ (v=0, j=1) shows similar behaviour as H + LiH^+ (v=0, j=0) except a drop in the magnitude at extreme forward and backward regions implying a similar mechanism for rotationally excited reagent. By comparing the total DCSs of R1 and R2 for reagent LiH^+ (v=0, j=0) it is seen that the DCS becomes more forward dominated upon substituting the attacking atom with heavier isotopes. This primarily suggests that the mechanism of reaction R2 may possibly show more direct nature as compared to R1.

The comparison of the present QM-CC total DCSs for H + LiH^+ (v=0, j=0) with that of Dong *et al.* [112] (displayed in the inset of each panel) shows very good agreement with each other at low collision energies except some minor differences at the extreme forward and backward directions. However, significant quantitative differences persist at high collision energies particularly in the forward direction. These quantitative differences can be attributed to the different PESs used in the theoretical investigations.

3.3.4 Rate constant

The initial state-specific thermal rate constants of the reactions R1 and R2 are shown in Figure 3.8 at temperatures ranging from 50 to 10000 K. The present QM-CC rate constant for H + LiH^+ (v=0, j=0) is compared in panel (a) with the QCT rate constant of Pino *et al.* [96] and the RCSA and RIOSA rate constants of Bovino *et al.* [102] It is to be noted here that the QCT rate constant of R1 shown in Figure 3.8(a) is derived from the QCT ICS of Pino *et al.* [96] for LiH^+ (v=0, j=0). The present rate constant of R1 exhibits negative temperature dependence above T = 180 K and shows a very good agreement with the QCT rate constant. However, small quantitative differences persist between the two. This is because the QCT ICS of Pino *et al.*, [96] from which the QCT rate constant is calculated, is from collision energy of 0.01 to 0.5 eV, whereas, the present QM-CC ICS is from 0.001 to 1.0 eV. The variation of the QM rate constants calculated by Bovino *et al.* [102] is found to be significantly different from the present

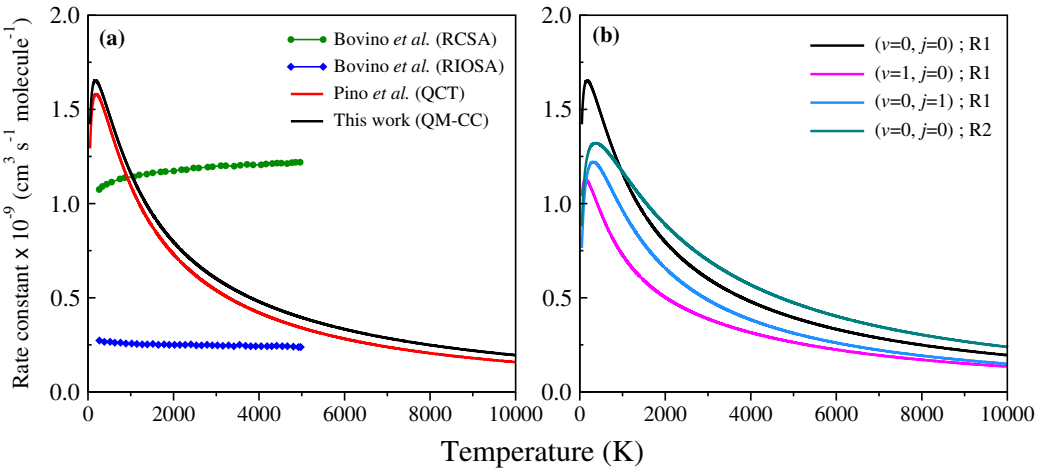

Figure 3.8: Initial state-specific thermal rate constants of reactions R1 and R2 as a function of temperature. (a) The present QM-CC rate constant of H + LiH^+ (v=0, j=0) is compared with the results available in the literature [96, 102]. The QCT rate constant shown here is calculated from the QCT ICS of Pino *et al.* [96] (b) Thermal rate constants of H + LiH^+ (v=0-1, j=0-1) and D + LiH^+ (v=0, j=0) showing the effect of reagent ro-vibrational excitation and isotopic substitution.

result. It is noteworthy to mention here that in the investigation by Bovino *et al.*, [102] the rate constants were computed only up to 100 K and were then extrapolated up to 5000 K by an equation proposed by Stancil *et al.* [87] We note here that the Boltzmann averaged rate constant of R1 obtained by Pino *et al.* [96] and Roy *et al.* [105] (not shown here) also have similar order of magnitude. Even though the same PES of Martinazzo *et al.* [92] was used in the above calculations, the differences are attributed to the severe approximations employed in the previous theoretical studies [102, 105]. Despite the differences, it can be seen that all the rate constants are of same order of magnitude.

The effect of reagent ro-vibrational excitation and isotopic substitution of the attacking atom on the initial state-specific rate constant is shown in Figure 3.8(b). It can be seen that the rate of the depletion reaction decreases at all temperatures with internal excitation of the reagent LiH^+ diatom. In particular, the vibrational excitation of the reagent is more effective in reducing the rate as compared to the rotational excitation. Moreover, it can be seen that for the reagent LiH^+ in its (v=0, j=0) level, the rate of reaction R2 is found to be a little higher than that of R1 above $T \approx 1000$ K, and is surprisingly lower in the temperature range below 1000 K. This suggests that the rate of the depletion reaction increases with substituting heavier isotopes for the attacking atom, but at higher temperatures.

In order to understand the rate of formation of product in its specific quantum state, the state-to-state rate constants of both the reactions are analyzed. The most probable

j'-resolved state-to-state rate constants of few selected v' levels are shown in Figure 3.9 for the H + LiH^+ (v=0, j=0) case at temperatures ranging from 50 to 4000 K. It

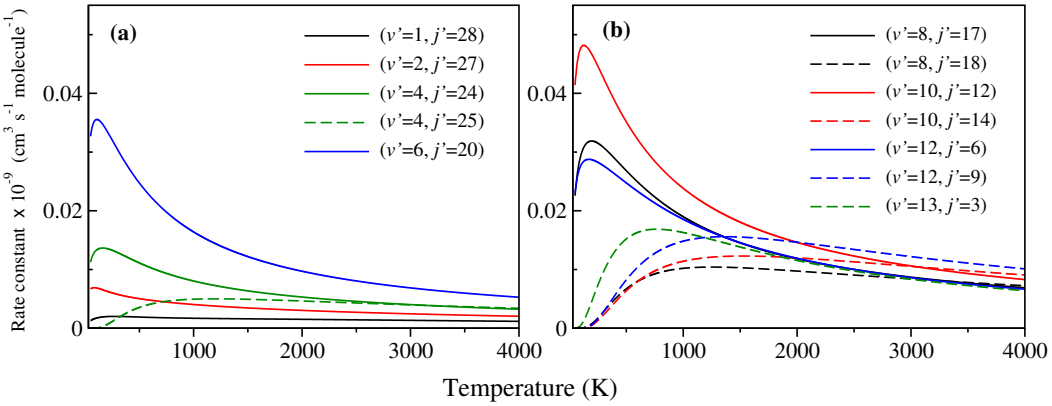

Figure 3.9: Product rotational level resolved state-to-state rate constants for the, H + LiH^+ (v=0, j=0) → H_2 (v', j', $\sum\Omega'$) + Li^+ reaction shown as a function of temperature. The state-to-state rate constants are shown by lines of different types and colours.

can be seen that threshold appears for the formation of product in some specific (v', j') states (shown by dashed lines in Figure 3.9). This is because these product energy levels lie above the LiH^+ (v=0, j=0). For the product states which does not exhibit threshold, the rate constant shows negative temperature dependence starting from T = 180 K. However, for others the rate constant increases with increase in temperature up to ≈ 1500 K and decreases afterwards. The same observation has also seen in case of teh reaction R2. It is found that the formation of H_2 is most probable in its (v'=10, j'=12) quantum state below 2000 K and in its (v'=12, j'=9) quantum state above 2000 K. Similarly, the formation of HD from reaction R2 is found to be most probable in its (v'=11, j'=16) quantum state below 1500 K and in its (v'=12, j'=16) quantum state above 1500 K. Therefore, it can be concluded that the product H_2 and HD preferably formed in their highly vibrationally and rotationally excited states.

3.3.5 Product ro-vibrational level distribution

So far we have discussed the initial state-selected dynamics of both reaction R1 and R2. In what follows next we discuss the state-to-state dynamics of both the reactions in order to understand the detailed reaction mechanism. The product vibrational level distributions (summed over j') of the reactions R1 and R2 are shown in Figure 3.10 in terms of ICS at three different collision energies. These distributions represent the product vibrational level resolved ICSs as a function of v' at selected collision energies. It can be seen from the figure that the products are highly vibrationally excited leading

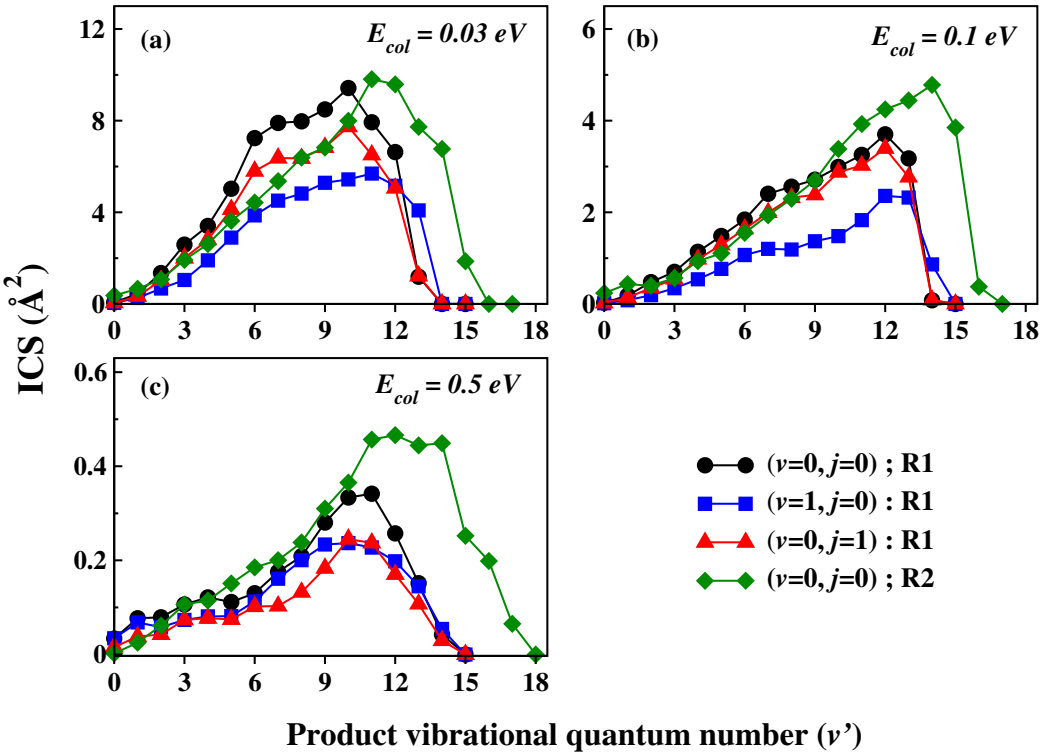

Figure 3.10: Product vibrational level distributions in terms of ICS for the H + LiH^+ (v=0-1, j=0-1) → H_2 (v', $\sum j'$, $\sum \Omega'$) + Li^+ and D + LiH^+ (v=0, j=0) → HD (v', $\sum j'$, $\sum \Omega'$) + Li^+ reactions at three different collision energies, E_{col} = 0.03, 0.1, and 0.5 eV.

to an inverse Boltzmann population distribution in both the cases of R1 and R2. This is a typical feature of the energy disposal on an attractive PES according to the Polanyi's rule. [53, 54] The rule suggests, if the energy releases before the formation of the product then it mainly goes into product vibration. It is evident from the minimum energy path of the reaction (cf., Figure 3.3) that the interaction energy decreases before the formation of Li^+—H_2 complex while the H atom is still approaching the LiH^+ diatom.

The effect of ro-vibrational excitation in reaction R1 is not so apparent as the qualitative as well as the quantitative features of the distributions are more or less the same for a fixed value of collision energy. However, differences persist between the distributions of R1 and R2 for LiH^+ (v=0, j=0). It can be seen that with substitution of heavier isotope on the attacking atom more vibrational levels of product get populated and the maximum of the vibrational distribution shifts towards higher v' levels at each collision energies. This is purely because of the kinematic effect as the product diatom HD of R2 has lower vibrational energy-spacing than H_2 due to heavier mass and consequently is able to populate more vibrational levels than R1. In fact it is because of this reason that the reaction R2 has higher reaction cross section than R1 [cf., Figure 3.6(b)]. This evident from the vibrational distribution plot that the population to the lower v' levels is

almost same for both R1 and R2, and the major contribution to the cross section of R2 mainly comes from the higher v' levels.

A close examination of Figure 3.10 reveals that the maximum of the vibrational distribution mildly shifts towards higher v' (reaching to a maximum at v'=12 for R1 and 14 for R2) as collision energy increases up to E_{col} = 0.1 eV. Afterwards, it shifts back to its original position when collision energy further increases [cf., Figure 3.10(c)]. This indicates a very mild effect of collision energy on the vibrational distribution of the reaction. An examination of the product vibrational energy levels at the asymptote of the LiH_2^+ PES shows that a total 15 vibrational levels of H_2 (v'=0 to 14) and 18 vibrational levels of HD (v'=0 to 17) lie below the three-body dissociation limit can be populated. Indeed, Figure 3.10 shows that the product states are populated up to the energetic limit *i.e.,* the energy available to the products except at the lowest collision energy. However, the most efficient energy transfer does not occur to the highest v' level. The maximum of the vibrational distribution lies at an intermediate v'. This is because of the availability of a fewer number of quantum states for higher vibrational levels and the possibility of secondary collisions of Li^+ ion with H_2 or HD particularly at low collision energy where complex-mode mechanism can dominate. The latter is indeed supported by the shallow well on the PES which may reduce the vibrational excitation of the products.

The above observations show that the product vibrational distribution of reaction R1 is hardly affected by any form of energy supplied to the reactive system. This is because the structure of the C_{2v} complex is such that it does not allow the relative translational and the vibrational mode of reagent to effectively couple with the vibrational mode of product as it is shown in Figure 3.11.

Due to the C_{2v} structure of the complex, the relative translational mode along R and the vibrational mode along r of the reagent couples weakly to the product's vibrational mode along r'. The vector $\vec{R}$ and $\vec{r}$ are almost perpendicular to $\vec{r'}$ and hence the coupling is not strong (cf., Figure 3.11). This indicates the energy released into product vibration must come from the exoergicity of the reaction; largely from the binding energy of the H_2 molecule. This reflects the dominant role of the exoergicity in the energy disposal mechanism of the reaction.

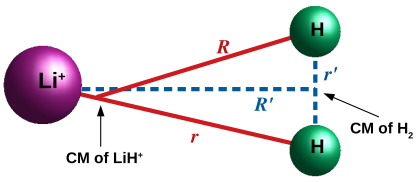

Figure 3.11: Cartoon diagram showing a qualitative scenario of coupling between various modes of reagent and product diatoms in the LiH_2^+ system.

The consideration of the couplings between various modes of reagent and product diatoms merits some justification here. First of all we would like to mention here that the well present at the product valley is not too deep. The depth of the well is only ~0.286 eV with respect to the product asymptote. Because of the shallow nature of the well, the intramolecular vibrational redistribution (IVR) can be very slow during the course of the reaction. In that limit the coupling between various modes of reagent and product diatoms can be assigned, provided there will be no energy flow among various internal modes of the complex [125]. This is indeed justified because of the large frequency difference of the H–H (~4000 cm^{-1}) and Li–H (~650 cm^{-1}) vibrations in the LiH_2^+ molecular system [126] which can result in slow IVR. Moreover, the reaction is found to proceed through a direct mechanism at higher collision energies which may not facilitate IVR. Hence, in the limit of minimal IVR, it is resonable to consider the couplings between various modes of reagent and product diatoms in the C_{2v} complex.

The product rotational level resolved state-to-state ICSs of reaction R1 and R2 are presented in Figure 3.12 for reagent LiH^+ (v=0, j=0). The state-to-state ICSs are shown here at two collision energies, E_{col} = 0.1 and 0.3 eV, in terms of "triangle plots" [53, 54] as a function of v' along the abscissa and j' along the ordinate. These plots represent the product ro-vibrational level population distributions at selected energies. The immediate observation that can be made from these plots is the appearance of a ridge structure of the distribution nearly along the diagonal. The ridge structure moves from the region of low v' and high j' to a region of high v' and low j'. This suggests that for every v' level a very narrow range of j' levels are populated. Almost similar observations are also found for LiH^+ (v=1, j=0) and LiH^+ (v=0, j=1) of R1 (not shown).

The above observation is in contrast with the neutral, H + LiH → H_2 + Li, reaction where a broad range of j' distribution has been found. [127] Such differences may arise due to the difference between the exoergicity of the two reactions as the neutral reaction is less exoergic ($\Delta E_0 \approx$ -2.258 eV [128]) than the present ionic reaction. For lower v' levels, products are rotationally excited and for higher v' levels products are rotationally cold akin to the j' distributions for the neutral counterpart of the reaction R1. [127] Similar observations are also reported in cold and ultracold conditions by Roy and Mahapatra [110]. This suggests that for the reaction R1 the energy disposal mechanism in thermal conditions is no longer different from that in cold and ultracold conditions. Moreover, the product rotational level resolved state-to-state ICSs are calculated at few more collision energies for LiH^+ (v=0-1, j=0-1). The results are not shown here for brevity but indicates a very similar behaviour. This reflects the independent

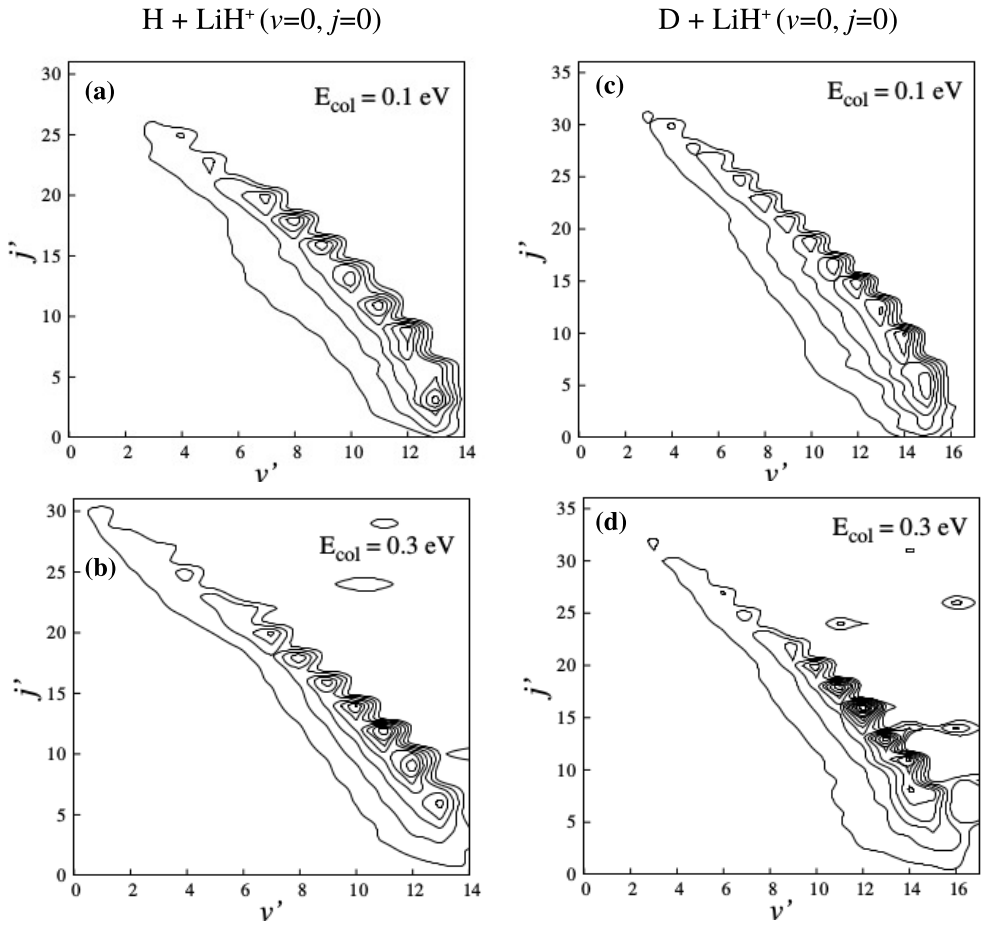

Figure 3.12: Contour plots of product rotational level resolved state-to-state ICS for the H + LiH^+ (v=0-1, j=0-1) → H_2 (v', j', $\sum\Omega'$) + Li^+ and D + LiH^+ (v=0, j=0) → HD (v', j', $\sum\Omega'$) + Li^+ reactions shown as a function of v' (abscissa) and j' (ordinate) quantum numbers at two collision energies, E_{col} = 0.1 and 0.3 eV. The contour lines in panels (a) and (c) are separated by 0.1 $Å^2$, while those in panels (b) and (d) are separated by 0.02 and 0.03 $Å^2$, respectively.

nature of the product rotational level distributions with increasing collision energy and reagent ro-vibrational excitation. Furthermore, the effect of the isotopic substitution of the attacking atom is not so significant as can be seen from Figure 3.12(c) and (d).

The diagonal nature of the "triangle plots" is quintessential for exoergic reactions where attractive energy release mainly dominates the energy disposal mechanism [54]. From the Figure 3.3 it can be seen that the minimum energy path for the reaction occurs in a bent geometry when the H or D atom approaches the LiH^+ diatom from the hydrogen side at an angle (∠LiHH) of ≈ 80°. Therefore, when the H or D atom approaches, it takes away the other H atom from LiH^+ diatom in a non-linear (bent) geometry leading to an efficient rotational excitation of the products. Moreover, the reactive system considered here belongs to Light (L) + Light (L)-Heavy (H) mass combination where the recoiling Li^+ ion is heavier compared to the incoming hydrogen or deuterium atom.

So the orbital angular momentum ($\boldsymbol{l'}$) associated with the heavier Li^+ will be much less than the rotational angular momentum ($\boldsymbol{j'}$) of lighter H_2 or HD, *i.e.*,, $\boldsymbol{l'} \ll \boldsymbol{j'}$. Since the total angular momentum is conserved ($\boldsymbol{J} = \boldsymbol{l'} + \boldsymbol{j'}$), it can be argued that $\boldsymbol{J} \approx \boldsymbol{j'}$. This subsequently leads to an efficient conversion of large $\boldsymbol{J}$ into rotationally excited ($\boldsymbol{j'}$) product. It, therefore, appears that the highly attractive and exoergic nature of the PES, the non-collinear abstraction of the H atom and the efficient disposal of $\boldsymbol{J}$ into $\boldsymbol{j'}$ are the reasons for the non-statistical inverse Boltzmann population distribution of products.

3.3.6 Energy disposal mechanism

In order to understand the product energy disposal in more detail the average fraction of the available energy entering into product vibration ($\langle f'_V \rangle$), rotation ($\langle f'_R \rangle$) and translation ($\langle f'_T \rangle$) have been calculated by using equations 2.43–2.46. The results are shown in Figure 3.13 for both R1 and R2 and for different initial states of reagent LiH^+ as a function of collision energy.

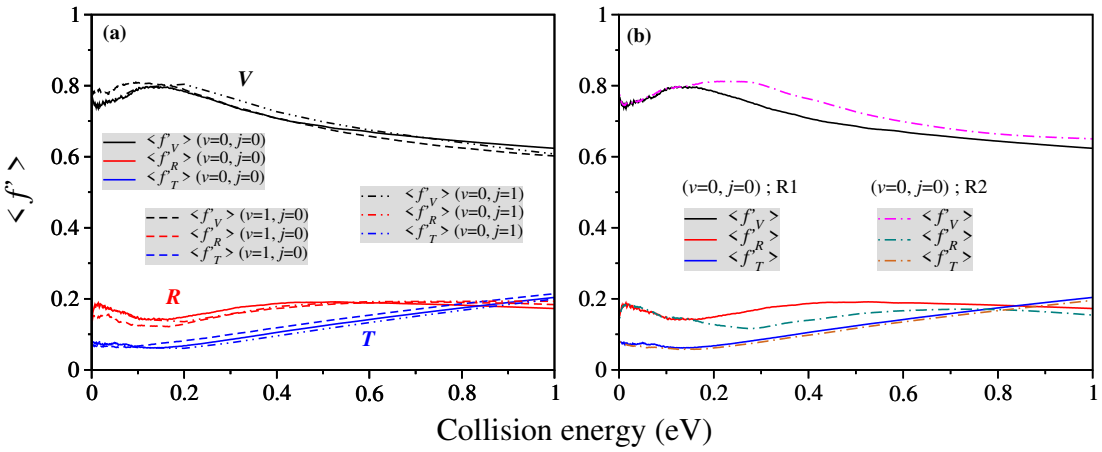

Figure 3.13: Average fraction of the available energy disposal into product vibration, rotation and translation ($\langle f'_V \rangle$, $\langle f'_R \rangle$ and $\langle f'_T \rangle$) for the H + LiH^+ (v=0-1, j=0-1) → H_2 + Li^+ and D + LiH^+ (v=0, j=0) → HD + Li^+ reactions as a function of collision energy. (a) The $\langle f' \rangle$ values of reaction R1 with LiH^+ (v=0-1, j=0-1) (b) The $\langle f' \rangle$ values of both reaction R1 and R2 with LiH^+ (v=0, j=0).

It can be seen that a larger portion of the available energy goes into product vibration which is almost 80% at low collision energy and varies up to 60% at high collision energy. This behaviour is consistent with the highly "attractive" nature of the PES and the fact that attractive energy release goes to product vibration for such exoergic reaction. The average fraction of the available energy entering into product rotation and

translation are very less (15% - 19% and 5% - 21%, respectively) compared to vibration. $\langle f_T' \rangle$ is the lowest at low collision energies and increases slowly with increasing collision energy up to 1.0 eV. However, $\langle f_R' \rangle$ attains almost a constant value above E_{col} $\approx$ 0.5 eV after increasing gradually in the low collision energy range. In order to understand the behaviour of the $\langle f_R' \rangle$, the $\langle f_R' \rangle^J$ values for different J are calculated by using equations 2.43–2.46 but with the total and state-to-state ICSs are replaced by the total and state-to-state reaction probabilities for a fixed value of J. The results are shown in Figure 3.14 for J = 0, 10, 30 and 50 as a function of collision energy for R1 with LiH^+ (v=0, j=0).

The $\langle f_R' \rangle^J$ values for LiH^+ (v=1, j=0) and LiH^+ (v=0, j=1) of R1 follow the similar trend as in case of LiH^+ (v=0, j=0) and are not shown here for brevity. It can be seen from Figure 3.14 that for J = 0, the $\langle f_R' \rangle^J$ increases up to E_{col} = 0.6 eV and then remains almost flat. The $\langle f_R' \rangle^J$ values increase from J = 0 to 10 at all collision energies. With further increase in J up to 50, the $\langle f_R' \rangle^J$ values remains higher than that of J = 0 in the low collision energy range but decreases at high collision energies. This is explained as follows. As in the present case, where the recoiling atom (Li^+) is heavier than the product diatom (H_2), ***J*** efficiently disposes to ***j'***. This means collisions with low ***J*** would yield products with low ***j'*** and vice versa. Generally, as collision energy increases, more partial waves contributes to the reactivity. However, as shown in Figure 3.5 and explained in section 3.3.1, the reactivity dominates in the low collision energy range and with increasing collision energy there is no significant contributions of the higher partial waves. Therefore, the $\langle f_R' \rangle^J$ values for higher J are highest in the low collision energy range but lowest in the high collision energies. As a result, at high collision energies, a smaller portion of the available energy disposes into product rotation. Hence, the $\langle f_R' \rangle$ values, as shown in Figure 3.13, increases slowly at low collision energies and remains almost flat at high collision energies.

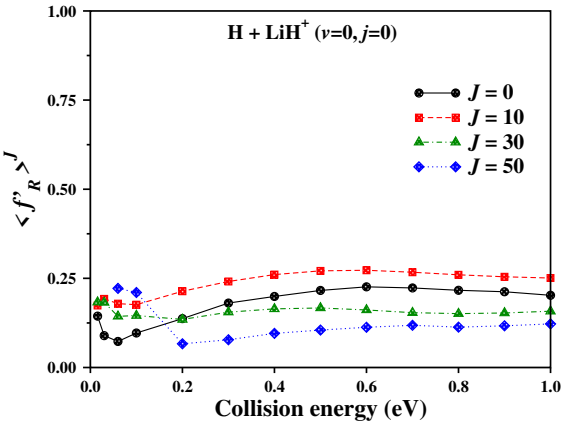

Figure 3.14: The $\langle f_R' \rangle^J$ values of H + LiH^+ (v=0, j=0) $\rightarrow$ H_2 + Li^+ reaction as a function of collision energy for a few fixed value of J.

The reactive system may explore more repulsive part of the PES at high collision energy since the cone of acceptance becomes more wider as collision energy increases.

[1] This inaccessibility of the attractive part of the PES leads to a reduction of $\langle f_V' \rangle$ values at high collision energies. The energy released from this repulsive part ($\approx 20\%$) goes into product translation. Moreover, it can be seen from Figure 3.11 that the relative translational mode of reagent can effectively couple with the relative translational (recoil) mode of product. This makes the $\langle f_T' \rangle$ values to increase monotonically with the increase in collision energy (cf., Figure 3.13).

The extent of energy disposal into various degrees of freedom of product barely changes with the ro-vibrational excitation of reagent LiH^+ diatom. [cf., Figure 3.13(a)] This implies that the energy disposal mechanism of the depletion reaction is practically insensitive to the internal excitation of the reagent. However, with the substitution of heavier isotope of the attacking atom more fractions of available energy goes to product vibration as compared to R1. This comes with the expense of the product rotational energy, as can be seen from Figure 3.13(b). It is seen that the $\langle f_R' \rangle$ values of R2 remain lower than that of R1, at the same time the $\langle f_V' \rangle$ values of R2 remain higher than that of R1, at collision energy above 0.2 eV. It is also interesting to see that the $\langle f_T' \rangle$ values of R2 are almost same as that of R1 in the entire range of collision energy. This suggests that the fraction of available energy entering to product translation does not change with isotopic substitution on the attacking atom. This is due to the "attractive" nature of the PES for the depletion reaction where the role of the recoil energy is minimal.

The major factors which can affect the product energy disposal of a particular reaction are the topography of the underlying PES, exoergicity or endoergicity of the reaction, the mass combination of the reactive system and some additional factors such as the energy supplied to the reagents in the form of vibration, rotation or translation. The unique combination of the two factors, exoergicity and the L + LH mass combination, for this particular reaction, makes the product energy disposal similar to that of a reaction occurring on an "attractive" PES.

3.3.7 State-to-state differential cross sections

DCS of a reactive scattering event provides the angular distribution of the products in various quantum states and hence the detailed reaction mechanism. In this section the product state-resolved DCSs of the reaction R1 calculated by the exact TDWP method (discussed in section 3.2) is presented over a wide range of collision energy. The collision energy below 0.2 eV is chosen as low energy regime and those above 0.2 eV as high energy regime.

The product rotational level resolved state-to-state DCSs of the H + LiH^+ (v=0, j=0) → H_2 (v', j') + Li^+ reaction are presented in Figures 3.15 and 3.16 at E_{col} = 0.1 and 0.3 eV, corresponding to low and high collision energy, respectively. The most

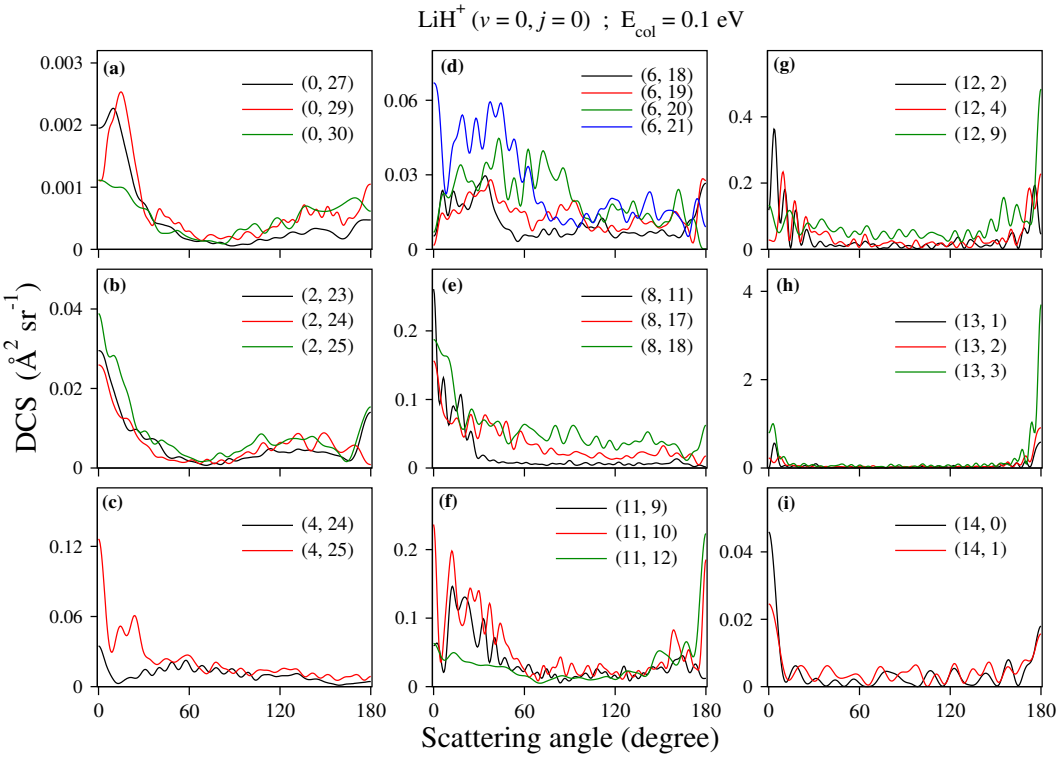

Figure 3.15: Product rotational level resolved state-to-state DCS of the H + LiH^+ (v=0, j=0) → H_2 (v', j') + Li^+, reaction as a function of θ at E_{col} = 0.1 eV for few selected v' levels of H_2. The (v', j') levels of product H_2 are given in the legend.

probable j'-resolved DCSs of few selected v' levels of product H_2 are shown here as a function of θ. It is found that (see section 3.3.5 and Figure 3.12) a very narrow range of j' levels are populated for every v' levels and therefore the most probable j' levels are considered here. Furthermore, it is found that the products are rotationally excited for lower v' levels and are rotationally cold for higher v' levels (cf., section 3.3.5). Similar behavior is observed at other collision energies and also for ro-vibrationally excited reagent, which will be discussed later in the text.

It can be seen from Figure 3.15 (for E_{col} = 0.1 eV) that for low v' levels, the rotationally excited products are mainly forward scattered. This behavior continues up to v'=8 and afterwards the backward scattering signal starts appearing in case of rotationally cold products from highly excited v' levels. Sideways scattering in the forward hemisphere can also be seen for some intermediate v' levels. The situation turns out to be different for v'=14 which shows forward dominated DCS as the reaction becomes endoergic for this highly excited vibrational level of H_2. However, it can be seen from

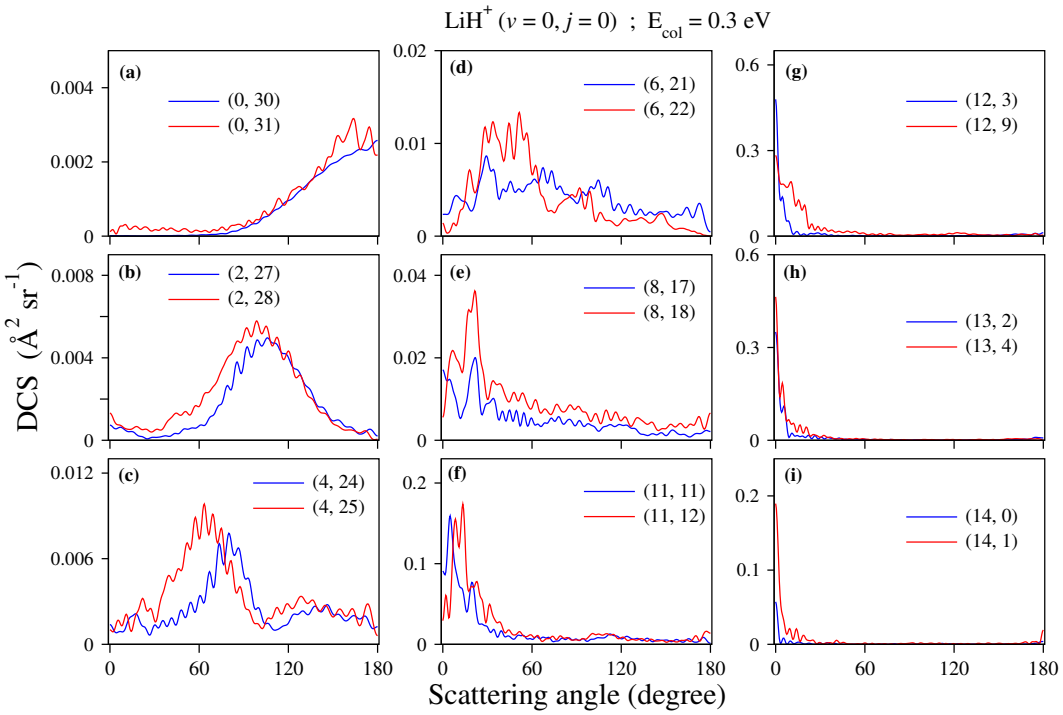

Figure 3.16: Same as in Figure 3.15, but at E_{col} = 0.3 eV.

Figure 3.16 (for E_{col} = 0.3 eV) that for lower v' levels, the rotationally excited products are backward scattered. Moreover, the scattering of products becomes sideways for intermediate v' levels and completely forward for higher v' levels.Therefore, a strong correlation can be seen between v' and θ for this attractive barrierless exoergic reaction. As it is found that the total DCS of reaction R1 at E_{col} = 0.3 eV shows completely forward scattering [cf., Figure 3.7(e)], backward scattering in the state-to-state DCSs at the same collision energy could be self-contradicting. However, the magnitude of the backward scattered state-to-state DCSs for lower v' is found to be very less as compared to that of the forward scattered state-to-state DCSs of higher v' levels (cf., Figure 3.16). This is because of the inverse Boltzmann v' distributions. So from a quantitative viewpoint, when these state-to-state DCSs are summed over final product states the minor contributions of backward scattering are not manifested in the total DCS showing a complete forward scattering.

It is now clear that the behavior of the state-to-state DCSs at high collision energy is completely in contrast to that at low collision energy. In order to verify this behavior further, a few more state-to state DCSs for LiH^+ (v=0, j=0) have been calculated at E_{col} = 0.05 and 0.5 eV, corresponding to low and high collision energy, respectively. The results are shown Figure 3.17 in terms of the most probable j'-resolved DCSs for some selected v' levels. At E_{col} = 0.05 eV [cf., Figure 3.17(a)-(f)], the products are found to be

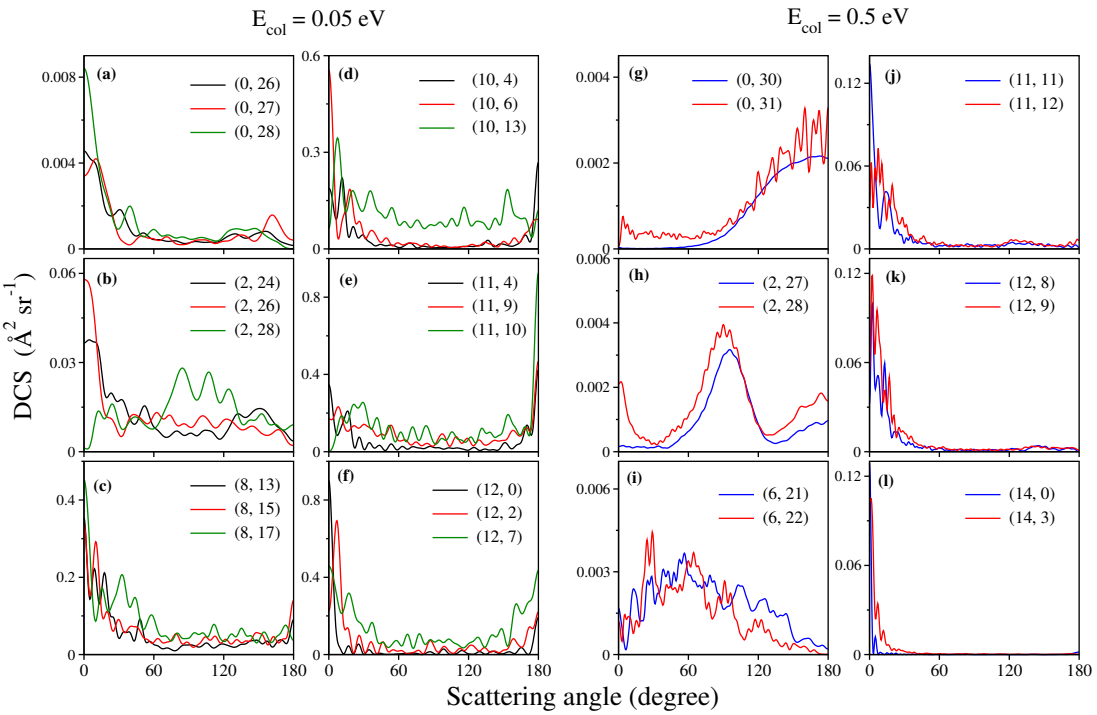

Figure 3.17: Same as in Figure 3.15, but at E_{col} = 0.05 and 0.5 eV.

mainly forward scattered whereas backward signal starts appearing for higher v' levels. This observation is similar to that found at E_{col} = 0.1 eV (cf., Figure 3.15). However, at E_{col} = 0.5 eV [cf., Figure 3.17(g)-(l)], the behavior of the state-to-state DCSs is very similar to that at E_{col} = 0.3 eV and shows a strong correlation between v' and θ. In this case the backward scattering at lower v' gradually changes to sideways and to forward with increasing v'. So it is clear that the state-to-state DCSs at two different collision energy regimes (low and high) are very different.

We note here that the state-to-state DCSs were also calculated by Zhu *et al.* [113] for the reaction R1 at E_{col} = 0.5 eV on the PES of Dong *et al.* [112] A complete forward scattering was found for all v' levels (cf., Figure 7 of Ref. 113) which is in contrast to the present findings at the same collision energy. This difference is likely to arise from the differences between the PESs used in the two studies. The PES of Martinazzo *et al.* used in the present study considers the long-range interactions between H_2 and Li^+ explicitly, [92] whereas, in the case of the PES of Dong *et al.*, these long-range interactions are not taken into account [112]. The state-to-state DCSs can be very sensitive to a small change in the topography of the underlying PES.

The effect of ro-vibrational excitation of the reagent LiH^+ on the state-to-state dynamics of the reaction R1 is also studied. The j'-resolved state-to-state DCSs of reaction R1 are calculated for LiH^+ (v=1, j=0) and (v=0, j=1) at the same collision energies,

but are not shown here as their overall behavior almost resemble to that of LiH^+ (v=0, j=0). This suggests that the microscopic scattering mechanism of the reaction is hardly affected by the internal excitation of reagent diatom. Rather it is susceptible to the collision energy where two completely different type of mechanisms can be observed at the state-to-state level corresponding to low and high collision energies.

3.3.8 Role of interference between partial waves

In the statistical limit, the contribution of the interference terms towards the exact QM DCS is considered to be zero. It is to be noted that the forward-backward symmetry of the DCS, resulting from the assumptions in statistical models, must not depend on the number of asymptotic states. This is because this symmetry is ensured by the micro-canonical distribution of the phase space states of the intermediate complex rather than the asymptotic states [75]. Therefore, the DCSs, whether state-resolved or not, must be symmetric around $\pi/2$ according to the statistical models. However, this does not happen even for complex-forming reactions because of significant interference between the partial waves especially around the extreme forward and backward regions, particularly at the state-to-state level [75]. In this section, the role of these interference terms (calculated by equation 2.53), which are essentially neglected in the statistical limit, are discussed both towards the state-to-state and total exact QM DCSs of reaction R1.

The product rotational level resolved state-to-state interference terms for LiH^+ (v=0, j=0) are shown in Figure 3.18 at E_{col} = 0.1 eV as a function of θ along with the state-to-state DCSs and the DCSs due to RPA. The results shown here are of the most probable j' level of some selected v' levels of product H_2. Similar results are also shown for LiH^+ (v=0, j=0) at E_{col} = 0.3 eV in Figure 3.19. It can be seen from Figures 3.18 and 3.19 that the variation of the state-to-state DCSs as a function of θ closely resemble that of the state-to-state interference terms. The DCSs due to RPA are found to be symmetric with respect to $\theta = \pi/2$ even at the state-to-state level as they should by definition. Therefore, it is clear that the asymmetry in the state-to-state DCSs arises from the interference terms. Futhermore, it can be seen that unlike the DCSs due to RPA, the state-to-state interference terms are highly oscillatory along θ. These oscillatory signatures are finally imprinted in the state-to-state DCSs. These oscillations are different for different (v', j') levels of product. Moreover, it can be seen that the interference terms become more prominent in the forward and backward regions as compared to the sideways regions and at some values of θ, they even become as significant as the

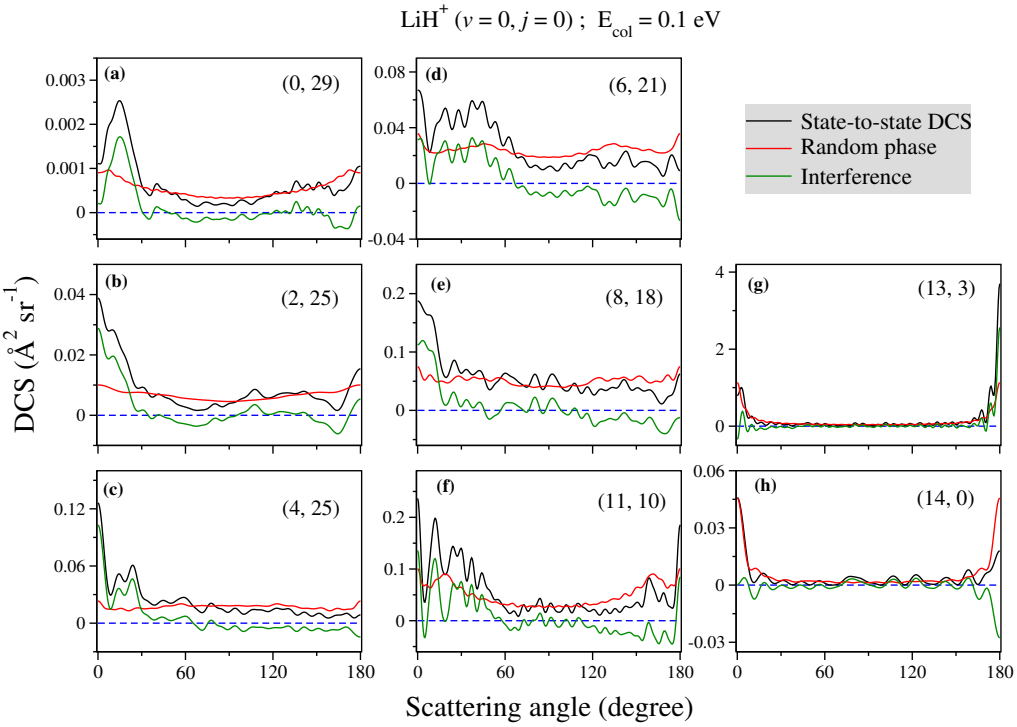

Figure 3.18: Product rotational level resolved state-to-state interference terms (green), state-to-state DCSs (black) and DCSs due to RPA (red) for the H + LiH^+ (v=0, j=0) $\rightarrow$ H_2 (v', j') + Li^+ reaction as a function of θ at E_{col} = 0.1 eV for a few selected (v', j') levels of H_2. The blue color dashed line along the abscissa represents the zero of ordinate.

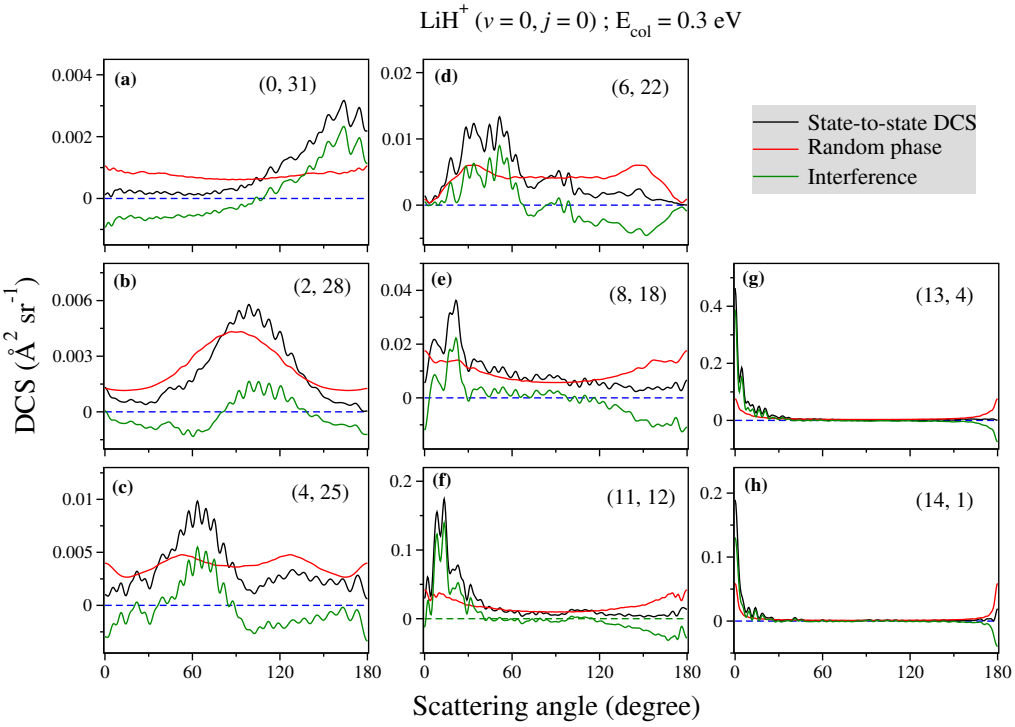

Figure 3.19: Same as in Figure 3.18, but at E_{col} = 0.3 eV.

DCSs due to RPA. Similar observations have been found for LiH^+ (v=1, j=0) at the same value of collision energy, hence not shown further here for brevity.

The total interference terms (summed over all final states) are shown in Figure 3.20 as a function of θ for LiH^+ (v=0, j=0) at E_{col} = 0.05, 0.1, 0.3 and 0.5 eV along with the total DCSs and the DCSs due to RPA. It can be seen that the interference

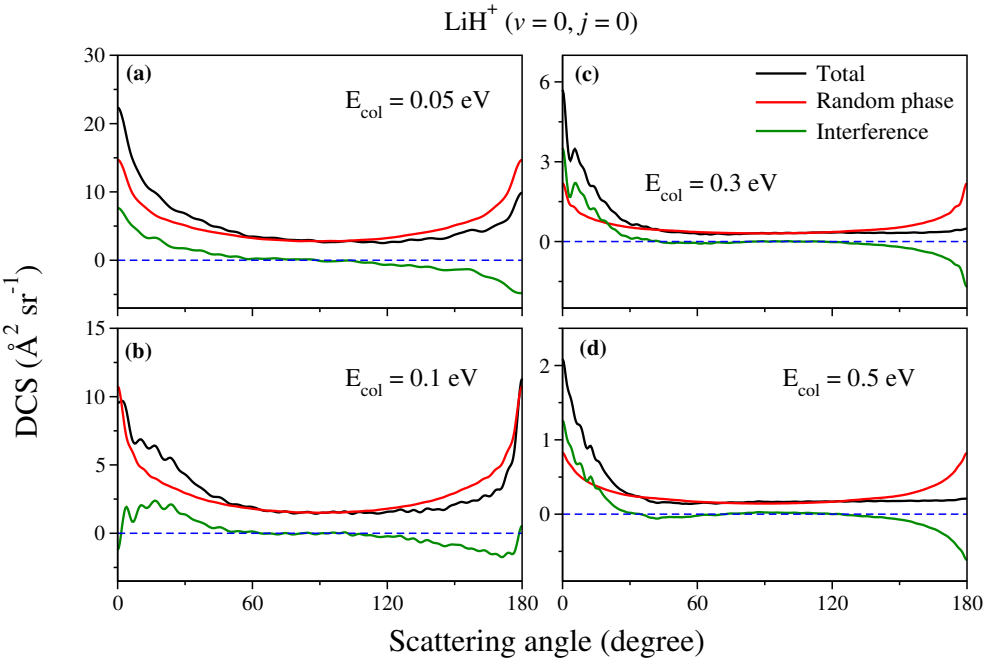

Figure 3.20: Total (summed over final states) interference terms (green), total DCSs (black) and DCSs due to RPA (red) for the H + LiH^+ (v=0, j=0) → H_2 ($\sum v'$, $\sum j'$, $\sum \Omega'$) + Li^+ reaction as a function of θ at E_{col} = 0.05, 0.1, 0.3 and 0.5 eV. The blue color dashed line along the abscissa represents the zero of ordinate.

between various partial waves practically becomes zero around $\theta = \pi/2$, when summed over the final states. But it remains significant in the forward and backward regions at all four collision energies. Similar behavior of the interference terms is also found at other collision energies and the results are not shown here for brevity. As expected, the DCSs due to RPA are found to be symmetric with respect to $\theta = \pi/2$. It is found that the interference between the partial waves is constructive in the forward and destructive in the backward regions at all collision energies. This is evident from the positive and negative values of σ^{INT} (θ) terms in the forward and backward directions, respectively. This results into forward dominated total DCSs, which are shown in Figure 3.20 by the black color lines. However, the nature of the interference switches at $\theta = 0°$ and 180° for E_{col} = 0.1 eV [cf., Figure 3.20(b)]. This gives rise to almost equal magnitudes of the forward and backward scattering.

The behavior of the total interference terms (summed over all final states) for LiH^+ (v=1, j=0) is found to be similar to that for LiH^+ (v=0, j=0). However, at E_{col} = 0.1 eV, the interference between partial waves remains constructive at θ = 0° and destructive at θ = 180°, unlike LiH^+ (v=0, j=0). This leads to unequal magnitudes of the forward and backward intensities in the total DCS with a forward dominance. This is shown in Figure 3.21. The oscillations along θ, which are present in the state-to-state interference

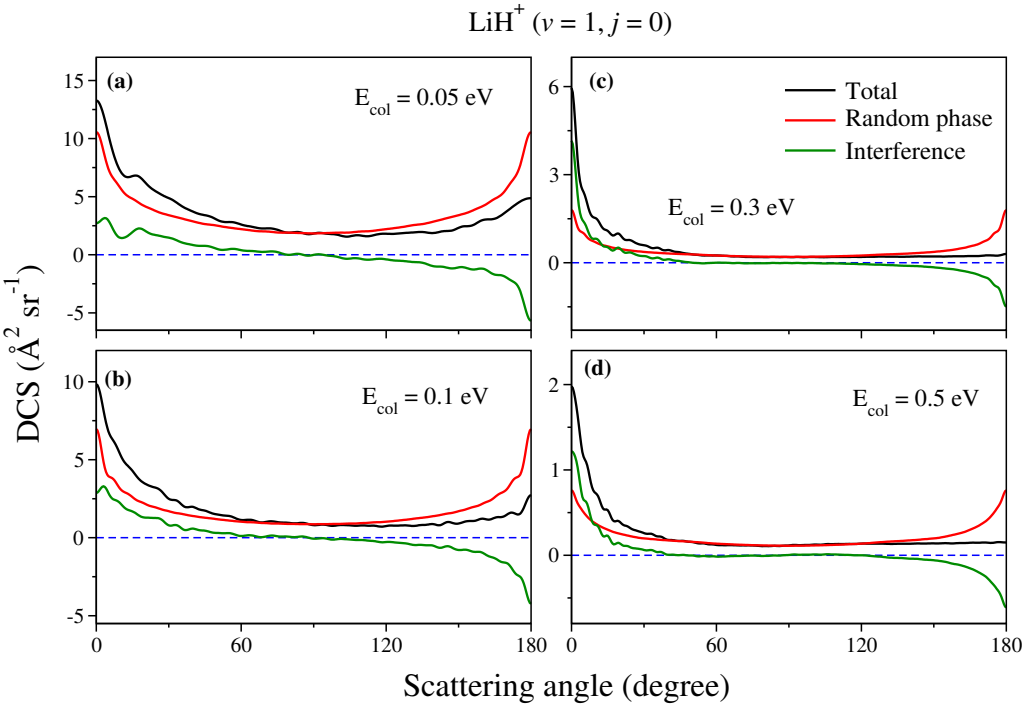

Figure 3.21: Same as in Figure 3.20, but for LiH^+ (v=1, j=0).

terms and in the state-to-state DCSs, disappear in the total interference terms and total DCSs. This is probably due to the sum over final states.

It is important to add few comments on the origin of such behavior of the interference terms. As these are calculated only for LiH^+ (v=0-1, j=0), the value of Ω = 0 in the present case. Hence, according to the properties of the reduced Wigner rotation matrix elements, that is, $d^J_{0\Omega'}(0) = \delta_{0\Omega'}$, and $d^J_{0\Omega'}(\pi) = (-1)^{J-\Omega'}\ \delta_{0-\Omega'}$, only $\Omega' = 0$ contributes to the interference term (and to the DCS) at θ = 0° and 180°. However, other Ω's, including $\Omega' = 0$, contribute over a broad range of θ around $\pi/2$. Therefore, the summation over Ω' in equation 2.51 can involve a substantial number of cancellation around $\theta = \pi/2$ resulting significant interference effects at the extreme forward and backward regions rather than the sideways region. It is interesting to note that the sideways region (around $\theta = \pi/2$) where the interference terms are zero (cf., Figures 3.20 and 3.21), becomes broader with increasing collision energy. This is because with

increasing collision energy, more partial waves contribute to the summation over J and J_a in equation 2.53 resulting into more cancellation around $\pi/2$.

It is now clear that the asymmetric nature of the DCSs, whether state-to-state or total, arises due to different types of interference (constructive or destructive) between various partial waves, which is neglected in the RPA. The forward-backward symmetry is generally, however, retrieved for deep well complex forming reactions when the state-to-state DCSs are summed over several final quantum states [75] and the reaction is said to behave statistically. This corresponds to an extremely small or even zero contribution of the interference terms to the total (summed over) DCS in case of a complex forming reaction behaving statistically. In contrast, if the interference terms survive after the summation over all product quantum states and become significant for any type of reaction, then it is worthwhile to say that non-statistical feature can appear in those reactions. In the present case also, the pronounced interference between the partial waves both at the state-to-state and total DCS levels indicates the non-statistical nature of reaction R1 to a considerable extent.

3.3.9 Statistical/non-statistical nature

The applicability of various statistical models is often valid for complex forming reactions occurring through deep wells on the PES, as far as the total DCS is concerned. However, at the state-to-state level, the inherent interference effects can prevail leading to asymmetry in the state-resolved DCSs questioning the assumptions of the statistical models. In the present case also the j'-resolved state-to-state DCSs of reaction R1 are found to be asymmetrical to a large extent (cf., Figures 3.15, 3.16 and 3.17) which results from the interference terms as shown above. Moreover, the total DCSs of reaction R1, as discussed in section 3.3.3 and shown in Figure 3.7 (see also Figure 3.20 and 3.21), do not possess a pure forward-backward symmetry. Rather almost equal magnitude of forward and backward scattering was observed for LiH^+ (v=0, j=0) at E_{col} = 0.1 eV. Nevertheless, it was not strictly symmetric around $\theta = \pi/2$. It was found in some studies that with a small change in collision energy, the extent of forward-backward symmetry can vary significantly [129, 130].

Keeping this in mind, the energy dependence of both forward and backward scattering of reaction R1 is presented in Figure 3.22. In the figure the total DCS at θ = 0° and 180° (corresponding to forward and backward scattering, respectively) are separately plotted as a function of collision energy for different initial states of reagent

LiH^+. It can be seen that the total DCS is forward dominated in the whole collision

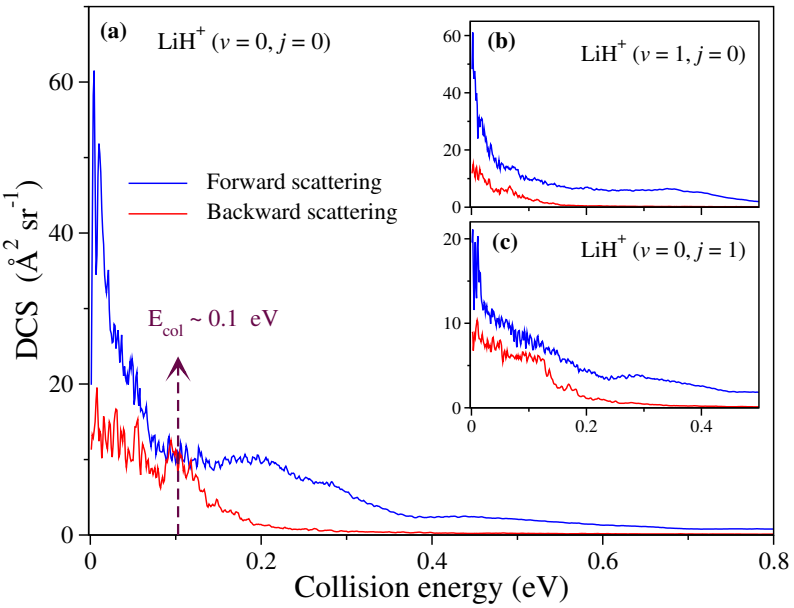

Figure 3.22: Forward and backward scattering of the H + LiH^+ (v=0-1, j=0-1) → H_2 ($\sum v'$, $\sum j'$, $\sum \Omega'$) + Li^+ reaction in terms of the total DCS at θ = 0° and 180° as a function of collision energy.

energy range for LiH^+ (v=1, j=0) and (v=0, j=1). The forward dominance in the total DCS is obvious for this exoergic barrierless reaction, since the well on the PES is not relatively deep (only ≈0.286 eV below the product asymptote). The same behavior can also be seen in case of LiH^+ (v=0, j=0). However, around E_{col} = 0.1 eV, the forward and backward intensities become almost equal with each other [cf., Figure 3.22(a)] questioning whether the reaction behaves statistically or not. However, this does not imply the statistical nature of the reaction R1 as equal magnitudes of the forward and backward scattering is seen only in a very small range of collision energy. In addition, the weakly-bound nature of the collision complex may not effectively facilitate the complete randomization of the available energy. This can be due to the slow IVR in the LiH_2^+ molecular system, as discussed in section 3.3.5. This incomplete IVR results into a non-statistical vibrational distribution of product even for E_{col} around 0.1 eV, as found shown in Figure 3.10(b).

3.3.10 Partial wave contributions to the DCS

In order to understand the detail mechanism and the origin of the forward and backward scattering in the DCSs of the reaction R1, the DCSs from different partial wave ranges are calculated by using equation 2.54 and are presented in this section. The partial DCSs

of reaction R1 for LiH^+ (v=0, j=0), summed over all final states, are presented in Figure 3.23 as a function of θ at E_{col} = 0.05, 0.1, 0.3 and 0.5 eV.

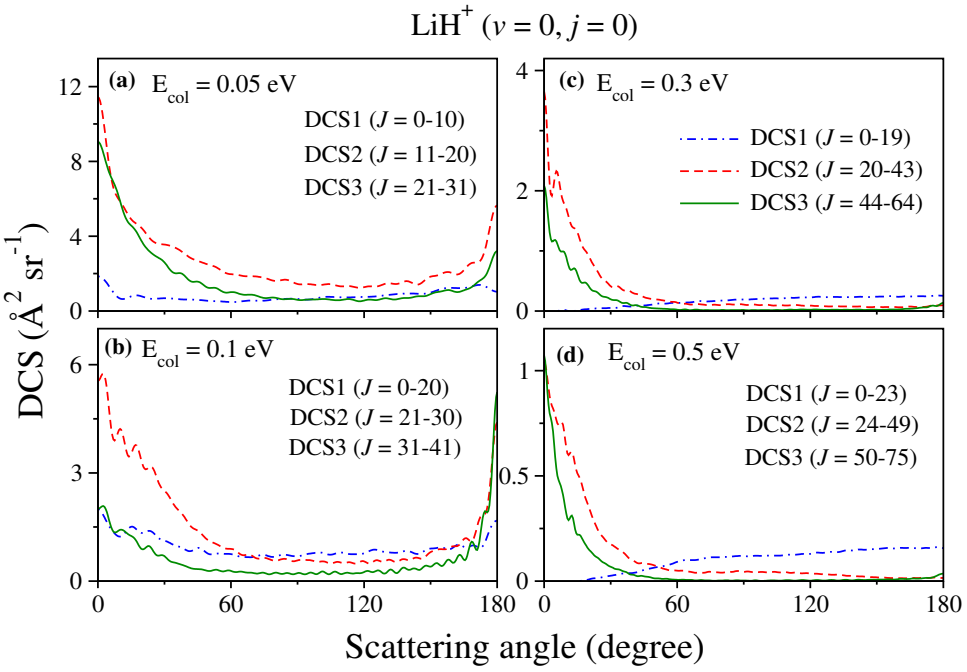

Figure 3.23: Initial state-selected partial DCSs (DCS1, DCS2 and DCS3) of the H + LiH^+ (v=0, j=0) → H_2 ($\sum v'$, $\sum j'$, $\sum \Omega'$) + Li^+ reaction as a function of θ at E_{col} = 0.05, 0.1, 0.3 and 0.5 eV. The three different ranges of the chosen partial wave, J, are mentioned inside each panel.

The whole J range (0-J_{max}) is divided into three different segments and the partial DCSs are calculated in each of these segments at a particular collision energy. It is important to note here that the partial DCS of a specific segment includes the coherent terms outside of that segment. The three different ranges of chosen partial wave are mentioned inside each panel of Figure 3.23. The partial DCSs calculated from the lower, intermediate and higher J ranges are referred to as DCS1, DCS2 and DCS3, respectively.

It can be seen from the figure that the contributions of partial DCS2 and DCS3 (calculated from the higher J ranges) are more prominent than that of DCS1 at all collision energies. In particular, DCS2 and DCS3 contribute both to the forward and backward scattering. However, DCS1 is almost isotropic over the whole range of θ at lower collision energies [cf., Figure 3.23(a)-(b)], and contributes mainly towards the sideways and backward scattering over broad range of θ at higher collision energies with very small scattering intensities [cf., Figure 3.23(c)-(d)].

It is found that DCS2 and DCS3 predominantly contribute to the forward scattering at higher collision energies. Similar behavior of the partial DCSs is also found at collision energy higher than 0.5 eV (not shown here). This indicates that the forward scattering is caused by the higher J partial waves or equivalently the high impact parameter collisions. This suggests that the reaction R1 follows a direct stripping mechanism at higher collision energies where the heavier Li^+ behaves like a spectator when the incoming H atom takes the other hydrogen away in the forward direction. This is indeed supported by the attractive nature of the PES and a little relative translational energy disposal in products. However, in the low collision energy regime, the partial DCS2 and DCS3 contribute to the forward as well as to the backward scattering. In particular, at E_{col} = 0.1 eV, the contribution to the backward scattering from DCS3 becomes larger than that to the forward scattering [cf., Figure 3.23(b)].

The appearance of the backward peak in the DCS of a reaction where the PES supports wells is not unknown in reaction dynamics [1]. However, the fact that it is produced from the contributions of higher Js in case of a reaction where the major energy release is attractive in nature, is certainly intriguing. Involvement of higher J partial waves in the backward scattering obviously discards the possibility of rebound mechanism for reaction R1. Rather it is indicative of an indirect complex-mode mechanism where the same range of J contributes to both forward and backward scattering. This is unlike the direct reactions where a one-to-one correlation between J and θ exists [76]. Moreover, an unequal contribution of the partial DCSs towards the forward and backward scattering suggests that the reaction does not follow a pure complex-mode mechanism at low collision energies, rather it follows a mixture of direct and indirect mechanisms.

The partial DCSs, summed over all final states, for LiH^+ (v=1, j=0) are shown in Figure 3.24 of the supplementary material at E_{col} = 0.05, 0.1, 0.3 and 0.5 eV. The three different ranges of the chosen partial waves corresponding to DCS1, DCS2 and DCS3 are mentioned inside each panel. Similar to LiH^+ (v=0, j=0), the partial DCS2 and DCS3 are found to be more prominent than partial DCS1 for LiH^+ (v=1, j=0). It is found that the partial DCS2 and DCS3 mainly contribute to the forward scattering, whereas, partial DCS1 contributes to all θ almost equally with very small magnitude at both higher and lower collision energies. Small backward scattering can be seen for DCS2 and DCS3 at low collision energies which is insignificant as compared to the forward peak. This observation indicates that the reaction follows a direct stripping mechanism for vibrationally excited reagent LiH^+ (v=1, j=0), with a very minor

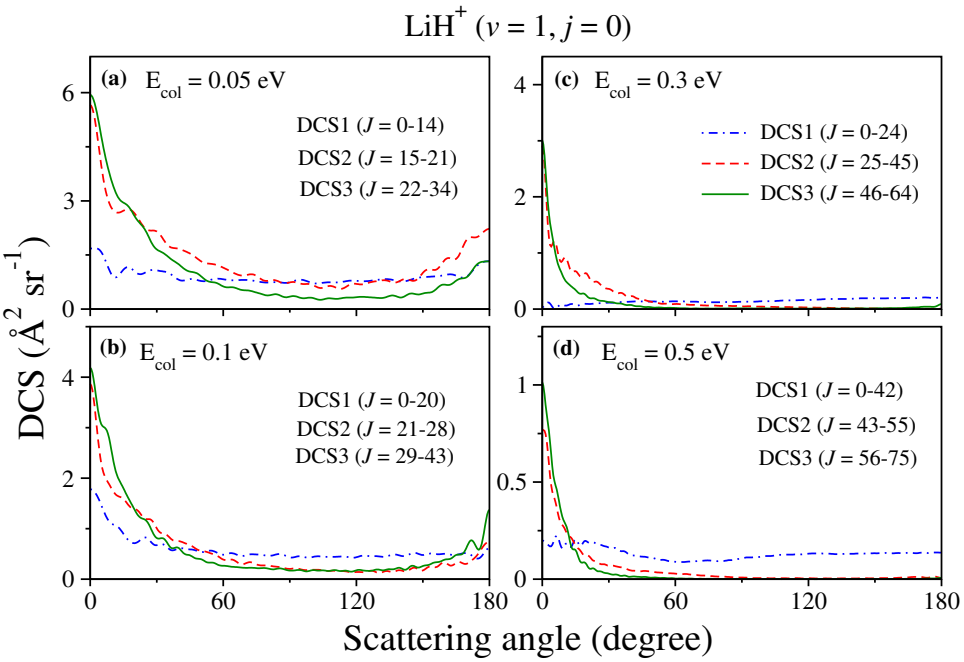

Figure 3.24: Same as in Figure 3.23, but for LiH^+ (v=1, j=0).

contribution from indirect mechanism.

3.4 Summary

A comprehensive state-to-state quantum dynamical study of the energy disposal and scattering mechanisms of the astrochemically relevant H + LiH^+ → H_2 + Li^+ and D + LiH^+ → HD + Li^+ reactions is presented in this chapter. Both initial state-selected total and product state-resolved ICSs and DCSs are calculated over a wide range of collision energies up to 1.0 eV by using a numerically exact TDWP method on the ground electronic state PES of the LiH_2^+ ionic system. State-specific and state-to-state rate constants are also reported and compared with the available literature results. The effect of collision energy and reagent ro-vibrational excitation on the state-to-state dynamical observables is examined to understand the detailed reaction mechanism.

The total ICS is found to decrease with ro-vibrational excitation of the reagent and with increasing collision energy, reflecting the barrierless nature of the minimum energy path of the reaction. With substitution of heavier isotope on the attacking atom the reactivity increases. The resonance oscillations in the reaction probabilities are found to be cancelled out in the ICSs, resulting in an excellent and "expected" agreement of the present QM-CC ICSs with the QCT ICSs of the previous theoretical studies on

the same PES in the whole collision energy range studied here. The products form in highly excited vibrational levels with inverse Boltzmann population distribution which is expected according to Polanyi's rule [53, 54] because of the "attractive" nature of the reaction path. It is found that ≈60-80% of the available energy is partitioned into the product vibration, and a very less amount of energy flows into product rotation and translation. The energy disposal mechanism is found to be unaffected by the ro-vibrational excitation of the reagent diatom and is mildly affected by the collision energy of the reagents.

Analysis of product state-resolved DCSs reveals that the microscopic scattering mechanisms of the reactions at low and high collision energy regimes are almost opposite to each other. The behaviour of the state-to-state DCSs is found to be insensitive to the ro-vibrational excitation of the reagent diatom. The interference due to the coherence between the partial waves is quantified and plotted along the scattering angle to illustrate their constructive or destructive nature. Moreover, their contribution to the total and state-to-state DCSs is examined. It is found that the forward-backward asymmetry in the total and state-to-state DCSs arises due to the constructive and destructive interference between various partial waves. Significant interference is found in the reaction, both at the state-to-state and total DCS levels, indicating its non-statistical nature to a considerable extent. By analyzing the partial wave contributions to the total DCSs, it is found that the reaction mainly follows a direct stripping mechanism at higher collision energies and a mixture of direct and indirect mechanisms, at lower collision energies. The indirect mechanism is found to be mostly due to the formation of loosely bound complexes which is supported by the shallow well present on the PES.

Chapter 4

Adiabatic and nonadiabatic state-to-state quantum dynamics of H + H_2 → H_2 + H reaction

4.1 Introduction

Since the inception of molecular reaction dynamics the hydrogen exchange reaction, H + H_2 → H_2 + H, and its isotopic variants have been playing a fundamental role in the advancement of both theory and experiment. This reaction has been productive in developing many rudimentary notions in reaction dynamics e.g., potential energy surface [131–133], transition-state [134, 135], reactive resonances [136–139], quantized bottleneck state (QBS) [18, 140–145], etc. Even after almost a hundred year of study the so called simplest chemical reaction still continues to surprise with new discoveries and important phenomena. This reaction has witnessed many new findings in reaction dynamics e.g., the time-delayed machanism [146], the appearance of Feshbach resonance below the reaction barrier [147, 148], glory scattering in the forward scattered DCSs [149, 150], etc. Most of all it has been considered as a benchmark reactive system to explore the electronic nonadiabatic effects [24–26, 55, 73, 74, 151–156] and the geometric phase (GP) effects [154, 157–171] in reaction dynamics in the thermal as well as ultracold temperature conditions. Most of the developments on this reaction starting from the twenties has been well documented in a number of excellent reviews [172–174]. Though the pioneering study on this reaction is a century old, still it is used

today along with its isotopic variants for the development of new concepts as well as theoretical and experimental methodologies.

Because of its simple electronic structure having only three electrons, computational calculations were affordable and have been carried out with optimal accuracy. Several global PESs for the H_3 reactive system have been reported in the literature which include the PK2 [175], LSTH [176, 177], DMBE [178], BKMP [179], BKMP2 [180], CCI [181] surface, and that of Wu *et al.* [182], Abrol and Kuppermann [183], Yuan *et al.* [169] and of Yin *et al.* [184]. With the availability of accurate PESs numerous dynamical calculations have been performed with the aid of quasi-classical and quantum mechanical formalisms (see Ref. 174 and references therein) to obtain accurate reaction cross sections.

On the other hand, availability of advanced experimental methods [18, 185, 186] and isotopic substitutions of reagent H_2 have made the measurement of the energy-resolved state-to-state DCS feasible [171]. In fact, the agreement between theory and experiment has become more closer than ever [169–171, 186–188]. Though the reactive system seems to be very simple, experimental outcomes made the theorists to look into the dynamics in more detail and indeed the findings are less simple [189].

Apart from its immense fundamental significance, the hydrogen exchange reaction has been found to have its importance in astrophysical application for the cooling process of the early universe and in the ortho-para H_2 conversion. Several state-to-state rate constants have been predicted for the reactive and non-reactive processes, and also for the rotational (de-)excitation of H_2 by H which further have been used to accurately model the cooling mechanism of the warm media and the early universe [190–194].

4.1.1 PES of H_3 reactive system

It is well established that the ground ($1^2E'$) electronic manifold of H_3 is orbitally double degenerate in its equilateral triangle geometry (D_{3h}). Upon distortion along its asymmetric stretching and degenerate bending vibrational modes the degeneracy is lifted to produce two Jahn-Teller split components which form a seam of CIs along the D_{3h} geometric configuration. [175] The energetic minimum of the CI seam occurs at ≈2.74 eV [180] with respect to the lower adiabatic H + H_2 asymptote. Figure 4.1 presents the three-dimensional perspective and contour diagram of both the lower (V_-) and upper (V_+) adiabatic components of the $1^2E'$ electronic manifold of H_3 system. Both the PESs

are plotted along the mass-scaled radial Jacobi coordinates R_s and r_s (see Ref. 195) at a fixed value of the Jacobi angle $\gamma = \pi/2$. The seam of the CIs can be seen occurring at $R_s = r_s$ (*i.e.*, $R = \sqrt{3}r/2$) which is represented by a straight line along the diagonal of the contour plot. The energetic minimum of the seam occurring in the interaction region is indicated by a point on the contour plot. The V_- component is higly repulsive wherein the H_3 system quickly dissociates into the H + H_2 channel [196–198], whereas, the V_+ component being reverse cone shaped supports bound states [196, 198].

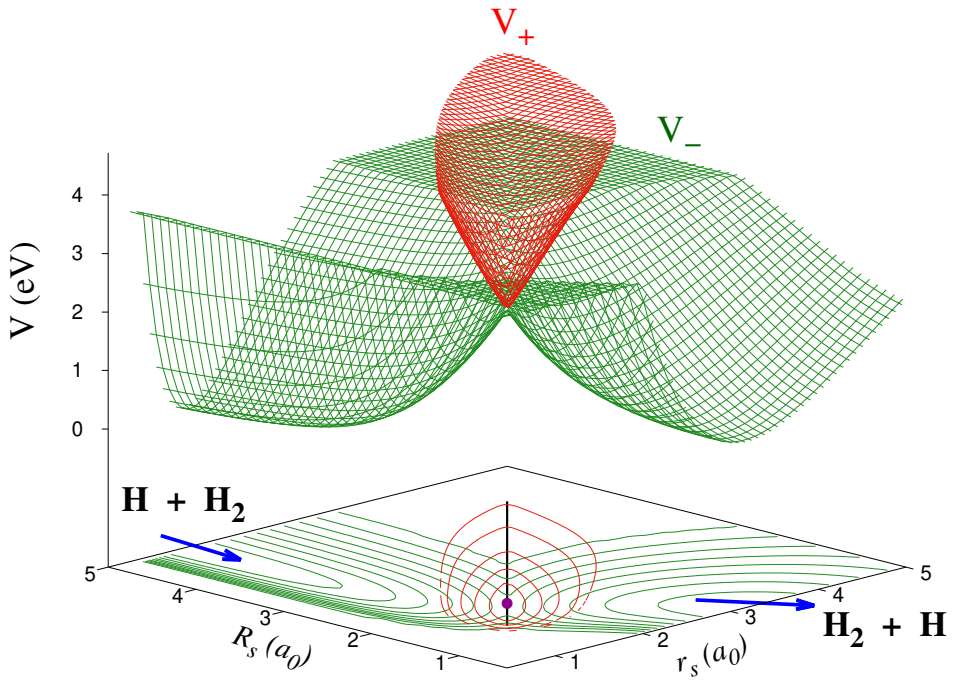

Figure 4.1: 3D perspective and contour plot of the DMBE PES of the $1^2E'$ electronic states of H_3 plotted along the mass-scaled Jacobi coordinates R_s and r_s at a fixed value of the Jacobi angle $\gamma = \frac{\pi}{2}$. The lower (V_-) and upper (V_+) adiabatic states are shown by green and red coloured lines, respectively. The straight line in the contour plot represents the seam of the CIs occurring at $R_s = r_s$ (or $R = \frac{\sqrt{3}r}{2}$). The point on it indicates the energetic minimum of the seam occurring at ≈2.74 eV.

The H + H_2 reaction predominantly takes place on the V_- component as there are no bound states of H_2 diatom in the H + H_2 asymptote of the V_+ component. In order to characterize the reaction paths of the H + H_2 reaction the MEPs for various angular approaches are plotted in Figure 4.2. These MEPs are constructed from the BKMP2 PES and are shown here as a function of the difference between the two bond distances at a fixed value of angle between them. It can be seen from the figure that the lowest energetic path of the reaction occurs at $\angle H_aH_bH_c = 180°$. This suggests that the most favourable path for the H + H_2 reaction is that when the attacking atom approaches the reagent diatom in a collinear fashion with a classical barrier height of ≈0.42 eV. With

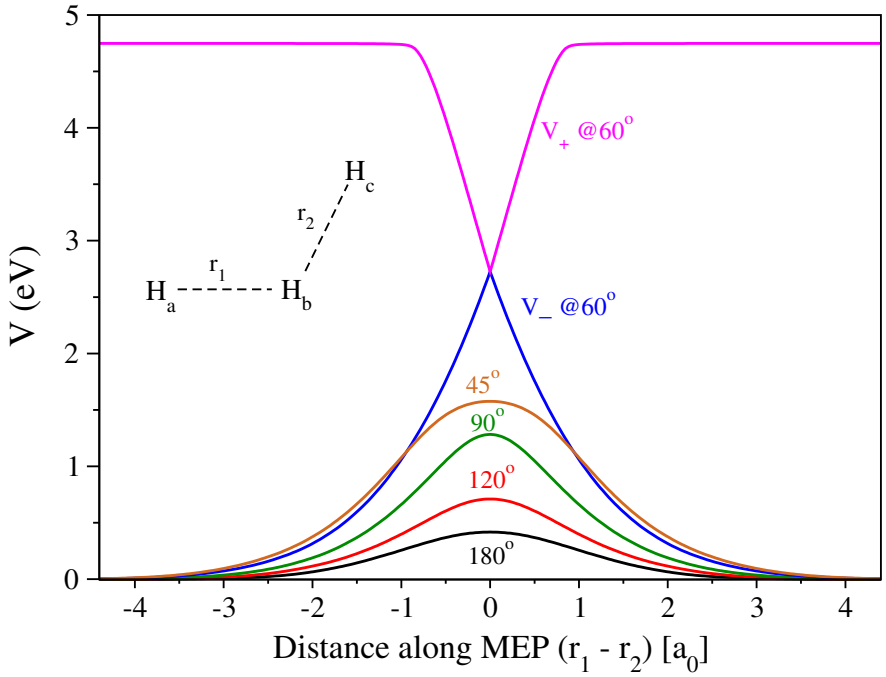

Figure 4.2: Minimum energy paths of the H + H_2 reaction at various fixed bond angles ($\angle H_aH_bH_c$).

increasing the noncollinear nature of the MEP, the barrier height increases to maximum value of ≈2.74 eV at $\angle H_aH_bH_c = 60°$. This configuration corresponds to the energetic minimum of the CI seam wherein the V_- and V_+ adiabatic components become degenerate (cf. Figure 4.2). The value of the barrier height decreases further with decrease in the bond angle. This phenomenon indicates that the CI may become accessible for the reaction at higher total energy (above 2.74 eV) where the reactive system can attain high energetic noncollinear configurations. In this nonadiabatic situation, the presence of a CI can make way for the reactive system to explore the coupled electronic manifold once it becomes energetically accessible.

Among the various PESs of H_3 system reported in the literature, the most accurate ones till date are the BKMP2 [180], CCI [181] and that of Yuan *et al.* [169] and Yin *et al.* [184]. The accuracy of these PESs have been checked precisely by comparing the accurate theoretical DCSs with that of experimental measurements for various isotopic variants of the hydrogen exchange reaction [169, 170, 186–188]. For the studies reported in this chapter, both the BKMP2 and DMBE PESs are used. These PESs were constructed by calculating the *ab initio* energies with resonably high level of theory (see Refs. 178–180 for more details).

4.1.2 Current state of research

Among many interesting dynamical features embedded in this reactive system, the most intriguing one is the GP effect which had puzzled both the theorists and the experimentalists over a long period of time [174]. The GP effect is a direct consequence of the CI where the real adiabatic wave function changes its sign, corresponding to a change in phase of π, upon any odd number of closed loop around the CI in the nuclear parameter space [199]. The GP may affect the reaction dynamics confined only to the lower adiabatic PES even at energies below the CI, whenever the nuclear wave function encircles it [160–162, 164, 165, 170].

The GP effect on the dynamics of this reaction was controversial for some time in the past [157–159, 200–202] and since then great effort had been made both experimentally [143, 186, 203–207] and theoretically [154, 158–164, 202] to search for any tiny evidence for this effect. There was no conlusive experimental evidence as such until recently. In 2018, using a high-resolution crossed-beam apparatus with velocity map imaging detector Yuan *et al.* [169] measured the product state-resolved angular distributions of the H + HD (v=0, j=0) → H_2 + D reaction at a collision energy of 2.77 eV (above the minimum of the CI seam) and also later at an energy below the CI seam [170]. Furthermore, theoretical calculations were carried out by a TDQM method in the adiabatic framework without including the GP (non-GP) and with the inclusion of GP. In addition, the quantum dynamics was also carried out in a two-state coupled diabatic framework to ascertain the effect of the upper adiabatic PES. An extremely good agreement of the experimental angular distributions with that of the adiabatic plus GP and a clear disagreement with that of non-GP verified the experimental detection of GP effect in the H + H_2 reaction dynamics [169, 170].

Early theoretical work on the electronic nonadiabatic effects in the H + H_2 reaction dynamics considered the inclusion of the GP in the single surface calculation on the lower adiabatic PES. Conventionally the GP can be incorporated by two different techniques, one is to impose a multi-valued boundary condition to the nuclear wave function [200, 201, 208] and the other one is to multiply the electronic wave function by a complex phase factor, which changes sign for any closed path around the CI, thereby introducing a vector potential into the nuclear Hamiltonian [209]. Furthermore, it was shown by Mead [210] that in case of three identical nuclei a phase factor of type $e^{3i\eta/2}$ (η, describes the coordinate of the path around the CI) must be multiplied to the nuclear

wave function to account for the correct permutation symmetry. Note that this prediction of Mead was for the nuclear wave functions which do not encircle the CI when unsymmetrized [210]. This phase change leads to a change in the relative sign of the reactive and nonreactive scattering amplitudes, and the effect of GP, which in this case is entirely based on the symmetry argument, is to change the interference between the reactive and nonreactive scattering amplitudes [210]. This interference is found to be manifested in the state-to-state DCS as "out-of-phase" oscillations along the scattering angle between the results computed with and without the GP [159, 201]. While these effects of GP are purely a consequence of permutation symmetry, the GP effect due to encirclement of the CI by the nuclear wave function (contribution from the vector potential) was found to be very small in the product state-resolved DCSs [159]. However, it showed up in the energy resolved state-to-state reaction probabilities above a total energy of 1.8 eV, but was surprisingly cancelled in the ICSs while summing over all partial wave contributions [158, 159, 202].

Later Althorpe and coworkers [160] studied the GP effect in the H + H_2 reaction based on the vector potential approach of Mead and Truhlar [209] by employing a quantum wave packet method. Similar to the results of Kendrick, the GP effect was found in the state-to-state reaction probability but got cancelled in the state-to-state ICSs. It should be emphasized that the GP effect found in the work of Althorpe and coworkers are solely due to the encirclement of the nuclear wave function around the CI rather than that due to the symmetry effect, since their work refrained from applying the permutation symmetry of the identical nuclei. Nevertheless, the GP effect appeared in the state-to-state DCSs as "out-of-phase" oscillations between the GP and non-GP DCSs along the scattering angle [160, 161]. However, the GP effect gets cancelled again in the state-to-state ICSs once the DCSs are integrated over the scattering angle. Using a topological argument these authors showed that these oscillations are produced due to the interference between two distinct topological paths, one that is going through one transition state (1-TS) and the other that is going through two transition states (2-TS) encircling the CI, as shown schematically in Figure 4.3. The 1-TS and 2-TS paths are sometimes called as the direct and looping paths (as it loops around the CI), respectively. The sole effect of GP is to change the relative sign between these two paths [161, 211]. It was found that for the 1-TS and 2-TS paths, the phases of the corresponding scattering amplitudes depend in opposite senses on the scattering angle, hence scattering their products into opposite regions of space (nearside and farside) [161]. As a result the interference term becomes highly oscillatory which when integrated over the scattering angle gives a very negligible contribution, effectively cancelling the GP effect in

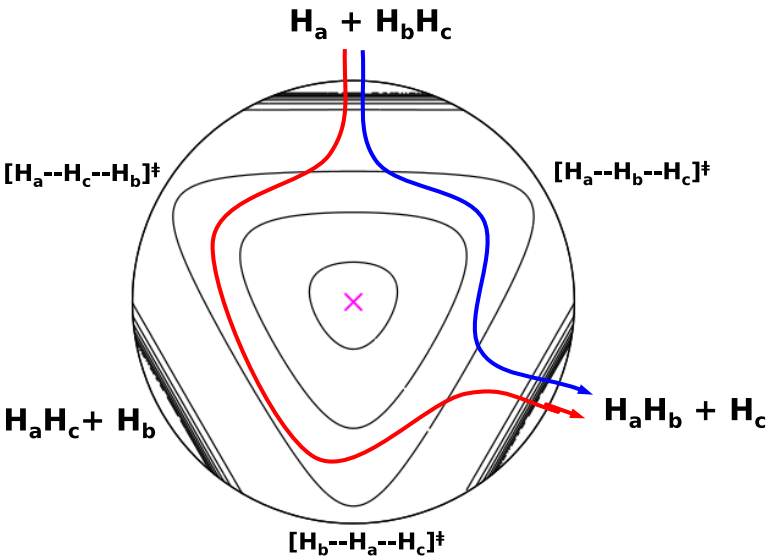

Figure 4.3: Schematic diagram of the 1-TS or direct (blue) and 2-TS or looping (red) reaction paths in the $H_a + H_bH_c \rightarrow H_aH_b + H_c$ reaction superimposed on a PES cut obtained in hyperspherical coordinates for a fixed value of hyperadius. The center of the circle represents the equilateral triangle (D_{3h}) configuration and the periphery of it represents the collinear configurations. The position of three H + H_2 arrangement channels, three transition states (‡), and the location of the CI (×) are also shown.

the state-to-state ICSs [154, 162]. Moreover, these oscillations bearing the signature of GP effect were even found recently in the energy dependence of the backward scattered state-to-state DCSs of the H + HD (v=0, j=0) → H_2 + D reaction in a combined theoretical and experimental study by Xie *et al.* [171]. The GP effect found in their work which is verified experimentally is solely due to the encirclement of the nuclear wave function around the CI.

In addition to GP, other nonadiabatic effects such as Born-Huang (BH) or Born-Oppenheimer diagonal correction and that due to the derivative coupling to the upper adiabatic PES, must be considered in the reaction dynamics when the total energy becomes higher than or close to the minimum of the CI seam [22, 212]. This is normally done in a numerically efficient manner by resorting to a suitable diabatic representation from the adiabatic one [29, 213, 214] where the complicacy due to singular nature of the derivative coupling is circumvented by a unitary transformation [21, 70, 215]. Such a two-state coupled diabatic theoretical model was devised in early 2000's by Mahapatra *et al.* [55] to include explicit surface coupling in a TDWP framework where the role of the upper adiabatic state on the reaction dynamics was examined for the first time. Since then various work has been done by using such approach to ascertain the role of the upper excited state PES and other nonadiabatic effects in the H + H_2 reaction and its

isotopic variants [55, 73, 74, 152–155, 169, 196]. However, the role of the upper adiabatic state in the reaction dynamics on lower adiabatic PES was found to be minimal [55, 73, 74, 152–155, 169, 196] and the electronic nonadiabatic effects are found to be mostly due to the GP effect [24, 25, 154, 169, 216].

Apart from the search for the effect of GP or nonadiabatic interactions, many other fascinating dynamical features have also been emerged by studying this reaction. It is generally believed that the H + H_2 reaction being direct in nature follows a conventional collinearly dominated rebound mechanism giving mostly backward scattered products. Nevertheless, forward scattering has been found for low rotational product states at relatively higher collision energies and was thought to be due to the quantum mechanical Feshbach resonances [174]. However, later studies showed that the forward scattering also appears in the QCT dynamics simulations and its origin is obviously not due to the quantum mechanical nature [217, 218]. Rather, it is actually due to a time-delayed mechanism [143, 146, 219], where the delay was found to be due to slow down of the triatomic complex near the top of an effective barrier of the QBSs corresponding to higher total angular momentum. With the advent of sophisticated high-resolution instruments it was possible to measure the previously unachievable forward-scattering fast angular oscillations in the hydrogen exchange reaction. Yuan *et al.* [186] for the first time measured the fast oscillatory state-to-state DCSs in the forward direction of the H + HD (v=0, j=0) → H_2 (v', j') + D reaction at E_{col} = 1.35 eV by using a D-atom near-threshold ionization VMI technique with an estimated angular resolution of ≈1.5°. They assumed that the origin of these forward scattering angular oscillations is similar to that in the optical corona phenomena in atmosphere. However, in a later theoretical study Xiahou and Connor [149, 150] predicted that the forward scattering mainly comes from the forward glory phenomena. In their semiclassical analysis, it was shown that these fast angular oscillations actually originate from the quantum interference between the nearside and farside scattering, as predicted earlier [220, 221].

In the hydrogen exchange reaction, backward scattering results from nearly head-on collisions with little rotational excitation, whereas, sideways scattering results from glancing interactions giving rotationally hot product diatoms [188, 222, 223]. This phenomenon is known as the *negative* $j' - \theta$ *correlation* [224]. In a recent work by Jankunas *et al.* [225], a combined theoretical and experimental study of the H + D_2 → HD + D reaction at a collision energy of 1.97 eV found an anomalous trend opposite to the usual *negative* $j' - \theta$ for vibrationally hot product HD (v'=4). This surprising behaviour could not be explained by the purely repulsive MEP of the H + H_2 reaction

with a barrier of ≈0.42 eV (cf. Figure 4.2). Rather it was found to be due to lack of enough recoil energy between the products while passing over the centrifugal barrier of the vibrationally adiabatic potential corresponding to v=4 [189]. A later study by Sneha *et al.* [224] at a higher collision energy of 3.26 eV confirmed this where the usual *negative* $j' - \theta$ trend was recovered as the products now have enough recoil energy to overcome the centrifugal barrier. It is important to note the interesting role of the vibrationally adiabatic potentials in the scattering mechanism of this so called simplest chemical reaction. The role of the vibrationally adiabatic potentials has been useful in explaining the behaviour of the so called barrier resonance [226] and QBSs [142, 145] in few of the earlier works on this reactive system. The QBSs are also shown to control the reactivity at the state-to-state level through quantum interference [142, 144, 145].

In the regard of a comprehensive mechanistic aspect, Goswami *et al.* [227] studied the effect of rovibrational excitation of the reagent diatom on the state-to-state dynamics of the H + H_2 (v=0-4, j=0-3) → H_2 (v', j') + H exchange reaction by a TDWP method using the BKMP2 PES. Total and state-to-state reaction probabilities, ICSs and product rovibrational level distributions were reported in order to elucidate the energy disposal in products. The onset of the reaction was found to shift towards lower collision energies with reagent vibrational excitation and finally the reaction with a classical barrier of ≈0.42 eV becomes barrierless for reagent H_2 (v=4). Vibrational adiabaticity was found to be followed for the situations where the total angular momentum quantum number (J) is zero, whereas, it is lost when contributions from all the Js are included in the ICS. The collision energy and reagent vibrational energy are found to affect the product vibrational distribution (in terms of ICS) in opposite manner. An overall enhancement of reactivity with reagent vibrational excitation is also noticed [227]. All these findings revealed that the dynamics of the hydrogen exchange reaction with vibrationally hot reagent diatom is different and somehow complicated from that occuring with H_2 at its ground rovibrational level.

4.1.3 Motivation of the present work

The previous studies of nonadiabatic effects on the H + H_2 reaction dynamics have been carried out either by including the GP and/or BH corrections in an adiabatic representation or by a two-state coupled model in the diabatic representation. It is important to note that the calculations in the diabatic representation involving both the electronic states is equivalent to that in the lower adiabatic state with the inclusion of GP and BH

corrections unless the effect of the excited electronic state is significant [24, 154]. Theoretically the GP and BH terms are inherently included in the diabatic representation through the adiabatic-to-diabatic transformation [24, 55, 228]. Hence for the H + H_2 reactive system the effect of GP can be eficiently incorporated by doing the calculation in the diabatic representation at least to some minor approximation. This is elegantly shown in a recent article by Huang and Zhang [216] in the TDQM framework. Even though some minor differences were noticed between the results obtained from adiabatic plus GP and diabatic calculations, the latter was found to essentially capture all the effects due to GP [216].

This motivates us to study the electronic nonadiabatic effects efficiently in a diabatic representation where the GP effect is implicitly included. Studies of nonadiabatic effects on this reaction so far considered the reagent diatom in either its (v=0, j=0) or (v=1, j=0) vibrational level. The dynamics of this reaction and its different isotopic variants has also been studied with vibrationally hot reagent by Kendrick and coworkers [24–26, 164–168] but the calculations were carried out in the cold and ultracold condition where the effect of GP and other nonadiabatic effects are examined mostly in terms of the initial state-specific and state-to-state rate constants. In this chapter the nonadiabatic effects in the state-to-state dynamics of the H + H_2 reaction with vibrationally excited reagent diatom H_2 (v=3,4, j=0) is reported at the thermal energies where the CI can be made accessible at a lower value of collision energies. This happens for collision energy higher than 1.0 and 0.57 eV for H_2 (v=3, j=0) and H_2 (v=4, j=0), respectively. In addition to the nonadiabatic effects, a comprehensive analysis of the effect of reagent vibrational and rotational excitation on the scattering mechanism of the hydrogen exchange reaction is also reported in order to extend the studies done in Ref. 227. As the DCS is the most subtle dynamical observable among all, it is expected that the present investigation can provide a better understanding of the dynamics of the hydrogen exchange reaction.

4.2 Theoretical and computational details

The dynamical calculations are performed by the TDWP method and employing a two-state coupled diabatic theoretical model, as described in section 2.2 of chapter 2, to include both lower and upper adiabatic states and the coupling between them. In addition, single surface (uncoupled) dynamics is also carried out on the lower adiabatic state

PES by the procedures described in section 2.1 of chapter 2 to differentiate the nonadiabatic effects in the reaction observables. In this work, the diabatic potential energy matrix elements are obtained from the diagonal adiabatic potential energy matrix by the adiabatic-to-diabatic transformation where the ADT angle (α) is approximated both up to the linear and quadratic coupling. This is given as [178],

$$\alpha^{(1)} = \frac{\phi}{2} \tag{4.1}$$

$$\alpha^{(2)} = \frac{\phi}{2} + \frac{1}{2}\tan^{-1}\left(\frac{g_0 s \sin 3\phi}{f_0 + f_1 s^2 + g_0 s \cos 3\phi}\right). \tag{4.2}$$

The angle ϕ is the pseudorotation angle that encircles the CI and defines the direction of $E-$type displacement in its two-dimensional (doubly degenerate) vibrational subspace of the D_{3h} point group. In the equation 4.2, the term s stands for the normalized radial distance from the D_{3h} CI in its two dimensional degenerate vibrational subspace; s=0 gives the seam of the CI. According to the analytic formulation of the DMBE PES of H_3 [178], ϕ and s are given as,

$$\phi = (\text{sgn}\ Q_y)\left[\pi - \cos^{-1}\left(\frac{Q_x}{sQ_z}\right)\right] \tag{4.3}$$

$$s = \frac{\sqrt{Q_x^2 + Q_y^2}}{Q_z}, \tag{4.4}$$

where Q_x and Q_y are the two cartesian components of the doubly-degenerate $E-$type vibrational mode and Q_z is the normal coordinate for the symmetric stretching (breathing) vibrational mode, and are given as [178],

$$Q_x = 2R_1^2 - R_2^2 - R_3^2 \tag{4.5}$$

$$Q_y = \sqrt{3}(R_2^2 - R_3^2) \tag{4.6}$$

$$Q_z = R_1^2 + R_2^2 + R_3^2, \tag{4.7}$$

where, R_1, R_2 and R_3 are the three internuclear distances of H_3, respectively. In equation 4.2 the quantities f_0, f_1 and g_0 are functions of the nuclear coordinate corresponding to the symmetric stretching (breathing) vibrational mode of the D_{3h} configuration of H_3. These are calculated by taking the derivatives of the difference between the two adiabatic PESs as given in equations 50-53 of Ref. [178].

It is necessary to mention here that the quadratic term in $\alpha^{(2)}$ is approximated in such a way that it avoids the unwanted CIs occuring at nonzero values of s [178, 229].

Up to the linear coupling approximation, the ADT angle is equal to half of the pseudorotation angle which eliminates the leading singular part of the derivative coupling [230] and is independent of the PESs [178]. The additional term on the right hand side of equation 4.2 eliminates the remaining non-singular part [24] and depends on the two adiabatic PESs. This term becomes important mostly near the collinear geometry [183]. Inclusion of the quadratic terms in the ADT angle makes the diabatic representation more accurate for reaction dynamical study. In the present work the BKMP2 [180] PES is used for the lower adiabatic component (V_-) and the upper part of the DMBE [178] PES is used for the upper adiabatic component (V_+). In order to ensure the degeneracy along the CI seam, a small correction term was introduced to the upper DMBE surface.

In order to understand the nonadiabatic effect in the state-to-state DCSs, the topological argument of Althorpe and co-workers [161, 211] can be used to calculate the 1-TS and 2-TS path contributions to the DCS and the possible interference between them. According to Refs. [161, 211], the scattering amplitudes corresponding to the 1-TS and 2-TS paths are given as,

$$f_1(\theta, E) = \frac{1}{\sqrt{2}} \left[f_{\mathrm{NGP}}(\theta, E) + f_{\mathrm{GP}}(\theta, E) \right] \tag{4.8}$$

$$f_2(\theta, E) = \frac{1}{\sqrt{2}} \left[f_{\mathrm{NGP}}(\theta, E) - f_{\mathrm{GP}}(\theta, E) \right], \tag{4.9}$$

respectively. Now, as it is discussed in the section 4.1.2 that as long as the upper adiabatic surface does not play a significant role in the reaction dynamics on the lower adiabatic surface then it is justified to a minor approximation that the term f_{GP} in equations 4.8 and 4.9 can be replaced by f_{CP}, which is the scattering amplitude obtained from the coupled surface calculation. In this case the DCSs corresponding to the 1-TS and 2-TS paths can be calculated as

$$\sigma_{1-\mathrm{TS}}(\theta, E) = \left| f_1(\theta, E) \right|^2 = \frac{1}{2} \left| f_{\mathrm{UC}}(\theta, E) + f_{\mathrm{CP}}(\theta, E) \right|^2 \tag{4.10}$$

$$\sigma_{2-\mathrm{TS}}(\theta, E) = \left| f_2(\theta, E) \right|^2 = \frac{1}{2} \left| f_{\mathrm{UC}}(\theta, E) - f_{\mathrm{CP}}(\theta, E) \right|^2, \tag{4.11}$$

where $f_{\mathrm{UC}}(\theta, E)$ is the scattering amplitude corresponding to the uncoupled lower adiabatic surface calculation and is similar to $f_{\mathrm{NGP}}(\theta, E)$.

The numerical parameters used in the present nonadiabatic TDWP study are taken from the Ref. [227] for reagent H_2 (v=3,4, j=0). The Coriolis coupling terms are treated here accurately for each J where the coupling between all Ω' substates are considered

explicitly. All the partial waves are included in the calculation of cross sections up to collision energy of 1.25 eV. It is important to note here that the computational time for the WP propagation in diabatic representation (involving both the electronic states) increases twice as compared to the adiabatic single surface propagation. This is because the number of operations of the Hamiltonian on the WPs become doubled in case of the former. Hence the calculations involving both the electronic states are more time consuming than the single surface adiabatic calculations.

The details of the converged numerical parameters used in the TDWP calculations in case of rotationally excited reagents are given in Table 4.1. Several test calculations are performed with respect to each numerical parameter by keeping the reagent diatom in its Ω=0 helicity state of each of its rotational level, and the same converged parameters are used for other (Ω ≠0) helicity states. It can be seen from Table 4.1 that with reagent rotational excitation, the details of the numerical parameter do not change significantly. However, the total propagation time of the WP increases to a small amount.

Table 4.1: Details of the numerical parameters used in the time-dependent wave packet calculations for the, H + H_2 (v=0, j=1−3) → H_2 (v', j') + H, reaction.

Parameter	H_2(v=0, j=1)	H_2(v=0, j=2)	H_2(v=0, j=3)
$N_{R'}/N_{r'}/N_{\gamma'}$	143/139/60	143/143/60	143/159/65
R'_{min}/R'_{max} (a_0)	0.2/18.0	0.2/19.0	0.2/20.0
r'_{min}/r'_{max} (a_0)	0.5/14.5	0.5/16.5	0.5/19.5
R'_d (a_0)	8.0	8.0	8.0
V_{cut} (E_h)	0.22	0.22	0.22
R'_{abs}/r'_{abs} (a_0)	8.5/8.0	9.5/8.0	9.5/8.5
C_{abs}/c_{abs}	20.0/20.0	20.0/20.0	20.0/20.0
R_0 (a_0)	7.0	7.0	7.0
E_{trans} (eV)	0.7	0.7	0.7
δ	8.0	8.0	8.0
β_s	0.5	0.6	0.7
$nvab$	3	3	3
$njab$	14	14	14
$nstep$	3000	4500	4500
Time (fs)	273.2	424.0	433.1
J range	J=0-29	J=0-30	J=0-31

It is worthwhile to note here that the calculations are carried out by considering the three hydrogen nuclei as distinguishable and hence considers only the reactive contributions. In other words the present calculation ignores the GP effect due to the permutation symmetry of three identical nuclei rather considers only that due to encirclement

of nuclei around CI.

4.3 Results and Discussion

The dynamical outcomes of the H + H_2 reaction with vibrationally excited reagent are presented and discussed here. The discussion part is divided into three parts. In the first part, the effect of nonadiabatic coupling in the state-to-state dynamics of the hydrogen exchange reaction with vibrationally hot reagent H_2 (v=3,4, j=0) is discussed. In the second part, the effect of reagent vibrational excitation from v=0 to v=4 on the scattering dynamics of the hydrogen exchange reaction is discussed from a mechanistic point of view. Finally, in the third part the effect of rotational excitation of the reagent diatom in its ground vibrational (v=0) manifold on the state-to-state as well as overall dynamics is discussed. It should be noted here that the dynamical calculations for reagent H_2 (v=0-2, j=0) are performed here only on the lower adiabatic surface without including the explicit surface coupling. This is because the CI is not accessible energetically for these vibrational levels within the energy range considered here.

4.3.1 Electronic nonadiabatic effects in the H + H_2 (v=3,4, j=0) → H_2 (v', j') + H reaction

4.3.1.1 Effect of quadratic coupling and the upper adiabatic state

In the present nonadiabatic calculation for reagent H_2 (v=3,4, j=0) the ADT angle is approximated up to the quadratic term, as mentioned in section 4.2. The effect of the quadratic term on few representative state-to-state reaction probabilities is shown in Figure 4.4. The probabilities obtained by considering the ADT angle within the linear approximation is also shown along with the uncoupled results for a detailed comparison. First of all it is clear that for zero total angular momentum significant nonadiabatic effects appear at collision energies higher than that correspond to the minimum of CI, both for reagent H_2 (v=3, j=0) and H_2 (v=4, j=0) (cf. panel a and c). The minimum value of the CI seam occurs at a collision energy of 1.0 eV for H_2 (v=3, j=0) and at 0.57 eV for H_2 (v=4, j=0). However, for higher total angular momentum J=15 the nonadiabatic effects start appearing even from lower collision energies, well below the minimum of CI (cf. panel b and d). It can be seen that the quadratic term only shows a

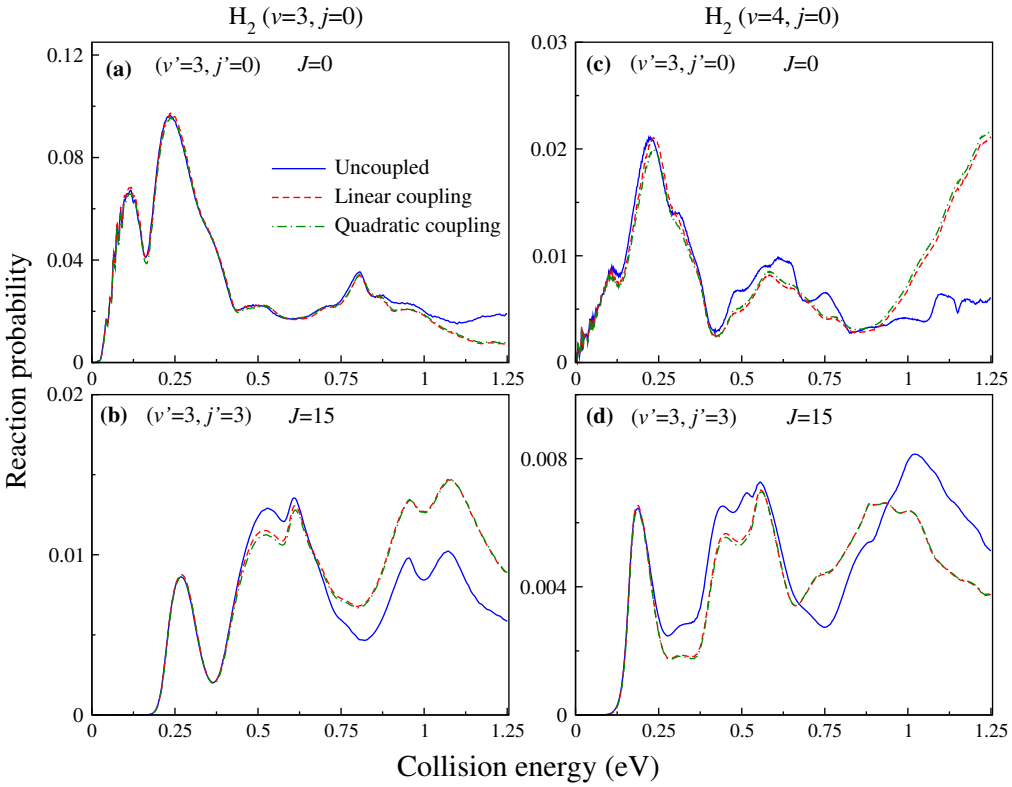

Figure 4.4: Product rotational level resolved state-to-state reaction probabilities obtained from uncoupled and coupled surface calculations both within linear and quadratic approximation for the H + H_2 (v=3,4, j=0) → H_2 (v'=3, j'=0,3) + H reaction as a function of collision energy for the total angular momentum J = 0 and 15.

very minor effect at lower collision energies where the collinear geometry is mostly explored. But, surely it does not show much effect at higher collision energies particularly when the CI becomes accessible. Most importantly at higher energies the probabilities obtained within the quadratic coupling approximation becomes almost identical to those obtained within the linear coupling approximation. The same has been found in many of the state-to-state reaction probabilities which are not shown here for brevity.

Moreover, the similar observation can be seen in case of initial state-selected total reaction probabilities shown in Figure 4.5 for different J. It is also clear from Figure 4.5 that the nonadiabatic effects seen in state-to-state reaction probabilities are found to be washed out when summed over final states. Such observations have been also found for H_2 (v=0,1, j=0) in the early work of Juanes-Marcos and Althorpe [160] where the GP effect is studied by the vector potential approach. Hence, it is clear that the quadratic term does not affect much the dynamics at energies where the nonadiabatic effects are important, but only has a minor effect at lower collision energies. However, still the inclusion of the quadratic term is considered here for the sake of completeness. It

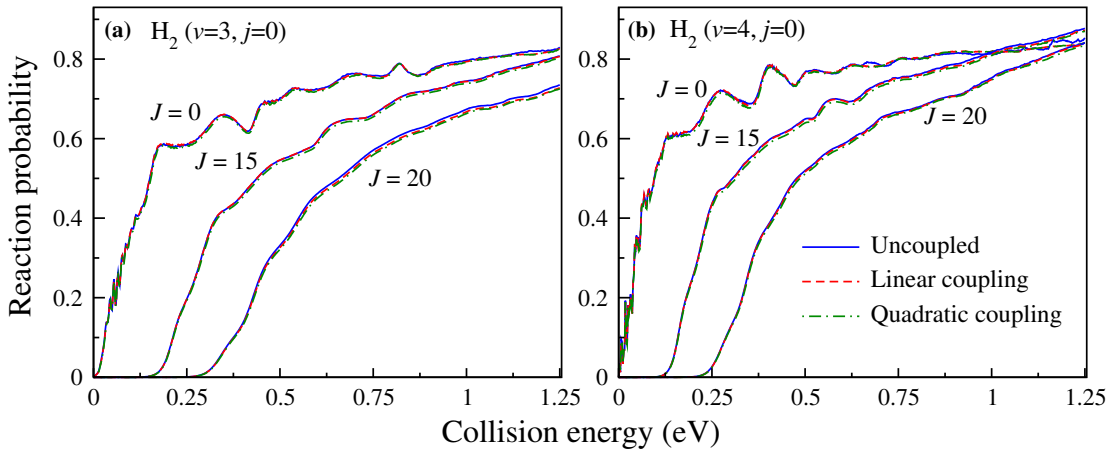

Figure 4.5: Initial state-selected total reaction probabilities obtained from uncoupled and coupled surface calculations both within linear and quadratic approximation for the H + H_2 (v=3,4, j=0) → H_2 ($\sum v'$, $\sum j'$, $\sum \Omega'$) + H reaction as a function of collision energy for the total angular momentum J = 0, 15 and 20.

should be kept in mind that it is the linear term which is responsible for the GP effect associated with Jahn-Teller CIs. [24, 199, 231]

It known in the literature that for the H + H_2 (v=0, j=0) → H_2 + H reaction a large part of the nonadiabatic effects at higher collision energies are mainly caused by the GP, and the upper adiabatic state has a very minor influence on the dynamics. We examine here the role of the upper adiabatic state in the reaction with vibrationally excited reagent H_2 (v=3,4, j=0) by studying the population dynamics.

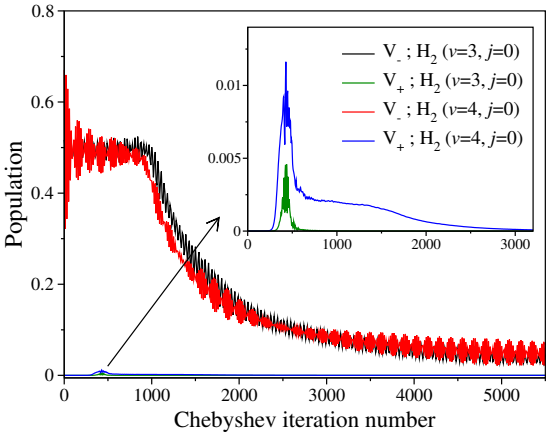

Figure 4.6: Adiabatic population dynamics for the H + H_2 (v=3,4, j=0) → H_2 + H reaction. The population of the upper adiabatic electronic state V_+ is shown in the inset.

The time evolution of the adiabatic electronic populations are shown in Figure 4.6 for H_2 (v=3,4, j=0) as a function of Chebyshev iteration number. It can be seen that almost all of the populations reside on the lower adiabatic state and a very tiny amount of the WP traverses to the upper adiabatic state. It is found that only ~ 0.8 % and ~ 2 % of the WP pass over to the upper adiabatic state in case of reagent H_2 (v=3, j=0) and H_2 (v=4, j=0), respectively (cf. inset of Figure 4.6), for a maximum collision energy of 1.25 considered in the present work. Hence, it is clear that even for vibrationally excited reagent (v=3,4, j=0) the role of the

upper adiabatic electronic state stays minimal in the reaction dynamics. The oscillations present in the populations are actually an artifact of the real wave packet method used in the current work where only the half of the wave packet *i.e.,* the real part is propagated. Therefore, the initial value of the square of the norm is centered around 0.5 instead of 1.

4.3.1.2 Nonadiabatic effects in state-to-state DCSs

In this section the nonadiabatic effects mostly due to GP (according to the discussion above) on the state-to-state DCSs of the H + H_2 (v=4, j=0) → H_2 (v', j') + H reaction is discussed. After analyzing a large number of state-to-state DCSs they are classified into two categories, one those represent strong nonadiabatic effects and the other which represent negligible nonadiabatic effects. The state-to-state DCSs for the product H_2 (v'=0, j'=12, Ω'=0) at E_{col} = 0.57 eV are analyzed in Figure 4.7 which represent strong nonadiabatic effects on the DCS. This value of collision energy for reagent H_2 (v=4, j=0) corresponds to the total energy of 2.73 eV which is approximately the minimum value of the CI seam. The DCSs obtained from both uncoupled and coupled surface calculations are shown in panel (a) as a function of θ. It can be seen from Figure 4.7(a) that "out-of-phase" oscillations between the uncoupled and coupled surface DCSs occur along θ in the backward hemisphere region. The "out-of-phase" behaviour of the oscillations are due to the GP effect which is implicitly included in the coupled surface diabatic treatment. The DCSs corresponding to the 1-TS and 2-TS paths are calculated from the scattering amplitudes of uncoupled and coupled surface results and are shown in Figure 4.7(a) for product H_2 (v'=0, j'=12, Ω'=0). It can be seen that the 1-TS DCS is much higher in magnitude than the 2-TS DCS in the range of θ where the "out-of-phase" oscillations are seen. Even though the magnitude of 2-TS DCS is less, it is rather non-negligible.

However, the origin of the "out-of-phase" oscillations can not be directly deduced from the 1-TS and 2-TS DCSs. This is because the calculation of σ_{1-TS} and σ_{2-TS} does not consider the inclusion of the interference term between $f_1(\theta, E)$ and $f_2(\theta, E)$. The 1-TS and 2-TS contributions with the inclusion of the interference term can demonstrate the origin of the "out-of-phase" oscillations as it will be shown. The expressions of the DCSs corresponding to the 1-TS and 2-TS contributions with the inclusion of the interference terms are given in the Appendix A. Since GP changes the relative sign between the 1-TS and 2-TS scattering amplitudes, as a result we get two 1-TS and two

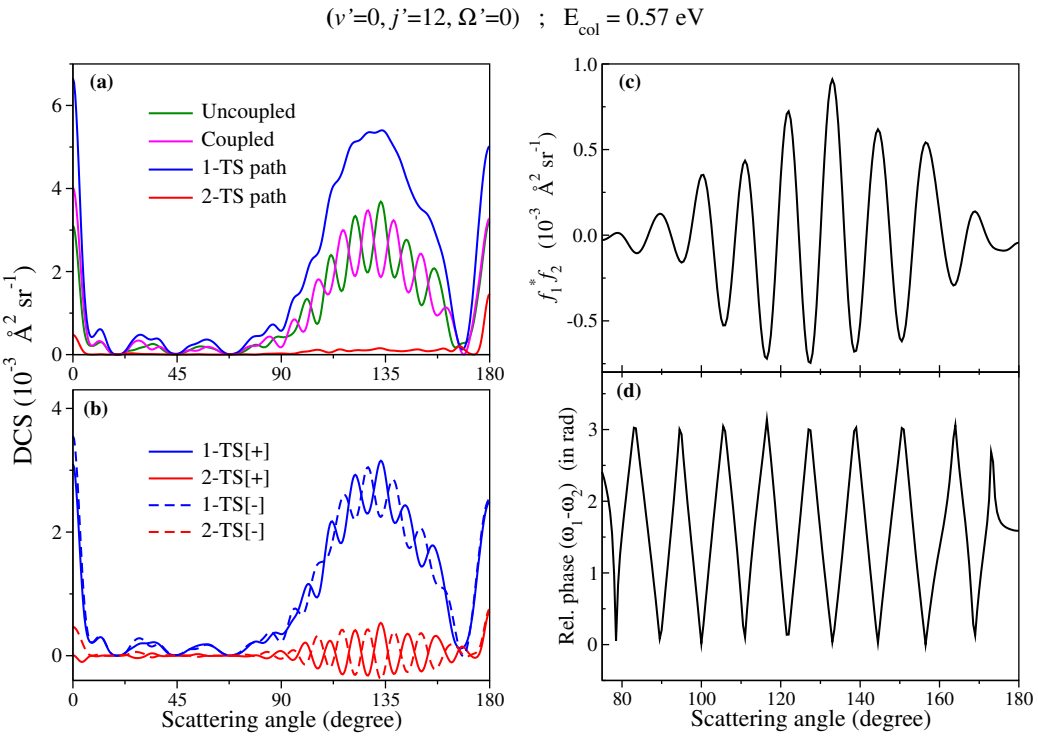

Figure 4.7: Electronic nonadiabatic effects in the state-to-state DCS of H + H_2 (v=4, j=0) → H_2 (v'=0, j'=12, Ω'=0) + H reaction at E_{col} = 0.57 eV. (a) The state-to-state DCSs obtained from both uncoupled and coupled surface calculations and those corresponding to the 1-TS and 2-TS paths as a function of θ. (b) The DCSs corresponding to 1-TS[+], 2-TS[+], 1-TS[-] and 2-TS[-] contributions as a function of θ. (c) The interference term between 1-TS and 2-TS path scattering amplitudes and (d) the relative phase between the 1-TS and 2-TS path scattering amplitudes as a function of θ (shown for θ = 75°-180°).

2-TS contributions. The corresponding DCSs $\sigma_{1-TS[+]}$, $\sigma_{2-TS[+]}$, $\sigma_{1-TS[-]}$ and $\sigma_{2-TS[-]}$ for the product H_2 (v'=0, j'=12, Ω'=0) are shown in Figure 4.7(b). It can be seen that these DCSs show proper oscillating behaviour in the backward hemisphere. Hence, these oscillations originate from the interference between the 1-TS and 2-TS paths. Moreover, the oscillations present in $\sigma_{1-TS[+]}$ and $\sigma_{1-TS[-]}$ DCSs show "out-of-phase" behaviour, similar to $\sigma_{2-TS[+]}$ and $\sigma_{2-TS[-]}$, which in turn translates to the "out-of-phase" oscillations found between the uncoupled and coupled DCSs in FIg. 4.7(a). This "out-of-phase" behaviour arises from the change in sign of the interference term as a result of GP as shown in equations 4.19–4.22. The interference term $f_1^* f_2$ and the relative phase between the two paths ($\omega_1 - \omega_2$) are also calculated (see Appendix B) and plotted in panel (c) and (d) of Figure 4.7 as a function of θ to understand the interference phenomenon. It can be seen that the phase difference between the scattering amplitudes of 1-TS and 2-TS paths oscillates rapidly in the range of 0 to π along θ. This leads to a constructive interference (+ve peaks in the $f_1^* f_2$ plot) wherever the phase difference

becomes maximum (out-of-phase) and destructive interference (-ve peaks in the $f_1^* f_2$ plot) wherever the phase difference touches a minimum value (in-phase).

For the product H_2 (v'=0, j'=12, $\Omega' \neq 0$) both the uncoupled and coupled state-to-state DCSs at E_{col} = 0.57 eV are shown in Figure as a function of θ for a few Ω' values. It can be seen from the figure that though difference between the coupled and

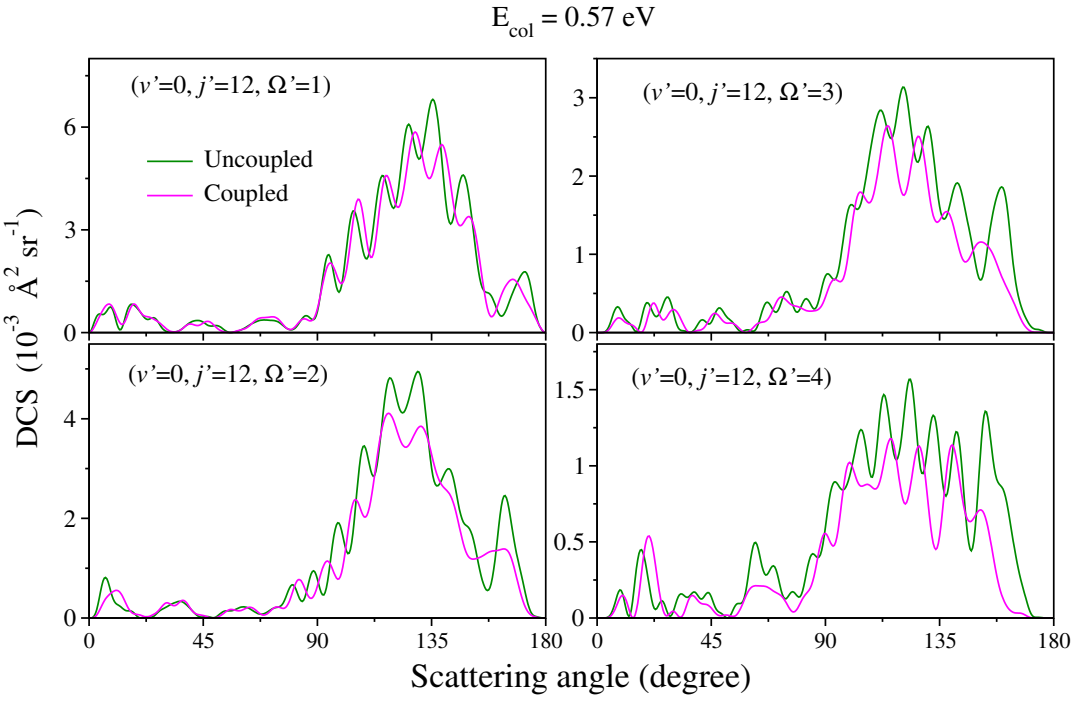

Figure 4.8: State-to-state DCSs of the H + H_2 (v=4, j=0) → H_2 (v'=0, j'=12, $\Omega' \neq 0$) + H reaction as a function of θ at E_{col} = 0.57 eV for some selected Ω' quantum numbers.

uncoupled DCSs exists as a result of the nonadiabatic effects, a clear "out-of-phase" oscillation does not occur in case of $\Omega' \neq 0$. This behaviour of Ω'=0 and $\Omega' \neq 0$ state-to-state DCSs in the sideways region is found to be general for products having low v' and relatively higher j' quantum numbers. It seen in all of the cases that the magnitude of 2-TS mechanism is comparatively low for Ω'=0 states but has significant interference with the 1-TS mechanism resulting an "out-of-phase" oscillations in the sideways direction. However, for $\Omega' \neq 0$ such oscillations are rare and the way GP affects the dynamics is quite arbitrary. Further stereodynamical study on the product polarization is required to understand the GP effect in case of $\Omega' \neq 0$ product states. Such studies are beyond the scope of the present work.

In what follows next the state-to-state DCSs that represent negligible nonadiabatic effects are presented and discussed. Such an example is given in Figure 4.9 where the DCSs for the product H_2 (v'=0, j'=0) at E_{col} = 0.57 eV are analyzed. The DCSs ob-

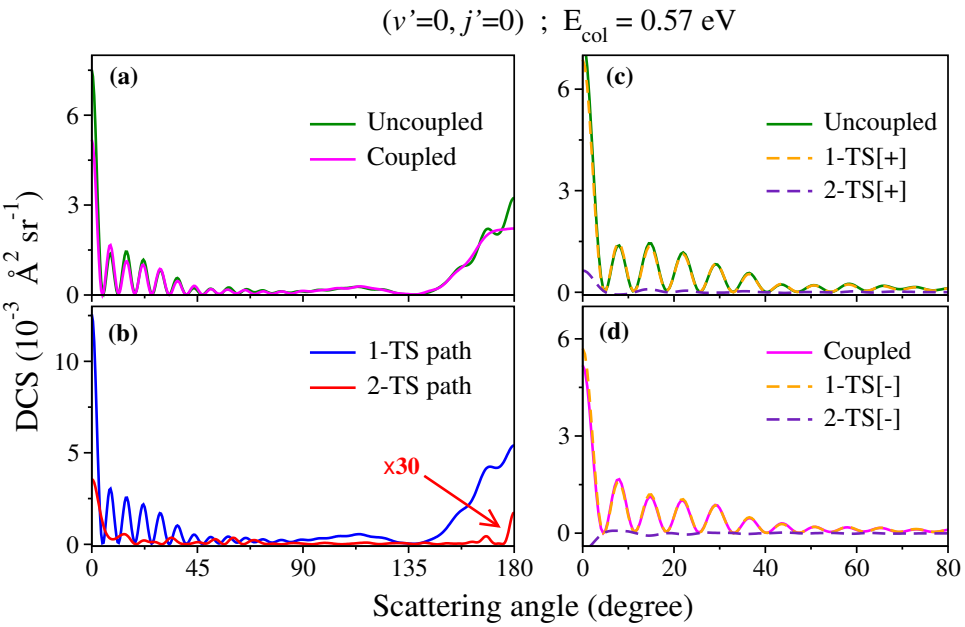

Figure 4.9: Electronic nonadiabatic effects in the state-to-state DCS of H + H_2 (v=4, j=0) → H_2 (v'=0, j'=0) + H reaction at E_{col} = 0.57 eV. (a) The state-to-state DCSs obtained from both uncoupled and coupled surface calculations as a function of θ. (b) The DCSs corresponding to the 1-TS and 2-TS paths as a function of θ. (c) The DCSs corresponding to 1-TS[+] and 2-TS[+] contributions along with the uncoupled DCS (d) The DCSs corresponding to 1-TS[-] and 2-TS[-] contributions along with the coupled DCS as a function of θ. In panels (c) and (d) θ is shown from 0° to 80° for a clear view of the oscillations.

tained from both uncoupled and coupled surface calculations are shown in panel (a) as a function of θ. It can be seen from Figure 4.9(a) that almost no difference exists between the uncoupled and coupled DCSs except at the extreme forward and backward region. Oscillations can be seen in both the DCSs in the forward scattering region which are in-phase with each other, and these oscillations show a very negligible nonadiabatic effects. The DCSs corresponding to the 1-TS and 2-TS path are shown in panel (b) as a function of θ. It can be seen that the 2-TS path has a negligibly small contribution (~2 orders of magnitude less than the 1-TS path) and most of the oscillating feature comes from the 1-TS DCS. Moreover, the 1-TS and 2-TS contributions with the inclusion of the interference term are calculated and the corresponding DCSs, $\sigma_{1-TS[+]}$, $\sigma_{2-TS[+]}$, $\sigma_{1-TS[-]}$ and $\sigma_{2-TS[-]}$ are shown in panel (c) and (d) along with the uncoupled and coupled DCSs. It can be seen from Figure 4.9(c)-(d) that the DCSs $\sigma_{1-TS[+]}$ and $\sigma_{1-TS[-]}$ almost perfectly reproduce the forward scattering oscillations present in the uncoupled and coupled DCSs. However, the 2-TS paths, both $\sigma_{2-TS[+]}$ and $\sigma_{2-TS[-]}$, even with the inclusion of interference term hardly contribute to the DCSs. This suggests that the interference between the 1-TS and 2-TS paths is negligibly small in this case.

Hence, it is safe to ascertain that these forward scattering oscillations do not originate from the interference between the 1-TS and 2-TS paths and are not a result of GP. These oscillations are rather signature of the typical glory interference pattern [220, 221] originating from the nearside-farside interference of *only* 1-TS paths. [162] Such glory phenomenon has recently been observed experimentally in the forward scattering of H + HD (v=0, j=0) → H_2 (v'=0, j'=1,3) + D reaction but at a collision energy much lower than the minimum of CI seam. [149, 150, 186] The negligible nonadiabatic effects in the forward scattering oscillations is found to be general for products having low j' quantum numbers irrespective of the product vibrational manifold. Few more examples are given in Figure 4.10 for two different values of collision energy E_{col} = 0.57 and 0.75 eV.

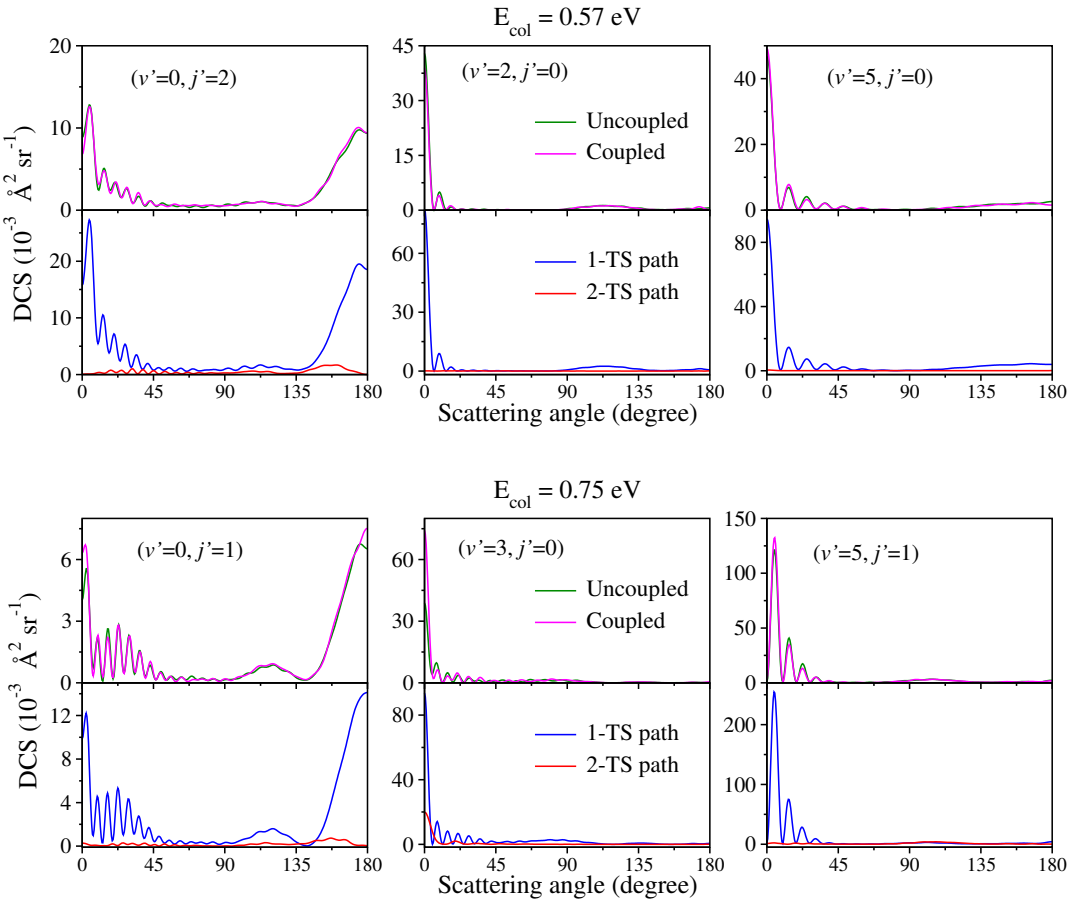

Figure 4.10: State-to-state DCSs, both uncoupled and coupled, and those corresponding to the 1-TS and 2-TS paths, of the H + H_2 (v=4, j=0) → H_2 (v', j', $\sum\Omega'$) + H reaction as a function of scattering angle for some selected (v', j') levels of product showing negligible electronic nonadiabatic effects in the forward scattering oscillations at E_{col} = 0.57 and 0.75 eV.

In addition to the two general phenomena discussed above, few exceptions have

also been noticed in the present investigation. Most importantly, in contrast to the negligible nonadiabatic effects in the forward scattering oscillations, strong nonadiabatic effects in the forward hemisphere is found in few cases. This is found to be most likely occur in case of higher vibrational levels of product. Figure 4.11 shows a few of such examples at two different collision energies, E_{col} = 0.57 and 0.75 eV for v'=4 manifold. It can be seen from the figure that the nonadiabatic effects appear in the forward

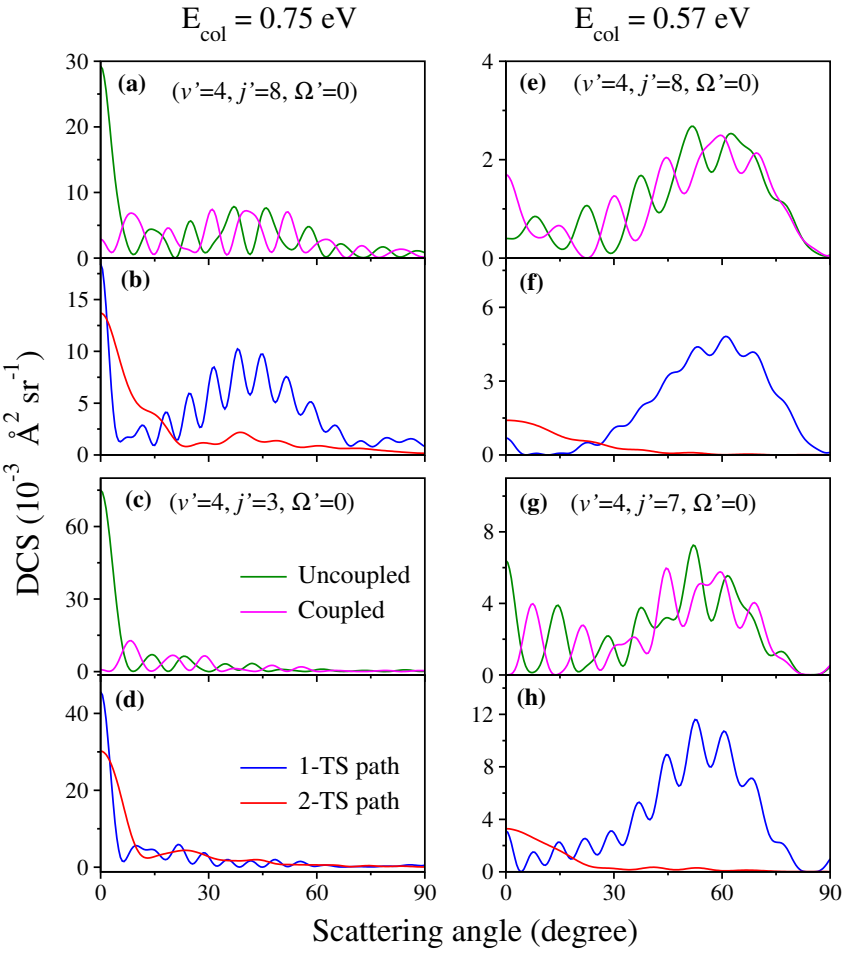

Figure 4.11: State-to-state DCSs of H + H_2 (v=4, j=0) → H_2 (v'=4, j', Ω'=0) + H reaction as a function of θ at E_{col} = 0.57 eV (a-d) and 0.75 eV (e-h) showing strong nonadiabatic effects in the forward scattering angular oscillation. The DCSs corresponding to the 1-TS and 2-TS paths are shown in the below panels. The DCSs are plotted here only for the forward hemisphere i.e., $\theta = 0° - 90°$.

scattering region in the form of "out-of-phase" oscillations between the uncoupled and coupled DCSs. The DCSs corresponding to the 1-TS and 2-TS path are also shown for the respective product states. It is seen that the 1-TS path contributes mainly towards the sideways scattering (in the forward hemisphere) for the (v'=4, j'=7-8, Ω'=0) product states and also to the extreme forward scattering for the (v'=4, j'=8, Ω'=0) product state at E_{col} = 0.75 eV, whereas the 2-TS path mainly contributes towards the extreme

forward scattering for these product states. For the (v'=4, j'=3, Ω'=0) at E_{col} = 0.75 eV, both the 1-TS and 2-TS paths have comparable magnitude and contribute mainly towards the forward scattering. The 2-TS path mechanism has appreciable magnitude in the forward scattering region in these cases, in contrast to the findings of Figure 4.9 and 4.10, and leads to a significant interference between the 1-TS and 2-TS path mechanisms consequently causing the "out-of-phase" oscillations between the uncoupled and coupled DCSs. These forward scattering oscillations are different from the glory interference phenomenon since the underlying mechanism by which they arise is different. These oscillations are not as regular as the former ones (shown in Figure 4.9 ans 4.10) where the 1-TS path mechanism is dominant. Moreover, the period of these oscillations is greater (≈9.5°−10.7°) than that of the former ones (≈6.7°−8.5°).

In order to learn more about the difference between these two types of oscillations, we consider a unique example of the state-to-state DCSs for the H_2 (v'=3, j'=8, Ω'=0) product state at E_{col} = 0.57 eV as given in Figure 4.12. The uniqueness of this product

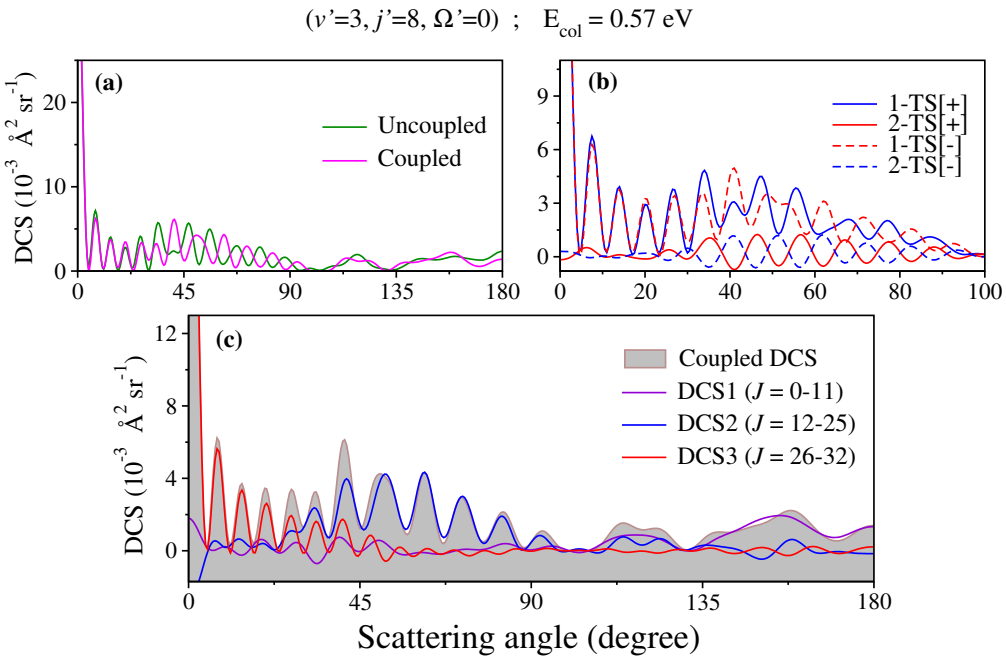

Figure 4.12: State-to-state DCSs of H + H_2 (v=4, j=0) → H_2 (v'=3, j'=8, Ω'=0) + H reaction at E_{col} = 0.57 eV showing both the glory interference pattern and "out-of-phase" oscillations in the forward scattering hemisphere. (a) The state-to-state DCSs obtained from both uncoupled and coupled surface calculations as a function of θ. (b) The DCSs corresponding to 1-TS[+], 2-TS[+], 1-TS[-] and 2-TS[-] contributions as a function of θ. (c) The partial DCSs corresponding to different J ranges (mentioned inside the panel) as a function of θ along with the coupled DCS.

state is that both the above discussed phenomena occur together in the DCS in forward hemisphere but at two different ranges of the scattering angle. It can be seen from

the Figure 4.12(a) that the glory interference pattern appears in both the coupled and uncoupled DCSs with a negligibly small nonadiabatic effect in the range of θ from 0° to 30°. However, strong nonadiabatic effects can be seen afterwards in the form of "out-of-phase" oscillations between the coupled and uncoupled DCSs in the range of θ from 30° to 90°. The DCSs corresponding to the 1-TS and 2-TS contribution with the inclusion of the interference terms *i.e.,* $\sigma_{1-TS[+]}$, $\sigma_{2-TS[+]}$, $\sigma_{1-TS[-]}$ and $\sigma_{2-TS[-]}$ are plotted in panel (b) as a function of θ. A negligibly small contribution of the 2-TS path mechanism can be seen for θ = 0°−30° which mainly dominated by the 1-TS path mechanism. However, in case of θ = 30°−90°, both the 1-TS and 2-TS path mechanisms have appreciable contributions which leads to the interference between these two causing the "out-of-phase" oscillations.

The angular period ($\Delta\theta$) of the glory oscillations is found to be ≈6.5° whereas it is ≈10.4° in case of the "out-of-phase" oscillations. This gives the most dominant J value, according to semiclassical theory [232] ($J = 180°/\Delta\theta - 1/2$) as ≈27 in case of the glory scattering and ≈17 in case of the "out-of-phase" oscillations. The partial wave mainly responsible for the glory oscillations generally occur at higher J values close to the J_{max}. In this case J=27 is close to the J_{max} which is found to be 32 at E_{col} = 0.57 eV. Hence, for θ = 0°−30°, the forward scattering oscillations are most likely due to the glory interference phenomena. It is also highly improbable that the partial waves around J=17 give rise to such glory scattering as they may scatter the product mostly into the sideways direction. This is indeed shown in panel (c) of Figure 4.12 where the DCSs (coupled surface) corresponding to three different ranges of J are plotted as a function of θ. The ranges of J are chosen so as to represent the lower, intermediate and higher partial waves and are denoted as DCS1, DCS2 and DCS3, respectively, in Figure 4.12(c). It is to be noted here that the calculation of these partial DCSs of a specific J range includes also the coherence terms outside that range. It can be seen from Figure 4.12(c) that the glory oscillations mainly originate from the DCS3 corresponding to the higher partial waves J = 26-32, which is in rather good agreement with the above analysis using semiclassical theory. The partial waves corresponding to the intermediate J range, J = 12-25, mainly contributes to the DCS in the range of θ = 30°−90° where the nonadiabatic effects are seen in the form of "out-of-phase" oscillations. The same behaviour is also found in case of the uncoupled DCS which is not shown here for brevity.

The correlation function between J and θ *i.e.,* the quantum mechanical generalized deflection function (see Ref. [76]) of the product states (v'=0, j'=0, Ω'=0), (v'=3, j'=8,

Ω′=0), (v'=4, j'=8, Ω′=0) and (v'=4, j'=8, Ω′=0) are shown in Figure 4.13 at E_{col} = 0.57 eV. As shown above the glory oscillations are seen only in the first two of them

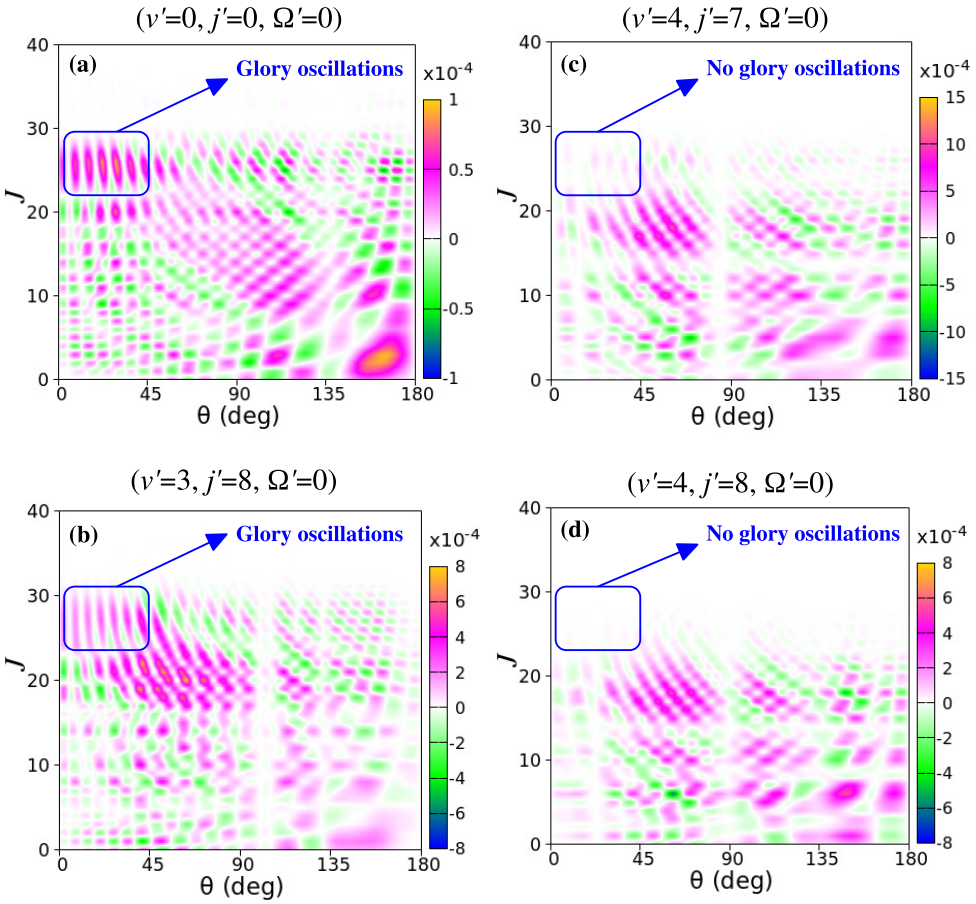

Figure 4.13: The quantum mechanical generalized deflection function of the H + H_2 (v=4, j=0) → H_2 (v', j', Ω′) + H reaction at E_{col} = 0.57 eV for different product quantum states differentiating the glory angular oscillations from the "out-of-phase" forward scattering oscillations. The quantum numbers of the product states are mentioned at the top of each panel.

and the second two carry "out-of-phase" oscillations due to GP in the forward scattering region. It is obvious from the Figure S6 that in case of the (v'=0, j'=0, Ω′=0) and (v'=3, j'=8, Ω′=0) product states (cf. panel a and b) the characteristic glory oscillations can easily be identified in the region of high J and low θ (marked in blue coloured box). However, in case of (v'=4, j'=8, Ω′=0) and (v'=4, j'=8, Ω′=0) product states no such oscillations are found (cf. panel c and d). Hence, it is safe to ascertain that the "out-of-phase" forward scattering oscillations discussed in Figure 4.11 are not due to the glory phenomenon. Moreover, it is clear that these two observations *i.e.,* the glory oscillations with negligible nonadiabatic effect and the "out-of-phase" forward scattering oscillations due to strong nonadiabatic effect are actually different and they originate from two different underlying mechanisms.

So far it is discussed that how the nonadiabatic effects appear in the state-to-state DCSs as a function of θ for the vibrationally excited reagent. In what follows the state-to-state DCSs are presented as a function of the collision energy for fixed values of θ corresponding to both forward and backward scattering. The collision energy dependence of a few selected state-to-state DCSs at θ = 0° and 180° are shown in Figure 4.14 for the H + H_2 (v=4, j=0) → H_2 (v', j') + H reaction. The DCSs obtained from

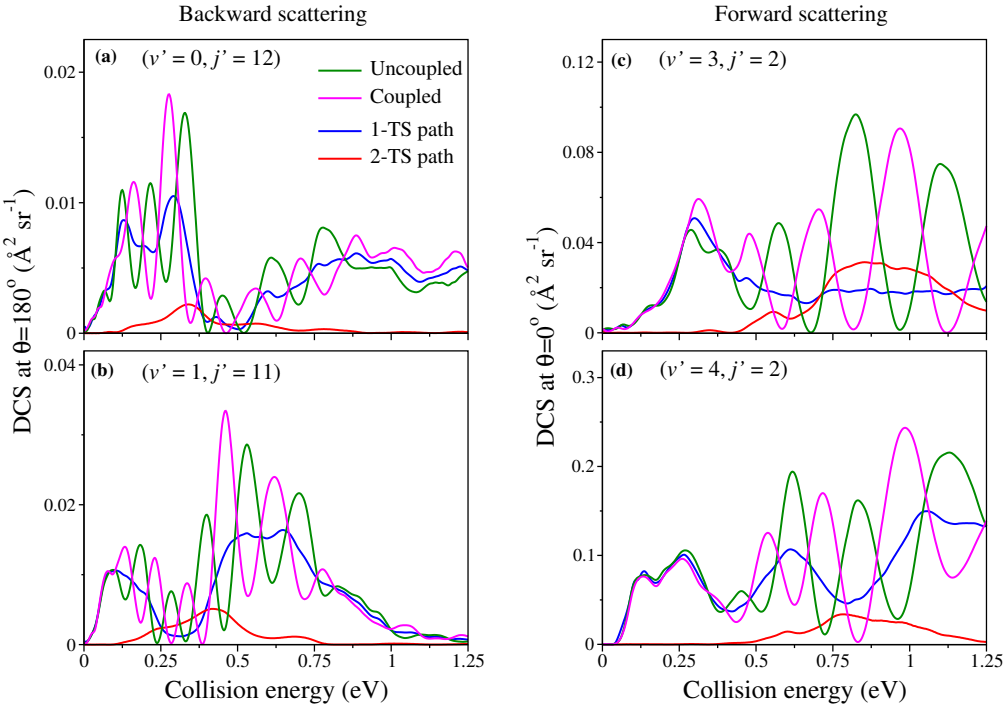

Figure 4.14: Collision energy dependence of some selected state-to-state DCSs for the H + H_2 (v=4, j=0) → H_2 (v', j') + H reaction in the backward (at θ = 180°; panels a and b) and forward (at θ = 0°; panels c and d) scattering direction. The DCSs obtained from both uncoupled and coupled surface calculations and those corresponding to the 1-TS and 2-TS paths are shown inside each panels. The 1-TS and 2-TS DCSs are divided by a factor of 2 for a clear presentation of the interference phenomenon.

both uncoupled and coupled surface calculations and those corresponding to the 1-TS and 2-TS paths are shown as a function of the collision energy. Note that these DCSs correspond to the Ω'=0 state of the product H_2 since according to the properties of the reduced Wigner rotation matrix elements $d^J_{\Omega\Omega'}(\theta)$ only Ω'=0 contributes to the DCS at θ = 0° and 180° (Ω=0 in the present case) [62, 63, 233]. It is readily seen from the figure that significant "out-of-phase" oscillations as a function of collision energy occur between the uncoupled and coupled DCSs. Such energy dependent oscillations were observed recently in the backward scattered DCS of H + HD (v=0, j=0) → H_2 (v', j') + D reaction in the work of Xie *et al.* [171]. However, such oscillations can also be

observed in the forward scattering direction as shown in Figure 4.14(c)-(d). Such oscillations are also found in a few more state-to-state DCSs and are not shown here for brevity. These oscillations appear as a result of the interference between the 1-TS and 2-TS paths and the "out-of-phase" behaviour between the uncoupled and coupled DCSs is because of the GP effect which is implicitly included in the coupled surface diabatic treatment. It can be seen that the oscillations are more pronounced at those energies where the 2-TS path contribution has appreciable magnitude. For energies where the 2-TS path has very negligible contribution, the oscillations are not so distinctive. This is true for both the backward and forward scattering. Moreover, the period of the energy dependent oscillations in case of forward scattering is found to be larger than that of the backward scattering.

4.3.1.3 Effect of sum over final states

As it is discussed in Sec 4.3.1.1 and also found in Ref. [160] that the nonadiabatic effects seen in the state-to-state reaction probabilities get washed out in the total reaction probabilities when summed over the final states, it would be interesting to see to what extent the same holds true in case of the DCSs. So, in this section the effect of sum over final states of product on the nonadiabatic effects found in the state-to-state DCSs is discussed. The product vibrational level resolved (summed over j' and Ω') DCSs are shown in Figure 4.15 as a function of θ for reagent H_2 (v=3, j=0) at E_{col} = 0.75 eV and H_2 (v=4, j=0) at E_{col} = 0.57 eV. The DCSs obtained both from the uncoupled and coupled surface calculations are shown for different v' levels of product. The v'-resolved DCSs at a few other collision energies are also calculated but are not shown here as the nonadiabatic effects in these cases is found to be less prominent compared to those shown in Figure 4.15. It can be seen from the figure that the nonadiabatic effects found in the state-to-state DCSs have disappeared substantially upon summing over the j' and Ω' quantum numbers. Nevertheless, there are non-negligible differences between the uncoupled and coupled surface results in form of the "out-of-phase" oscillations in the v'-resolved DCSs. These oscillations are found to occur only in the sideways direction, both in the backward hemisphere (for lower v' levels) and in the forward hemisphere (for higher v' levels).

In order to examine the effect of summation over v' quantum numbers, the initial state-selected total (summed over all v', j' and Ω' levels) DCSs for the reagent H_2 (v=3, j=0) and H_2 (v=4, j=0) are shown in Figure 4.16 as a function of θ. The DCSs

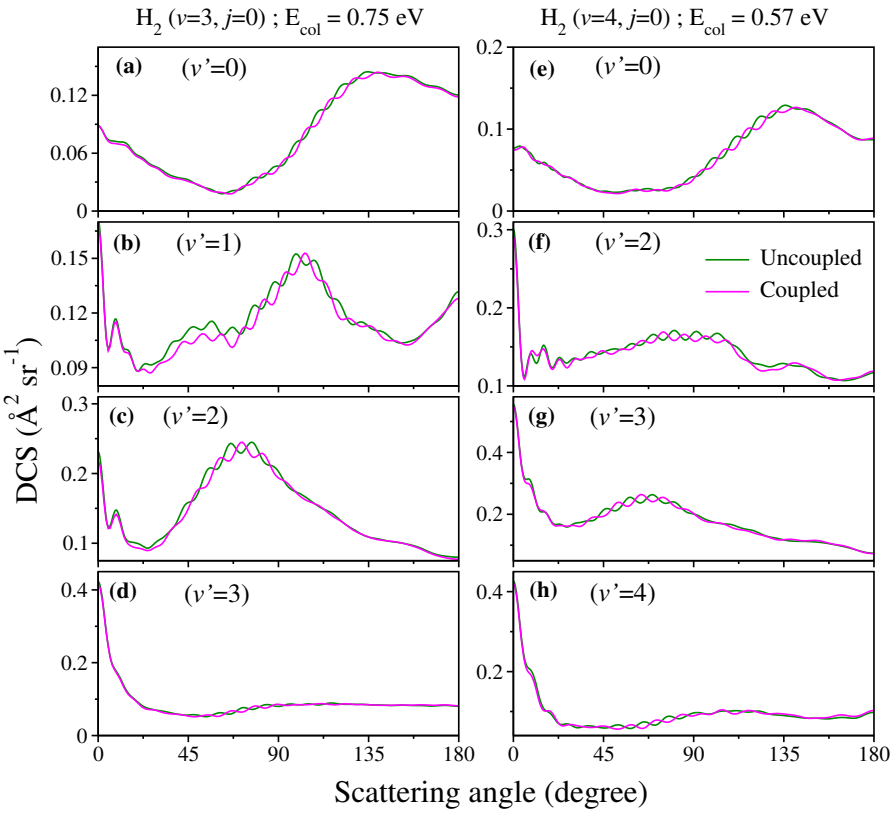

Figure 4.15: Product vibrational level resolved DCSs obtained from both uncoupled and coupled surface calculations of the H + H_2 (v=3,4, j=0) → H_2 (v', $\sum j'$, $\sum \Omega'$) + H reaction as a function of θ at E_{col} = 0.75 and 0.57 eV.

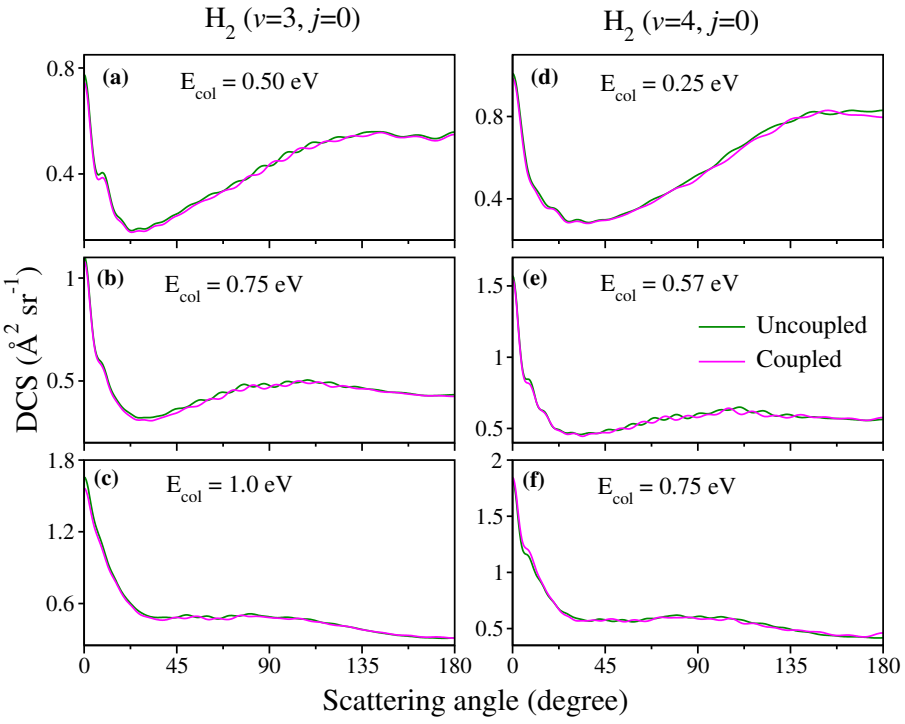

Figure 4.16: Initial state-selected total DCSs obtained from both uncoupled and coupled surface calculations of the H + H_2 (v=3,4, j=0) → H_2 ($\sum v'$, $\sum j'$, $\sum \Omega'$) + H reaction as a function of θ at various collision energies.

obtained both from the uncoupled and coupled surface calculations are shown for different value of collision energies. These collision energies are selected so as to represent the maximum possible nonadiabatic effects in both the (v=3, j=0) and (v=4, j=0) cases of reagent H_2. It can be seen form the figure that the nonadiabatic effects have significantly disappeared in the total DCSs after summing over all the final product states. However, it is surprising to notice that still small differences exists between the uncoupled and coupled surface results particularly in the sideways direction in form of the "out-of-phase" oscillations. This suggests that the interference between the 1-TS and 2-TS paths somewhat survives after summing over all product states resulting the very small nonadiabatic effects in the total DCSs. The 1-TS and 2-TS path contributions to the total DCSs are shown in Figure 4.17 for the reagent H_2 (v=3, j=0) and H_2 (v=4, j=0) as a function of θ at the same collision energies as shown in Figure 4.16. It is seen

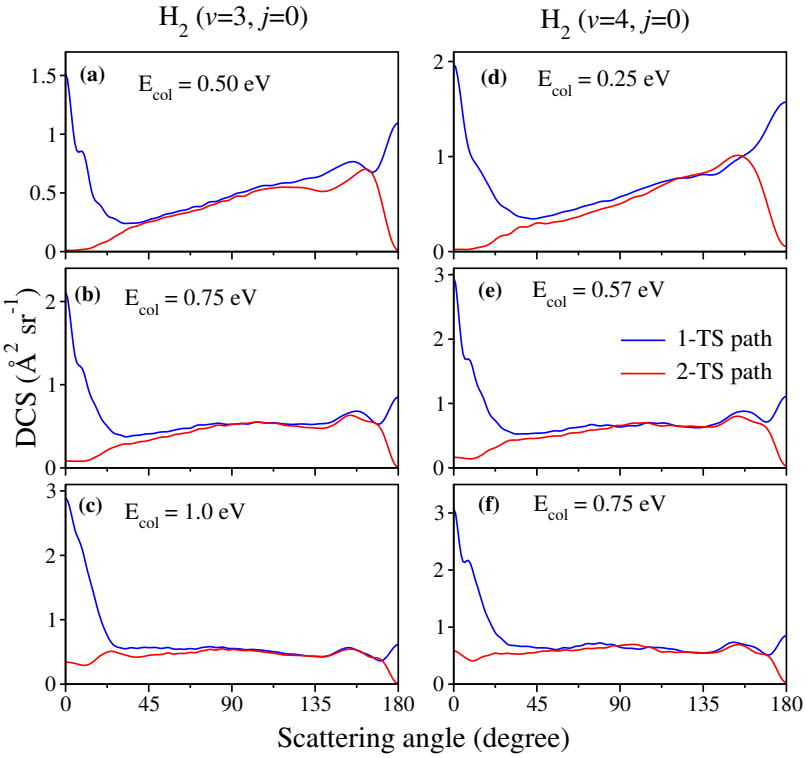

Figure 4.17: Initial state-selected total (summed over all final states) DCSs corresponding to the 1-TS and 2-TS paths for the H + H_2 (v=3,4, j=0) → H_2 ($\sum v'$, $\sum j'$, $\sum \Omega'$) + H reaction as a function of θ at various collision energies.

from the figure that the contribution from 1-TS path mainly dominates the total DCS particularly in the forward and backward directions. However, contribution from the 2-TS path surprisingly has a comparable and sometimes equal magnitude with that from the 1-TS path in the sideways direction. Even though the 2-TS path has fairly significant contribution in the total DCS a very minor nonadiabatic effect is found in the total DCSs

as shown in Figure 4.16. This suggests the cancellation of the nonadiabatic effect (to a considerable extent) in the total DCS can be due to the sum over the product quantum states. So it is clear that there is a role of the summation over final states in cancelling the nonadiabatic effects which is seen both in the case of reaction probabilities (cf. Figs. 4.4 and 4.5) and the DCSs.

4.3.1.4 State-to-state ICSs

In this section the nonadiabatic effect in the state-to-state ICSs is discussed. The ICSs are obtained by integrating the DCSs over θ. The state-to-state ICSs for reagent H_2 (v=3, j=0) and H_2 (v=4, j=0) are plotted in Figure 4.18 in terms of product rotational level distributions at E_{col} = 0.5, 0.57 and 0.75 eV. A few selected state-to-state ICSs are also

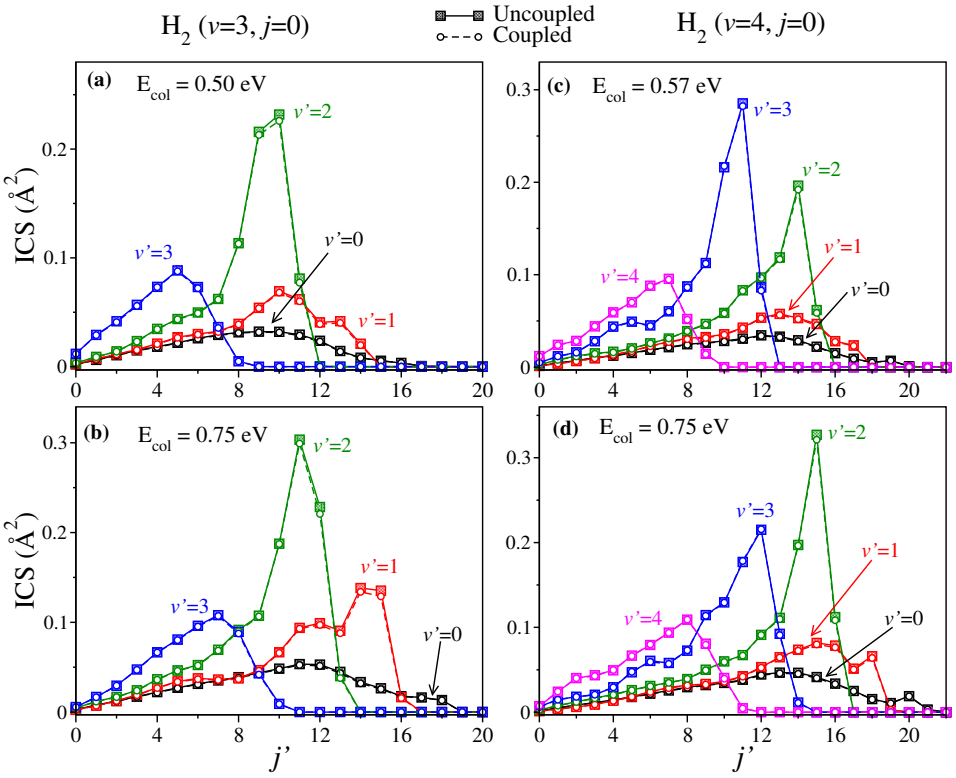

Figure 4.18: Product rotational level distributions for the H + H_2 (v=3,4, j=0) → H_2 (v') + H reaction in terms of ICSs at different collision energies mentioned inside the panels. The distributions for each v' manifold are shown by different colours. The ICSs obtained from both uncoupled and coupled surface calculations are shown by lines of different types and symbols.

presented as a function of collision energy in Figure 4.19 for both H_2 (v=3, j=0) and H_2 (v=4, j=0). The ICSs obtained from both the uncoupled and coupled surface calculation are shown in these figures. It can be seen from the figures that almost no difference

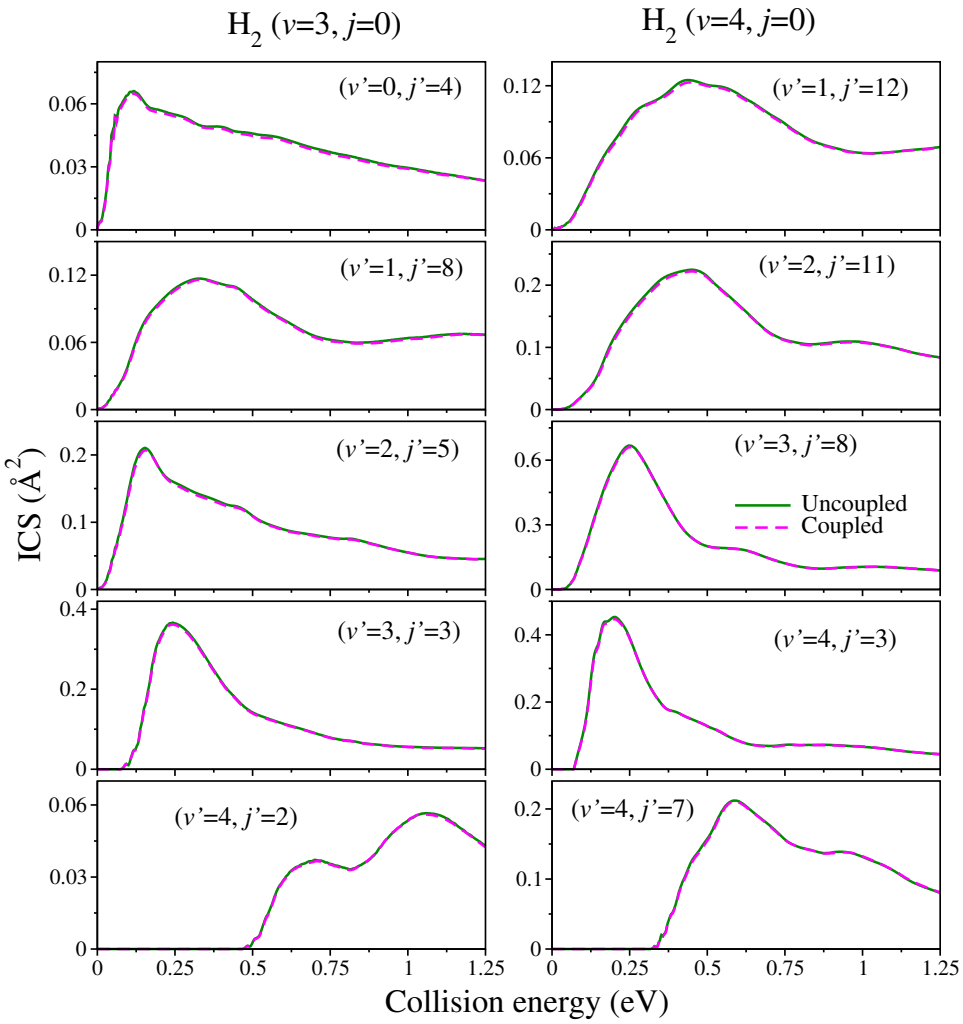

Figure 4.19: Product rotational level resolved state-to-state ICSs obtained from both uncoupled and coupled surface calculations for the H + H_2 (v=3,4, j=0) → H_2 (v', j', $\sum\Omega'$) + H reaction as a function of collision energy for some selected (v', j') levels of product.

exists between the uncoupled and coupled surface results indicating a negligibly small nonadiabatic effect in the state-to-state ICSs. The nonadiabatic effects found in the state-to-state DCSs almost completely disappeared after integrating over θ. In other words, the nonadiabatic effects found in the state-to-state reaction probabilities got washed out in the state-to-state ICSs upon summing over all the partial waves. This observation is similar to that found in case of reagent H_2 (v=0,1, j=0) by Kendrick [158, 159, 202] and Althorpe and coworkers [154, 160] where the GP effect was found to be cancelled in the state-to-state ICSs. The origin of this dramatic cancellation of GP in the state-to-state ICSs have been rigorously explained in Refs. [161, 162]. It was shown that [162] the interference term between the 1-TS and 2-TS paths, which is mainly responsible for the GP effect in state-to-state DCSs, when integrated over θ gives a very minor contribution

to the state-to-state ICSs because of its highly oscillatory natue. The same argument can be used to explain the cancellation of the nonadiabatic effect in the state-to-state ICSs seen above in case of the vibrationally excited reagent H_2 (v=3,4, j=0). As shown in Figure 4.7(c), the interference term, $f_1^* f_2$, for many of the state-to-state transitions with strong nonadiabatic effects, showed such highly oscillating behaviour. It is found that the interference term acquires both positive and negative values and oscillates around zero. Therefore, after integration over θ (with a weight factor of $\sin\theta$) it gives a very small value and hence a negligible contribution to the ICS.

4.3.2 Effect of reagent vibrational excitation (v=0–4) on the scattering dynamics

4.3.2.1 Effect of reagent vibrational excitation on total DCSs

In order to show the effect of reagent vibrational excitation on the overall dynamics the initial state-selected total DCSs for the H + H_2(v=0-4, j=0) reaction are shown in Figure 4.20 in terms of three-dimensional perspective plot as a function of both center-of-mass scattering angle and collision energy. The DCSs for reagent H_2 (v=0-2, j=0) (panels a-c) are obtained from uncoupled surface calculations and that for H_2 (v=3-4, j=0) (panels d-e) are obtained from coupled surface calculations. It can be seen from Figure 4.20(a) that for H_2 (v=0, j=0) the total DCS is dominated by backward scattering and forward scattering appears at higher collision energies. With increase in vibrational excitation of reagent diatom the forward scattering becomes more dominant than the backward scattering and for the higher vibrational level of reagent, H_2 (v=3-4, j=0), a completely forward dominated total DCS can be observed at higher collision energies. Moreover, it can be seen that for reagent H_2 (v=0-3, j=0), the threshold for the forward scattering appears at higher energy as compared to the backward scattering. The difference between the thresholds of forward and backward DCSs is found to decrease with vibrational excitation of the reagent diatom. The threshold energies for both forward and backward DCSs for reagent H_2 (v=4, j=0) tend to zero suggesting a barrierless nature of the reaction for highly vibrationally excited reagent. The forward scattering DCS increases with increase in collision energy for reagent H_2 (v=0-4, j=0), however, the backward scattering DCS first increases and then decreases slowly at higher collision energies after attaining a maximum. Hence it can be said that the increase in reactivity in the ICSs with reagent vibrational excitation mainly comes from the forward scattered products. It can also be seen that for H_2 (v=2-4, j=0), the variation of the forward and

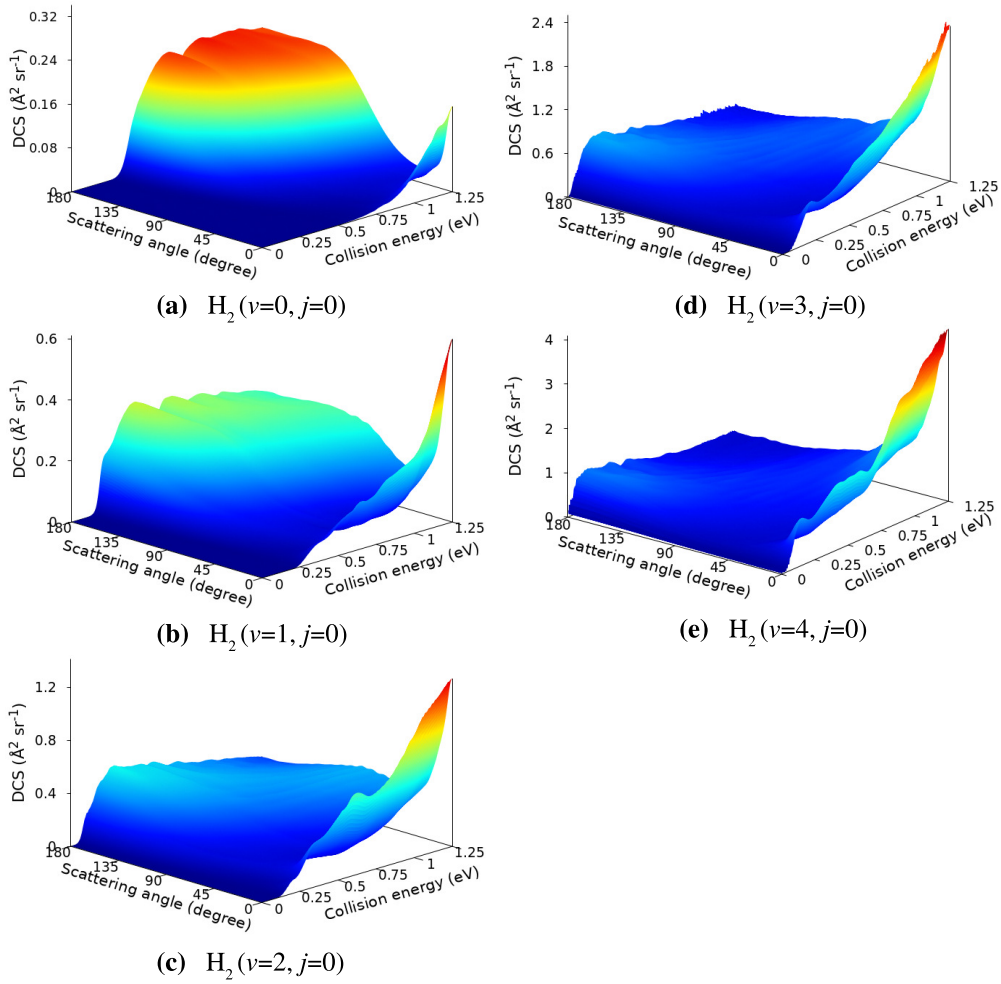

Figure 4.20: Three-dimensional perspective plot of initial state-selected total DCSs for the H + H_2 (v=0-4, j=0) → H_2 ($\sum v'$, $\sum j'$, $\sum \Omega'$) + H reaction as a function of collision energy and center-of-mass scattering angle (θ). The DCSs for reagent H_2 (v=0-2, j=0) are obtained from uncoupled surface calculations and that for H_2 (v=3-4, j=0) are obtained from coupled surface calculations.

backward scattering DCSs as a function of collision energy is qualitatively similar for different vibrational level of reagent H_2 irrespective of the magnitude of the DCS.

As it is well understood that for reagent H_2 (v=0, j=0) the forward scattering in hydrogen exchange reaction stems from the time-delayed mechanism involving contributions from higher total angular momentum. However, the question remains whether the overall scattering mechanism of the reaction with vibrationally excited reagent will be any different from that with reagent H_2 (v=0, j=0). In order to understand the origin of forward and backward scattering, the J-dependent partial DCSs are calculated for each vibrational level of reagent. The total (summed over final states) J-dependent partial DCSs at θ = 0° and 180° (corresponding to forward and backward scattering, respectively) are shown in Figure 4.21 for reagent H_2 (v=0, 2, 4, j=0). These partial

DCSs are shown in terms of colour map plots as a function of E_{col} and J in order to understand the contribution of each partial wave at different collision energies. The J-dependent partial DCSs for reagent H_2 (v=1, 3, j=0) are not shown here as a similar trend is followed from v=0 to 4.

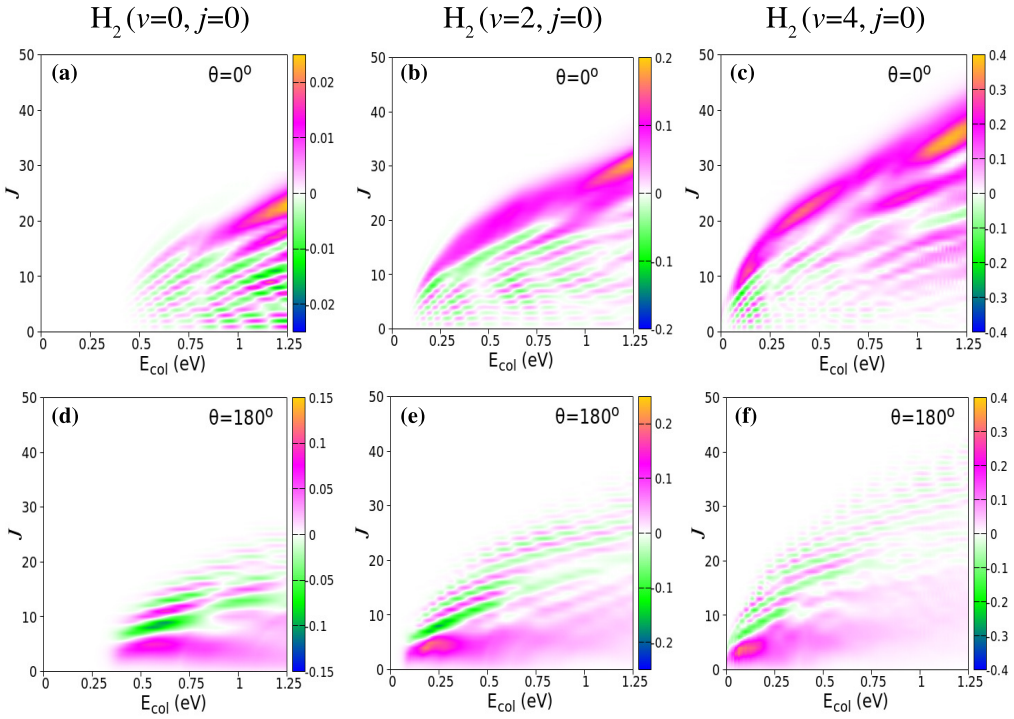

Figure 4.21: Total (summed over final states) J-dependent partial DCSs for the H + H_2 (v=0, 2, 4, j=0) → H_2 ($\sum v'$, $\sum j'$, $\sum \Omega'$) + H reaction as a function of E_{col} (abscissa) and J (ordinate) at θ = 0° (panels a-c) and 180° (panels d-f) corresponding to forward and backward scattering, respectively. The partial DCSs for reagent H_2 (v=0,2, j=0) are obtained from uncoupled surface calculations and that for H_2 (v=4, j=0) are obtained from coupled surface calculations.

It can be seen from Figure 4.21 that the forward scattering mainly comes from the higher partial waves and backward scattering from the lower partial waves. Most importantly this is same for each vibrational level of the reagent. In case of forward scattering the partial waves closer to J_{max} (the maximum value of J to obtain the converged cross section at a particular E_{col}) contribute significantly to the DCS at θ = 0°. Note that the value of the J_{max} increases with increase in E_{col}. In addition, the contribution of higher Js towards forward scattering increases with increase in collision energy. However, this is opposite in case of backward scattering where the contribution of lower Js decreases with increase in collision energy. It is known from the knowledge of the opacity function of the H + H_2 reaction that as collision energy between the reagents increases contribution of any particular higher J towards the overall reactivity increases

[227, 234]. However, for any lower value of J it remains almost same with change in collision energy [227, 234].

For instance, consider the case of H_2 (v=4, j=0). For J = 28 the weighted partial wave contribution $(2J + 1)P(J; E)$ to the cross section is 16.66, 31.83 and 39.21 at E_{col} = 0.75, 1.0 and 1.25 eV. However, the $(2J + 1)P(J; E)$ values are 14.96, 15.96 and 16.31 for J = 9 at the same collision energies (cf. Figure 4.22). Moreover, as collision energy increases more and more higher partial waves contribute to the overall reactivity. Since the higher J corresponds to forward scattering, the DCS at $\theta = 0°$ increases with increase in collision energy. The backward scattered DCS decreases with increase in collision energy as it corresponds to lower Js. The same analogy can be applied towards the increase in forward scattering with increase in reagent vibrational excitation. In this case at a fixed value of E_{col} the weighted partial wave contribution for any particular higher J increases significantly with increase in reagent vibrational excitation, however, the same increases only mildly for any lower value of J (cf. Figure 4.22). In addition, the maximum number of J to obtain the converged cross section at a particular E_{col} increases with increase in reagent vibrational excitation [227]. This explanation also clarifies the higher threshold values of forward scattering than the backward one for reagent H_2 (v=0-3, j=0).

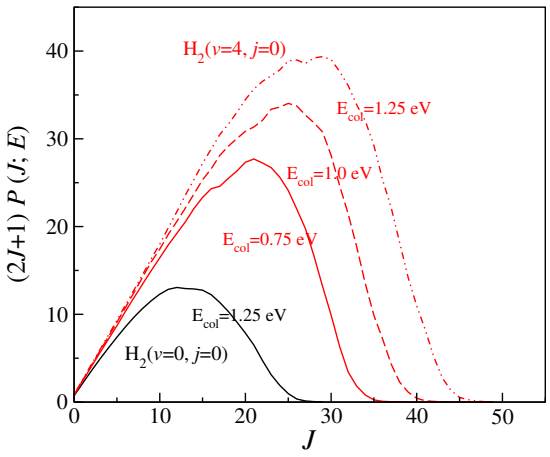

Figure 4.22: $(2J+1)$ weighted opacity functions for H_2 (v=0, j=0) and H_2 (v=4, j=0) at three different collision energies.

We reiterate here that in the calculation of J-dependent partial DCSs the cross terms are included in the equation 2.55 in order to ensure the full coherence among all the partial waves. This may lead to constructive and destructive interference between the partial waves which corresponds to the positive and negative values of the J-dependent partial DCSs. This can be seen from Figure 4.21 as magenta and green coloured stripes. It can be seen that in contrast to a small set of J, a broad range of J actually contributes to the forward and backward scattered DCS through interference. However, their collective effect wil be minimal once they are summed up. It can be observed that the interference both at forward and backward scattering is strong in case of H_2 (v=0, j=0) and it gets weaker with increasing reagent vibrational excitation.

4.3.2.2 Product vibrational level resolved DCSs and energy disposal of angle resolved products

The effect of reagent vibration on the product vibrational level resolved DCSs is presented in Figure 4.23. Here, the v'−resolved DCSs are shown in terms of product vibrational level distribution for fixed value θ at 0° and 180°, corresponding to forward and backward scattering respectively, at different collision energies. For reagent H_2 (v=3,4, j=0), the solid lines in panels (c), (d), (g) and (h) represent the DCSs obtained from coupled surface treatment. The uncoupled surface results are also shown by dashed lines for the sake of comparison. It can be seen from the Figure that for reagent H_2 (v=1,

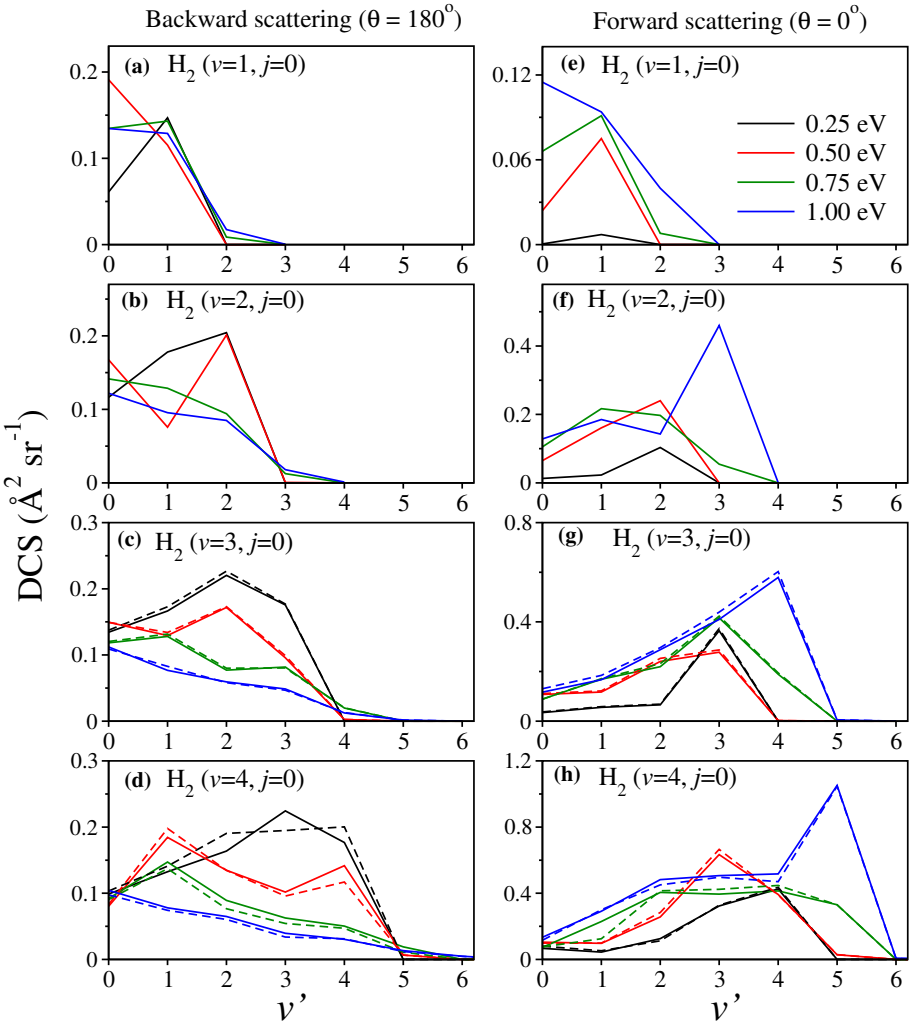

Figure 4.23: Product vibrational level distributions in terms of DCS at θ = 180° (panels a-d) and 0° (panels e-h) for the H + H_2 (v=1-4, j=0) → H_2 (v', $\sum j'$, $\sum \Omega'$) + H reaction at E_{col} = 0.25, 0.50, 0.75 and 1.0 eV shown by lines of different colours. The coupled and uncoupled surface results for reagent H_2 (v=3-4, j=0) (panels c, d, g and h) are shown by solid and dashed lines, respectively, whereas the uncoupled surface results for reagent H_2 (v=1-2, j=0) (panels a, b, e and f) are shown by solid lines.

j=0), both the forward and backward scattered products are formed most probably in the v'=1 level maintaining the vibrational adiabaticity (although not fully) except for E_{col} = 0.5 eV at θ = 180° and E_{col} = 1.0 eV at θ = 0°, where the v'=0 level is found to be the most probable one. However, with increase in reagent vibrational excitation a few important observations can be made. First, at fairly lower value of collision energies both the forward and backward scattered products are most probably formed in the higher v' levels (v' being same as or close to v) in case of the vibrationally excited reagent. Second, at higher collision energies, the backward scattered products predominantly formed in the lower v' levels exhibiting a statistical vibrational distribution. However, the forward scattered products predominantly formed in the higher v' levels where the most probable v' in some cases is even greater than the corresponding v. As can be seen from Figure 4.23(f)-(h) that at E_{col} = 1.0 eV the most probable v' for reagent H_2 (v=2-4, j=0) is v+1. This interestingly showcases a certain type of opposite behaviour between the forward and backward scattered products in vibrational energy disposal at higher collision energies. This strong dependence of the forward and backward scattered vibrational distributions on the collision energy is also found for other forward and backward angles. It is found that increase in collision energy in case of vibrationally excited reagent reduces the vibrational excitation in case of the backward scattered products to a large extent but not in case of forward scattered products. This as a consequence raises the question that where does the lost vibrational energy go as the total energy to be conserved. This is answered in the next paragraph. Moreover, the $v'-$resolved $J-$dependent partial DCSs are calculated at θ = 0° and 180° (not shown here for brevity) in order to understand the partial wave contribution to the forward and backward scattering. It is found that similar to the total DCSs the forward scattering in $v'-$resolved DCSs mainly comes from the higher partial waves and the backward scattering from the lower partial waves.

In order to understand further the energy disposal in angle-resolved products, the average fraction of the total available energy entering into product vibration, rotation and relative translation are calculated individually for products scattered at θ = 0° and 180°. The results are shown in Figure 4.24 for reagent H_2 (v=4, j=0) where the $\langle f' \rangle$ values are plotted as a function of collision energy. It can be seen that in case of forward scattering [cf. panel (b)] a larger portion of the available energy goes into product vibration which is almost 70% at E_{col} = 0.25 eV and varies up to 52% at E_{col} = 1.25 eV. This is consistent with the fact that the forward scattered products are formed in the vibrationally excited levels both at lower and higher collision energies in case of vibrationally excited reagent as seen in Figure 4.23. The average fraction of available energy

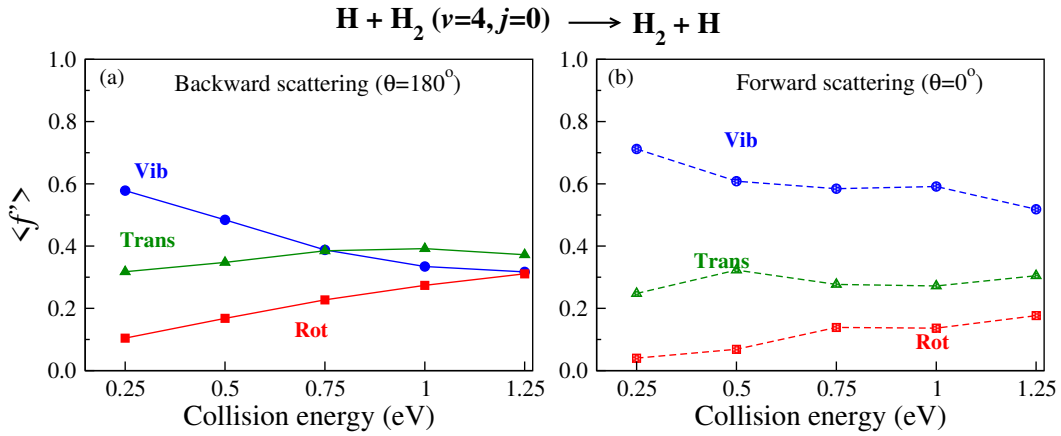

Figure 4.24: Average fractions of the total available energy entering into product vibration, rotation and relative translation shown individually for the products scattered at θ = 180° (solid line) and θ = 0° (dashed line) for the H + H_2 (v=4, j=0) → H_2 + H reaction as a function of collision energy.

entering into products' relative translation is relatively less as compared to vibration and varies in an average of 30% throughout the collision energy from 0.25 to 1.25 eV. The fraction of energy entering into product rotation is the least among all which varies from 4% at E_{col} = 0.25 eV to almost 18% at E_{col} = 1.25 eV. The situation is however quite different in case of backward scattering [cf. panel (a)]. It can be seen that the fraction of available energy going into product vibration is significantly reduced as compared to the case of forward scattering and the reduction is the largest at higher collision energies. It can also be noticed that the $\langle f_V' \rangle$, $\langle f_R' \rangle$ and $\langle f_T' \rangle$ values come quite close to each other at E_{col} = 1.25 eV. This showcases an almost equal partitioning of the total available energy into product vibration, rotation and relative translation in case of the backward scattered products at higher collision energies. This equipartitioning of the available energy can be related to the statistical vibrational distribution of the backward scattered products at higher collision energies as seen in Figure 4.23(b)-(d). At low collision energies however the fraction of energy going to product vibration remains at highest then relative translation and then rotation. Moreover, the fraction of energy going to product rotation and relative translation for backward scattered products increases in comparison to the forward scattering. This comes as in expense of the reduction of vibrational energy disposal in backward scattered products. Hence, it is safe to assume that the loss in the vibrational energy disposal in case of the backward scattered products is transfered to product rotation and relative translation; little more to rotation than translation. It is to be noted here that the $\langle f' \rangle$ values are also calculated for other forward and backward scattering angles, and it is found that their corresponding energy disposal is similar to that seen at θ = 0° and 180°.

So it is clear that there exists two scenarios depending upon whether the reagent diatom, particularly vibrationally excited, encounters a slow collision or a relatively faster collision with the attacking atom. It is found in earlier studies that with increasing reagent vibrational excitation the threshold for the reaction decreases [227] and for H_2 (v=4) it behaves like barrierless *i.e.,* zero threshold [165, 189]. However, when the reaction asseses higher partial waves or equivalently high impact parameter collisions, dynamical barriers can be formed corresponding to the higher orbital angular momentum even for the higly vibrationally excited reagent which can slow down the incoming atom to some extent as a consequence of converting a part of its relative translational energy to the centrifugal energy. The products formed in such cases are forward scattered as discussed in section 4.1.2 and reported in Refs. [143, 146, 219]. Now, a slow collision is very much unlikely to disrupt the vibrational motion of the reagent diatom as compared to a fast collision. Hence, the products formed from the slow collisions (low collision energy) are more likely to retain the reagent diatom's vibrational energy both in case of forward and backward scattering. The disruption in fact would be more when the fast collisions are mediated by low impact parameters (or lower partial waves) where they barely face any dynamical barriers. This explains why at higher collision energies the reagent vibrational energy could not efficiently be converted into product vibrational energy in case of backward scattered products [cf. Figure 4.23(b)-(d) and 4.24(a)]. However, in case of forward scattering dominated by higher partial waves, the dynamical centrifugal barriers may cause the slow down of the fast moving attacking atom where the disruption of reagent vibrational motion would not be effective and the reagent vibrational energy can be efficiently converted into product vibrational energy [cf. Figure 4.23(f)-(h) and 4.24(b)].

4.3.2.3 Effect of reagent vibration on product rotational level resolved DCSs

The effect of reagent vibration on the product rotational level resolved DCSs is presented and discussed in this section. The $j'-$resolved state-to-state DCSs are presented here in terms of gradational contour map as function of θ along the abscissa and j' along the ordinate. The $j'-$resolved DCSs of the H + H_2 (v=0-4, j=0) $\rightarrow$ H_2 (v'=0, j') + H reaction is shown in Figure 4.25 for E_{col} = 0.5 eV and in Figure 4.26 for E_{col} = 0.75 eV. The individual figures show the DCSs for a particular product vibrational manifold and for different reagent vibrational level so as to indicate the effect of reagent vibrational excitation.

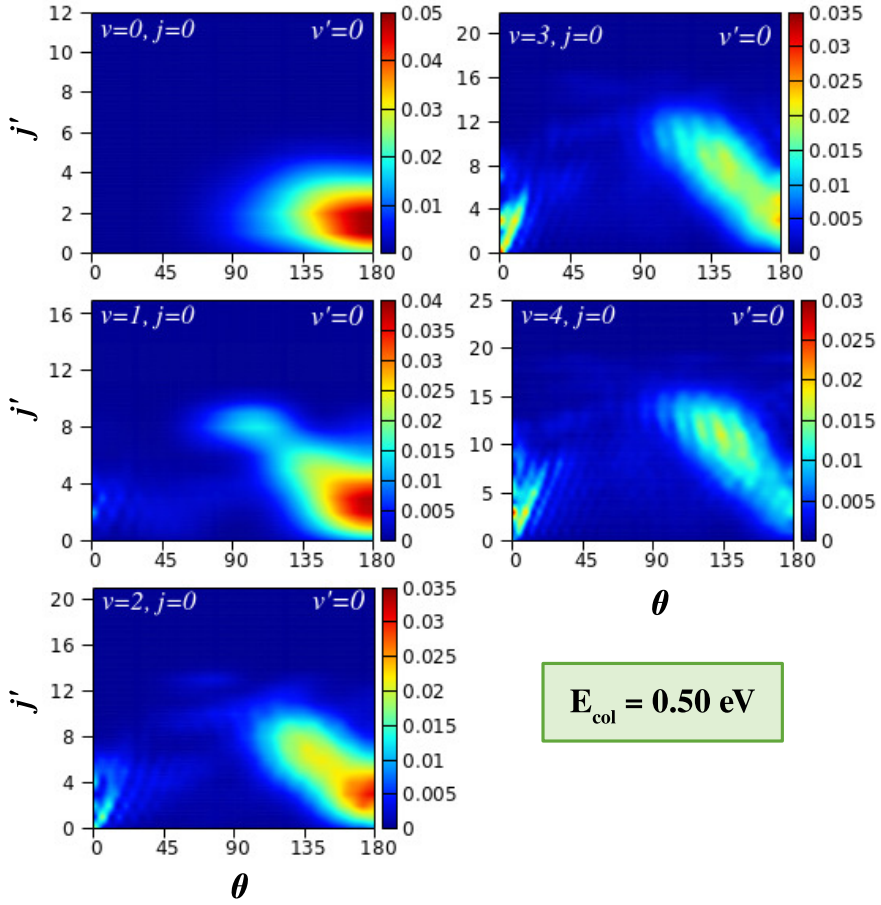

Figure 4.25: Product rotational level resolved state-to-state DCSs of the H + H_2 (v=0-4, j=0) → H_2 (v'=0, j') + H reaction as a function of j' and θ at E_{col} = 0.5 eV.

It can be seen from Figure 4.25 that for reagent H_2 (v=0, j=0) the DCSs are dominated by backward scattering with the peak of the angular distribution, θ_{peak} close to 180°. Moreover, the products are formed in the lower rotational levels, within j' = 4. This behaviour, that is, backward scattering with low rotational excitation of product diatom supports the conventional rebound or direct recoil mechanism, where a head-on collision between the reagent atom and diatom with very low impact parameter (b or J ≈ 0) results in backward scattered products with very low rotational excitation. Such mechanisms which are dominant at low collision energy, access the collinear transition-state and are a consequence of the MEP of the H + H_2 reaction. It is to be noted here that the collision energy 0.5 eV is very close to the threshold energy of the (v=0, j=0) vibrationally adiabatic potential. With the successive vibrational excitation of the reagent diatom at the same collision energy it can be seen that the backward scattering found in H_2 (v=0, j=0) now gradually changes to sideways scattering (but in the backward hemisphere). These sideways scattered products are now rotationally excited and the rotational excitation increases with increase in reagent vibrational excitation. For the

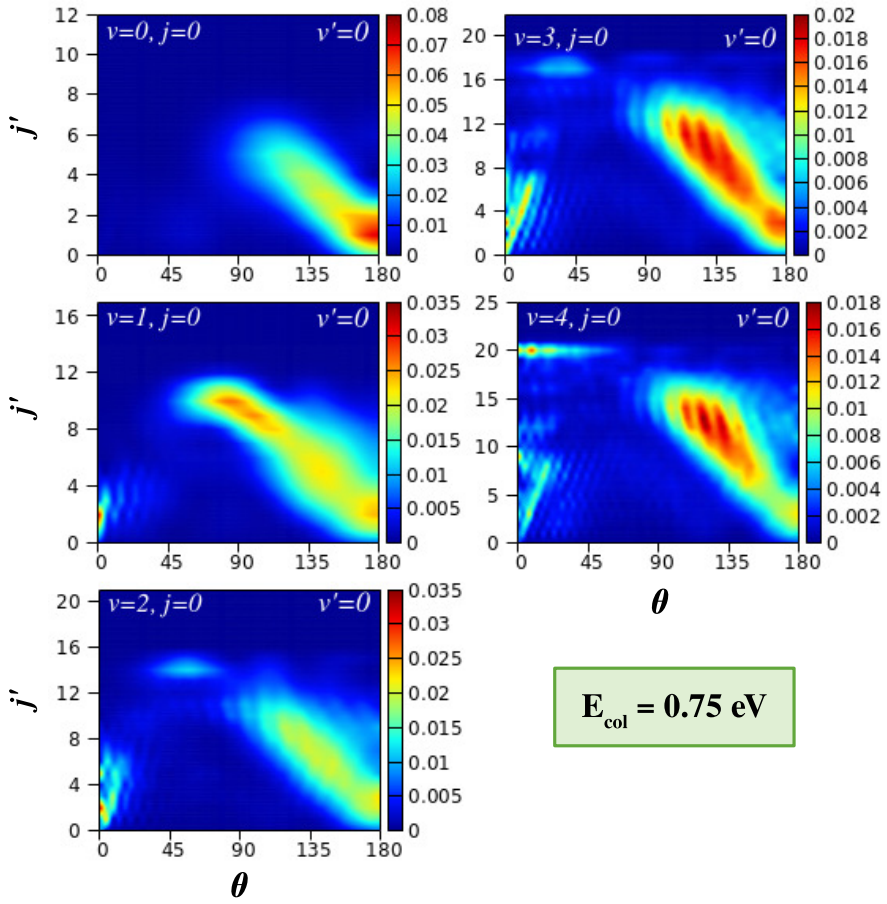

Figure 4.26: Same as in Figure 4.25, but for E_{col} = 0.75 eV.

highly vibrationally excited reagent H_2 (v=3-4, j=0), it can be seen that a relatively large range of product rotational levels are populated and the peak value of the angular distribution decreases as the j' quantum number increases. Such phenomenon is well known in the H + H_2 reaction dynamics [188, 222, 223] and has been termed as "*negative* $j' - \theta$ *correlation*" [224]. It is believed that the rotationally excited products those scatter into the sideways direction of backward hemisphere results from the glancing collision [222, 223]. This means that the head-on or zero-impact-parameter collisions lead to rotationally cold products in the extreme backward direction, and as the impact parameter increases the collisions become more glancing which leads to rotationally excited products in the sideways direction. This phenomenon has been found in the crossed molecular beam experiment of H + D_2 (v=0, j) → HD (v', j') + D reaction [188, 204, 222–224] and recent experimental work on the H + HD (v=0, j=0) → H_2 (v', j') + H reaction [235] at various collision energy ranging from low to high. It is important to note here that the transition to such mechanism, from the conventional rebound, generally occurs when the collision energy between the reagents increases, as it is well established in the literature for the case of (v=0, j=0) level of reagent diatom

[204, 222, 223]. This can be understood in the present case by comparing the (v=0, j=0) panels of Figure 4.25 and 4.26, where the latter displays the j'−resolved DCSs at little higher collision energy of 0.75 eV. At this energy, in addition to the rebound mechanism for the low j' levels, the glancing collision mechanism also appears for higher j' states showcasing the "*negative* $j' - \theta$ *correlation*" for H_2 (v=0, j=0). The gradual transition of the mechanism is due to the fact that with increase in collision energy the colliding partners can access the region of high impact parameter and hence can undergo glancing collisions. However, in the present study it is found that the transition of the mechanism from rebound to glancing can also occur by increasing the vibrational energy of the reagent diatom at the same collision energy (cf. Figure 4.25). This is supported by the fact that the reaction is dominated by higher partial waves in case of vibrationally excited reagent as compared to the case of H_2 (v=0, j=0) at the same value of collision energy, which is already discussed in Section 4.3.2.1 (cf. Figure 4.22).

The j'−resolved DCSs at E_{col} = 0.75 eV (cf. Figure 4.26) show strong dependence between j' and θ as compaed to that at E_{col} = 0.5 eV (cf. Figure 4.25) for each of the reagent vibrational level. The correlation between the impact parameter b, j' and θ_{peak} in case of the glancing collision mechanism has been qualitatively explained by the line-of-centers nearly elastic specular scattering model (LOCNESS) [222, 223]. This model predicts a linear correlation between the cosine of the most probable scattering angle and the square of the reduced impact parameter (b^2/b^2_{max}; b_{max} being the maximum impact parameter) by considering the colliding entities as hard-spheres (see Ref [222] for more details). Now it is well known that the impact parameter is directly proportional to the orbital angular momentum which is equal to the total angular momentum J for j=0 case. Moreover, according to the kinematic constraints the rotational angular momentum of product diatom has an approximately linear relation (directly proportional) with the initial orbital angular momentum for collinearly dominated reactions such as H + H_2 with vibrationally and/or rotationally cold reagents [236]. Hence, for this reaction, J and j' or more precisely b and j' has an approximately linear relation. This suggests that according to the LOCNESS model $\cos\theta_{peak}$ and j'^2 should have an approximately linear correlation between them. This in fact has already been shown in case of the other isotopic variants of this reaction where the reagent diatom is in its ground rovibrational level [188, 222, 223, 235].

In order to understand the present scenario in a similar spirit the correlation among θ_{peak}, j' and J in case of the glancing collision mechanism (in the backward hemisphere) at E_{col} = 0.75 eV for H_2 (v=3, j=0) and product v'=0 is examined here. More precisely,

the correlation between j' and θ_{peak}, and that between j' and J_{peak} are considered. The J_{peak} here denotes the most dominant peak value of J in the state-to-state opacity function. The J_{peak} and θ_{peak} values are extracted from the respective opacity function and state-to-state DCSs for different values of j'. The correlation between $\cos\theta_{peak}$ and j'^2, and that between j' and J_{peak} are plotted in Figure 4.27(a) and (b), respectively. It can

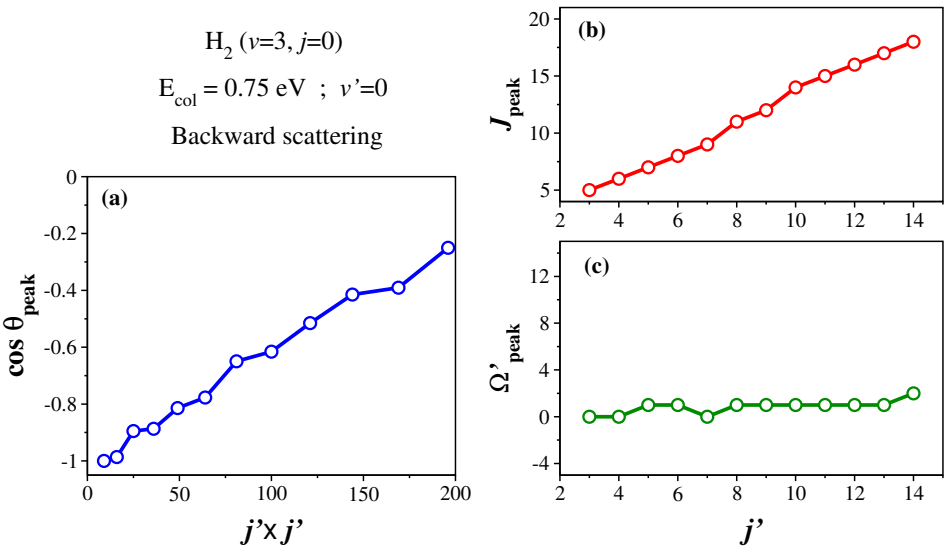

Figure 4.27: Correlation between the cosine of the peak value of the scattering angle, θ_{peak} and square of the rotational quantum number j' (panel a), J_{peak} and j' (panel b), and Ω'_{peak} and j' (panel c) in the backward scattering of the H + H_2 (v=3, j=0) → H_2 (v'=0, j') + H reaction at E_{col} = 0.75 eV.

be seen that the cosine of θ_{peak} values and j'^2 have an approximately linear correlation. This observation is in line with the LOCNESS model. Moreover, the J_{peak} and j' quantum numbers also have an approximately linear correlation [cf. Figure 4.27(b)] suggesting the lower j' products are formed from low J and higher j' products from high J collisions which falls under the prediction of the above model. In addition to the $\cos\theta_{peak} - j'^2$ and $J_{peak} - j'$ correlation, the relationship between the product rotational angular momentum and its most probable helicity state (represented by the projection quantum number, Ω'_{peak}) is also evaluated for each j' state. The Ω'_{peak} values are extracted by plotting the state-to-state DCSs as a function of Ω' at the corresponding θ_{peak} values of each j' and then selecting the most probable Ω' quantum number. The correlation between the Ω'_{peak} and j' is shown in panel (c) of Figure 4.27. It can be seen that unlike the θ_{peak} and J_{peak}, the Ω'_{peak} values are almost independent of the corresponding j' quantum number and tend to be in the lowest possible helicity states. This happens even for the highly rotationally excited product states e.g. Ω'_{peak}=1 for j'=13. This indicates that the rotational angular momentum vector of product diatom preferentially remains perpendicular to the products' recoil direction suggesting an almost

coplanar detachment mechanism. This finding is also in accordance with the kinematic constraints predictions for the collinearly dominated encounters in the H + H_2 reaction as described in Ref. [236]. It is worthwhile to note here that similar type of correlation among θ_{peak}, J_{peak}, Ω'_{peak} and j' has been found in case of other vibrational level of reagent.

It is surprising to notice that the present behaviour of the rotationally excited product in the sideways direction for vibrationally excited reagent has a remarkable resemblance with the prediction of the LOCNESS model, even though the underlying presumption of the kinematic constraints of Ref. [236] is applicable only for vibrationally and/or rotationally cold reagents. This resemblance between the present numerically exact quantum scattering results and the prediction of the above model suggests that the dynamics of the sideways scattered products from the vibrationally excited reagent can be understood by the help of the LOCNESS model. Therefore, it can be said that the scattering of these products in the backward hemisphere follows the similar glancing collision mechanism as that found in case of ground rovibrational level reagent.

In addition to the backward scattering and the sideways scattering in the backward hemisphere, it can be seen from the Figures 4.25 and 4.26 that forward scattering appears with successive vibrational excitation of the reagent diatom. There is no forward scattering for the reagent H_2 (v=0, j=0) at the two collision energy considered in the figures, however, it appears with increasing collision energy [cf. Figure 4.20(a)]. The forward scattering is seen for low j' product states and becomes more prominent with increasing reagent vibrational excitation at the same value of collision energy. The lowest j' product states are peaked at the extreme forward direction ($\theta \simeq 0°$), and with increasing the j' quantum number it is seen that the peak value of the forward angular distribution gradually shifts towards the sideways direction (but in the forward hemisphere). This results in a situation where the θ_{peak} value increases with increasing the j' quantum number in the forward scattering region. This phenomenon can be dubbed as "*positive* $j' - \theta$ *correlation*" in the forward scattering. In the present investigation this phenomenon is found in case of vibrationally hot reagent at relatively low collision energy and also for vibrationally cold reagent at relatively high collision energy. In some situation this is also found in case of vibrationally excited products. In contrast to the "*negative* $j' - \theta$ *correlation*" in the backward hemisphere, a relatively low number of product rotational states are populated in the forward scattering which is why it does not extend to the extreme sideways region. Moreover, in contrast to the broad angular distribution in the backward hemisphere, which originate from a broad range of impact

parameters, the forward scattering angular distributions are found to be narrow and are dominated by angular oscillations.

Similar to the analysis done in case of the glancing collision mechanism (cf. Figure 4.27), the correlation among θ_{peak}, j', J_{peak} and Ω'_{peak} is examined here for the "*positive* $j' - \theta$ *correlation*" in the forward scattering in case of reagent H_2 (v=3, j=0) and product v'=0 at E_{col} = 0.75 eV. The results are plotted in Figure 4.28. Note that instead of the cosine of the θ_{peak}, the value of the θ_{peak} is plotted against the j' quantum number. The

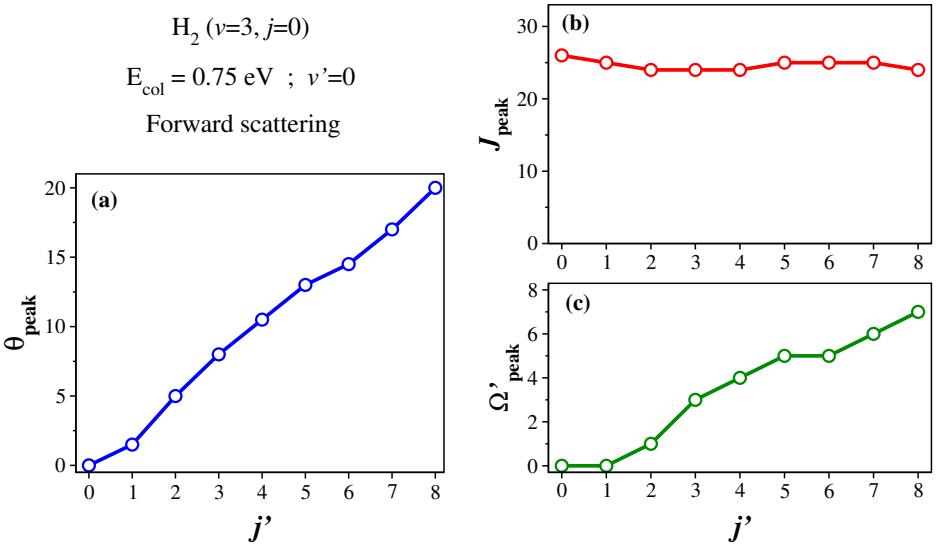

Figure 4.28: Correlation between the peak value of the scattering angle, θ_{peak} and the rotational quantum number j' (panel a), J_{peak} and j' (panel b), and Ω'_{peak} and j' (panel c) in the forward scattering of the H + H_2 (v=3, j=0) → H_2 (v'=0, j') + H reaction at E_{col} = 0.75 eV.

J_{peak} values are extracted here from the J−dependent partial DCSs, instead of the state-to-state opacity functions, by plotting them against J for the corresponding θ_{peak} for each j'. The θ_{peak} and Ω'_{peak} values are extracted in a similar fashion as that is done in the analysis of the glancing collision mechanism. It can be seen from Figure 4.28(a) that the θ_{peak} values and the j' quantum number have an approximately linear correlation qualitatively similar to that seen in the "*negative* $j' - \theta$ *correlation*" in the backward hemisphere. This suggests that the rotationally excited products going to the forward hemisphere tend to scatter into the sideways region but not too far from the extreme forward direction. In contrast to the Figure 4.27(b), the correlation between J_{peak} and j' here is not linear as can be seen from the panel (b) of Figure 4.28. Rather, the J_{peak} values are almost independent of the j' quantum number and acquire the highest possible values. This suggests that unlike the glancing collision mechanism, both the rotationally excited and rotationally cold forward scattered products are formed from

a similar type of high impact parameter collisions. In order to understand further, the correlation between the Ω'_{peak} and j' is plotted in panel (c) of Figure 4.28. It can be seen that the Ω'_{peak} values have an almost linear relation with the j' quantum number and tend to possess the highest possible helicity quantum number. This indicates that the most dominant contribution to the "*positive* $j' - \theta$ *correlation*" comes from those helicity states whose quantum number lie close to the value of the corresponding j' quantum number. In such cases the rotational angular momentum vector of product diatom preferentially remains parallel to the products' recoil direction while departing from the triatomic complex. This suggests a non-coplanar detachment mechanism for the forward scattered products those are relatively rotationally excited.

Hence, it is the helicity state of the product rotational angular momentum which is responsible for the "*positive* $j' - \theta$ *correlation*" observed in the forward scattering. This is in contrast to the "*negative* $j' - \theta$ *correlation*" in the backward hemisphere where the orbital angular momentum or the impact parameter was actually responsible. Moreover, the underlying mechanisms of the two $j' - \theta$ correlations are in contrast with each other. One undergoes a coplanar detachment mechanism with glancing collisions (negative $j' - \theta$), whereas the other undergoes a non-coplanar detachment mechanism involving high impact parameter collisions (positive $j' - \theta$). These two contrasting scenarios are shown in Figure 4.29 in terms of cartoon diagrams.

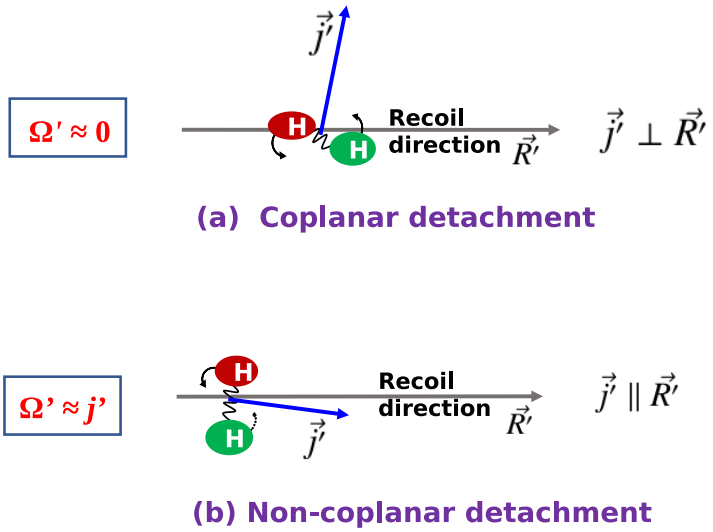

Figure 4.29: Cartoon diagrams showing the two contrasting mechanisms in the "negative $j' - \theta$" in backward scattering and in the "positive $j' - \theta$" in forward scattering of the $H + H_2 \rightarrow H_2 + H$ reaction.

4.3.3 Effect of rotational excitation of the reagent diatom H_2 (v=0, j=0−3)

The effect of reagent rotational excitation, up to j=3 in its v=0 vibrational level, on the H + H_2 reaction dynamics is discussed here. It is worthwhile to mention here that all the calculations for rotationally excited reagent are performed only on the lower adiabatic surface of BKMP2 PES without including the explicit surface coupling since the CI is not accessible within the energy range considered here. The initial state-selected total (summed over final states) reaction probability for J=0 and ICSs for the H + H_2 (v=0, j=0−3) reaction are shown in Figure 4.30 as a function of collision energy. The results

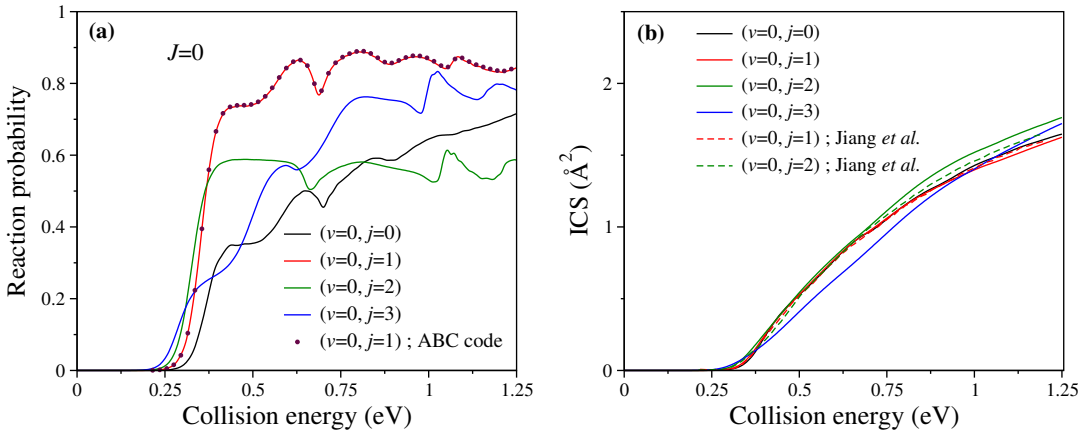

Figure 4.30: Initial state-selected total (summed over final states) reaction probabilities for J=0 (panel a) and ICSs (panel b) for the H + H_2 (v=0, j=0−3) → H_2 ($\sum v'$, $\sum j'$, $\sum \Omega'$) + H reaction as a function of collision energy. The reaction probability for H_2 (v=0, j=1) calculated by the present TDWP method is compared with that calculated by the ABC code [237] in panel (a). The ICSs for reagent H_2 (v=0, j=1−2) are compared with the result of Jiang *et al.* [123] in panel (a).

for different rotational level of reagent are shown by lines of different colours. In order to compare with the available literature data, the ICSs of Jiang *et al.* [123] for reagent H_2 (v=0, j=1−2) (cf. Figure 3 of Ref. [123]) are digitized and plotted in panel (b) of Figure 4.30 in terms of dashed lines. A very good agreement between the present results and those of Jiang *et al.* can be seen despite some differences at higher energies. Moreover, the total reaction probabilities for reagent H_2 (v=0, j=1) are calculated within a collision energy of 1.25 eV by means of a TIQM method as implemented in the ABC code [237] in order to cross-check the present results (see Table 4.2 for the parameters used in the TIQM calculation). The TIQM results are plotted in panel (a) of Figure 4.30 in terms of filled circles. An excellent agreement between the present TDWP and the TIQM probabilities can be seen which validates the present results and convergence of the TDWP numerical parameters for rotationally excited reagents.

The effect of reagent rotation on the overall reactivity of the H + H_2 reaction can also be deduced from Figure 4.30. It can be seen that with reagent rotational excitation the reaction probabilities do not follow a regular trend [cf. Figure 4.30(a)]; rather, it strongly depends on the collision energy. The probabilities for reagent H_2 (v=0, j=1) are found to be larger than the others throughout the energy range considered here except near the threshold region. Moreover, it can be seen from Figure 4.30(b) that the overall reactivity of the reaction is hardly affected by rotational excitation of the reagent diatom up to j=3. However, small differences can be sighted among the ICSs. In particular, the reactivity is found to be enhanced a little for j=2 at higher collision energies, whereas, it has decreased slightly for j=3 at lower collision energies. Hence, unlike reagent vibration [227], the effect of reagent rotational excitation on the total ICSs is not so straightforward.

The effect of reagent rotation on product vibrational and rotational level resolved ICSs are shown in Figure 4.31. In the figure, the product vibrational level resolved ICSs

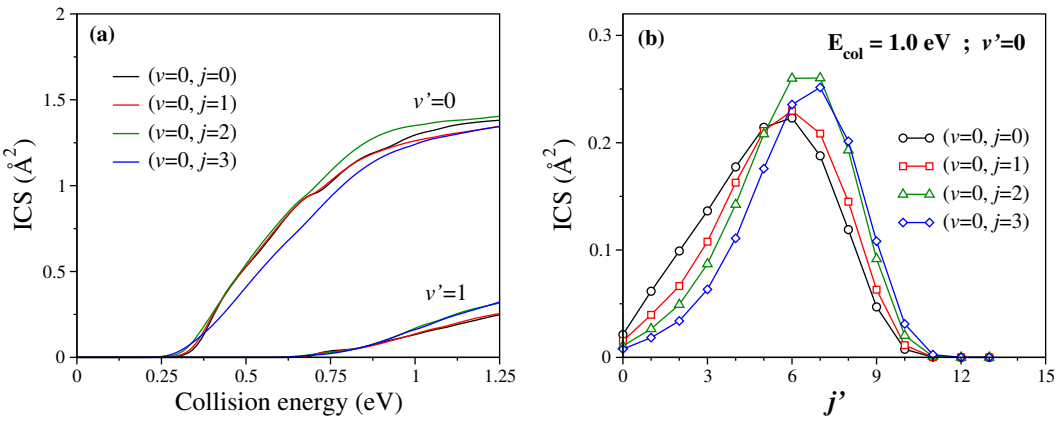

Figure 4.31: Product vibrational level resolved ICSs as a function of collision energy (panel a) and product rotational level distribution in terms of ICS as a function of j' (panel b) for the H + H_2 (v=0, j=0−3) → H_2 (v', j', $\sum \Omega'$) + H reaction. The rotational level distributions are at E_{col}=1.0 eV.

are shown as a function of collision energy for v' = 0 and 1, whereas, the rotational level resolved ICSs are shown only for v'=0 as a function of j' (in terms of distribution) at a fixed E_{col} = 1.0 eV. It can be seen from Figure 4.31(a) that with reagent rotational excitation, there is not much effect found in the v'−resolved ICSs. It is found that the ICS for v'=0 dominates the total reactivity for all the rotational excited reagent considered here. However, a slight effect of reagent rotation is seen in case of v'=0 similar to that seen in the total ICSs. In case of v'=1, the ICS increased slightly at higher collision energies with excitation to j=2 and 3 rotational level. It can be seen from Figure 4.31(b) that the product rotational distributions hardly changes with increasing

reagent rotational excitation. However, comparing the distributions of j=0 and j=3 it is found that the j'−distributions become slightly rotationally hotter for rotationally excited reagent.

The Boltzmann averaged rate constant of the H + H_2 reaction calculated in the present work is shown in Figure 4.32 in terms of Arrhenius plot. The initial state-

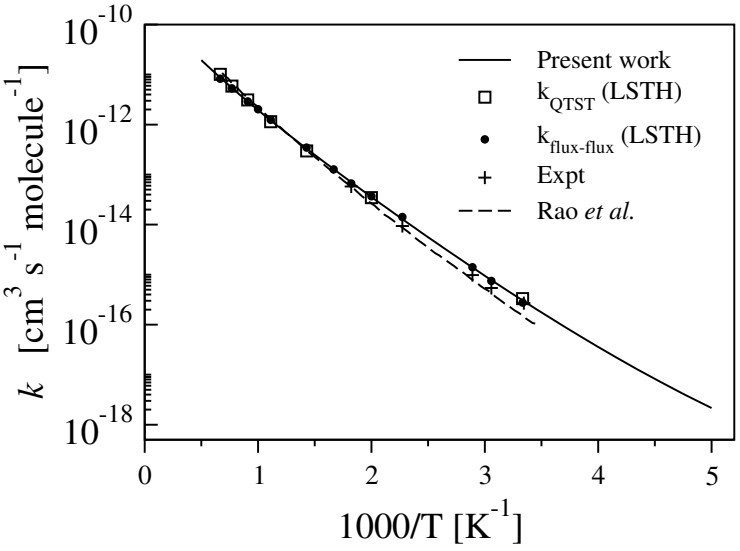

Figure 4.32: Arrhenius plots of the Boltzmann averaged thermal rate constants of the H + H_2 reaction. The present result is compared with those available in the literature [73, 238, 239]. The rate constants are plotted in semi-logarithmic scale against 1000/T.

specific rate constants for reagent H_2 (v=0, j=0−3) are used to obtain the Boltzmann averaged rate constant. Moreover, it is compared with the available theoretical [73, 238, 239] and experimental [239] results. An excellent quantitative agreement of the present result with that of the literature data can be seen except minor difference with the result of Rao *et al.* [73] at low temperatures. This difference can be attributed to the use of less accurate DMBE PES and the CS approximation in the investigation by Rao *et al.* [73].

4.4 Summary

A comprehensive adiabatic and nonadiabatic quantum dynamics of the benchmark H + H_2 reaction is presented in this chapter. The effect of electronic nonadiabatic interaction in the state-to-state dynamics with vibrationally excited (v=3,4, j=0) reagent is reported. The nonadiabatic calculations are performed by the RWP based TDWP approach in conjuction with a two-state coupled diabatic theoretical model (see section

2.1) to include both the lower and upper adiabatic electronic states of H_3 and the nonadiabatic coupling between them. The diabatic Hamiltonian is constructed by considering the ADT angle up to the quadratic coupling. Furthermore, uncoupled single surface dynamics is also performed on the lower adiabatic PES in order to examine the nonadiabatic effects in total as well as state-to-state reaction probabilities, ICSs and DCSs. In addition to the nonadiabatic effects, a comprehensive analysis of the effect of reagent vibrational (v=0−4) and rotational (j=0−3) excitation on the scattering dynamics of the reaction is also reported.

It is found that the quadratic term only shows a very minor effect and does not affect much the dynamics at energies where the nonadiabatic effects are important. The role of the upper adiabatic state is found to remain minimal even for the vibrationally excited H_2 (v=3,4, j=0) reagent diatom. Nonadiabatic effect shows up in the state-to-state DCSs in the form of "out-of-phase" oscillations along the scattering angle between the uncoupled and coupled surface results. The "out-of-phase" behaviour arises due to the change in sign of the interference term between the 1-TS and 2-TS paths as a result of the GP. These oscillations could exactly be infered only by calculating the 1-TS and 2-TS contributions with the inclusion of the interference term between the two. Such oscillations also persist in the forward scattering of higher product vibrational levels showing strong nonadiabatic effect and are found to be different from those due to the glory interference. In fact the glory oscillations showed a very negligibly small nonadiabatic effect and found to occur in case of the products having low j' quantum number regardless of the product vibrational manifold. Nonadiabatic effect also showed up in the energy dependence of both backward and forward scattering of state-resolved products in the form of the "out-of-phase" oscillations. The amplitude of these energy dependent oscillations is found be nearly directly proportional to the magnitude of the 2-TS path DCS. The important role of sum over product quantum states is also addressed and it is found that the nonadiabatic effects in state-to-state reaction probabilities and state-to-state DCSs get reduced to a considerable extent when summed over all the product quantum levels. Similar to the early work with reagent H_2 (v=0,1, j=0), [154, 159, 161, 162] the nonadiabatic effects are found to be dramatically cancelled or reduced in the state-to-state ICSs.

Vibrational excitation of the reagent diatom is found to enhance the forward scattering of the products and makes the backward scattering less prominent. The magnitude of forward scattering increases with increase in collision energy whereas the backward scattering decreases. The analysis of the J−dependent partial DCSs revealed

that the forward scattering mainly comes from the higher partial waves and backward scattering from the lower partial waves. In case of vibrationally excited reagent, a certain type of opposite behaviour between the forward and backward scattered products is found in the product vibrational energy disposal at higher collision energies. It is found that increase in collision energy reduces the vibrational excitation of the backward scattered products to a large extent but not in case of forward scattered products. This is due to the fact that an ample amount of available energy goes to the product rotation of the backward scattered products. The effect of reagent vibration on the $j'-$resolved state-to-state DCSs is also examined. Two different mechanisms corresponding to two contrasting phenomena are noticed. One is the "*negative* $j' - \theta$ *correlation*" in the backward hemisphere and the other one is the "*positive* $j' - \theta$ *correlation*" in the forward scattering. It is found that the underlying mechanisms of the two phenomena are different; the former one is due to a coplanar detachment mechanism, whereas the latter one is due to a non-coplanar detachment mechanism. The effect of reagent rotation (up to j=3) on the overall dynamics of the reaction is found to be not so significant.

Appendix A

The calculation of the 1-TS and 2-TS contributions with the inclusion of the interference between the two is given in this appendix. From equations 4.10 and 4.11, the 1-TS and 2-TS scattering amplitudes can be written as

$$f_1(\theta, E) = \frac{1}{\sqrt{2}}\Big[f_{\mathrm{UC}}(\theta, E) + f_{\mathrm{CP}}(\theta, E)\Big] \tag{4.12}$$

$$f_2(\theta, E) = \frac{1}{\sqrt{2}}\Big[f_{\mathrm{UC}}(\theta, E) - f_{\mathrm{CP}}(\theta, E)\Big]. \tag{4.13}$$

Solving for $f_{\mathrm{UC}}(\theta, E)$ and $f_{\mathrm{CP}}(\theta, E)$ from the above equations we get

$$f_{\mathrm{UC}}(\theta, E) = \frac{1}{\sqrt{2}}\Big[f_1(\theta, E) + f_2(\theta, E)\Big] \tag{4.14}$$

$$f_{\mathrm{CP}}(\theta, E) = \frac{1}{\sqrt{2}}\Big[f_1(\theta, E) - f_2(\theta, E)\Big]. \tag{4.15}$$

The uncoupled DCS is then given as

$$\begin{aligned}
\sigma_{\mathrm{UC}}(\theta, E) = \Big|f_{\mathrm{UC}}(\theta, E)\Big|^2 &= \frac{1}{2}\Big|f_1 + f_2\Big|^2 \qquad (4.16)\\
&= \frac{1}{2}\left(f_1^* f_1 + f_1^* f_2\right) + \frac{1}{2}\left(f_2^* f_2 + f_2^* f_1\right)\\
&= \frac{1}{2}\left(\big|f_1\big|^2 + f_1^* f_2\right) + \frac{1}{2}\left(\big|f_2\big|^2 + f_2^* f_1\right)\\
&= \frac{1}{2}\left(\sigma_{1-\mathrm{TS}} + f_1^* f_2\right) + \frac{1}{2}\left(\sigma_{2-\mathrm{TS}} + f_2^* f_1\right)\\
&= \sigma_{1-\mathrm{TS[+]}} + \sigma_{2-\mathrm{TS[+]}} \qquad (4.17)
\end{aligned}$$

Similarly, the coupled DCS can be given as

$$\begin{aligned}
\sigma_{\mathrm{CP}}(\theta, E) = \Big|f_{\mathrm{CP}}(\theta, E)\Big|^2 &= \frac{1}{2}\Big|f_1 - f_2\Big|^2\\
&= \frac{1}{2}\left(f_1^* f_1 - f_1^* f_2\right) + \frac{1}{2}\left(f_2^* f_2 - f_2^* f_1\right)\\
&= \frac{1}{2}\left(\big|f_1\big|^2 - f_1^* f_2\right) + \frac{1}{2}\left(\big|f_2\big|^2 - f_2^* f_1\right)\\
&= \frac{1}{2}\left(\sigma_{1-\mathrm{TS}} - f_1^* f_2\right) + \frac{1}{2}\left(\sigma_{2-\mathrm{TS}} - f_2^* f_1\right)\\
&= \sigma_{1-\mathrm{TS[-]}} + \sigma_{2-\mathrm{TS[-]}} \qquad (4.18)
\end{aligned}$$

Hence, the 1-TS and 2-TS DCSs with the inclusion of the interference terms are given as

$$\sigma_{1-\mathrm{TS}[+]} = \frac{1}{2}\left(\sigma_{1-\mathrm{TS}} + f_1^* f_2\right) \tag{4.19}$$

$$\sigma_{1-\mathrm{TS}[-]} = \frac{1}{2}\left(\sigma_{1-\mathrm{TS}} - f_1^* f_2\right) \tag{4.20}$$

$$\sigma_{2-\mathrm{TS}[+]} = \frac{1}{2}\left(\sigma_{2-\mathrm{TS}} + f_2^* f_1\right) \tag{4.21}$$

$$\sigma_{2-\mathrm{TS}[-]} = \frac{1}{2}\left(\sigma_{2-\mathrm{TS}} - f_2^* f_1\right) \tag{4.22}$$

Appendix B

The calculation of relative phase between the 1-TS and 2-TS path scattering amplitudes is given in this appendix. Since $f_1(\theta, E)$ and $f_2(\theta, E)$ are both complex functions, they can be written as

$$f_1(\theta, E) = \left|f_1(\theta, E)\right| \exp[i\omega_1(\theta, E)] \tag{4.23}$$

$$f_2(\theta, E) = \left|f_2(\theta, E)\right| \exp[i\omega_2(\theta, E)], \tag{4.24}$$

where $\omega_1(\theta, E)$ and $\omega_2(\theta, E)$ are the phases of the scattering amplitudes of the two paths. Now rewriting equation 4.16 as

$$\begin{aligned} & 2\left|f_{\mathrm{UC}}\right|^2 = \left|f_1 + f_2\right|^2 \\ \Rightarrow\ & 2\left|f_{\mathrm{UC}}\right|^2 = \left|f_1\right|^2 + \left|f_2\right|^2 + f_1^* f_2 + f_2^* f_1 \\ \Rightarrow\ & 2\left|f_{\mathrm{UC}}\right|^2 - \left|f_1\right|^2 - \left|f_2\right|^2 = f_1^* f_2 + f_2^* f_1 \end{aligned} \tag{4.25}$$

Now substituting equations 4.23 and 4.24 on the right hand side of equation 4.25

$$\begin{aligned} 2\left|f_{\mathrm{UC}}\right|^2 - \left|f_1\right|^2 - \left|f_2\right|^2 &= \left|f_1\right|\left|f_2\right| e^{-i(\omega_1-\omega_2)} + \left|f_1\right|\left|f_2\right| e^{i(\omega_1-\omega_2)} \\ &= \left|f_1\right|\left|f_2\right|\left[e^{-i(\omega_1-\omega_2)} + e^{i(\omega_1-\omega_2)}\right] \\ &= 2\left|f_1\right|\left|f_2\right| \cos(\omega_1 - \omega_2) \end{aligned}$$

The relative phase between the 1-TS and 2-TS scattering amplitudes can be calculated as

$$\cos(\omega_1 - \omega_2) = \frac{2\left|f_{\mathrm{UC}}\right|^2 - \left|f_1\right|^2 - \left|f_2\right|^2}{2\left|f_1\right|\left|f_2\right|} \tag{4.26}$$

Table 4.2: Numerical parameters used in the TIQM calculation to obtain the probability of H + H_2 (v=0, j=1) → H_2 + H reaction for J=0 by using the ABC code [237].

Parameter	Value
Total angular momentum quantum number, *jtot*	0
Triatomic parity eigenvalue, *ipar*	1
Triatomic parity eigenvalue, *jpar*	-1
Maximum internal energy in any channel, *emax*	2.5 eV
Maximum rotational quantum number of any channel, *jmax*	16
Helicity truncation parameter, *kmax*	0
Maximum hyperadius, *rmax*	12.0 a_0
Number of log derivative propagation sectors, *mtr*	250
Initial scattering energy, *enrg*	0.5 eV
Scattering energy increment, *dnrg*	0.02 eV
Total number of scattering energies, *nnrg*	52

Chapter 5

State-to-state quantum dynamics of S + OH → SO + H reaction on its ground electronic state

5.1 Introduction

The chemistry of low-temperature interstellar environment is generally thought to be dominated by electrically charged species. That is why only the prototypical ion-molecule models were used to predict the abundances of chemical species in the interstellar clouds [240]. Although a chain of ion-molecule reactions make dominant contribution in the formation of most complex molecules, a significant number of reactions associated with the interstellar medium are found to be of neutral-neutral or atom-neutral type [240, 241]. This has become possible due to the recent advances in the experimental and theoretical techniques. It was even showed that these reactions involving neutral species may become more rapid at low temperature than usually thought [240]. Such reactions generally involve collision between open-shell atoms and radicals, due to which the underlying PES comprises of deep potential wells corresponding to stable intermediate species. The participation of heavier atoms and the complex topography of the underlying PESs have made the theoretical and experimental investigations difficult and challenging. Nevertheless, due to their astrophysical importance and significance in the atmospheric environment and combustion processes, studies on these reactions has progressed remarkably in the recent years [242, 243].

The chemistry of sulfur containing compounds has received a great deal of attention in recent time due to their detection in interstellar medium, particularly the observation of sulfur monoxide [244, 245]. Moreover, this compound has been observed in the atmospheres of Venus [246] and Jupiter's satellite Io [247]. The rotational excitation of SO by collision with H_2 and He is also predicted to play important role in the spectral signature of SO in the interstellar medium [248]. The collision of S atom with the hydroxyl radical OH is one of the many important processes which plays a significant role in the formation of sulfur monoxide in the interstellar dust clouds [245]. The S (^{3}P) + OH ($\tilde{X}^2\Pi$) $\rightarrow$ SO ($\tilde{X}^3\Sigma^-$) + H (^{2}S) reaction occurs on the electronic ground state through the formation of two stable intermediate complexes, HOS and HSO, inside the deep potential wells present on the underlying PES [249]. The relative stability of these two isomers, HOS and HSO was controversial for a long time and they were subjected to various theoretical and experimental investigations [250–253]. Later studies [249, 254, 255] found that the HSO isomer is more stable than HOS despite very little difference in energy. Being a reaction between a diatom free radical and an open-shell atom, the theoretical and experimental studies were rather difficult to carry out. Experimentally it was very inconvenient to measure the concentrations to determine the rate constant because of the high reactivity of the reagent species. On the theoretical side, the presence of deep wells on the PES made the dynamical calculations difficult to converge due to the formation of long-lived intermediate complexes. In spite of the difficulty, a few investigations were performed for the S + OH $\rightarrow$ SO + H reaction to understand its detailed dynamics.

5.1.1 Electronic ground state PES of HSO reactive system

The reaction, S (^{3}P) + OH ($\tilde{X}^2\Pi$) $\rightarrow$ SO ($\tilde{X}^3\Sigma^-$) + H (^{2}S), takes place on the electronic ground state ($\tilde{X}^2A''$) PES of the HSO reactive system. In the present work the global PES constructed by Martínez-Núñez and Varandas [249] have been used. This PES was constructed by generating *ab initio* points at 500 different geometries by full valence complete active space (FVCAS) and multireference configuration interaction (MRCI) methods. These energy values were then corrected by using double many-body expansion-scaled external correlation (DMBE-SEC) method [256], in order to account for the complete basis set/complete CI limit [249]. The aug-cc-pVTZ (AVTZ) basis set of Dunning [257–259] have been used for the calculation of *ab initio* points. The resulting energy values were then fitted by a method based on the DMBE formalism

[260, 261]. This PES also incorporates the correct long-range behavior of all dissociation channels. The detailed topographical properties of the DMBE PES of HSO reactive system is discussed in the following.

The DMBE PES comprises three atom-diatom asymptotes, the S + OH, the SO + H and the SH + O [249]. The exo- and endoergicity of the, S + OH → SO + H and S + OH → SH + O, reactions are ≈0.78 eV and ≈0.84 eV, respectively. There are eight stationary points present on the PES, four of them are minimum and the remaining fours are saddle points. Out of these eight stationary points, two minima (potential wells) and two saddle points (or transition states) play important role in the, S + OH → SO + H, reaction. These two minima correspond to the HSO and HOS isomers. The other two minima are the two van der Walls complexes energetically below the S + OH and O + SH asymptotes and correspond to the S...OH and SH...O structures, respectively. The stationary points are schematically shown along with the S + OH and SO + H asymptotes in Figure 5.1. The energy of the diatomic vibrational levels of reagent OH and product SO are also schematically depicted in the Figure for the ease of understanding of the energetics of the reaction. Among the four transition states, the TS1 connects the

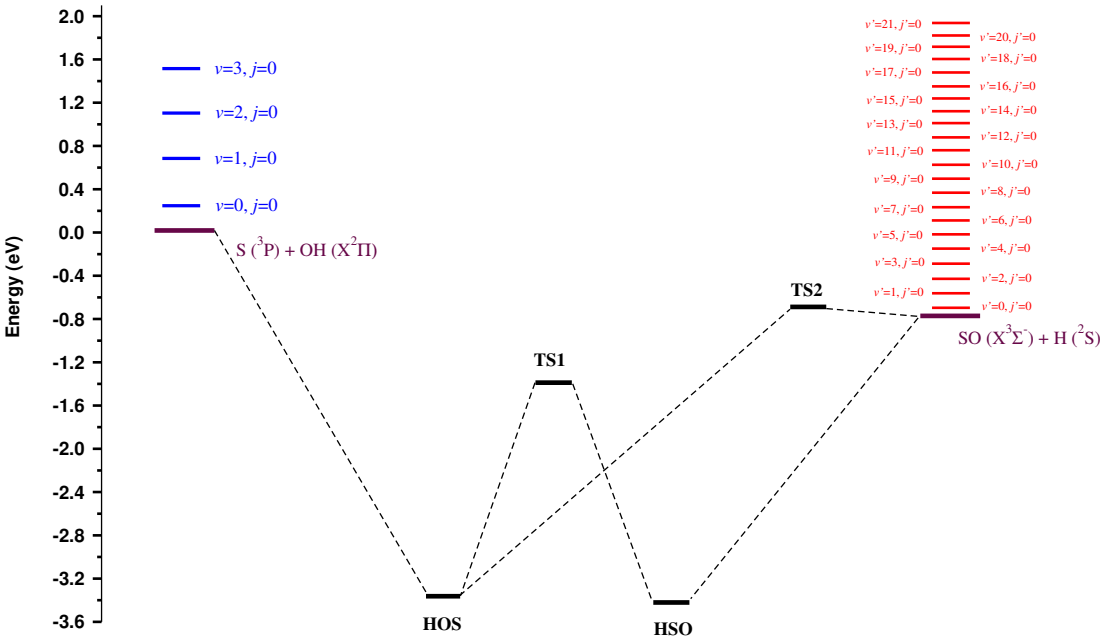

Figure 5.1: Schematic representation of the energy profile diagram corresponding to the S (^{3}P) + OH ($\tilde{X}^2\Pi$) → SO ($\tilde{X}^3\Sigma^-$) + H (^{2}S) reaction. The four important stationary points on the electronic ground DMBE [249] PES of HSO along with the S + OH and SO + H asymptotes are shown. The vibrational energy levels of the OH and SO diatoms considered in the present investigation are also shown. $v(v')$ and $j(j')$ represent the vibrational and rotational quantum number of the reagent (product) diatom, respectively. Energies are plotted here relative to the S + OH reagent asymptote.

two deep potential wells of HSO and HOS isomers and lies ≈2.03 eV in energy above the HSO global minimum. It can be seen from the energy profile diagram of Figure 5.1 that though neither of the transition states behaves as classical barrier for the reaction, TS2 can be considered as a late barrier near the product asymptote as it possesses ≈0.07 eV more energy than the SO + H product asymptote. The other two transition states, TS3 and TS4 connect the HSO and HOS minima to their corresponding van der Walls minima. The energetics of these stationary points are presented in the Table 5.1 which are obtained by using a small in-house computer program. The readers are referred to Table 10 Ref. [249] for more detail information of the stationary points.

Table 5.1: Energy of the stationary points of the HSO reactive system on its electronic ground PES. The abbreviation, TS, here represents transition state or saddle point. All energies presented here are with respect to the energy of the S + OH asymptote which is set to 0.

Stationary points	Energy (eV)
HSO minimum	-3.43
HOS minimum	-3.39
S···HO minimum	-0.14
SH···O minimum	0.78
TS1	-1.40
TS2	-0.71
TS3	0.83
TS4	0.0

In order to have a better understanding of the topographical details, the gradational contour map plots of the HSO PES are shown Figure 5.2 along the Jacobi coordinates. These plots are prepared in reagent and product Jacobi coordinate systems by fixing the r_{OH} and r_{SO} distances at their equilibrium bond lengths, 1.85 a_0 and 2.8 a_0, respectively. The contour plots prepared in reagent and product Jacobi coordinate systems are shown in panel (a) and (b), respectively and the schematics of the respective Jacobi coordinates are shown at the top of each panel. The energy is given in eV unit. The HOS well is clearly visible in Figure 5.2(a), whereas, no trace of the HSO well is found here. It can be seen from Figure 5.2(a) that the S atom faces no barriers when it approaches the OH diatom from the oxygen side. In this case the reactive system slides down to the HOS well at the beginning of the reaction as the r_{OH} distance at the HOS configuration is very close to the equilibrium bond length of OH (cf., Table 10 of Ref. [249]). The favorable approach of the S atom to the OH reagent is sideways or angular which is schematically shown by an arrow in Figure 5.2(a). The two HSO and HOS wells and the two transition states, TS1 and TS2 are clearly visible in panel (b) of Figure 5.2. The

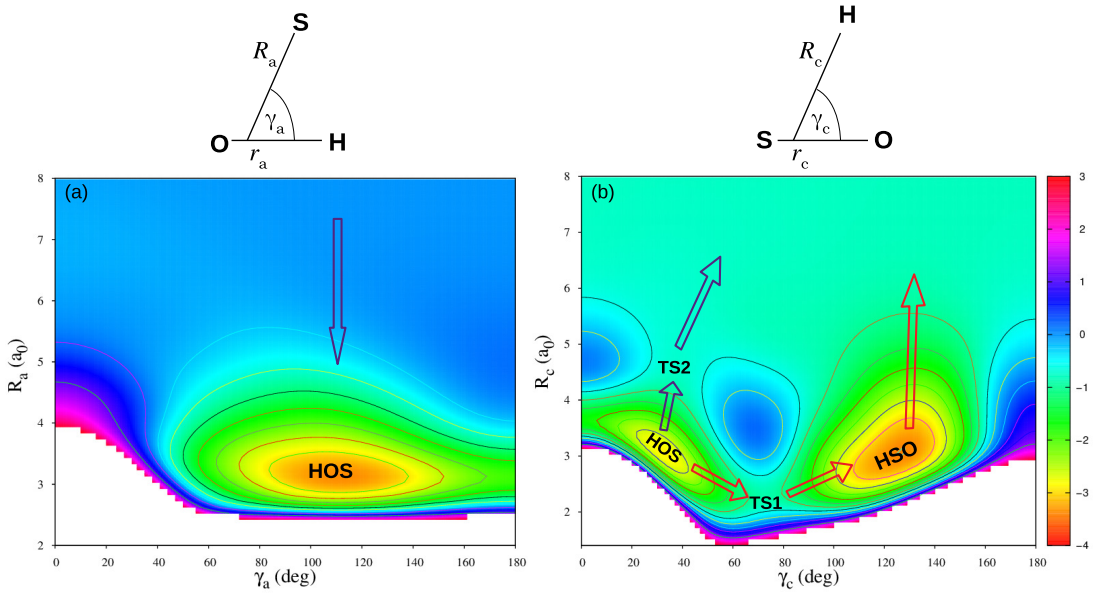

Figure 5.2: Gradational contour map plots of the HSO PES in reagent and product Jacobi coordinate systems shown in panel (a) and (b), respectively. The energy is in eV unit. The favorable sideways/angular approach of the S atom to the OH diatom and the course of the reaction are schematically shown by arrow(s) in panel (a) and (b), respectively. The schematics of the corresponding Jacobi coordinates are also shown on top of each panel.

course of the reaction is also schematically shown by the arrows in Figure 5.2(b). It can be seen from the Figure 5.2(b) and also from the Figure 5.1 that after entering to the HOS well from the reagent channel, the system faces two competing pathways to proceed to the SO + H product channel. One is that where the system directly goes to the product channel after passing over the TS2 transition state, S + OH → HOS → TS2 → SO + H (marked by blue coloured arrows), whereas the other one is that where the system first enters to the more stable HSO well after passing over the isomerization barrier (TS1) and then proceeds to the SO + H product channel, S + OH → HOS → TS1 → HSO → SO + H (marked by red coloured arrows). It is the second pathway that encompasses both the deep wells present on the PES. The isomerization process from HOS to HSO along this pathway involves a bending motion of the triatomic complex where the light H atom seems to move away from the oxygen side to the sulfur side while the overall bond distance of the SO diatom barely change. The difference in the nature of the product formed by these two competing pathways can be discerned by studying the dynamics of the reaction.

5.1.2 Current state of research

Prior to the comprehensive investigations carried out by Jorfi and Honvault [262, 263], the minimum energy path for the formation of the HSO and HOS isomers was computed by Xantheas and Dunning [255]. An energy barrier of ≈2.4 kcal/mol was found by them along this path leading to the formation of the HOS, whereas, a barrierless path was observed along the path leading to HSO [255]. Martínez-Núñez *et al.* found that the isomerization path is favored at low energies, whereas, the dissociation of the complex to SO + H becomes important with an increase of energy [264]. Jourdain *et al.* [265] have measured the rate constant at 298 K and found a value of $(6.6 \pm 1.4) \times 10^{-11}$ cm^3 s^{-1} $molecule^{-1}$. On the other hand, Sendt and Haynes [266] calculated the rate constant by employing the Rice-Ramsperger-Kassel-Marcus (RRKM) theory and reported a value of 6.6×10^{-10} cm^3 s^{-1} $molecule^{-1}$, which differs by an order of magnitude with the measured one. The calculated rate constants in recent theoretical investigations do not agree well with the measured value [78, 263, 265, 267] either.

As far as the theoretical study on the S + OH → SO + H reaction dynamics is concerned, there are a few investigations carried out so far. Jorfi and Honvault were the first to carry out a quantum mechanical investigation of the reaction by a TIQM method [262]. They calculated the total and state-to-state reaction probabilities and product distributions at some energies for the total angular momentum, J=0. They also reported an approximate rate constant by using the J-shifting approach [268] for J >0. The reagent OH was kept in its ground rovibrational level and the reaction involved a mixture of direct and indirect mechanistic pathways through the passage involving HSO and HOS isomers on the underlying surface [262]. The TIQM investigation [262] was followed by quasi-classical trajectory (QCT) calculations [263], by the same authors. They calculated the ICSs, DCSs, product level distributions, lifetime distributions and rate constants [263]. The effect of reagent rotational excitation to j=1 on the ICSs was also shown and it was concluded that the reaction follows a complex-mode mechanism. Unfortunately, in a recent quantum mechanical investigation by Goswami *et al.* [78], it is found that the TIQM results of Jorfi and Honvault [262] were not converged due to lack of enough channels necessary to be considered. Goswami *et al.* [78] have investigated the initial state-selected dynamics of the S + OH (v=0-3, j=0-2) → SO + H reaction by using a TDWP approach and the electronic ground PES [249]. They calculated total reaction probabilities, ICSs and state-specific rate constants within the coupled states (CS) approximation [269, 270]. The resonance oscillations found in the reaction probabilities and ICSs were attributed to the formation of quasi-bound complexes supported

by the two deep potential wells on the underlying PES [78]. The reactivity was found to increase with reagent vibrational excitation, whereas, reagent rotational excitation diminished the same. It is noteworthy to mention here that Goswami *et al.* [78] did not resolve the dynamical attributes into the open vibrational and rotational levels of the product, rather these were summed up to obtain total values.

5.1.3 Motivation of the present work

Although the above studies employed the same DMBE PES of Martínez-Núñez and Varandas [249], the cross sections were calculated within various dynamical approximations. The only quantum state-to-state results of Jorfi and Honvault [262] were not converged properly due to numerical difficulty [78]. Moreover, the only accurate state-to-state dynamical study for this reaction so far is that employed a QCT method [263]. Therefore, it is clear that a comprehensive state-to-state quantum dynamical investigation is required for the S + OH → SO + H reaction to understand its mechanistic details. Furthermore, the cross sections of the reaction are needed to be computed beyond any dynamical approximations, that is, including the Coriolis coupling terms in the calculation.

We note here that the exoergic, S + OH → SO + H, reaction is only considered in the present investigation because the other product channel, SH + O is highly endoergic and has very less reaction probability. Therefore, the reactive system is expected to move over an exoergic barrierless path having two fairly deep potential wells, to reach at the SO + H product asymptote from the reagent channel.

5.2 Computational details

The theoretical method described in section 2.1 of chapter 2 is followed here to carry out the dynamical calculations for the S + OH (v=0-3, j=0-3) → SO (v', j') + H reaction on the DMBE PES of Martínez-Núñez and Varandas [249]. First, extensive number of test calculations are performed to ensure the convergence of the TDWP numerical parameters. The convergence of each parameter is checked with respect to the energy resolved total reaction probability for J=0 by varying the concerned parameter. The convergence tests are carried out for each vibrational level of reagent OH (v=0-3, j=0). However, for the rotationally excited reagent OH (v=0, j=1-3), the numerical parameters of OH

(v=0, j=0) are used to obtain the reaction observables. After the convergence of the parameters is achieved for total angular momentum J=0, the same parameters are used for the J >0 calculations. The details of the converged parameters are given in Table 5.2 for each of the rovibrational level of the reagent OH. It can be seen from the Ta-

Table 5.2: Details of the numerical parameters used in the RWP based TDWP calculation of the S + OH (v=0-3, j=0-3) → SO (v', j') + H reaction.

Parameter	(v=0, j=0-3)	(v=1, j=0)	(v=2, j=0)	(v=3, j=0)
$N_{R'}/N_{r'}/N_{\gamma'}$	215/499/100	215/499/135	215/499/155	215/539/170
R'_{min}/R'_{max} (a_0)	0.1/23.0	0.1/23.0	0.1/23.0	0.1/23.0
r'_{min}/r'_{max} (a_0)	0.1/20.0	0.1/20.0	0.1/19.5	0.1/20.0
R'_d (a_0)	14.5	14.5	14.5	14.5
V_{cut} (E_h)*	0.22	0.22	0.22	0.22
R'_{abs}/r'_{abs} (a_0)	19.0/15.0	19.0/16.0	19.0/16.0	19.0/16.0
C_{abs}/c_{abs}	0.2/0.3	0.4/0.4	0.4/0.5	0.4/0.4
R_0 (a_0)	12.0	13.0	12.5	15.0
E_{trans} (eV)	0.175	0.175	0.175	0.2
δ	16.0	20.0	23.0	24.0
β_s	0.8	0.9	1.0	1.0
$nvab$	11	15	19	22
$njab$	65	70	70	75
$nstep$	80000	80000	80000	80000
Time (fs)	4266.34	4201.65	4153.70	4086.85

*V_{cut} = 0.74 E_h is used for J=50 and for OH (v=0-1, j=0).

ble that the value of all the parameters barely change with vibrational excitation of the reagent OH diatom to v=3 level, except for the width of the initial WP, α, the number of angular grid points, $N_{\gamma'}$, and the number of rotational ($njab$) and vibrational ($nvab$) levels of the product diatom. The number of angular grid points increases with increase in reagent vibrational excitation. Moreover, the values of $nvab$ and $njab$ also increases with increase in reagent vibrational excitation. This suggests that more product rovibrational levels are required in case of vibrationally excited reagent to converge the results. This is because increase in total energy of the system with vibrational excitation of the reagent diatom.

As mentioned above the participation of heavier atoms (S and O) and the presence of deep potential wells, which can support long-lived triatomic complexes, make the theoretical results difficult to converge. In the present work, the reaction probabilities are converged up to 0.5 eV of collision energy. This includes the results for J=0−50 for reagent OH (v=0-1, j=0). The calculations for higher Js are tedious at the moment and require a huge computational overhead. One of the difficulty in performing calculations of higher J is that the parameter V_{cut} (cut-off potential; also used to limit the centrifugal

energy) poses the real trouble as it indirectly affects the scaling of the Hamiltonian in the Chebyshev propagation of the WP. The value of V_{cut} has to be converged for higher Js, and testing the convergence of V_{cut} for each J is rather a tedious task. Nevertheless, the converged reaction probabilities are obtained up to J=0−50 for OH (v=0-1, j=0) in the present work. The converged cross sections are calculated only for OH (v=0, j=0) up to 0.011 eV of collision energy by including the partial wave contribution of J=0−50.

In addition to the state-to-state dynamical calculations by the RWP based TDWP method, the initial state-selected reaction probabilities for reagent OH (v=3, j=0) are also calculated by using the flux operator based TDWP approach for a detail comparison. Several additional tests are performed in order to converge the numerical parameters involved in the TDWP method. The converged parameters are listed in Table 5.3.

Table 5.3: Details of the numerical parameters used in the flux operator based TDWP calculation of the S + OH (v=3, j=0) → SO + H reaction.

Parameter	Numerical value	Description
$N_R/N_r/N_\gamma$	1024/128/99	Number of grid points along R, r and γ
R_{min}/R_{max} (a_0)	0.1/36.0	Extension of grid along R
r_{min}/r_{max} (a_0)	0.1/12.0	Extension of grid along r
r_d (a_0)	7.03	Location of the dividing surface in product channel
R_{damp}/r_{damp} (a_0)	25.5/9.28	Starting point of the damping function
ΔR_{damp} (a_0)	10.5	Range of the damping function along R
Δr_{damp} (a_0)	2.72	Range of the damping function along r
R_0 (a_0)	14.5	Location of the initial WP in coordinate space
E_{trans} (eV)	0.25	Initial relative translational energy
δ (a_0)	0.04	Width parameter of the initial WP
Δt (fs)	0.135	Length of the time step used in the WP propagation
Time (fs)	4049.0	Total propagation time

5.3 Results and Discussion

The reaction probabilities, integral and differential cross sections, and product vibrational and rotational level distributions of the S + OH → SO + H reaction on its electronic ground state are presented and discussed in this section. The probabilities are shown up to 0.5 eV collision energy. The effect of reagent vibrational and rotational excitations and the effect of Coriolis coupling on the dynamics is shown in terms of the reaction probability. The average fraction of available energy entering into product

vibration, rotation and translation are calculated from the state-to-state reaction probabilities for J=0 in order to examine the energy disposal mechanism of the reaction. The ICSs and DCSs are calculated and shown for the reagent OH (v=0, j=0).

5.3.1 Reaction probability and effect of coriolis coupling

Initial state-selected total reaction probabilities of the S + OH (v=0-3, j=0-3) → SO ($\sum v'$, $\sum j'$, $\sum \Omega'$) + H reaction for J=0 are shown in Figure 5.3 as function of collision energy. The probabilities calculated in the present investigation by the RWP based TDWP approach are shown in terms of blue colour solid lines. The results calculated by Goswami *et al.* [78, 271] for reagent OH (v=0-2, j=0-3) are shown in the panels (a)-(c) and (e)-(g) of Figure 5.3 by the red colour dotted lines for comparison. The probabilities of reagent OH (v=3, j=0) obtained by a flux operator based TDWP approach in the present work are also plotted in panel (d) by magenta colour dotted lines for comparison with the present RWP results. It can be seen from Figures 5.3(a)-(g) that except very little difference for OH (v=3, j=0) at low collision energies [cf., panel (d)], the probabilities calculated in the present work by the RWP formalism are in excellent agreement with the results of Refs. [78, 271] [cf. panel (a)-(c) and (e)-(g)] and with the results calculated by the flux operator based approach [cf., panel (d)].

It can be seen from Figure 5.3 that the probabilities exhibit resonance oscillations. The amplitude of these oscillations is very large at low collision energies which gets reduced at the intermediate and high collision energies for reagent OH (v=0-1, j=0-1) [cf., panels (a), (b) and (e)]. The sharpness of these resonances is largely reduced at the intermediate energies (≈ 0.1 - 0.35 eV) and the oscillations become broad for vibrationally hot reagent OH [cf., Figures 5.3(c)-(d)]. However, the oscillations remain sharp and narrow but less intense for rotationally excited reagent OH [cf., Figures 5.3(f)-(g)]. Furthermore, it can be seen from Figures 5.3(a)-(d) that the overall magnitude of probability increases with reagent vibrational excitation and the effect is more pronounced at the higher collision energies. The sharp decrease of probability at ≈0.1 eV [cf., Figs 5.3(a)-(c)] is completely absent for reagent OH (v=3, j=0) rather a sharp peak at very low collision energy appears in case of the latter. The probability acquires an average value of ≈0.5 throughout the energy range considered here [cf., Figure 5.3(d)]. Though the variation of the overall magnitude of probability with reagent rotation is not so regular, a sharp decrease of the reactivity for OH (v=0, j=3) can be seen from Figure 5.3(g)

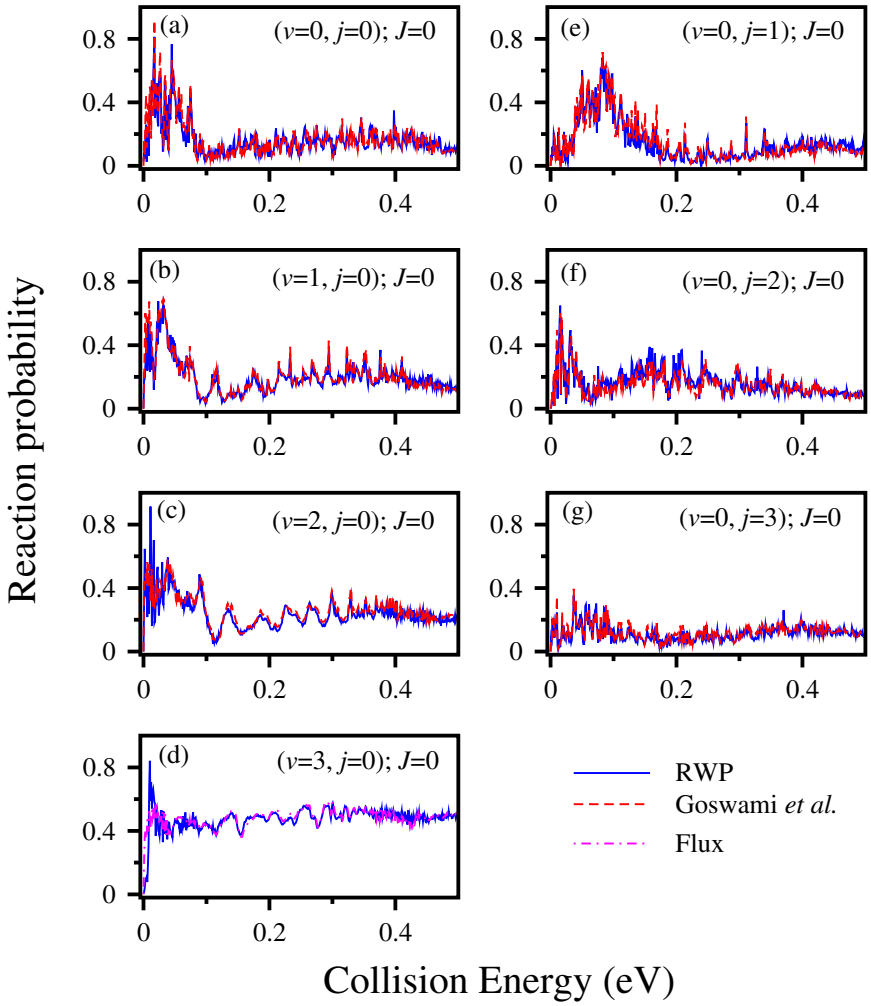

Figure 5.3: Initial state-selected total reaction probabilities of the S + OH (v=0-3, j=0-3) → SO ($\sum v'$, $\sum j'$, $\sum \Omega'$) + H reaction for J=0 as function of collision energy. The probabilities calculated by the RWP based TDWP approach in the present investigation are shown in terms of solid blue lines. The probabilities calculated by Goswami *et al.* [78, 271] for OH (v=0-2, j=0-3) are shown in the panels (a)-(c) and (e)-(g) as red dotted line for comparison. The probabilities obtained by a flux operator based TDWP approach in the present work for OH (v=3, j=0) are plotted in magenta colour dotted lines in panel (d).

and the decrease is more at low collision energies. The decrease of the reactivity with reagent rotational excitation was also found in earlier investigations [78, 263].

The resonance oscillations observed in Figure 5.3 merits some justifications here. These are attributed to the formation of intermediate collision complexes inside the two fairly deep wells on the PES. Sharp and intense resonances are also found for the C + OH reaction on its first ($1^2A''$) and second ($1^4A''$) excited states which is in strong contrast with the results on the electronic ground state [79, 80, 272–277]. No actual resonance was found on the electronic ground state and the probability was found to

be ∼1.0 up to 1.0 eV collision energy [272, 274]. On the other hand, the resonances found in the N + OH reaction on its electronic ground (^{3}A″) state are not so dense and the probabilities show large and broad oscillations [278–281]. These observations are related to the topographical details of the underlying PESs of these reactive systems. The C + OH, S + OH and N + OH reactions, forming CO, SO and NO products, are exoergic and barrierless except the HCO system on its second excited (1^4A″) state. Two potential wells exist on the respective PESs along their reaction path [262, 272, 273, 276, 278]. However the well depths and the exoergicity are different for each system. The exoergicity of the C + OH reaction on its electronic ground and excited states are ≈6.5 eV and ≈0.41 eV, respectively [272, 273]. The depth of the HCO and COH wells, respectively, is ≈7.26 eV and ≈5.50 eV on the electronic ground state [272], ≈6.16 eV and ≈4.63 eV on the first excited state [273], and ≈2.25 eV and 1.85 eV on the second excited state. On the other hand, the exoergicity of the S + OH reaction on the electronic ground state is ≈0.78 eV [249]. The well depths corresponding to the HOS and HSO minimum are ≈3.39 eV and ≈3.43 eV, respectively (cf., Table 5.1). The exoergicity of the N + OH reaction is ≈2.0 eV and the well depths corresponding to the NOH and HNO minimum are ≈3.1 eV and ≈3.4 eV, respectively [262, 278]. Therefore, the exoergicity is least for the C + OH reaction on its excited states and is highest for the same reaction on its electronic ground state. The large exoergicity on the latter state leads faster transition of the intermediate complexes into products and reduction of the lifetime of these complexes. Consequently, the signature of the resonances in the probability curve becomes less prominent. The exoergicity value and the well depths of the S + OH and N + OH reactions lie in between of the C + OH reaction on its electronic ground and excited states. Although the well depths are comparable for the HNO and HSO reactive systems, the exoergicity of the N + OH reaction is two and half times larger than the S + OH reaction. As a consequence, the resonances in the probability curve of the N + OH reaction are broad and result into wide oscillations at few energies [280, 281]. We note that all the above mentioned exoergicities and well depths of the HCO, HSO and HNO reactive systems are relative to the C + OH, S + OH and N + OH reagent asymptotes, respectively.

Initial state-selected total reaction probabilities for some selected values of J >0 of the S + OH (v=0-1, j=0) reaction are shown as a function of collision energy in Figure 5.4. These probabilities are calculated including the CC and are shown by the blue color lines. The probabilities of Goswami *et al.* [78, 271] calculated by the flux operator based TDWP approach within the CS approximation are shown by the red color lines. It can be seen from Figure 5.4 that for lower J values there is not much

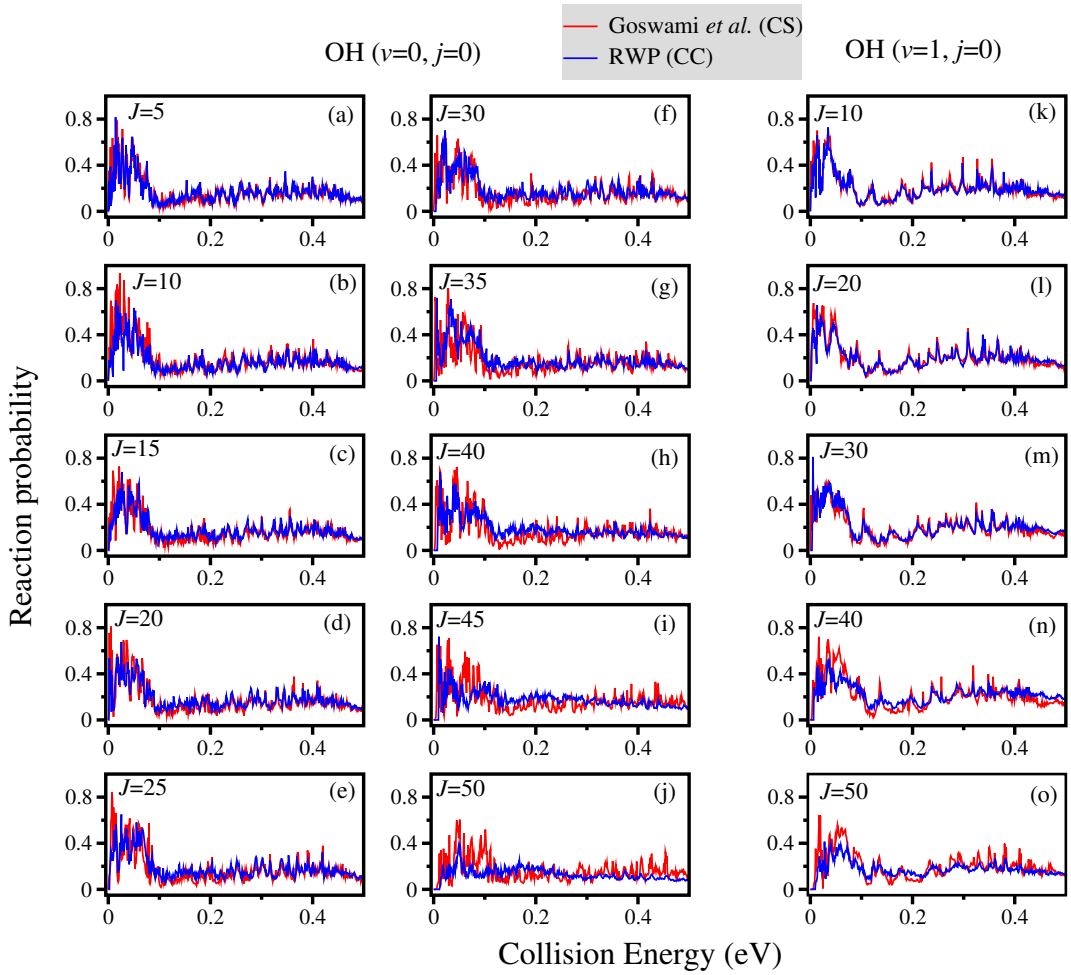

Figure 5.4: Initial state-selected total reaction probabilities of the S + OH (v=0-1, j=0) → SO ($\sum v'$, $\sum j'$, $\sum \Omega'$) + H reaction as function of collision energy for some selected values of $J \neq 0$. The results for OH (v=0, j=0) and OH (v=1, j=0) are shown in panels (a)-(j) and (k)-(o), respectively. The probabilities calculated by the present RWP based TDWP methodology are shown in blue color lines, whereas, those of Goswami *et al.* [78, 271] (within the CS approximation) are shown in red color lines.

difference exist between the CS and CC probabilities. However, the CC effect for OH (v=0-1, j=0) becomes more prominent with increasing J. A similar feature is also found for other reactions [80, 282–284]. It can be seen from panels (j) and (o) of Figure 5.4 that for J=50, the CC effect slightly underestimates the probability with respect to that obtained within the CS approximation at low collision energies. A similar decrease of reactivity due to the CC effect is found for the $H^- + D_2$ and $D^- + H_2$ reactions [284]. This is in contrast to the findings for the $He + H_2^+$ and C + OH (on its second excited state) reactions. Furthermore, a comparison of results presented in panels (b), (f), (h) of Figure 5.4 with that in panels (b), (f), (h) of Figure 2 of Ref. [80] reveals that the effect of CC is more prominent for the C + OH reaction on its second excited state compared to the S + OH reaction on its electronic ground state. These two reactions proceed

to the product valley *via* the formation of intermediate complexes inside the potential wells on the underlying PESs which is considered as the important step for complex-forming reactions. The exoergicity of the C + OH reaction on its second excited state is almost two times lower than that of the S + OH reaction (vide supra). Furthermore, the C + OH reaction on the second excited state possesses a barrier of height ≈0.03 eV at the exit channel (cf., Refs. [273, 285]). These two features of the second excited PES of HCO make the breaking of the intermediate collision complex into products more difficult despite smaller well depths as compared to the S + OH reaction (vide supra). However, the vibrational modes excited through CC can favor the breaking of the complex [284] facilitating the formation of CO + H products, thus enhancing the probability (cf., Figure 2 of Ref. [80]).

Product vibrational level resolved reaction probabilities for J=0 of the S + OH (v=0, j=0) → SO (v', $\sum j'$) + H reaction are shown in Figure 5.5 as a function of collision energy for some selected v' levels. The product vibrational quantum number is mentioned in each panel. It can be seen from Figure 5.5(a)-(e) that the product vi-

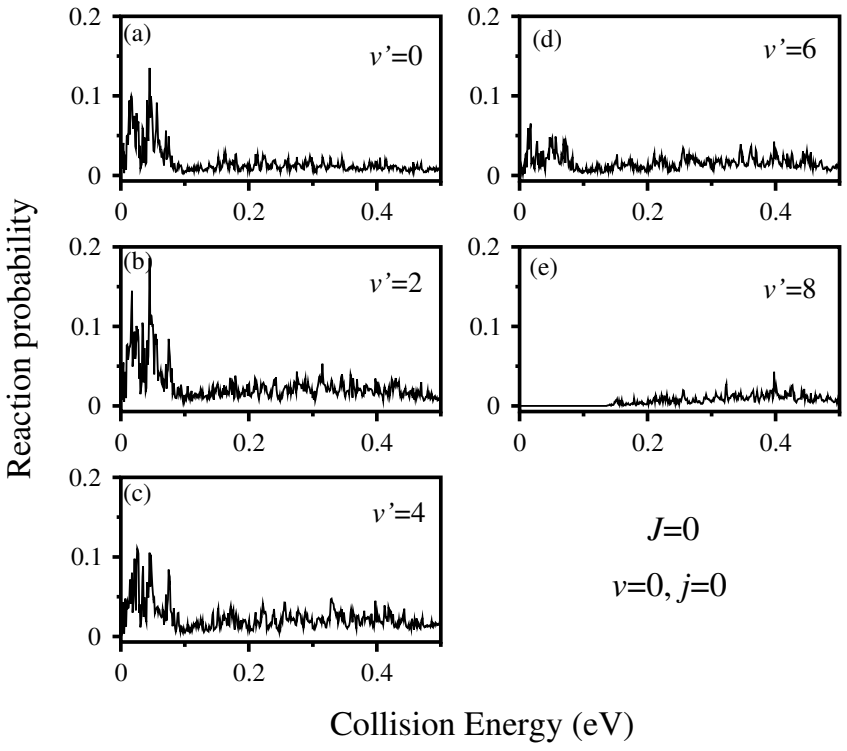

Figure 5.5: Product vibrational level resolved reaction probabilities for J=0 and for some selected v' levels for the S + OH (v=0, j=0) → SO (v', $\sum j'$, $\sum \Omega'$) + H reaction as a function of collision energy.

brational level resolved probabilities also exhibit dense oscillations similar to the total reaction probabilities [cf., Figure 5.3(a)]. It can also be seen from Figure 5.5 that v'=0-6

predominantly contribute to the reactivity and energy threshold appears for $v' > 6$ despite the fact that the overall reaction is exoergic. The threshold appears for SO ($v' > 6$) as these levels possess internal energy more than the zero-point energy of reagent OH (cf., Figure 5.1). The results of Figure 5.5 are similar to the findings of the N + OH reaction on its electronic ground state and the C + OH reaction on its first excited state (cf., Figure 2 of Ref. [281], Figure 3 of Ref. [280], and Figure 5 of Ref. [277]). In all these cases the higher product vibrational levels contributed significantly to the overall reactivity [277, 280, 281], whereas, the v'=0-1 are mainly populated for the C + OH reaction on its second excited state (cf., Figure 6 of Ref. [277]). The barrier at the exit channel in the latter makes the formation of vibrationally hot product less probable [277].

The effect of reagent vibrational excitation on the product vibrational level resolved reaction probabilities is shown in Figure 5.6. The probabilities for OH (v=1, j=0), OH (v=2, j=0) and OH (v=3, j=0) are shown in black, red and green lines, respectively. It can be seen from panels (a)-(v) of Figure 5.6 that more product vibrational

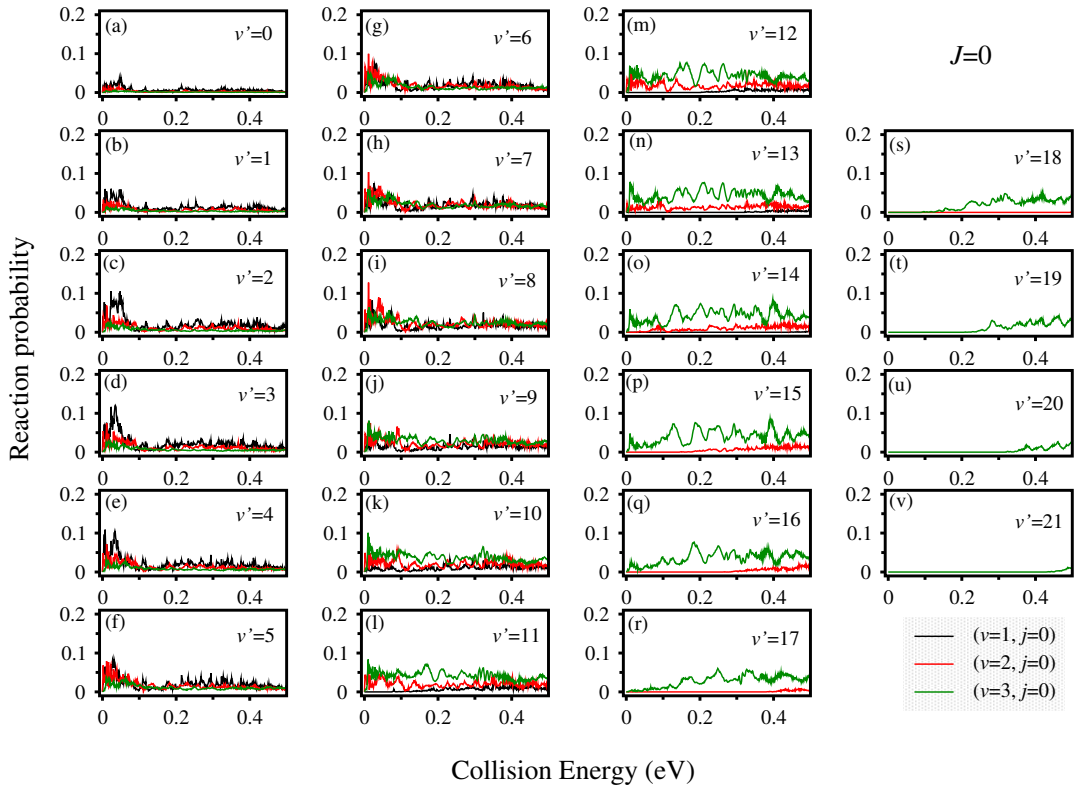

Figure 5.6: Same as in Figure 5.5, but for the S + OH (v=1−3, j=0) → SO (v', $\sum j'$, $\sum \Omega'$)+ H reaction.

levels open up with reagent vibrational excitation and therefore the energy supplied to reagent vibration is partially disposes into product vibration. A similar feature is also

observed for the C + OH reaction on its excited states [277]. Furthermore, it can also be seen from Figure 5.6 that v'=2-7, v'=5-12 and v'=10-17 mainly contribute to the overall reactivity of the reagent OH excited to v=1, v=2 and v=3 levels, respectively. This pattern is also similar to the C + OH reaction on its first excited state [277]. Energy threshold in the reaction probabilities for OH (v=1, j=0), OH (v=2, j=0) and OH (v=3, j=0) can be seen from v'=11, v'=14 and v'=18, respectively [cf., panels (l), (o) and (s) of Figure 5.6]. This can be justified from the energy levels of the reagent OH and product SO depicted in Figure 5.1.

The effect of reagent rotational excitation on the product vibrational level resolved reaction probabilities is shown in Figure 5.7. It can be seen from the figure that increase

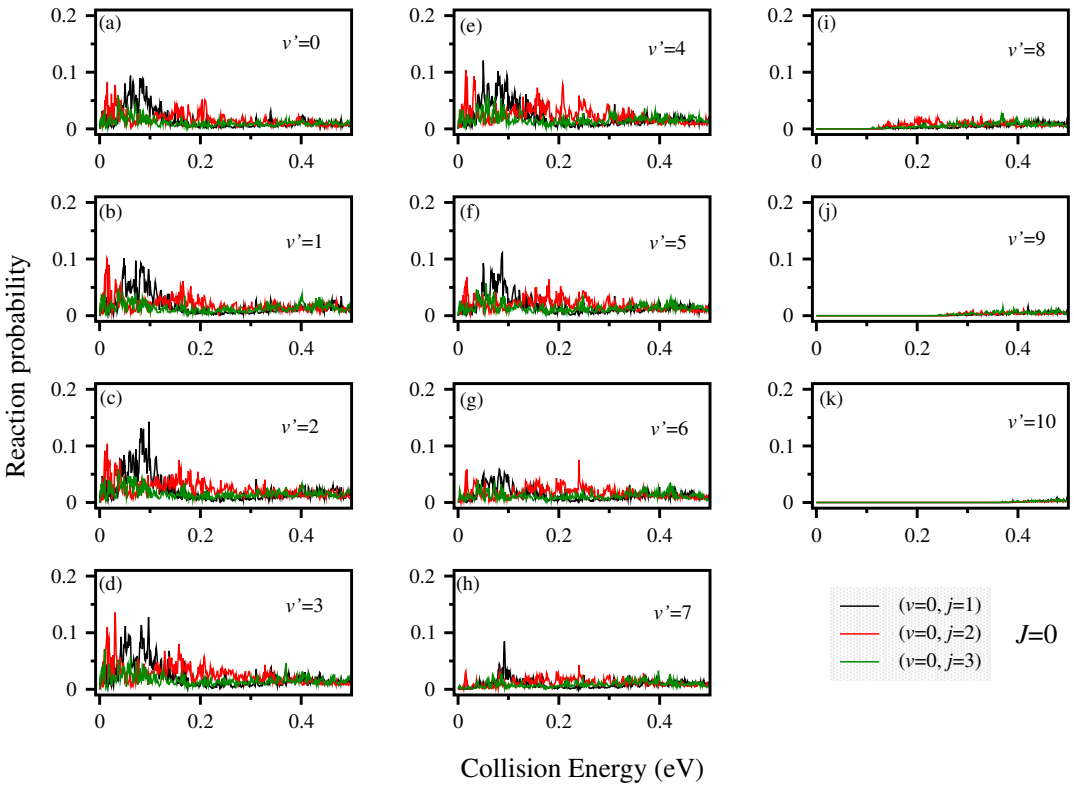

Figure 5.7: Same as in Figure 5.5, but for the S + OH (v=0, j=1−3) → SO (v', $\sum j'$, $\sum \Omega'$)+ H reaction.

in reagent rotational excitations do not affect the product vibrational level resolved probabilities significantly. The pattern and the relative magnitude of the state-to-state reaction probabilities resemble with that of the total reaction probabilities, as can be seen from Figure 5.7(a)-(g) and Figure 5.3(e)-(g).

5.3.2 Product vibrational and rotational level distributions

Product vibrational level population distributions in the S + OH (v=0-3, j=0) reaction are shown in Figure 5.8 as function of v' at four different collision energies, 0.005, 0.1, 0.3 and 0.5 eV. The distributions are shown in terms of reaction probabilities for J=0. It

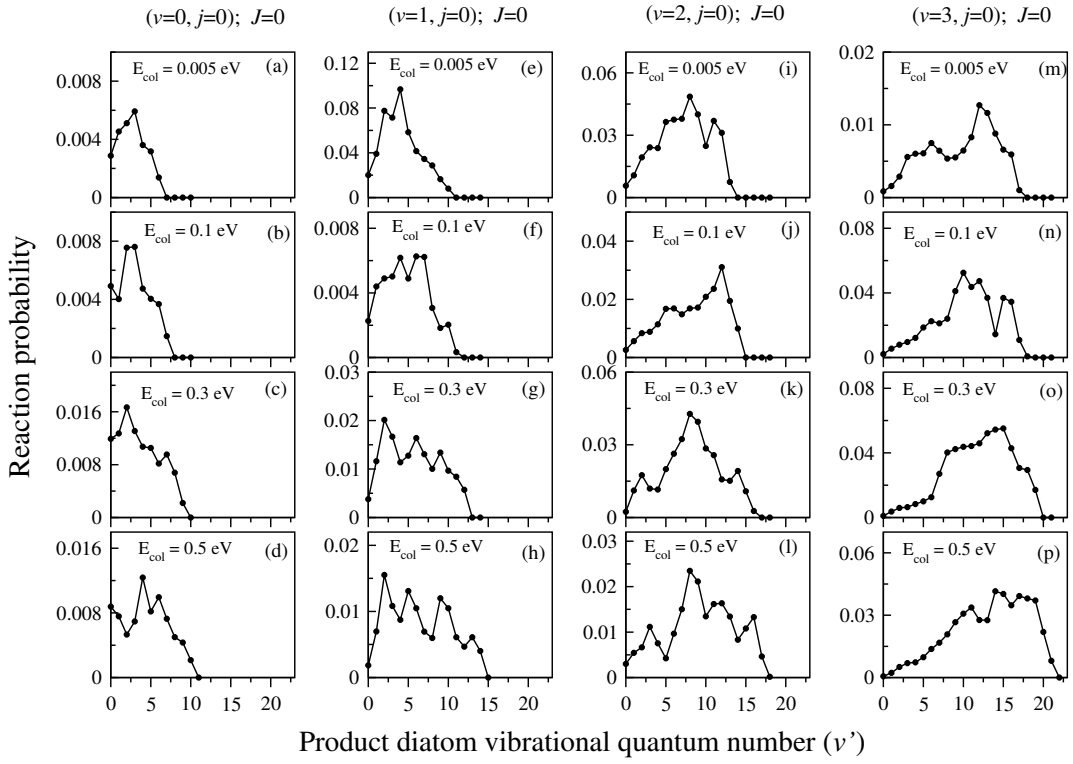

Figure 5.8: Product vibrational level population distribution in terms of reaction probabilities for J=0 of the S + OH (v=0-3, j=0) → SO (v', $\sum j'$) + H reaction at E_{col} = 0.005, 0.1, 0.3 and 0.5 eV.

can be seen from Figure 5.8 that the products are formed with an inverse Boltzmann type non-statistical vibrational distribution. The distributions at other collision energies (not shown here) also show similar behavior. This is in strong contrast with the distributions found in the C + OH reaction on its second excited state, where the distributions for OH (v=0-1, j=0) is predominantly statistical [277]. On the contrary, the distributions shown in Figure 5.8 have resemblance with the results of the C + OH reaction on its first excited state and N + OH reaction on its electronic ground state [277, 280, 281]. It can be seen from each row of Figure 5.8 that at each collision energy, the maximum of the distribution shifts to higher v' value with reagent vibrational excitation. Therefore, the additional energy supplied to reagent vibration is preferentially disposed into product vibration. The maximum of the distribution is found to shift towards higher and lower v' value irregularly with increasing collision energy (cf., each column of Figure 5.8).

This is because of the strong oscillating nature of the product vibrational level resolved reaction probabilities as a function of collision energy shown in Figures 5.5 and 5.6. The effect of rotational excitation of reagent diatom on the product vibrational distribution is shown in Figure 5.9. It can be seen that the effect of reagent rotational excitation to j=3

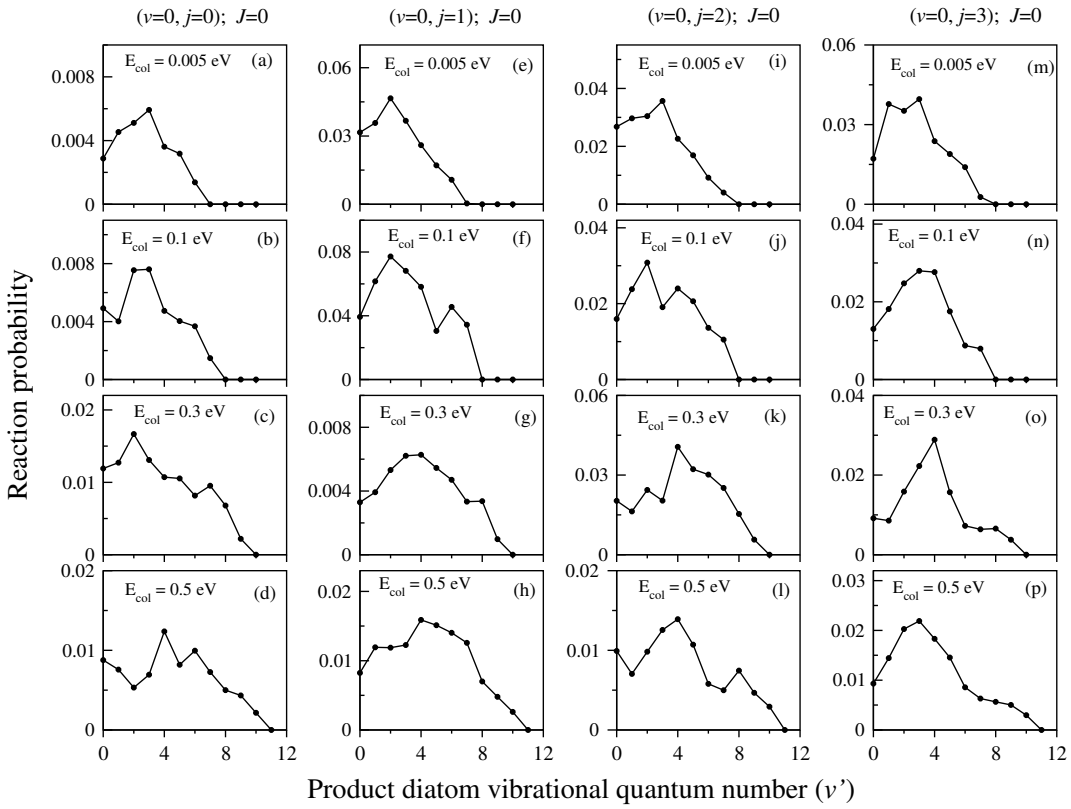

Figure 5.9: Same as in Figure 5.8, but for the S + OH (v=0, j=0–3) → SO (v', $\sum j'$) + H reaction.

on the product vibrational distribution is rather not significant. and it does not result into more inverted vibrational distribution as compared to the vibrational excitation.

The above population distributions can also be investigated in terms of ICSs where the partial wave contributions for J >0 are included. Such an attempt is made for OH (v=0, j=0) and the results are shown in Figure 5.10. The product vibrational level population distributions are plotted in Figure 5.10 in terms of ICSs at two different collision energies, 0.005 eV and 0.01 eV as function of v'. It can be seen from Figure 5.10 that the distribution at both energies are inverted. Similar observation was also made by Jorfi and Honvault from QCT calculations (cf., Figure 5 of Ref. [263]). Therefore, from the features of Figure 5.8 and Figure 5.10 it can be inferred that despite the formation of intermediate complexes inside the wells on the underlying PES, the S + OH reaction does not follow a purely indirect mechanistic pathway. This results into the inverted vibrational population distributions. The extent of the latter increases with increasing

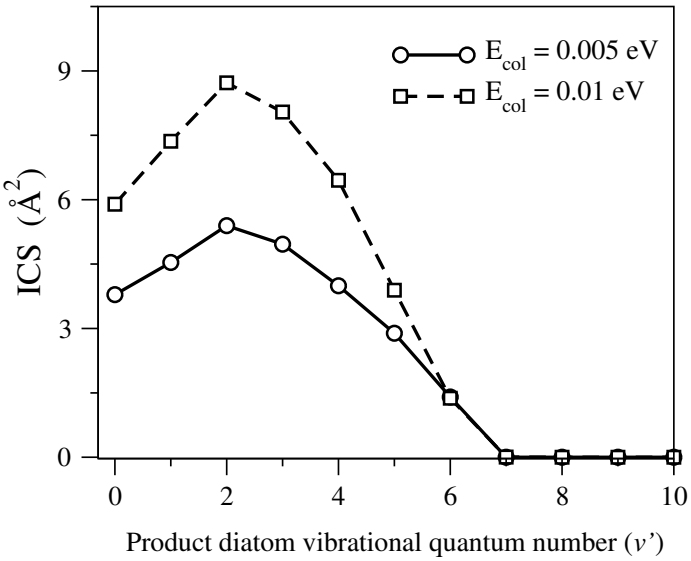

Figure 5.10: Product vibrational level population distribution in terms of ICS for the S + OH (v=0, j=0) → SO (v', $\sum j'$) + H reaction at E_{col} = 0.005 and 0.01 eV.

reagent vibration (cf., Figure 5.8) and therefore the mechanism becomes more direct. Quenching of the amplitude of resonance oscillations [cf., Figs. 5.3(a)-(d) and 5.6] and total reaction time (cf., Table 5.2) with reagent vibrational excitation also justify this.

The product rotational level population distribution of the S + OH (v=0, j=0) → SO (v'=0−6) + H reaction is shown as bar diagrams in Figure 5.11. The distributions presented here in terms of ICSs at two different collision energies, 0.005 and 0.01 eV. It can be seen from Figure 5.11 that at both energies the value of the ICS rises monotonically with increasing j', reaches to a maximum and smoothly decreases afterwards at higher j'. As a consequence, the distributions become bell shaped. Furthermore, from panels (e)-(g) and (l)-(n) it can be seen that the distributions become colder for v'=5-6. It is to be noted here that there are sufficient j' levels up to the energetic limit (the total available energy), those can be populated when E_{col} = 0.005 and 0.01 eV. The j' value corresponding to the energetic limit (j'_{lim}) in each v' manifold are given in Table 5.4 for OH (v=0, j=0) and E_{col} = 0.01 eV. The quantity j'_{lim} denotes the value of j' up to which the product channels in each v' manifold are open for a certain value of collision energy. The j'_{lim} values for v'=0-6 at E_{col} = 0.005 eV are found to be same as those at E_{col} = 0.01 eV and are not shown here for brevity. It can be seen from Table 5.4 and Figure 5.11 that except for v'= 5 and 6, the j' levels for each v' manifold are not populated up to the energetic limit and the value of j' up to which the product is populated (say, j'_{max}) occurs well below the j'_{lim}. In contrast, the j'_{max} values become approximately equal to the j'_{lim} values only for v'= 5 and 6. This is because the available energy is not sufficient to open up highly excited j' levels when the product is formed at higher

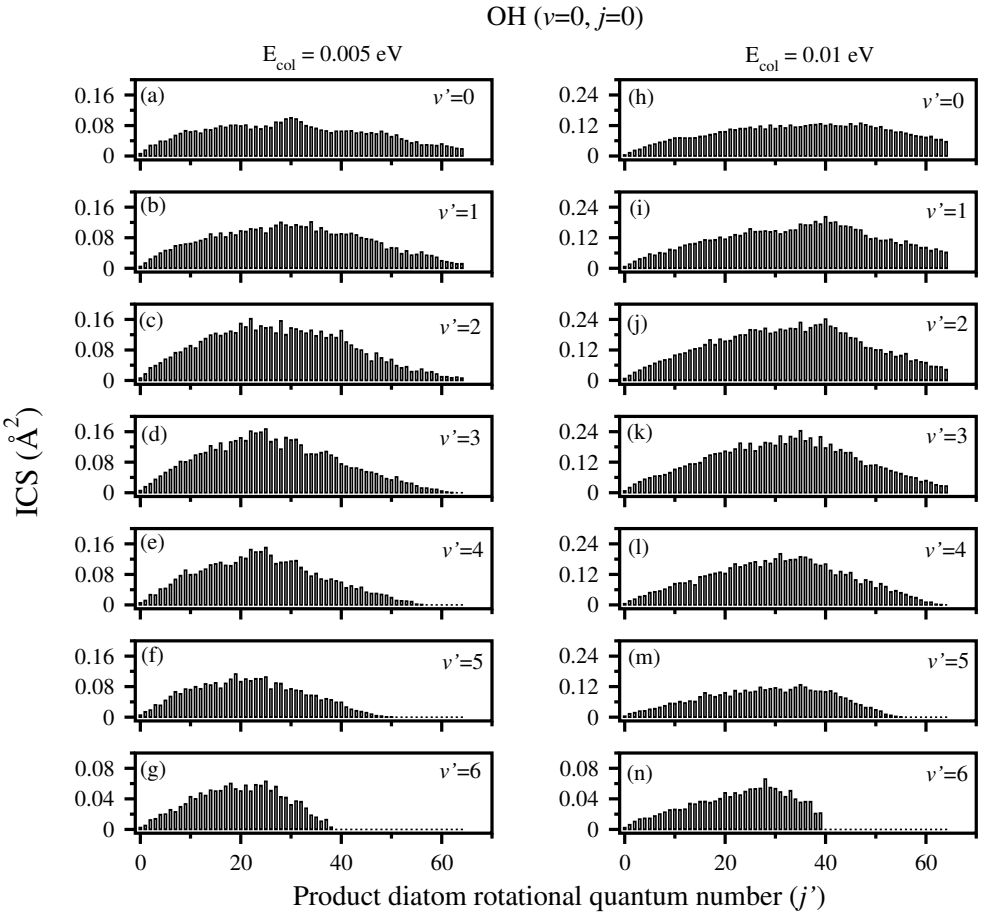

Figure 5.11: Product rotational level population distribution in terms of ICS for the S + OH (v=0, j=0) → SO (v'=0−6, j') + H reaction at E_{col} = 0.005 and 0.01 eV.

Table 5.4: The product rotational levels corresponding to the energetic limit (j'_{lim}) in each v' manifold, for OH (v=0, j=0) and for E_{col} = 0.01 eV. The value of the energetic limit here is $\epsilon_{v=0,j=0}$ + E_{col} = 0.22817 + 0.01 = 0.23817 eV. The rovibrational energies corresponding to the j'_{lim} are also given. All the energy values are relative to the energy of the S + OH asymptote.

v'	j'_{lim}	$\epsilon_{v j'_{lim}}$ (eV)
0	103	0.22120
1	96	0.23310
2	87	0.22356
3	78	0.22823
4	67	0.22379
5	55	0.23068
6	39	0.23419

v' levels. The above observations, in general, indicate that the available energy does not flow effectively into product rotation rather it is deposited into product translational or recoil energy. This is indeed justified because the SO diatom is much heavier than the H atom which can lead to its low rotational excitation. A further look at Figure 5.11 reveals that the maximum of the distribution shifts to higher j' with increasing collision energy for all v' values. Therefore, unlike product vibrational distribution (cf., Figure 5.10), product rotational level population distribution is sensitive to the collision energy and the latter favors the formation of rotationally hot products (cf., Figure 5.11). A similar feature is also found by Jorfi and Honvault in a QCT investigation [263].

The effect of collision energy and reagent vibrational excitation on the product rotational population distribution is shown in Figure 5.12. In the figure, the product rotational level resolved reaction probabilities of the S + OH (v=0−2, j=0) → SO (v'=0, j') + H reaction are shown as function a of j' at four different collision energies, 0.005, 0.1, 0.3 and 0.5 eV. It can be seen from the distribution diagrams of Figure 5.12 that

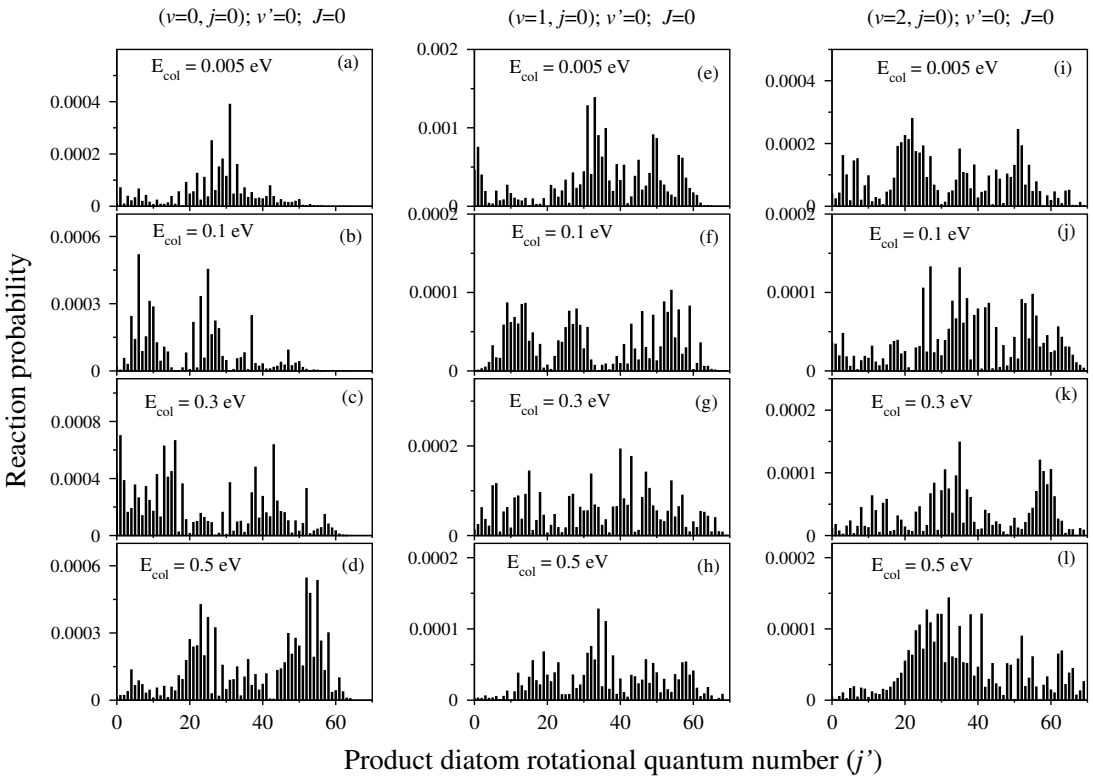

Figure 5.12: Product rotational level population distribution in terms of reaction probability for J=0 of the S + OH (v=0−2, j=0) → SO (v'=0, j') + H reaction at E_{col} = 0.005, 0.1, 0.3 and 0.5 eV.

the rotational excitation of the product SO increases with increasing collision energy at a given vibrationallevel. Moreover, the product becomes more rotationally excited

with increase in reagent vibrational excitation for a fixed value of collision energy (cf., each row of Figure 5.12). Therefore, the additional energy supplied to the vibrational and relative translational degrees of freedom of the reagent OH molecule leads to the formation of rotationally hot product SO in the v'=0 level. Product rotational level distributions for the C + OH and N + OH reactions were also reported in the literature [275–277, 280]. The distribution in the N + OH reaction was found to be rotationally hot as collision energy increases and it strongly depends on the collision energy [280]. The distribution remains rotationally cold in the C + OH reaction on its second excited state, whereas it is neither hot nor cold on its first excited state [275–277]. Therefore, the product rotational distribution in the S + OH reaction shown in Figure 5.12 bears a similarity with the N + OH reaction on its electronic ground state.

The effect of reagent rotational excitation on the product rotational distribution is shown in Figure 5.13 for SO (v'=0). It can be seen that with reagent rotational excitation

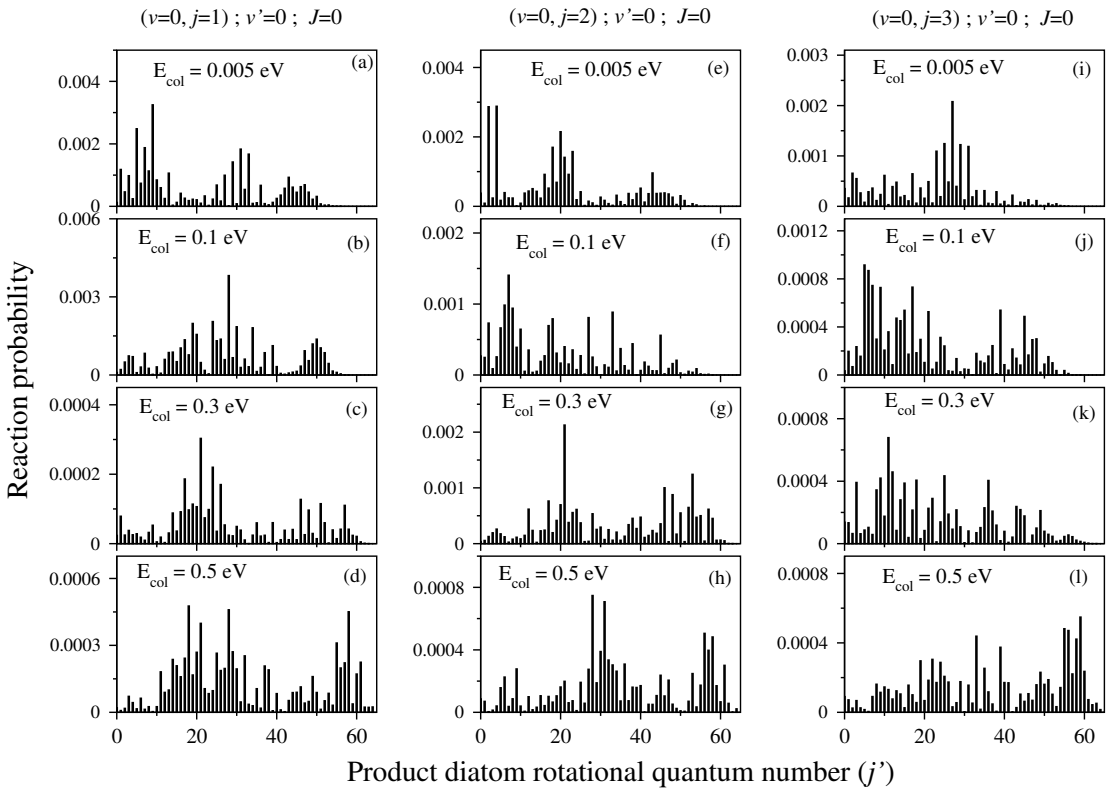

Figure 5.13: Same as in Figure 5.12, but for the S + OH (v=0, j=1−3) → SO (v'=0, j') + H reaction.

the overall pattern of the distribution remains similar for a particular value of collision energy. However, for rotationally hot reagent, the product rotational distribution becomes hotter with increase in collision energy, analogous to the results obtained with

vibrationally excited reagent. The rotational distributions in higher v' levels of SO for rotationally excited reagent (not shown here) also show a similar behavior.

In a recent quantum dynamics investigation on the benchmark H + H_2 reaction Goswami *et al.* have found that the product rotational level resolved state-to-state attributes largely depend on the chosen v' value [227]. Therefore, it would be interesting to examine the same issue in case of the S + OH reaction. The product rotational distributions of the S + OH (v=0, j=0) → SO (v'=0, 2, 3) + H reaction for J=0 are plotted in Figure 5.14 at four collision energies, 0.005, 0.1, 0.3 and 0.5 eV. The $j'_{\rm lim}$ values are also shown in each panel. It can be seen that for all v' levels, the distribution becomes

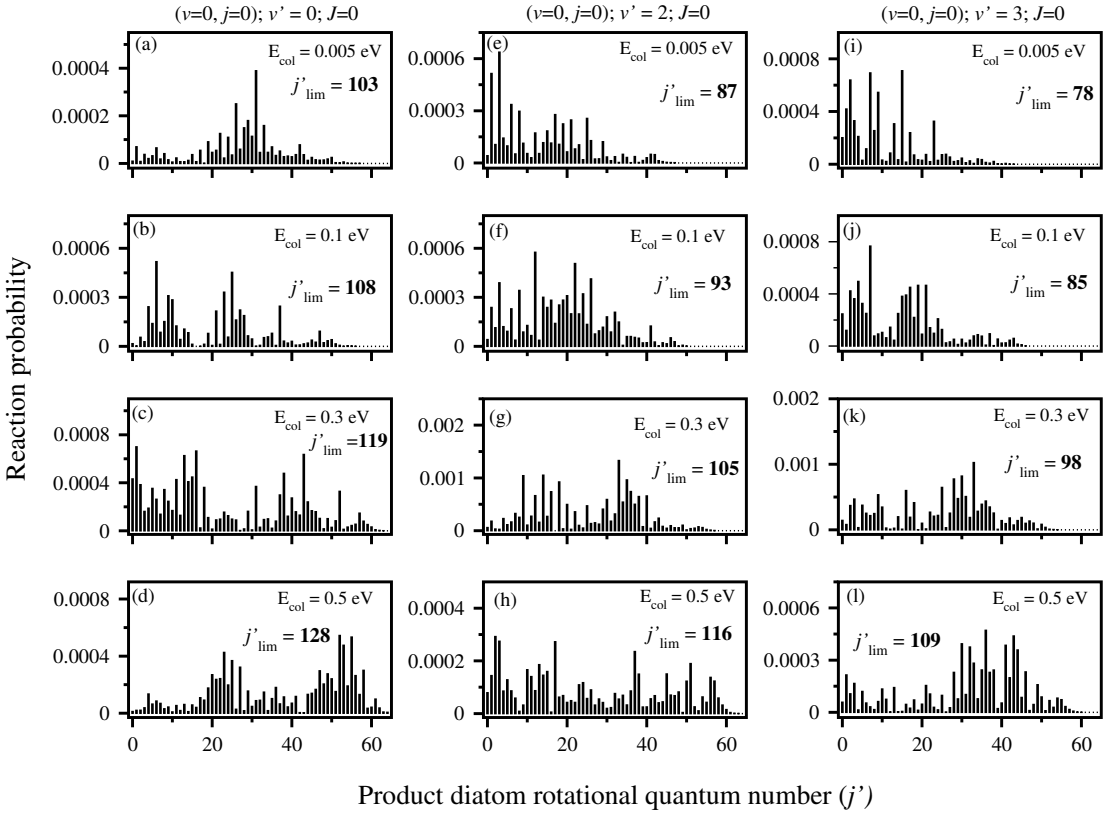

Figure 5.14: Same as in Figure 5.12, but for the S + OH (v=0, j=0) → SO (v'=0, 2, 3, j') + H reaction. The $j'_{\rm lim}$ values are given in each panel to show the energetic limit.

hotter with increase in collision energy even though the j' levels are not populated up to the energetic limit. The collision energy flows to product rotation for all v', favoring the formation of rotationally hot product diatom. Thus, the results of Figure 5.11 and Figure 5.14 reveal that the mechanistic details of the dynamics of the HSO reactive system to form the product in different vibrational levels is similar when the reagent is kept in its ground rovibrational level. The product rotational distribution in the S + OH (v=3, j=0) reaction for J=0 is plotted in Figure 5.15 to examine the dynamics of the highly

vibrationally excited products. It can be seen from Figure 5.15(a)-(d) that the collision

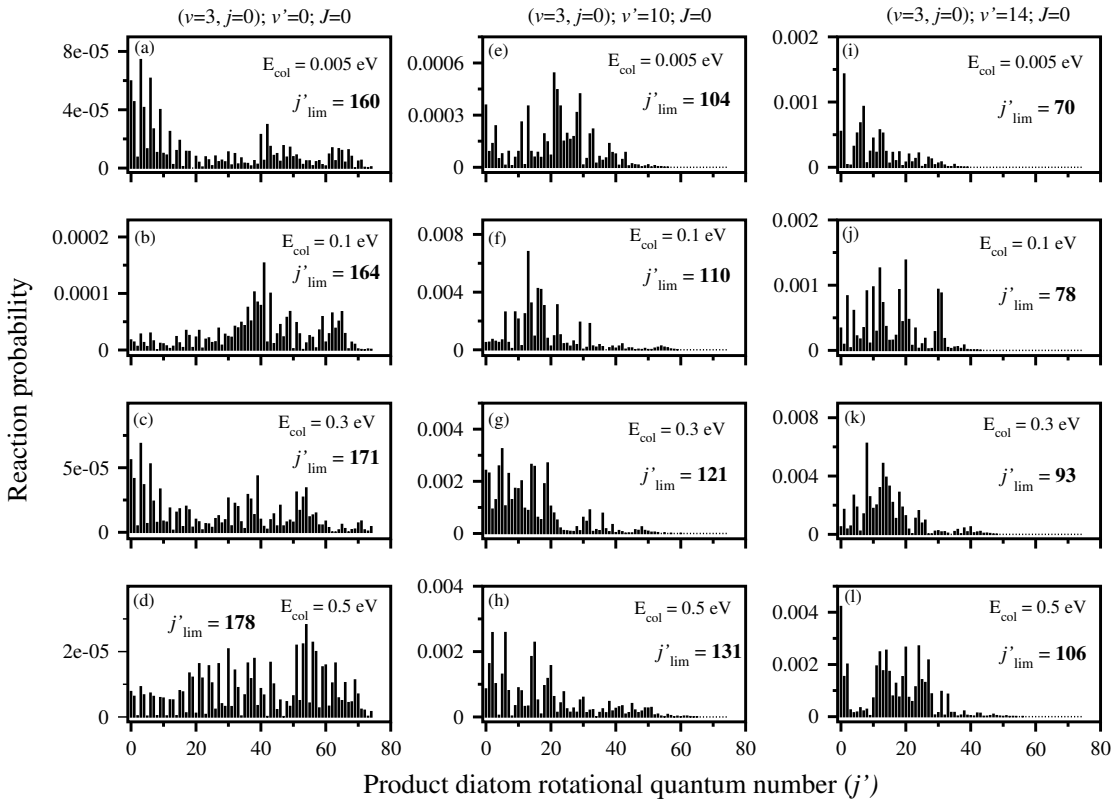

Figure 5.15: Same as in Figure 5.12, but for the S + OH (v=3, j=0) → SO (v'=0, 10, 14, j') + H reaction. The j'_{lim} values are given in each panel to show the energetic limit.

energy favors the formation of rotationally excited products for v'=0 as is found for OH (v=0, j=0) in FIG. 5.14. However, it can be seen form panels (e)-(l) of Figure 5.15 that the collision energy does not flow effectively to product rotation when the product is excited to v'=10 and 14 levels. In this case, the j'_{max} values of the distributions are much below the j'_{lim} values (shown inside each panel of Figure 5.15) leading to colder distributions in highly excited v' levels. In summary the relative translational energy of the reagent effectively flows to product rotation when the product is formed in lower vibrational levels, whereas, the translational energy is not disposed to product rotation for highly vibrationally excited products. Thus, the dynamics followed by the reactive system to produce the products in lower and higher vibrational levels is different for the vibrationally excited.

5.3.3 Energy disposal mechanism

In order to understand the overall energy disposal mechanism of the reaction, the average fraction of the available energy entering into product vibration, rotation and translation have been calculated for J=0. The results are presented in Figure 5.16 as a function of collision energy up to 0.5 eV for reagent OH (v=0-3, j=0) to show the effect of vibrational excitation of the reagent. One general feature can be seen from Figure 5.16(a)-(d)

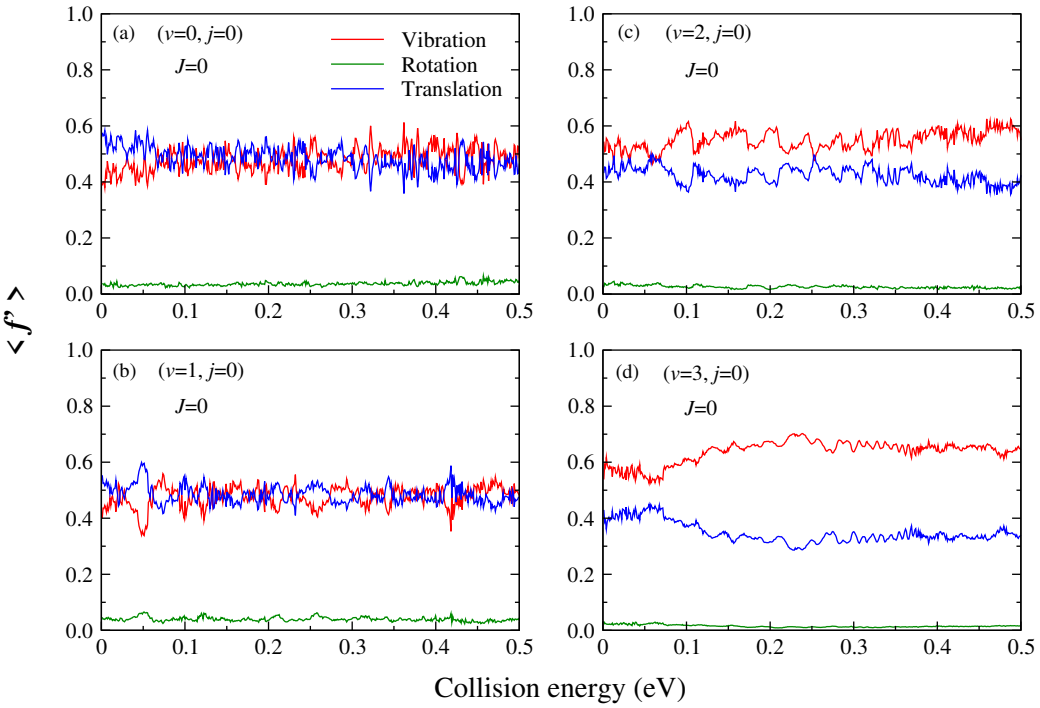

Figure 5.16: Average fraction of the available energy disposal into product vibration (red), rotation (green) and translation (blue) for J=0 in the S + OH (v=0-3, j=0) → SO ($\sum v'$, $\sum j'$) + H reaction as a function of collision energy. The $\langle f' \rangle$ values for different vibrational levels of OH are shown in different panels.

that the available energy mostly releases as product vibration and translation for OH (v=0-3, j=0). The fraction of energy released to product rotation is very less (1% - 4%), consistent with the fact that the j' levels are not populated up to the energetic limit leading to a relatively colder rotational distributions of product (cf., Figs. 5.11 – 5.15). Moreover, the slight increase of $\langle f'_R \rangle$ values for OH (v=0-2, j=0) at higher collision energies agree with the finding that the product rotational distribution becomes hotter with increase in collision energy. For OH (v=0-1, j=0) [cf., Figure 5.16(a)-(b)], the $\langle f'_V \rangle$ and $\langle f'_T \rangle$ are almost same ($\approx$ 50%) throughout the collision energy range. However, with reagent vibrational excitation to (v=2-3, j=0) levels [cf., Figure 5.16(c)-(d)], the fraction of energy going to product vibration increases and that going to product translation decreases throughout the collision energy range. Hence, it can be concluded that the

extra energy supplied in terms of reagent vibration predominantly flows to the product vibration. The effect of collision energy on the overall energy disposal mechanism is found to be insignificant for OH (v=0-1, j=0). However, for vibrationally excited OH, a slight increase in $\langle f'_V \rangle$ and a slight decrease in $\langle f'_T \rangle$ values can be seen with increase in collision energy. The oscillations in the $\langle f'_V \rangle$ and $\langle f'_T \rangle$ values as a function of collision energy actually originates due to the resonance oscillations found in the reaction probabilities for J=0. One interesting observation that can be noted here is the interplay of the vibration and translation energy release in products. It can be seen from Figure 5.16(a)-(d) that the variation of $\langle f'_V \rangle$ values as a function of collision energy is exactly opposite to that of $\langle f'_T \rangle$ values. Such an observation has been made also for the N + OH → NO + H reaction [281].

5.3.4 Differential Cross Section

The DCSs, both total and product state-resolved, calculated for OH (v=0, j=0) are presented and discussed in this section. Moreover, the role of the interference among the partial wave towards the DCS is also examined. The initial state-selected total DCSs for reagent OH (v=0, j=0) are shown in panesls (a) and (b) of Figure 5.17 as a function of center-of-mass scattering angle (θ) at E_{col} = 0.005 and 0.01 eV. The DCSs (black solid lines) show peaks at extreme forward and backward regions with small intensity in the sideways direction. This behavior is expected and generally appears in complex-forming reactions [242, 243]. It can be seen that at E_{col} = 0.005 eV [cf., Figure 5.17(a)], the backward peak is ~1.5 times greater than the forward one leading to a backward baised asymmetric forward-backward scattering. However, at E_{col} = 0.01 eV [cf., Figure 5.17(b)], the total DCS looks symmetric with respect to θ = 90° and the forward and backward peaks have almost equal magnitude. The forward-backward symmetric nature of the total DCS is well known for reactions proceeding via the formation of long-lived collision complexes and mostly it is related to the statistical nature of the complex-forming reactions. This turns out to be the case for the present, S + OH → SO + H, reaction which proceeds through two fairly deep wells on the underlying PES. However, the extent of the forward-backward symmetry can be highly dependent on the collision energy and the asymmetry in the total DCS can be found even with a small change in E_{col} [129, 130]. Moreover, the interference among various partial waves, which is neglected in the statistical limit due to the random phase approximation (RPA) [44], can result into the asymmetric nature. It was shown in Ref. [75] that the interference can be significant at state-to-state level in the quantum limit especially around

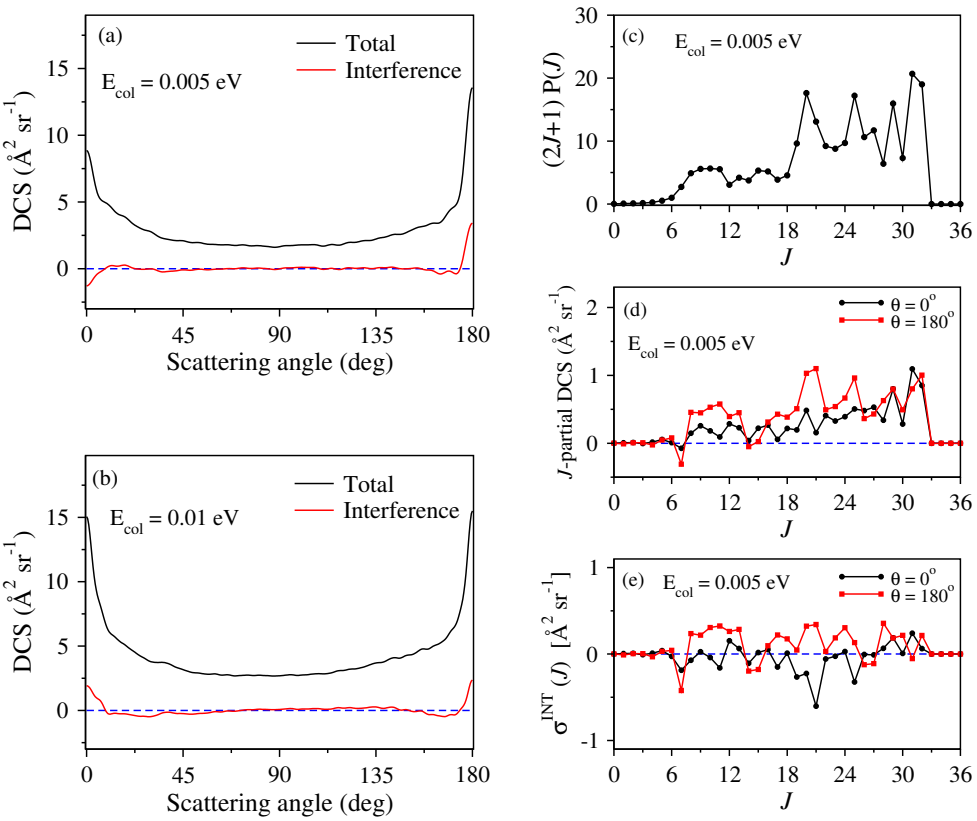

Figure 5.17: Total DCSs and DCS due to interference between partial waves (panels a and b) for the S + OH (v=0, j=0) → SO ($\sum v'$, $\sum j'$, $\sum \Omega'$) + H reaction as a function of θ at E_{col} = 0.005 and 0.01 eV. The ppacity function, (2J+1)P(J), summed over all final states (panel c) as a function of J at E_{col} = 0.005 eV. J-partial DCS as a function of J (panel d) for forward (θ = 0°) and backward (θ = 180°) scattering at E_{col} = 0.005 eV. Interference at θ = 0° and 180° as a function of J (panel e) for E_{col} = 0.005 eV. The blue color dashed line represents zero along the abscissa.

the extreme forward and backward regions even though the summed-over DCSs show forward-backward symmetry. In the present case, the asymmetric nature of the total DCS at E_{col} = 0.005 eV is examined with respect to inherent interference effects of the various partial waves. For this, the interference term among the partial waves is calculated by the equation 2.53. It is important to note here that the interference terms can have both positive and negative values corresponding to constructive and destructive interference among the partial waves [76, 286]. Moreover, these can be plotted along θ to illustrate the type of interference. The initial state-selected total (summed-over) interference terms for OH (v=0, j=0) are shown in panel (a) and (b) of Figure 5.17 by red color solid line. It can be seen that the interference terms are nearly zero in the sideways direction (30°< θ <155°) at both the collision energies. However, these terms are significant around the extreme forward and backward regions. At E_{col} = 0.005 eV, the positive value of the interference terms around θ = 180° denotes the constructive

interference and the negative values around $\theta = 0°$ denote the destructive interference among various partial waves. Therefore, the interference terms around $\theta = 0°$ and 180° affect the DCS in opposite way leading to a backward baised forward-backward asymmetry. However, at E_{col} = 0.01 eV, the interference terms both around $\theta = 0°$ and 180° are positive and are constructive in nature with almost equal magnitude. This results into a forward-backward symmetric DCS at E_{col} = 0.01 eV. We note here that the DCS due to RPA (in the statistical limit) are not shown here since these are by definition symmetric with respect to $\theta = \pi/2$ and hence do not affect the DCS qualitatively.

In order to understand more about the interference effects at E_{col} = 0.005 eV, the contribution of different partial waves towards the total DCS is examined. This is done by calculating the J-partial DCSs for specific J values at $\theta = 0°$ and 180°. The results are shown in Figure 5.17(d) as a function of J. The J-partial DCSs calculated here include the coherence terms of a specific J among others due to which these can take negative values. Moreover, the opacity function, $(2J+1)P(J)$, calculated at E_{col} = 0.005 eV is plotted in Figure 5.17(c) as a function J. It can be seen that the higher partial waves (J = 6-32) mostly contribute to the reactivity. Figure 5.17(d) shows the contribution of each J towards the forward and backward scattering at E_{col} = 0.005 eV. It can be seen that almost all $J > 7$, except J = 14, 17 for forward and J = 14, 15 for backward scattering, contribute to the DCS at $\theta = 0°$ and 180°, respectively. This is expected for a deep well complex-forming reaction, where all partial waves seem to contribute at each θ, which is in contrast to direct reactions where a one-to-one correlation between J and θ exists [76]. The partial waves, J = 26-32 contribute equally towards the forward and backward scattering. However, the partial waves, J = 8-13 and 17-25, contribute more towards backward scattering than the forward one resulting into the asymmetric feature of the total DCS. Figure 5.17(e) displays the nature of interference among the various partial waves at $\theta = 0°$ and 180° for E_{col} = 0.005 eV. The J-dependent interference term, $\sigma^{INT}(J)$, can be obtained from equation 2.53 by omitting the first summation over J. It is found that all partial waves, except J = 7, 14, 15, 26, 27 and 31 interfere constructively among others at θ = 180°. This in contrast to $\theta = 0°$, where most of the partial waves interfere destructively, except J = 12, 13, 16, 28, 29, 31 and 32. This interference effect is reflected in the total DCS of OH (v=0, j=0) at E_{col} = 0.005 eV [cf., Figure 5.17(a)].

The product vibrational level resolved DCSs for reagent OH (v=0, j=0) are shown in Figure 5.18 at E_{col} = 0.005 eV. Moreover, the DCS due to interference among the partial waves are resolved for each v' level and are shown in the figure by red color solid line. It can be seen that v' = 0, 4 (and also 5 and 6 which are not shown here for

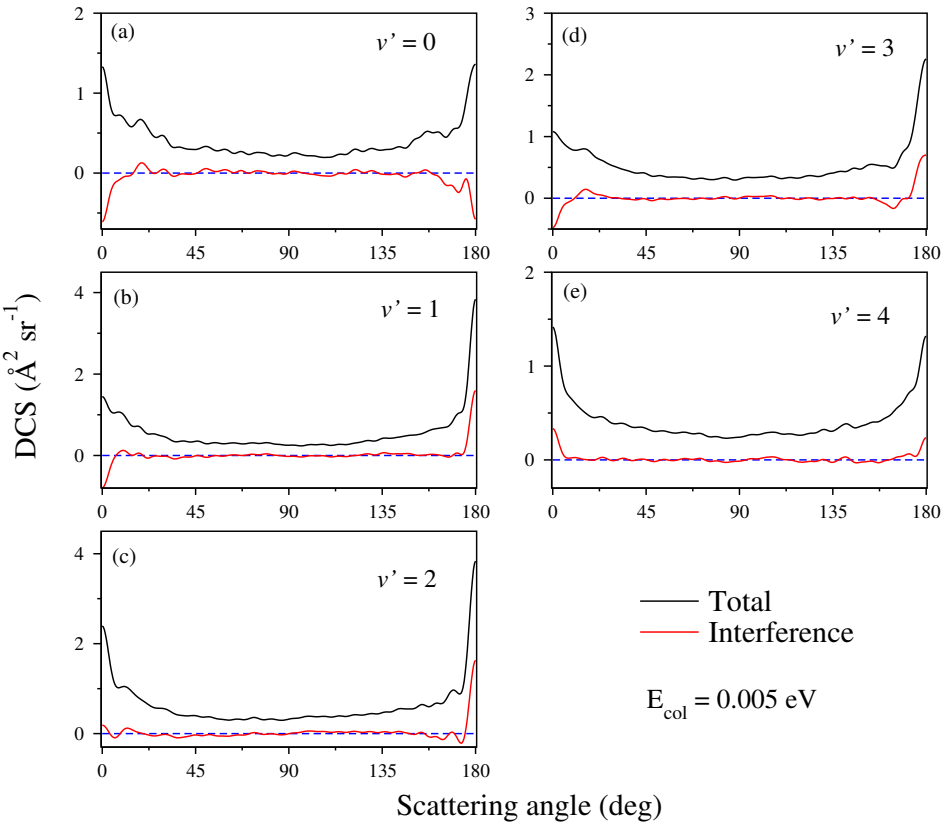

Figure 5.18: Product vibrational level resolved DCSs and DCS due to interference between partial waves for the, S + OH (v=0, j=0) → SO (v', $\sum j'$, $\sum \Omega'$) + H, reaction as a function of center-of-mass scattering angle (θ) at E_{col} = 0.005 eV. The blue color dashed line represents zero along the abscissa.

brevity) show near forward-backward symmetric DCS. However, for v' = 1, 2 and 3, the DCS is baised towards backward scattering. This baisness is because of the constructive interference of the partial waves around θ = 180° and destructive interference around θ = 0° [cf., Figure 5.18(b)-(d)]. Therefore, the asymmetry in the total DCS at E_{col} = 0.005 eV is found to be originated mainly from v' = 1-3 levels of product.

The product rotational level resolved DCSs for the S + OH (v=0, j=0) → SO (v', j', $\sum \Omega'$) + H reaction at E_{col} = 0.005 eV are shown in Figure 5.19 in terms of three dimensional perspective plot. The state-to-state DCSs are shown here as a function of θ and j' for various v' levels of product SO. It can be seen that similar to the total and v'-resolved DCS, the j'-resolved state-to-state DCSs are peaked at the extreme forward and backward regions with a very little intensity in the sideways direction. There is no direct correlation between j' and θ and the feature of the perspective plots is highly selective to each v' level. As can be seen from Figure 5.19, for v' = 0, the rotationally cold products are mostly forward-backward symmetric and the rotationally hot products are dominantly scattered to either forward or backward direction. However, for v' = 1,

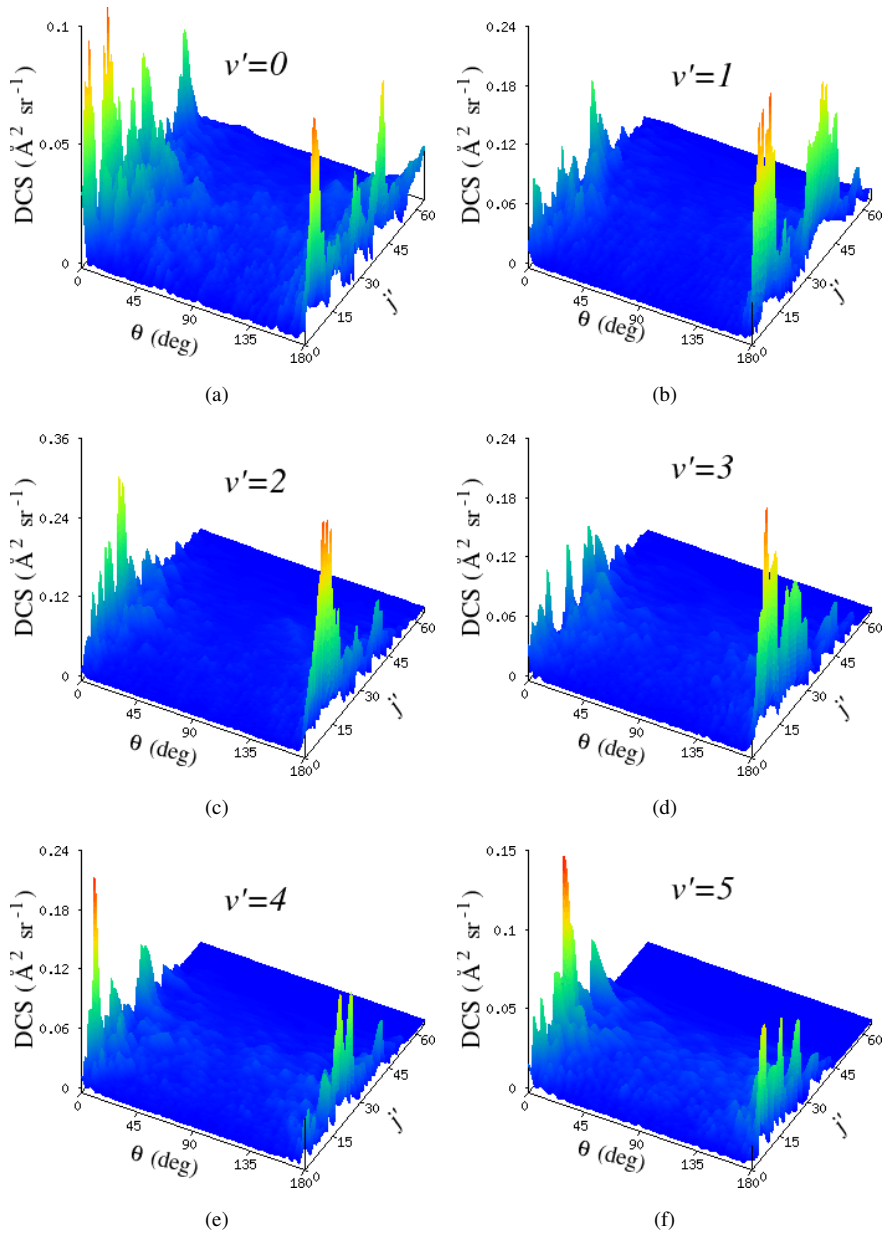

Figure 5.19: Three dimensional perspective plots of product rotational level resolved state-to-state DCSs of the S + OH (v=0, j=0) → SO (v'=0-5, j', $\sum\Omega'$) + H reaction at E_{col} = 0.005 eV shown as a function of θ and j'.

2 and 3, the products are mostly backward scattered with a small forward scattering for few selected product states. For $v' = 4$ and 5, the DCSs are either forward or backward dominated which depends highly on the j' value. It is found that the state-to-state DCSs are somewhat symmetric with respect to θ=π/2 for some specific product states and are also dominated to either forward or backward directions for few other product states. A pure forward-backward symmetry, as seen in the total DCS [cf., Figure 5.17(b)], is not found when the DCS is resolved into rotational levels of products. This is because the interferences among the partial waves, as shown by Larrégaray and Bonnet [75], becomes significant with strong oscillatory structure at the state-to-state level, especially around $\theta = 0°$ and 180°. However, the forward-backward symmetry is recovered when the state-to-state DCSs are summed over product quantum states [75] [cf., Figure 5.17(b)].

5.4 Summary

A comprehensive state-to-state quantum dynamical study of the S + OH → SO + H reaction is presented in this chapter. The calculations are carried out by employing a RWP based TDWP approach (cf., section 2.1) on the *ab initio* electronic ground DMBE PES [249]. Total and state-to-state reaction probabilities, ICSs and DCSs are calculated including the Coriolis coupling terms present in the nuclear Hamiltonian. Product vibrational and rotational distributions at few selected collision energies are also presented in terms of reaction probability and ICS. The effect collision energy and reagent vibrational and rotational excitation on the state-to-state reaction probabilities is examined in order to understand the mechanistic details of the reaction. Fractions of available energy entering into product vibration, rotation and translation are also calculated to elucidate the energy disposal mechanism.

The total and state-to-state reaction probabilities exhibit resonance oscillations which are due to the formation of quasi-bound collision complexes supported by the two fairly deep potential wells on the underlying PES. The reactivity is found to increase with reagent vibrational excitation and decrease with reagent rotational excitation. The effect of CC underestimates the reactivity at low collision energies and becomes more important with increasing J. Despite having two potential wells on the PES, purely statistical product vibrational distribution is not found for J=0 which primarily suggests that the reaction may not follow an entirely indirect mechanistic pathway. The available energy mainly goes to product vibration and translation, and very less to product

rotation. The effect of collision energy on the overall energy disposal mechanism is found to be insignificant for lower vibrational levels of reagent, whereas, a mild effect of the former is found when the reagent OH is excited to higher vibrational levels. It is found that the product rotational levels are not populated up to the energetic limit resulting into a relatively colder rotational distributions of product. The total and state-to-state DCSs show both forward and backward scattering with a very little intensity in the sideways direction as expected for complex-forming reactions. It is shown that the forward-backward asymmetry found in the total DCS is due to the opposite interference effects among the partial waves at the extreme forward and backward regions. The products are found to be scattered in either forward, backward or both irregularly as the feature of the state-to-state DCSs highly depends on the (v', j') quantum numbers.

Chapter 6

Summary and outlook

A theoretical account of both adiabatic and nonadiabatic quantum reactive scattering of a few atom-diatom bimolecular reactions is reported in this thesis. The reactions considered in the present work are the H (D) + $LiH^+ \rightarrow H_2$ (HD) + Li^+ on its electronic ground state [92], the benchmark hydrogen-exchange reaction, H + $H_2 \rightarrow H_2$ + H, in its coupled $1E'$ electronic manifold [178, 180] and the S + OH $\rightarrow$ SO + H reaction on its electronic ground state [249] PES. The reactive dynamics of these reactions is carried out numerically by a TDWP method based on a real wave packet approach [34, 36] and using the state-of-the-art *ab initio* electronic PES available in the literature. The first three reactions are studied in the adiabatic framework where single state adiabatic state-to-state dynamics is investigated to obtain the necessary reaction observables. For the hydrogen-exchange reaction, the dynamics is studied both in the adiabatic and nonadiabatic framework in order to illustrate the effect of nonadiabatic coupling on its state-to-state reactive scattering dynamics. For this the RWP based TDWP method is modified and extended to electronic nonadiabatic picture involving two strongly coupled electronic states where the nonadiabatic state-to-state dynamics is studied in the coupled $1E'$ electronic manifold of H_3 system. The dynamical results obtained are numerically accurate as the calculations are performed without any dynamical approximation. Various reaction observables like reaction probabilities, ICS, DCS, product rovibrational level distribution and thermal rate constants for the above mentioned reactions are calculated and reported in this thesis. A few of them are also compared with the previous theoretical and experimental results available in the literature. The energy disposal mechanism of the reactions is examined by calculating the fractions of available energy entering into different degrees of freedom of products. Moreover, the

scattering mechanism of the reactions is examined by analyzing the partial wave contributions to the DCS. The interference terms due to the coherence among the partial waves are quantified which is used to distinguish any non-statistical nature of the reactions. The effect of rovibrational excitation of the reagent diatom on various reaction observables and hence on the reaction mechanism is also examined.

The resonance oscillations seen in the reaction probabilities of the $H + LiH^+ \rightarrow H_2 + Li^+$ reaction are found to be cancelled out in the ICS when summed over all partial waves. This resulted an excellent agreement of the present QM-CC ICS with the previous QCT ICS results on the same PES in the whole collision energy range considered here, which is expected for this barrierless reaction. The total ICS is found to decrease with rovibrational excitation of the reagent and with increasing collision energy, reflecting the barrierless nature of the minimum energy path. The reactivity of the reaction is found to increase with the substitution of heavier isotope on the attacking atom. The products form in highly excited vibrational levels with inverse Boltzmann population distribution which is expected according to Polanyi's rule [53, 54] because of the "attractive" nature of the reaction path. It is found that a large portion of the available energy is partitioned into the product vibration, and a very less amount of energy flows into product rotation and translation. The behaviour of the state-to-state DCSs is found to be different for the low and high collision energy regime, and also it is found to be insensitive to the rovibrational excitation of the reagent diatom. It is found that the forward-backward asymmetry in the total and state-to-state DCSs arises due to the constructive and destructive interference between various partial waves. Significant interference is found in the reaction, both at the state-to-state and total DCS levels, indicating its non-statistical nature to a considerable extent. The reaction mainly follows a direct stripping mechanism at higher collision energies and a mixture of direct and indirect mechanisms at lower collision energies, which is deduced by analyzing the partial wave contributions to the total DCSs.

The nonadiabatic dynamical calculations of the $H + H_2 \rightarrow H_2 + H$ reaction are carried out in a quasi-diabatic representation for the vibrationally excited reagent H_2 (v=3,4, j=0). For this the diabatic Hamiltonian is constructed from the adiabatic PESs and by considering the ADT angle within the linear as well as the quadratic coupling approximation. However, the effect of the quadratic term is found to be very small and it does not affect the dynamics at energies where the nonadiabatic effects are important. A minimal participation of the upper adiabatic state is found even for vibrationally excited reagent. Nonadiabatic effect shows up in the state-to-state DCSs in the form of

"out-of-phase" oscillations between the uncoupled and coupled surface results. These oscillations are found as a function of both the scattering angle as well as the collision energy. The "out-of-phase" behaviour of the oscillations arises due to the change in sign of the interference term between the 1-TS and 2-TS paths as a result of the GP which could exactly be infered by calculating the 1-TS and 2-TS contributions with the inclusion of the interference term between them. Such oscillations in the forward scattering region are found to be different from those due to the glory interference. In fact the glory oscillations showed negligibly small nonadiabatic effect. In the energy dependence of both backward and forward scattering of state-resolved products, the amplitude of these "out-of-phase" oscillations is found be nearly directly proportional to the magnitude of the 2-TS path contribution. It is found that the nonadiabatic effects in state-to-state reaction probabilities and state-to-state DCSs get reduced to a considerable extent when summed over all the product quantum levels. The effect of successive vibrational excitation of the reagent diatom on the scattering mechanism of the H + H_2 $\rightarrow$ H_2 + H reaction is also examined. Vibrational excitation of the reagent is found to enhance the forward scattering of the products and decreases the backward scattering. The forward scattering mainly comes from the higher partial waves. It is found that increase in collision energy reduces the vibrational excitation of the backward scattered products to a large extent but not in case of forward scattered products. This is due to the fact that lost vibrational energy goes to the product rotation of the backward scattered products. Two different mechanisms corresponding to two contrasting phenomena are noticed while analyzing the product rotational level resolved DCSs. One is the well known "*negative* $j' - \theta$ *correlation*" in the backward hemisphere and the other one is the newly found "*positive* $j' - \theta$ *correlation*" in the forward scattering. The underlying mechanisms of these two phenomena are found to be different. The former one is due to a coplanar detachment mechanism involving glancing collisions, whereas, the latter one is due to a non-coplanar detachment mechanism involving high impact parameter collisions. The effect of reagent rotation (up to j=3) on the overall dynamics of the reaction is found to be not so significant.

The total as well as state-to-state reaction probabilities of the S + OH $\rightarrow$ SO + H reaction are found to exhibit sharp resonance oscillations. These are due to the formation of quasi-bound collision complexes supported by the two fairly deep potential wells on the underlying PES of HSO reactive system. The reactivity is found to increase with reagent vibrational excitation, however, it decreases with reagent rotational excitation. The inclusion of coriolis coupling is found to be important for higher partial waves

where it underestimates the reactivity. A purely statistical product vibrational distribution is not found for J=0 case which primarily suggests that the reaction may not follow an entirely indirect mechanistic pathway. The available energy mainly goes to product vibration and translation, and very less to product rotation for J=0 case. It is found that the product rotational levels are not populated up to the energetic limit resulting into a relatively colder rotational distributions of product. The total and state-to-state DCSs show both forward and backward scattering with a very little magnitude in the sideways direction. This is expected for this complex-forming reaction. It is shown that the forward-backward asymmetry found in the total DCS is due to the opposite interference effects among the partial waves at the extreme forward and backward regions. The products are found to be scattered in either forward, backward or both irregularly as the feature of the state-to-state DCSs is found to highly depend on the (v', j') quantum numbers of the product.

To this end we note that the present observations of these reaction reported in this thesis encourage some future studies. First of all for the $H + LiH^+ \rightarrow H_2 + Li^+$ reaction, seeking a desired agreement bewteen the QM and QCT results, particularly ICSs and rate constant, is necessary at the state-to-state level and also for other isotopic variants of the reaction. This is due to the fact the QCT calculations are computationally very less expensive as compared to the TDWP or TIQM calculations, due to which this method can be used with ease to obtain the accurate ICSs and rate constants of these astrophysically relevant processes for numerous number of initial states of reagent. Hence, a good agreement between the QM and QCT results can give us the confidence to accurately model the corresponding chemical reaction network of the reaction only by using the QCT data. Next, from a mechanistic point of view quantum mechanical studies on the stereodynamics of the reaction can reveal interesting observations regarding the product polarization, as all of the stereodynamical studies on this reaction so far are based on the QCT method. Similarly for the S + OH reaction, computation of accurate cross sections and rate constants for a wide range of energy and temperature are necessary for astrochemical application. In this regard, a combined QCT and QM study may become valuable.

It is obvious that the benchmark $H + H_2 \rightarrow H_2 + H$ reaction is no longer now a "simple" one, after encountering so much of unforeseen and phenomenal observations. However, there is still room for more. Particularly, the reactive scattering experiments

with rovibrationally excited reagent are yet to be explored. In this respect, several attempts have recently been made to efficiently prepare the reagent H_2 diatom and its isotopic cousins in the excited rovibrational states by the SARP technique and they have been successful [287–291]. Therefore, theoretical calculations of the isotopic variants of this reaction with rovibrationally excited reagent can be performed with the inclusion of GP and nonadiabatic effect up to the three-body dissociation energetic limit for a meaningful comparison with experiments. This may reveal more interesting feature of the reaction. Another aspect can be to quantify the GP or nonadiabatic effect for each of the product levels so as to see how much these effects influence the dynamics of the state-resolved products.

Bibliography

[1] R. D. Levine, *Molecular Reaction Dynamics*, Cambridge University Press, New York, 2005.

[2] D. J. Auerbach, J. C. Tully, and A. M. Wodtke, Nat Sci. **1**, e10005 (2021).

[3] J. Li, B. Zhao, D. Xie, and H. Guo, J. Phys. Chem. Lett. **11**, 8844 (2020).

[4] Y. Liu and K.-K. Ni, Annu. Rev. Phys. Chem. **73**, 73 (2022).

[5] J. T. Hynes, Annu. Rev. Phys. Chem. **36**, 573 (1985).

[6] E. T. Nibbering, H. Fidder, and E. Pines, Annu. Rev. Phys. Chem. **56**, 337 (2005).

[7] M. Brouard and C. Vallance, *Tutorials in Molecular Reaction Dynamics*, RSC Publishing, UK, 2011.

[8] N. E. Shafer-Ray, A. J. Orr-Ewing, and R. N. Zare, J. Phys. Chem. **99**, 7591 (1995).

[9] M. Brouard, S. Duxon, P. A. Enriquez, and J. P. Simons, J. Chem. Soc. Faraday Trans. **89**, 1435 (1993).

[10] F. J. Aoiz, M. Brouard, P. A. Enriquez, and R. Sayos, J. Chem. Soc. Faraday Trans. **89**, 1427 (1993).

[11] N. E. Shafer, A. J. Orr-Ewing, W. R. Simpson, H. Xu, and R. N. Zare, Chem. Phys. Lett. **212**, 155 (1993).

[12] A. J. O.-E. William R. Simpson and R. N. Zare, Chem. Phys. Lett. **212**, 163 (1993).

[13] T. Yang et al., Nat. Chem. **11**, 744 (2019).

[14] N. Mukherjee, W. E. Perreault, and R. N. Zare, Chapter 1 - stark-induced adiabatic passage processes to selectively prepare vibrationally excited single and superposition of quantum states, in *Frontiers and Advances in Molecular Spectroscopy*, edited by J. Laane, pages 1–46, Elsevier, 2018.

[15] H. Zhou, W. E. Perreault, N. Mukherjee, and R. N. Zare, Science **374**, 960 (2021).

[16] W. E. Perreault, H. Zhou, N. Mukherjee, and R. N. Zare, Frontiers in Physics **9** (2021).

[17] H. Zhou, W. E. Perreault, N. Mukherjee, and R. N. Zare, J. Chem. Phys. **154**, 104309 (2021).

[18] X. Yang, Annu. Rev. Phys. Chem. **58**, 433 (2007).

[19] M. Born and R. Oppenheimer, Ann. Phys. **84**, 457 (1927).

[20] P. O. Dral, J. Phys. Chem. Lett. **11**, 2336 (2020).

[21] W. Domcke, D. R. Yarkony, and H. Köppel, *Conical Intersections: Electronic Structure, Dynamics and Spectroscopy*, World Scientific, Singapore, 2004.

[22] S. Mahapatra, Int. Rev. Phys. Chem. **23**, 483 (2004).

[23] T.-S. Chu, Y. Zhang, and K.-L. Han, Int. Rev. Phys. Chem. **25**, 201 (2006).

[24] B. K. Kendrick, J. Chem. Phys. **148**, 044116 (2018).

[25] B. K. Kendrick, Chem. Phys. **515**, 387 (2018).

[26] B. K. Kendrick, J. Phys. Chem. A **123**, 9919 (2019).

[27] B. K. Kendrick et al., Phys. Chem. Chem. Phys. **23**, 5096 (2021).

[28] W. Lichten, Phys. Rev. **131**, 229 (1963).

[29] F. T. Smith, Phys. Rev. **179**, 111 (1969).

[30] R. G. Newton, *Scattering Theory of Waves and Particles*, Springer-Verlag, New York, 1982.

[31] S. Gomez-Carrasco and O. Roncero, J. Chem. Phys. **125**, 054102 (2006).

[32] Z. Sun, X. Lin, S.-Y. Lee, and D. H. Zhang, J. Phys. Chem. A **113**, 4145 (2009).

[33] Z. Sun, H. Guo, and D. H. Zhang, J. Chem. Phys. **132**, 084112 (2010).

[34] S. K. Gray and G. G. Balint-Kurti, J. Chem. Phys. **108**, 950 (1998).

[35] S. Y. Lin and H. Guo, Phys. Rev. A **74**, 022703 (2006).

[36] M. Hankel, S. C. Smith, R. J. Allan, S. K. Gray, and G. G. Balint-Kurti, J. Chem. Phys. **125**, 164303 (2006).

[37] T. Peng and J. Z. H. Zhang, J. Chem. Phys. **105**, 6072 (1996).

[38] S. C. Althorpe, J. Chem. Phys. **114**, 1601 (2001).

[39] R. Welsch, F. Huarte-Larranaga, and U. Manthe, J. Chem. Phys. **136**, 064117 (2012).

[40] R. Welsch and U. Manthe, J. Chem. Phys. **140**, 244113 (2014).

[41] B. Zhao, Z. Sun, and H. Guo, J. Chem. Phys. **140**, 234110 (2014).

[42] J. Huang, S. Liu, and D. H. Z. R. V. Krems, Phys. Rev. Lett. **120**, 143401 (2018).

[43] W. H. Miller, J. Chem. Phys. **52**, 543 (1970).

[44] E. J. Rackham, T. González-Lezana, and D. E. Manolopoulos, J. Chem. Phys. **119**, 12895 (2003).

[45] R. B. Bernstein, A. Dalgarno, H. Massey, and I. C. Percival, Proc. R. Soc. Lond. A **274**, 427 (1963).

[46] P. Pechukas and J. C. Light, J. Chem. Phys. **42**, 3281 (1965).

[47] P. Pechukas, J. C. Light, and C. Rankin, J. Chem. Phys. **44**, 794 (1966).

[48] E. J. Rackham, F. Huarte-Larranaga, and D. E. Manolopoulos, Chem. Phys. Lett. **343**, 356 (2001).

[49] S. Y. Lin and Guo, J. Chem. Phys. **120**, 9907 (2004).

[50] T. González-Lezana, Int. Rev. Phys. Chem. **26**, 29 (2007).

[51] S. C. Althorpe and D. C. Clary, Annu. Rev. Phys. Chem. **54**, 493 (2003).

[52] D. H. Zhang and H. Guo, Annu. Rev. Phys. Chem. **67**, 135 (2016).

[53] J. C. Polanyi, Acc. Chem. Res. **5**, 161 (1972).

[54] J. C. Polanyi, Science **236**, 680 (1987).

[55] S. Mahapatra, H. Köppel, and L. S. Cederbaum, J. Phys. Chem. A **105**, 2321 (2001).

[56] S. K. Gray, J. Chem. Phys. **96**, 6543 (1992).

[57] R. Chen and H. Guo, J. Chem. Phys. **105**, 3569 (1996).

[58] G. G. Balint-Kurti, A. I. Gonzalez, E. M. Goldfield, and S. K. Gray, Faraday Discuss. **110**, 169 (1998).

[59] G. G. Balint-Kurti, Int. Rev. Phys. Chem. **27**, 507 (2008).

[60] M. Hankel, G. G. Balint-Kurti, and S. K. Gray, Int. J. Quant. Chem. **92**, 205 (2003).

[61] D. T. Colbert and W. H. Miller, J. Chem. Phys. **96**, 1982 (1992).

[62] A. R. Edmonds, *Angular Momentum in Quantum Chemistry*, Princeton University Press, Princeton, 1960.

[63] R. N. Zare, *Angular Momentum*, Willey, New York, 1988.

[64] D. Kosloff and R. Kosloff, J. Comput. Phys. **52**, 35 (1983).

[65] J. C. Light, I. P. Hamilton, and J. V. Lill, J. Chem. Phys **82**, 1400 (1985).

[66] J. V. Lill, G. A. Parker, and J. C. Light, Chem. Phys. Lett. **89**, 483 (1982).

[67] I. P. Hamilton and J. C. Light, J. Chem. Phys. **84**, 306 (1986).

[68] M. Hankel, S. C. Smith, S. K. Gray, and G. G. Balint-Kurti, Comput. Phys. Commun. **179**, 569 (2008).

[69] I. Miquel et al., J. Chem. Phys. **118**, 3111 (2003).

[70] H. Köppel, W. Domcke, and L. S. Cederbaum, Adv. Chem. Phys. **57**, 59 (1984).

[71] R. Englman, *The Jahn-Teller Effect in Molecules and Crystals*, Wiley, New York, 1972.

[72] J. Z. H. Zhang and W. H. Miller, J. Chem. Phys. **91**, 1528 (1989).

[73] B. J. Rao, R. Padmanaban, and S. Mahapatra, Chem. Phys. **333**, 135 (2007).

[74] T. R. Rao, B. J. Rao, and S. Mahapatra, Chem. Phys. **365**, 129 (2009).

[75] P. Larrégaray and L. Bonnet, J. Chem. Phys. **143**, 144113 (2015).

[76] P. G. Jambrina, M. Menéndez, and F. J. Aoiz, Chem. Sci. **9**, 4837 (2018).

[77] A. N. Panda et al., Phys. Chem. Chem. Phys. **14**, 13067 (2012).

[78] S. Goswami, T. R. Rao, S. Mahapatra, B. Bussery-Honvault, and P. Honvault, J. Phys. Chem. A **118**, 5915 (2014).

[79] T. R. Rao, S. Goswami, S. Mahapatra, B. Bussery-Honvault, and P. Honvault, J. Chem. Phys. **138**, 094318(1 (2013).

[80] S. Goswami, B. Bussery-Honvault, P. Honvault, and S. Mahapatra, Mol. Phys. **115**, 2658 (2017).

[81] S. Mahapatra and N. Sathyamurthy, J. Chem. Soc., Faraday Trans **93**, 773 (1997).

[82] D. Galli and F. Palla, Astron. Astrophys. **335**, 403 (1998).

[83] S. Lepp, P. C. Stancil, and A. Dalgarno, J. Phys. B: At. Mol. Opt. Phys. **35**, R57 (2002).

[84] D. Galli and F. Palla, Annu. Rev. Astron. Astrophys. **51**, 163 (2013).

[85] R. Güsten et al., Nature **568**, 357 (2019).

[86] S. Lepp, Nat. Astron. **3**, 382 (2019).

[87] P. C. Stancil and S. Lepp, Astrophys. J. **458**, 401 (1996).

[88] D. J. Searles and E. I. von Nagy-Felsobuki, Phys. Rev. A **43**, 3365 (1991).

[89] E. Bodo, F. A. Gianturco, R. Martinazzo, and M. Raimondi, Chem. Phys. **271**, 309 (2001).

[90] E. Bodo, F. A. Gianturco, R. Martinazzo, and M. Raimondi, J. Phys. Chem. A **105**, 10986 (2001).

[91] R. Martinazzo, E. Bodo, F. A. Gianturco, and M. Raimondi, Chem. Phys. **287**, 335 (2003).

[92] R. Martinazzo, G. F. Tantardini, E. Bodo, and F. A. Gianturco, J. Chem. Phys. **119**, 11241 (2003).

[93] C. Sanz, E. Bodo, and F. A. Gianturco, Chem. Phys. **314**, 135 (2005).

[94] W. P. Kraemer and V. Špirko, Chem. Phys. **330**, 190 (2006).

[95] A. J. Page and E. I. von Nagy-Felsobuki, J. Phys. Chem. A **111**, 4478 (2007).

[96] I. Pino, R. Martinazzo, and G. F. Tantardini, Phys. Chem. Chem. Phys. **10**, 5545 (2008).

[97] X. Li, M. Wang, I. Pino, C. Yang, and L. Ma, Phys. Chem. Chem. Phys. **11**, 10438 (2009).

[98] L. Duan, W. Zhang, X. Xu, S. Cong, and M. Chen, Mol. Phys. **107**, 2579 (2009).

[99] N. Bulut, J. F. Castillo, L. B. nares, and F. J. Aoiz, J. Phys. Chem. A **113**, 14657 (2009).

[100] X. H. Li et al., Chin. Chem. Lett. **21**, 376 (2010).

[101] X. Li, M. Wang, I. Pino, C. Yang, and J. Wu, Phys. Chem. Chem. Phys. **12**, 7942 (2010).

[102] S. Bovino, T. Stoecklin, and F. A. Gianturco, Astrophys. J. **708**, 1560 (2010).

[103] S. Bovino, M. Tacconi, F. A. Gianturco, and T. Stoecklin, Astrophys. J. **724**, 126 (2010).

[104] W. P. Kraemer and V. Špirko, J. Phys. Chem. A **115**, 11313 (2011).

[105] T. Roy, T. R. Rao, and S. Mahapatra, Chem. Phys. Lett. **501**, 252 (2011).

[106] E. Aslan et al., J. Phys. Chem. A **116**, 132 (2012).

[107] E. Aslan et al., Astrophys. J. **759**, 1 (2012).

[108] T. Yang, J. Yuan, D. Cheng, and M. Chen, Commun. Comput. Chem. **1**, 15 (2013).

[109] S. Gómez-Carrasco et al., Astrophys. J. **784**, 55 (2014).

[110] T. Roy and S. Mahapatra, Chem. Phys. **448**, 34 (2015).

[111] X. He, S. Lv, T. Hayat, and K. L. Han, J. Phys. Chem. A **120**, 2459 (2016).

[112] M. Dong, W. Li, D. He, and M. Chen, RSC Adv. **7**, 7008 (2017).

[113] Z. Zhu, H. Wang, and X. Wang, Mol. Phys. **117**, 340 (2019).

[114] Y. M. Li and Y. Lei, J. Theor. Comput. Chem. **19**, 2050002 (2020).

[115] H. Wu and X. He, Astrophys. J. **891**, 60 (2020).

[116] E. Bodo, F. A. Gianturco, and R. Martinazzo, J. Phys. Chem. A **105**, 10994 (2001).

[117] W. A. L. Jr., J. Chem. Phys. **53**, 1511 (1970).

[118] W. A. L. Jr., J. Chem. Phys. **54**, 3179 (1971).

[119] W. Kutzelnigg, V. Staemmler, and C. Hoheisel, Chem. Phys. **1**, 27 (1973).

[120] R. Martinazzo, A. Famulari, M. Raimondi, E. Bodo, and F. A. Gianturco, J. Chem. Phys. **115**, 2917 (2001).

[121] B. Jiang and H. Guo, J. Chem. Phys. **138**, 234104 (2013).

[122] H. Guo and B. Jiang, Acc. Chem. Res. **47**, 3679 (2014).

[123] B. Jiang, J. Li, and H. Guo, J. Chem. Phys. **140**, 034112 (2014).

[124] J. Yuan, D. He, and M. Chen, Phys. Chem. Chem. Phys. **17**, 11732 (2015).

[125] M. Gustafsson and R. T. Skodje, J. Chem. Phys. **124**, 144311 (2006).

[126] N. D. Silva, B. Njegic, and M. S. Gordon, J. Phys. Chem. A **115**, 3272 (2011).

[127] X. He, H. Wu, P. Zhang, and Y. Zhang, J. Phys. Chem. A **119**, 8912 (2015).

[128] M. Wernli, D. Caruso, E. Bodo, and F. A. Gianturco, J. Phys. Chem. A **113**, 1121 (2009).

[129] P. G. Jambrina et al., Phys. Chem. Chem. Phys. **12**, 1102 (2010).

[130] Z. Shen, J. Cao, and W. Bian, J. Chem. Phys. **142**, 164309 (2015).

[131] F. London, Z. Elektrochem **35**, 552 (1929).

[132] H. Eyring and M. Polanyi, Z. Phys. Chem. **227**, 1221 (2013).

[133] H. Eyring and S. H. Lin, *Potential Energy Surfaces*, volume VIA, chapter 3, pages 121–186, Academic Press, New York, 1974.

[134] H. Eyring, J. Chem. Phys. **3**, 107 (1935).

[135] M. G. Evans and M. Polanyi, Trans. Faraday Soc. **31**, 875 (1935).

[136] R. D. Levine and S.-F. Wu, Chem. Phys. Lett. **11**, 557 (1971).

[137] G. C. Schatz and A. Kuppermann, Phys. Rev. Lett. **35**, 1266 (1975).

[138] W. H. Miller and J. Z. H. Zhang, J. Phys. Chem. **95**, 12 (1991).

[139] F. Fernández-Alonso and R. N. Zare, Annu. Rev. Phys. Chem. **53**, 67 (2002).

[140] D. C. Chatfield, R. S. Friedman, D. G. Truhlar, B. C. Garrett, and D. W. Schwenke, J . Am. Chem. Soc. **113**, 486 (1991).

[141] D. C. Chatfield, R. S. Friedman, D. G. . Truhlar, and D. W. Schwenke, Faraday Discuss. Chem. Soc. **91**, 289 (1991).

[142] D. C. Chatfield, R. S. Friedman, D. W. Schwenke, and D. G. Truhlar, J. Phys. Chem. **96**, 2414 (1992).

[143] S. A. Harich et al., Nature **419**, 281 (2002).

[144] D. Dai et al., Science **300**, 1730 (2003).

[145] R. T. Skodje and X. Yang, Int. Rev. Phys. Chem. **23**, 253 (2004).

[146] S. C. Althorpe et al., Nature **416**, 67 (2002).

[147] B. Zhou, B. Yang, N. Balakrishnan, B. K. Kendrick, and P. C. Stancil, J. Phys. Chem. Lett. **11**, 4970 (2020).

[148] Y. Bai, B. Buren, Z. Yang, B. Zhou, and M. Chen, J. Comput. Chem. **42**, 2334 (2021).

[149] C. Xiahou and J. N. L. Connor, Phys. Chem. Chem. Phys. **23**, 13349 (2021).

[150] C. Xiahou and J. N. L. Connor, J. Phys. Chem. A **125**, 8734 (2021).

[151] R. F. Lu et al., J. Chem. Phys. **125**, 133108 (2006).

[152] B. J. Rao and S. Mahapatra, Ind. J. Phys. **81**, 1003 (2007).

[153] S. Ghosal, B. J. Rao, and S. Mahapatra, J. Chem. Sci. **119**, 401 (2007).

[154] F. Bouakline, S. C. Althorpe, and D. P. Ruiz, J. Chem. Phys. **128**, 124322 (2008).

[155] B. J. Rao and S. Mahapatra, J. Chem. Sci. **121**, 789 (2009).

[156] T.-S. Chu et al., J. Chem. Phys. **130**, 144301 (2009).

[157] A. Kuppermann and Y. M. Wu, Chem. Phys. Lett. **205**, 577 (1993).

[158] B. K. Kendrick, J. Chem. Phys. **112**, 5679 (2000).

[159] B. K. Kendrick, J. Phys. Chem. A **107**, 6739 (2003).

[160] J. C. Juanes-Marcos and S. C. Althorpe, J. Chem. Phys. **122**, 204324 (2005).

[161] J. C. Juanes-Marcos, S. C. Althorpe, and E. Wrede, Science **309**, 1227 (2005).

[162] J. C. Juanes-Marcos, S. C. Althorpe, and E. Wrede, J. Chem. Phys. **126**, 044317 (2007).

[163] F. Bouakline, S. C. Althorpe, P. Larregaray, and L. Bonnet, Mol. Phys. **108**, 969 (2010).

[164] B. K. Kendrick, J. Hazra, and N. Balakrishnan, Phys. Rev. Lett. **115**, 153201 (2015).

[165] B. K. Kendrick, J. Hazra, and N. Balakrishnan, J. Chem. Phys. **145**, 164303 (2016).

[166] J. Hazra, B. K. Kendrick, and N. Balakrishnan, J. Phys. B: At. Mol. Opt. Phys. **49**, 194004 (2016).

[167] B. K. Kendrick, J. Hazra, and N. Balakrishnan, New J. Phys. **18**, 123020 (2016).

[168] B. K. Kendrick, J. Hazra, and N. Balakrishnan, J. Chem. Phys. **147**, 074302 (2017).

[169] D. Yuan et al., Science **362**, 1289 (2018).

[170] D. Yuan et al., Nat. Commun. **11**, 3640 (2020).

[171] Y. Xie et al., Science **368**, 767 (2020).

[172] D. G. Truhlar and R. E. Wyatt, Annu. Rev. Phys. Chem. **27**, 1 (1976).

[173] H. Buchenau, J. P. Toennis, J. Arnold, and J. Wolfrum, Ber. Bunsenges. Phys. Chem. **94**, 1231 (1990).

[174] F. J. Aoiz, L. Banares, and V. J. Herrero, Int. Rev. Phys. Chem. **24**, 119 (2005).

[175] R. N. Porter and M. Karplus, J. Chem. Phys. **40**, 1105 (1964).

[176] D. G. Truhlar and C. J. Horowitz, J. Chem. Phys. **68**, 2466 (1978).

[177] D. G. Truhlar and C. J. Horowitz, J. Chem. Phys. **71**, 1514 (1979).

[178] A. J. C. Varandas, F. B. Brown, C. A. Mead, D. G. Truhlar, and N. C. Blais, J. Chem. Phys. **86**, 6258 (1987).

[179] A. I. Boothroyd, W. J. Keogh, P. G. Martin, and M. R. Peterson, J. Chem. Phys. **95**, 4343 (1991).

[180] A. I. Boothroyd, W. J. Keogh, P. G. Martin, and M. R. Peterson, J. Chem. Phys. **104**, 7139 (1996).

[181] S. L. Mielke, B. C. Garrett, and K. A. Peterson, J. Chem. Phys. **116**, 4142 (2002).

[182] Y.-S. M. Wu, A. Kuppermann, and J. B. Anderson, Phys. Chem. Chem. Phys. **1**, 929 (1999).

[183] R. Abrol and A. Kuppermann, J. Chem. Phys. **116**, 1035 (2002).

[184] Z. Yin, B. J. Braams, Y. Guan, B. Fu, and D. H. Zhang, Phys. Chem. Chem. Phys. **23**, 1082 (2021).

[185] M. Qiu et al., Rev. Sci. Instrum. **76**, 083107 (2005).

[186] D. Yuan et al., Nat. Chem. **10**, 653 (2018).

[187] P. G. Jambrina et al., Nat. Chem. **7**, 661 (2015).

[188] D. Yuan et al., J. Phys. Chem. Lett. **11**, 1222 (2020).

[189] J. Jankunas et al., Proc. Natl. Acad. Sci. U.S.A **111**, 15 (2014).

[190] Y. Sun and A. Dalgarno, Astrophys. J. **427**, 1053 (1994).

[191] F. Lique, P. Honvault, and A. Faure, J. Chem. Phys. **137**, 154303 (2012).

[192] F. Lique, Mon. Not. R. Astron. Soc. **453**, 810 (2015).

[193] D. Bossion, S. Ndengué, H.-D. Meyer, F. Gatti, and Y. Scribano, J. Chem. Phys. **153**, 081102 (2020).

[194] B. Zhou et al., Mon. Not. R. Astron. Soc. **507**, 6012 (2021).

[195] R. Padmanaban, *Time-dependent Wave Packet Dynamics of H + HLi Reaction*, PhD thesis, School of Chemistry, University of Hyderabad, 2005.

[196] T. R. Rao and S. Mahapatra, J. Chem. Phys. **134**, 204307 (2011).

[197] S. Mahapatra and H. Köppel, Phys. Rev. Lett. **81**, 3116 (1998).

[198] S. Mahapatra and H. Köppel, J. Chem. Phys. **109**, 1721 (1998).

[199] G. Herzberg and H. C. Longuet-Higgins, Discuss. Faraday Soc. **35**, 77 (1963).

[200] B. Lepetit and A. Kuppermann, Chem. Phys. Lett. **166**, 581 (1990).

[201] Y. M. Wu, A. Kuppermann, and B. Lepetit, Chem. Phys. Lett. **186**, 319 (1991).

[202] B. K. Kendrick, J. Chem. Phys. **118**, 10502 (2003).

[203] L. Schnieder, K. Seekamp-Rahn, E. Wrede, and K. H. Welge, J. Chem. Phys. **107**, 6175 (1997).

[204] E. Wrede et al., J. Chem. Phys. **110**, 9971 (1999).

[205] J. Jankunas, M. Sneha, R. N. Zare, F. Bouakline, and S. C. Althorpe, J. Chem. Phys. **139**, 144316 (2013).

[206] J. Jankunas, M. Sneha, R. N. Zare, F. Bouakline, and S. C. Althorpe, Z. Phys. Chem. **227**, 1281 (2013).

[207] H. Gao, M. Sneha, F. Bouakline, S. C. Althorpe, and R. N. Zare, J. Phys. Chem. A **119**, 12036 (2015).

[208] C. A. Mead, Rev. Mod. Phys. **64**, 51 (1992).

[209] C. A. Mead and D. G. Truhlar, J. Chem. Phys. **70**, 2284 (1979).

[210] C. A. Mead, J. Chem. Phys. **72**, 3839 (1980).

[211] S. C. Althorpe, J. Chem. Phys. **124**, 084105 (2006).

[212] S. Mahapatra, Acc. Chem. Res. **42**, 1004 (2009).

[213] M. Baer, Chem. Phys. Lett. **35**, 112 (1975).

[214] M. Baer, Chem. Phys. **15**, 49 (1976).

[215] G. A. Worth and L. S. Cederbaum, Annu. Rev. Phys. Chem. **55**, 127 (2004).

[216] J. Huang and D. H. Zhang, J. Chem. Phys. **153**, 141102 (2020).

[217] F. J. Aoiz, V. J. Herrero, and V. S. Rábanos, J. Chem. Phys. **97**, 7423 (1992).

[218] F. J. Aoiz et al., J. Chem. Phys. **101**, 5781 (1994).

[219] S. J. Greaves, D. Murdock, and E. Wrede, J. Chem. Phys. **128**, 164307 (2008).

[220] D. Sokolovski, Chem. Phys. Lett. **370**, 805 (2003).

[221] J. N. L. Connor, Phys. Chem. Chem. Phys. **6**, 377 (2004).

[222] F. Fernández-Alonso, B. D. Bean, and R. N. Zare, J. Chem. Phys. **111**, 1035 (1999).

[223] F. Fernández-Alonso, B. D. Bean, and R. N. Zare, J. Chem. Phys. **111**, 2490 (1999).

[224] M. Sneha et al., J. Chem. Phys. **145**, 024308 (2016).

[225] J. Jankunas et al., Science **336**, 1687 (2012).

[226] T. C. Allison, R. S. Friedman, D. J. Kaufman, and D. G. Truhlar, Chem. Phys. Lett. **327**, 439 (2000).

[227] S. Goswami, J. Sahoo, S. K. Paul, T. R. Rao, and S. Mahapatra, J. Phys. Chem. A **124**, 9343 (2020).

[228] N. Sathyamurthy and S. Mahapatra, Phys. Chem. Chem. Phys. **23**, 7586 (2021).

[229] T. C. Thompson and C. A. Mead, J. Chem. Phys. **82**, 2408 (1985).

[230] A. Thiel and H. Köppel, J. Chem. Phys. **110**, 9371 (1999).

[231] M. S. Child, Adv. Chem. Phys. **124**, 1 (2002).

[232] C. Xiahou and J. N. L. Connor, Mol. Phys. **104**, 159 (2006).

[233] J. Sahoo, A. M. S. Rawat, and S. Mahapatra, Phys. Chem. Chem. Phys. **23**, 27327 (2021).

[234] J. Zhao et al., Chin. Phys. B **30**, 073102 (2021).

[235] C. Luo et al., J. Phys. Chem. A **126**, 4444 (2022).

[236] I. Schechter, R. D. Levine, and R. G. Gordon, J. Phys. Chem. **95**, 8201 (1991).

[237] D. Skouteris, J. F. Castillo, and D. E. Manolopoulos, Comput. Phys. Commun. **133**, 128 (2000).

[238] Y. Zheng, J. Chem. Phys. **122**, 094316 (2005).

[239] T. J. Park and J. C. Light, J. Chem. Phys. **91**, 974 (1989).

[240] E. Herbst, H. H. Lee, D. A. Howe, and T. J. Millar, Mon. Not. R. Astron. Soc. **268**, 335 (1994).

[241] J. Daranlot et al., Science **334**, 1538 (2011).

[242] F. J. Aoiz, L. B. nares, and V. J. Herrero, J. Phys. Chem. A **110**, 12546 (2006).

[243] H. Guo, Int. Rev. Phys. Chem. **31**, 1 (2012).

[244] C. A. Gottlieb, E. W. Gottlieb, M. M. Litvak, J. A. Ball, and H. Penfield, Astrophys. J. **219**, 77 (1978).

[245] S. S. Prasad and W. T. H. Jr., Astrophys. J. **260**, 590 (1982).

[246] C. Y. Na, L. W. Esposito, and T. E. Skinner, J. Geophys. Res. **95**, 7485 (1990).

[247] C. T. Russell and M. G. Kivelson, Science **287**, 1998 (2000).

[248] F. Lique, J. Cernicharo, and P. Cox, Astrophys. J. **653**, 1342 (2006).

[249] E. Martinez-Nunez and A. J. C. Varandas, J. Phys. Chem. A **105**, 5923 (2001).

[250] A. K. Wilson and T. H. D. Jr., J. Phys. Chem. A **108**, 3129 (2004).

[251] M. Kawasaki, K. Kasatani, S. Tanahashi, H. Sato, and Y. Fujimura, J. Chem. Phys. **78**, 7146 (1983).

[252] B. T. Luke and A. D. McLean, J. Phys. Chem. **89**, 4592 (1985).

[253] P. L. M. Plummer, J. Chem. Phys. **92**, 6627 (1990).

[254] S. S. Xantheas and T. H. D. Jr., J. Phys. Chem. **97**, 18 (1993).

[255] S. S. Xantheas and T. H. D. Jr., J. Phys. Chem. **97**, 6616 (1993).

[256] A. J. C. Varandas, J. Chem. Phys. **90**, 4379 (1989).

[257] T. H. D. Jr., J. Chem. Phys. **90**, 1007 (1989).

[258] R. A. Kendall, T. H. D. Jr., and R. J. Harrison, J. Chem. Phys. **92**, 6796 (1996).

[259] D. E. Woon and T. H. D. Jr., J. Chem. Phys. **98**, 1358 (1993).

[260] A. Varandas, J. Mol. Struct.: THEOCHEM **120**, 401 (1985).

[261] A. Varandas, Adv. Chem. Phys. **74**, 255 (1988).

[262] M. Jorfi and P. Honvault, J. Chem. Phys. **133**, 144315 (2010).

[263] M. Jorfi and P. Honvault, Phys. Chem. Chem. Phys. **13**, 8414 (2011).

[264] E. Martinez-Nunez, S. A. Vazquez, and A. J. C. Varandas, Phys. Chem. Chem. Phys. **4**, 279 (2002).

[265] J. L. Jourdain, G. L. Bras, and J. Combourieu, Int. J. Chem. Kinet. **11**, 569 (1979).

[266] K. Sendt and B. S. Haynes, Proc. Combust. Inst. **31**, 257 (2007).

[267] T. Stoecklin, B. Bussery-Honvault, P. Honvault, and F. Dayou, Comput. Theor. Chem. **990**, 39 (2012).

[268] J. M. Bowman, J. Phys. Chem. **95**, 4960 (1991).

[269] P. McGuire and D. J. Kouri, J. Chem. Phys. **60**, 2488 (1974).

[270] R. T. Pack, J. Chem. Phys. **60**, 633 (1974).

[271] S. Goswami, *State-selected and state-to-state dynamics of chemical reactions*, PhD thesis, School of Chemistry, University of Hyderabad, 2017.

[272] A. Zanchet, B. Bussery-Honvault, and P. Honvault, J. Phys. Chem. A **110**, 12017 (2006).

[273] A. Zanchet, B. Bussery-Honvault, M. Jorfi, and P. Honvault, Phys. Chem. Chem. Phys. **11**, 6182 (2009).

[274] N. Bulut, A. Zanchet, P. Honvault, B. Bussery-Honvault, and L. Banares, J. Chem. Phys. **130**, 194303 (2009).

[275] M. Jorfi and P. Honvault, J. Phys. Chem. A **114**, 4742 (2010).

[276] M. Jorfi and P. Honvault, J. Phys. Chem. A **115**, 8791 (2011).

[277] S. Goswami et al., Eur. Phys. J. D. **72**, 225(1 (2018).

[278] R. Guadagnini, G. C. Schatz, and S. P. Walch, J. Chem. Phys. **102**, 774 (1995).

[279] M. H. Ge, T. S. Chu, and K. L. Han, J. Theor. Comput. Chem. **7**, 607 (2008).

[280] M. Jorfi and P. Honvault, J. Phys. Chem. A **113**, 2316 (2009).

[281] N. Bulut, O. Roncero, M. Jorfi, and P. Honvault, J. Chem. Phys. **135**, 104307 (2011).

[282] A. J. H. M. Meijer and E. M. Goldfiled, J. Chem. Phys. **108**, 5404 (1998).

[283] A. J. H. M. Meijer and E. M. Goldfield, J. Chem. Phys. **110**, 870 (1999).

[284] T.-S. Chu and K.-L. Han, Phys. Chem. Chem. Phys. **10**, 2431 (2008).

[285] A. Zanchet et al., J. Chem. Phys. **136**, 164309 (2012).

[286] P. G. Jambrina, M. Menéndez, A. Zanchet, E. García, and F. J. Aoiz, Phys. Chem. Chem. Phys. **21**, 14012 (2019).

[287] W. E. Perreault, N. Mukherjee, and R. N. Zare, J. Chem. Phys. **145**, 154203 (2016).

[288] N. Mukherjee, W. E. Perreault, and R. N. Zare, J. Phys. B: At. Mol. Opt. Phys. **50**, 144005 (2017).

[289] W. E. Perreault, N. Mukherjee, and R. N. Zare, J. Chem. Phys. **150**, 234201 (2019).

[290] W. E. Perreault, H. Zhou, N. Mukherjee, and R. N. Zare, Phys. Rev. Lett. **124**, 163202 (2020).

[291] Y. Wang, W. Wang, Y. Xie, T. Wang, and X. Yang, Rev. Sci. Instrum. **91**, 053001 (2020).

List of publications

[1] Sugata Goswami, **Jayakrushna Sahoo**, T. Rajagopala Rao, B. Bussery-Honvault, Pascal Honvault and S. Mahapatra, "*A theoretical study on the C + OH reaction dynamics and product energy disposal with vibrationally excited reagent*", Eur. Phys. J. D **72**, 225 (2018).

[2] Sugata Goswami[†], **Jayakrushna Sahoo**[†], Suranjan K. Paul, T. Rajagopala Rao, and S. Mahapatra, "*Effect of reagent vibration and rotation on the state-to-state dynamics of the hydrogen exchange reaction, $H + H_2 \rightarrow H_2 + H$*", J. Phys. Chem. A **124**, 9343 (2020)([†] equal contribution).

[3] **Jayakrushna Sahoo**, Ajay Mohan Singh Rawat and S. Mahapatra, "*Theoretical study of the energy disposal mechanism and the state-resolved quantum dynamics of the $H + LiH^+ \rightarrow H_2 + Li^+$ reaction*", J. Phys. Chem. A **125**, 3387 (2021).

[4] **Jayakrushna Sahoo**, Ajay Mohan Singh Rawat and S. Mahapatra, "*Quantum interference in the mechanism of $H + LiH^+ \rightarrow H_2 + Li^+$ reaction dynamics* ", Phys. Chem. Chem. Phys. **23**, 27327 (2021).

[5] **Jayakrushna Sahoo**, Sugata Goswami and S. Mahapatra, "*Understanding the effect of reagent vibrational excitation on the scattering mechanism of the benchmark hydrogen exchange reaction, $H + H_2 \rightarrow H_2 + H$*", (manuscript under preparation).

[6] **Jayakrushna Sahoo**, and S. Mahapatra, "*Electronic nonadiabatic effects in the state-to-state dynamics of the $H + H_2 \rightarrow H_2 + H$ reaction with vibrationally excited reagent*", (manuscript under preparation).

[7] Ajay Mohan Singh Rawat[†], **Jayakrushna Sahoo**[†], and S. Mahapatra, "*A combined quantum mechanical and quasi-classical state-to-state dynamical study to understand the isotopic effect in $H/D + LiH^+/LiD^+ \rightarrow H_2/HD/D_2 + Li^+$ reactions*", (manuscript under preparation, [†] equal contribution).

Posters and Oral presentations in conferences/Symposia

[1] Poster presentation in "16th Theoretical Chemistry Symposium (TCS-2019), 13-16 February, 2019, at BITS Pilani, Pilani campus, Rajasthan, India".

[2] Poster presentation in "CHEMFEST-2019, annual in-house symposium, 22-23 February, 2019, at School of Chemistry, University of Hyderabad, India".

[3] Poster presentation in "CHEMFEST-2020, annual in-house symposium, 27-28 February, 2020, at School of Chemistry, University of Hyderabad, India".

[4] Poster presentation in "The DAE Symposium in Current Trends in Theoretical Chemistry (CTTC-2020), 23-25 September, 2021, (Virtual) by Chemistry Division, Bhabha Atomic Research Centre, Mumbai, India".

[5] Poster presentation in "17th Theoretical Chemistry Symposium (TCS-2021), 11-14 December, 2021, (Virtual) by Department of Chemistry, IISER Kolkata, India".

[6] Oral presentation in "CHEMFEST-2021, 18th annual in-house symposium, 19-20 March, 2021, at School of Chemistry, University of Hyderabad, India".

Time-dependent wave packet dynamics of adiabatic and nonadiabatic reactive scattering

by Jayakrushna Sahoo

Time-dependent wave packet dynamics of adiabatic and nonadiabatic reactive scattering

ORIGINALITY REPORT

33%	8%	31%	1%
SIMILARITY INDEX	INTERNET SOURCES	PUBLICATIONS	STUDENT PAPERS

PRIMARY SOURCES

1	Jayakrushna Sahoo, Ajay Mohan Singh Rawat, S. Mahapatra. " Theoretical Study of the Energy Disposal Mechanism and the State-Resolved Quantum Dynamics of the H + LiH → H + Li Reaction ", The Journal of Physical Chemistry A, 2021 Publication	10%
2	Jayakrushna Sahoo, Ajay Mohan Singh Rawat, Susanta Mahapatra. " Quantum interference in the mechanism of H + LiH → H + Li reaction dynamics ", Physical Chemistry Chemical Physics, 2021 Publication	7%
3	Jayakrushna Sahoo, Ajay Mohan Singh Rawat, S. Mahapatra. " Quantum interference in the mechanism of H + LiH → H + Li reaction dynamics ", Physical Chemistry Chemical Physics, 2021 Publication	3%

4	Sugata Goswami, Jayakrushna Sahoo, Suranjan K. Paul, T. Rajagopala Rao, S. Mahapatra. " Effect of Reagent Vibration and Rotation on the State-to-State Dynamics of the Hydrogen Exchange Reaction, H + H → H + H ", The Journal of Physical Chemistry A, 2020 Publication	3%
5	chemistry.uohyd.ac.in Internet Source	2%
6	Submitted to Curtin University of Technology Student Paper	1%
7	Sugata Goswami, T. Rajagopala Rao, S. Mahapatra, B. Bussery-Honvault, P. Honvault. "Time-Dependent Quantum Wave Packet Dynamics of S + OH Reaction on Its Electronic Ground State", The Journal of Physical Chemistry A, 2014 Publication	<1%
8	epdf.pub Internet Source	<1%
9	"The Jahn-Teller Effect", Springer Science and Business Media LLC, 2009 Publication	<1%
10	B. Jayachander Rao, R. Padmanaban, S. Mahapatra.. "Nonadiabatic quantum wave	<1%

S Mahapatra

Susanta Mahapatra
Professor
School of Chemistry
University of Hyderabad
Hyderabad-500 046 A.P Indi

packet dynamics of H+H2 (HD) reactions", Chemical Physics, 2007
Publication

---

11 Sugata Goswami, Jayakrushna Sahoo, Tammineni Rajagopala Rao, Béatrice Bussery-Honvault, Pascal Honvault, Susanta Mahapatra. "A theoretical study on the C + OH reaction dynamics and product energy disposal with vibrationally excited reagent", The European Physical Journal D, 2018
Publication

<1 %

---

12 Sugata Goswami, B. Bussery-Honvault, P. Honvault, S. Mahapatra. " Effect of internal excitations of reagent diatom on initial state-selected dynamics of C + OH reaction on its second excited (1 ") electronic state ", Molecular Physics, 2017
Publication

<1 %

---

13 Susanta Mahapatra, Horst Köppel, Lorenz S. Cederbaum. " Reactive Scattering Dynamics on Conically Intersecting Potential Energy Surfaces: The H + H Exchange Reaction ", The Journal of Physical Chemistry A, 2001
Publication

<1 %

---

14 Sugata Goswami, Juan Carlos San Vicente Veliz, Meenu Upadhyay, Raymond J. Bemish, Markus Meuwly. " Quantum and Quasi-classical Dynamics of the C(P) + O (Σ) →CO(

<1 %

Σ)+O(D) Reaction on Its Electronic Ground State ", Physical Chemistry Chemical Physics, 2022
Publication

15	dokumentix.ub.uni-siegen.de Internet Source	<1 %
16	T. Rajagopala Rao, B. Jayachander Rao, S. Mahapatra. "Quantum nonadiabatic dynamics of hydrogen exchange reactions", Chemical Physics, 2009 Publication	<1 %
17	Foudhil Bouakline, Stuart C. Althorpe, Pascal Larregaray, Laurent Bonnet. "Strong geometric-phase effects in the hydrogen-exchange reaction at high collision energies: II. Quasiclassical trajectory analysis", Molecular Physics, 2010 Publication	<1 %
18	Foudhil Bouakline, Stuart C. Althorpe, Daniel Peláez Ruiz. "Strong geometric-phase effects in the hydrogen-exchange reaction at high collision energies", The Journal of Chemical Physics, 2008 Publication	<1 %
19	Jun Li, Bin Zhao, Daiqian Xie, Hua Guo. "Advances and New Challenges to Bimolecular Reaction Dynamics Theory", The Journal of Physical Chemistry Letters, 2020	<1 %

Publication

20	aip.scitation.org Internet Source	<1 %
21	resolver.caltech.edu Internet Source	<1 %
22	Xiaohu He, Hui Wu, Peiyu Zhang, Yan Zhang. " Quantum State-to-State Dynamics of the H + LiH → H + Li Reaction ", The Journal of Physical Chemistry A, 2015 Publication	<1 %
23	F. J. Aoiz *, L. BaÑares, V. J. Herrero. " The H+H reactive system. Progress in the study of the dynamics of the simplest reaction ", International Reviews in Physical Chemistry, 2005 Publication	<1 %
24	Xiaohu He, Shuangjiang Lv, Tasawar Hayat, Keli Han. " Potential Energy Surfaces for the First Two Lowest-Lying Electronic States of the LiH System, and Dynamics of the H + LiH ⇌ H + Li + Reactions ", The Journal of Physical Chemistry A, 2016 Publication	<1 %
25	www.fulviofrisone.com Internet Source	<1 %
26	"Theory of Chemical Reaction Dynamics", Springer Nature, 2005	<1 %

	Publication	
27	pubs.rsc.org Internet Source	<1 %
28	www.ncbi.nlm.nih.gov Internet Source	<1 %
29	Bayaer Buren, Maodu Chen. "Stereodynamics-Controlled Product Branching in the Nonadiabatic H + NaD → Na(3s, 3p) + HD Reaction at Low Temperatures", The Journal of Physical Chemistry A, 2022 Publication	<1 %
30	F. J. Aoiz, L. Bañares, V. J. Herrero. " Dynamics of Insertion Reactions of H Molecules with Excited Atoms ", The Journal of Physical Chemistry A, 2006 Publication	<1 %
31	Sandip Ghosh, Tapas Sahoo, Michael Baer, Satrajit Adhikari. " Charge Transfer Processes for H + H Reaction Employing Coupled 3D Wavepacket Approach on Beyond Born–Oppenheimer Based Ab Initio Constructed Diabatic Potential Energy Surfaces ", The Journal of Physical Chemistry A, 2021 Publication	<1 %
32	T. Rajagopala Rao, Sugata Goswami, S. Mahapatra, B. Bussery-Honvault, P. Honvault.	<1 %

"Time-dependent quantum wave packet dynamics of the C + OH reaction on the excited electronic state", The Journal of Chemical Physics, 2013
Publication

33	authors.library.caltech.edu Internet Source	<1 %
34	Jing Zhang, Shou-Bao Gao, Hui Wu, Qing-Tian Meng. " State-to-State Quantum Dynamics of Reactions O(P) + HD (= 0–1, = 0) → OH+D and OD+H: Reaction Mechanism and Vibrational Excitation ", The Journal of Physical Chemistry A, 2015 Publication	<1 %
35	B. Jayachander Rao. "Nonadiabatic quantum wave packet dynamics of the H + H2 reaction including the coriolis coupling", Journal of Chemical Sciences, 09/2009 Publication	<1 %
36	R. Padmanaban, S. Mahapatra. "Coriolis-Coupled Wave Packet Dynamics of H + HLi Reaction", The Journal of Physical Chemistry A, 2006 Publication	<1 %
37	Tanmoy Roy, S. Mahapatra. "H + LiH + collision dynamics at ultracold temperature conditions", Chemical Physics, 2015 Publication	<1 %

38	A. Zanchet, O. Roncero, T. González-Lezana, A. Rodríguez-López, A. Aguado, C. Sanz-Sanz, S. Gómez-Carrasco. " Differential Cross Sections and Product Rotational Polarization in A + BC Reactions Using Wave Packet Methods: H + D and Li + HF Examples ", The Journal of Physical Chemistry A, 2009 Publication	<1 %
39	Ye Mao, Bayaer Buren, Zijiang Yang, Maodu Chen. " Electronically Nonadiabatic Effects on the Quantum Dynamics of the H + BeH → Be + H H ; H + BeH Reactions ", The Journal of Physical Chemistry A, 2022 Publication	<1 %
40	Debasish Koner, Lizandra Barrios, Tomás González-Lezana, Aditya N. Panda. " Quantum, Statistical, and Quasiclassical Trajectory Studies For the Ne + HeH → NeH + He Reaction on the Ground Electronic State ", The Journal of Physical Chemistry A, 2015 Publication	<1 %
41	Koushik Naskar, Sandip Ghosh, Satrajit Adhikari. " Accurate Calculation of Rate Constant and Isotope Effect for the F + H Reaction by the Coupled 3D Time-Dependent Wave Packet Method on the Newly Constructed Ground Potential Energy Surface ", The Journal of Physical Chemistry A, 2022 Publication	<1 %

42	Boyi Zhou, Benhui Yang, N. Balakrishnan, B. K. Kendrick, P. C. Stancil. "Prediction of a Feshbach Resonance in the Below-the-Barrier Reactive Scattering of Vibrationally Excited HD withH", The Journal of Physical Chemistry Letters, 2020 Publication	<1 %
43	Chang Luo, Yuxin Tan, Shihao Li, Zhibing Lu, Yiyang Shu, Wentao Chen, Daofu Yuan, Xueming Yang, Xingan Wang. " Crossed Molecular Beam Study of the H + HD → H + D Reaction at 0.60 and 1.26 eV Using the Near-Threshold Ionization Velocity Map Ion Imaging ", The Journal of Physical Chemistry A, 2022 Publication	<1 %
44	Haixiang He, Weimin Zhu, Wenli Su, Lihui Dong, Bin Li. " Accurate Quantum Wave Packet Study of the Deep Well D + HD Reaction: Product Ro-vibrational State-Resolved Integral and Differential Cross Sections ", The Journal of Physical Chemistry A, 2018 Publication	<1 %
45	Brian K. Kendrick. " Nonadiabatic Ultracold Quantum Reactive Scattering of Hydrogen with Vibrationally Excited HD(= 5–9) ", The Journal of Physical Chemistry A, 2019 Publication	<1 %

46	P. D. D. Monks, J. N. L. Connor, F. Bouakline. " Filtering Reaction Dynamics Using Nearside−Farside Theory and Local Angular Momentum Theory: Application to the Angular Scattering of the H + D (= 0, = 0) → HD(= 3, = 0) + D Reaction in the Energy and Time Domains ", The Journal of Physical Chemistry A, 2009 Publication	<1 %
47	Nadia Balucani, Piergiorgio Casavecchia, Luis Bañares, F. Javier Aoiz et al. " Experimental and Theoretical Differential Cross Sections for the N(D) + H Reaction ", The Journal of Physical Chemistry A, 2006 Publication	<1 %
48	Alexey Teslja, James J. Valentini. "State-to-state reaction dynamics: A selective review", The Journal of Chemical Physics, 2006 Publication	<1 %
49	Francisco J. Aoiz, Luis Bañares. " Reaction Cross Sections and Rate Constants for the Cl + H (D) → HCl(DCl) + H(D) Reaction from Quasiclassical Trajectory Calculations on an Potential Energy Surface ", The Journal of Physical Chemistry, 1996 Publication	<1 %
50	Zhigang Sun, Xin Lin, Soo-Y. Lee, Dong H. Zhang. " A Reactant-Coordinate-Based Time-	<1 %

Dependent Wave Packet Method for Triatomic State-to-State Reaction Dynamics: Application to the H + O Reaction ", The Journal of Physical Chemistry A, 2009
Publication

---

51 Debasish Koner, Lizandra Barrios, Tomás González-Lezana, Aditya N. Panda. " State-to-State Dynamics of the Ne + HeH (= 0, = 0) → NeH (', ') + He Reaction ", The Journal of Physical Chemistry A, 2016
Publication

<1 %

---

52 B. Jayachander Rao, S. Mahapatra. "Quantum wave packet dynamics of N(D2)+H2 reaction", The Journal of Chemical Physics, 2007
Publication

<1 %

---

53 Ahmad W. Huran, L. González-Sánchez, S. Gomez-Carrasco, J. Aldegunde. " A Quantum Mechanical Study of the – and '– ' Vector Correlations for the H + LiH → Li + H Reaction ", The Journal of Physical Chemistry A, 2017
Publication

<1 %

---

54 Tanmoy Roy, S. Mahapatra. "Quantum dynamics of H + LiH reaction and its isotopic variants", The Journal of Chemical Physics, 2012
Publication

<1 %

---

55 hdl.handle.net
Internet Source

<1 %

56	etheses.dur.ac.uk Internet Source	<1%
57	N. Balakrishnan. "Perspective: Ultracold molecules and the dawn of cold controlled chemistry", The Journal of Chemical Physics, 2016 Publication	<1%
58	Tiangang Yang, Long Huang, Tao Wang, Chunlei Xiao, Yurun Xie, Zhigang Sun, Dongxu Dai, Maodu Chen, Donghui Zhang, Xueming Yang. " Effect of Reagent Vibrational Excitation on the Dynamics of F + H (= 1, = 0) → HF(', ') + H Reaction ", The Journal of Physical Chemistry A, 2015 Publication	<1%
59	Tomás González-Lezana, Yohann Scribano, Pascal Honvault. " The D + H Reaction: Differential and Integral Cross Sections at Low Energy and Rate Constants at Low Temperature ", The Journal of Physical Chemistry A, 2014 Publication	<1%
60	"New methods for quantum mechanical reaction dynamics", 'Office of Scientific and Technical Information (OSTI)' Internet Source	<1%

61	Hong Gao, Mahima Sneha, Foudhil Bouakline, Stuart C. Althorpe, Richard N. Zare. " Differential Cross Sections for the H + D → HD(' = 3, ' = 4–10) + D Reaction above the Conical Intersection ", The Journal of Physical Chemistry A, 2015 Publication	<1 %
62	Tomás González-Lezana. "Statistical quantum studies on insertion atom–diatom reactions", International Reviews in Physical Chemistry, 2007 Publication	<1 %
63	M. Jorfi, P. Honvault. " Quantum Dynamics at the State-to-State Level of the C + OH Reaction on the First Excited Potential Energy Surface ", The Journal of Physical Chemistry A, 2010 Publication	<1 %
64	M. Jorfi, P. Honvault. "State-to-State Quantum Dynamics Calculations of the C + OH Reaction on the Second Excited Potential Energy Surface", The Journal of Physical Chemistry A, 2011 Publication	<1 %
65	cjcp.ustc.edu.cn Internet Source	<1 %

66	F. J. Aoiz, L. Bañares, V. J. Herrero, V. Sáez Rábanos, I. Tanarro. " The H + D → HD + D Reaction. Quasiclassical Trajectory Study of Cross Sections, Rate Constants, and Kinetic Isotope Effect ", The Journal of Physical Chemistry A, 1997 Publication	<1 %
67	Submitted to Indian Institute of Technology, Madras Student Paper	<1 %
68	Submitted to Alvernia University Student Paper	<1 %
69	Jisha Hazra, Brian K. Kendrick, Naduvalath Balakrishnan. "Importance of Geometric Phase Effects in Ultracold Chemistry", The Journal of Physical Chemistry A, 2015 Publication	<1 %
70	N. Bulut, J.F. Castillo, P. G. Jambrina, J. Kłos, O. Roncero, F. J. Aoiz, L. Bañares. " Accurate Time-Dependent Wave Packet Calculations for the O + H → OH + H Ion–Molecule Reaction ", The Journal of Physical Chemistry A, 2015 Publication	<1 %
71	Alejandro Rivero Santamaría, Fabrice Dayou, Jesus Rubayo-Soneira, Maurice Monnerville. "Time-Dependent Quantum Wave Packet Study of the Si + OH → SiO + H Reaction:	<1 %

Cross Sections and Rate Constants", The Journal of Physical Chemistry A, 2017
Publication

72 Cleghorn, William. "Mechanics of Machines", Oxford University Press <1%
Publication

73 Jadson Jose Monteiro Oliveira. "Unsupervised Dimensionality Reduction in Big Data via Massive Parallel Processing with MapReduce and Resilient Distributed Datasets", Universidade de Sao Paulo, Agencia USP de Gestao da Informacao Academica (AGUIA), 2020 <1%
Publication

74 McKee, James R & McKee, Trudy. "Biochemistry- The Molecular Basis of Life", Oxford University Press, 2020 <1%
Publication

75 Di He, Jiuchuang Yuan, Maodu Chen. "Influence of rovibrational excitation on the non-diabatic state-to-state dynamics for the Li(2p) + H2 → LiH + H reaction", Scientific Reports, 2017 <1%
Publication

76 Jordi Mayneris, José Daniel Sierra, Miguel González. "Time dependent quantum dynamics study of the Ne+H2+(v=0– <1%

4)→NeH++H proton transfer reaction", The Journal of Chemical Physics, 2008
Publication

77 Daofu Yuan, Wentao Chen, Chang Luo, Yuxin Tan, Shihao Li, Yin Huang, Zhigang Sun, Xueming Yang, Xingan Wang. " Imaging the State-to-State Dynamics of the H + D → HD + D Reaction at 1.42 eV ", The Journal of Physical Chemistry Letters, 2020 <1%
Publication

78 Jayachander Rao, B.. "Nonadiabatic quantum wave packet dynamics of H+H"2 (HD) reactions", Chemical Physics, 20070330 <1%
Publication

Exclude quotes	On	Exclude matches	< 14 words
Exclude bibliography	On		